PONTIFICIA UNIVERSIDAD CATÓLICA DEL PERÚ

ESCUELA DE POSTGRADO

PONTIFICIA UNIVERSIDAD CATÓLICA DEL PERÚ

Optical characterization and thermal activation of Tb doped amorphous SiC, AlN and SiN thin films

A thesis submitted for the degree of

Doctor in Physics

presented by

Jorge Andrés Guerra Torres

Advisors:

Prof. Dr. Albrecht Winnacker

Prof. Dr. Roland Weingärtner

Lima 2017

Tesis publicada con autorización del autor
No olvide citar esta tesis

PUCP

“Optical characterization and thermal activation of Tb doped amorphous SiC, AlN and SiN thin films”

Optische Charakterisierung und thermische Aktivierung von Tb-dotierten amorphen SiC, AlN und SiN Dünnfilmen

Der Technischen Fakultät der Friedrich-Alexander Universität Erlangen-Nürnberg zur Erlangung des Grades

DOKTOR-INGENIEUR

vorgelegt von

Jorge Andres Guerra Torres

aus

Miranda / Venezuela

Tesis publicada con autorización del autor
No olvide citar esta tesis

PUCP

Als Dissertation genehmigt von
der Technischen Fakultät der

Friedrich-Alexander-Universität Erlangen-Nürnberg

Tag der mündlichen Prüfung: 10.05.2017

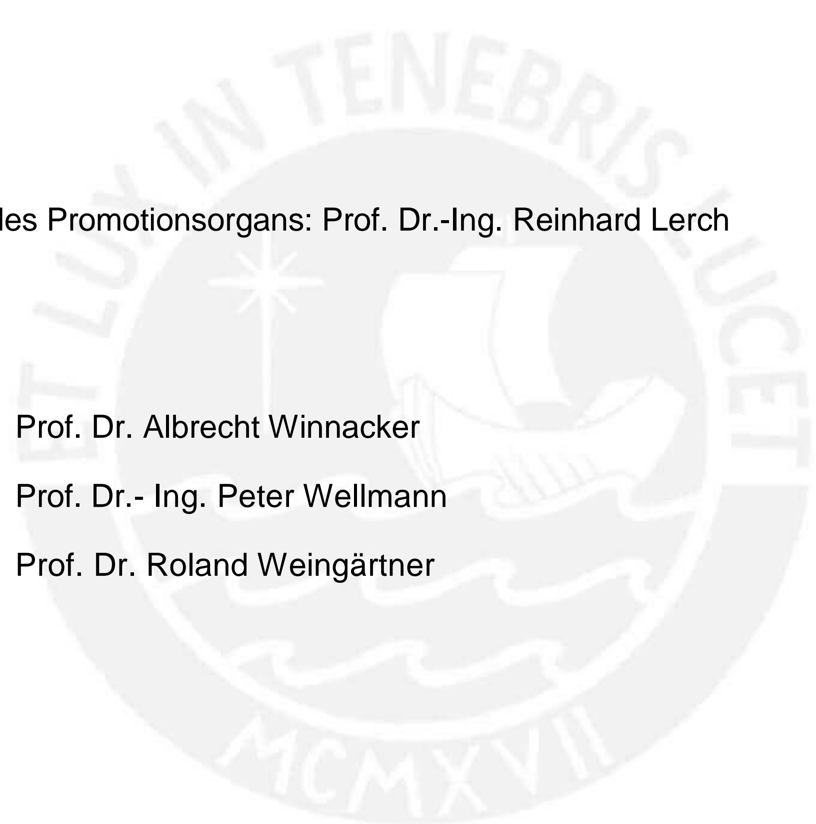

Vorsitzender des Promotionsorgans: Prof. Dr.-Ing. Reinhard Lerch

Gutachter/in: Prof. Dr. Albrecht Winnacker

Prof. Dr.- Ing. Peter Wellmann

Prof. Dr. Roland Weingärtner

Tesis publicada con autorización del autor
No olvide citar esta tesis

PUCP

This page was intentionally left in blank

Tesis publicada con autorización del autor
No olvide citar esta tesis

Zusammenfassung (Deutsch)

In dieser Arbeit werden die optischen Eigenschaften und die Lichtemission der dünnen amorphen Schichten AlN, SiN und SiC:H dotiert mit Tb untersucht. Die optische Charakterisierung beschränkt sich auf die Bestimmung der Bandlücke, der Urbachenergie und den Urbachfokus. Basierend auf thermischen Fluktuationen der Bandlücke wird ein Modell entwickelt, welches die fundamentale Absorption in Überlapp mit den Urbachausläufern beschreibt. Es wird die Existenz und die Bedeutung des Urbachfokus analysiert und mit dem vorher entwickelten Modell verglichen. Eine der wichtigsten Ergebnisse dieser Untersuchungen ist die Fähigkeit dieses Modells, den Urbach-Bereich von dem Tauc-Bereich des Abrorptionskoeffizienten zu trennen. Zum Beispiel zeigen dünne Filme aus SiC:H abgeschieden mit unterschiedlichen Wasserstoffflüssen unter Verwendung dieses Modells eine Bandlücke, die nicht mit der Urbach-Energie korreliert ist. Dies unterscheidet sich typischerweise von der Beobachtung der Bandlückenvariation unter Verwendung des Tauc-Modells. Die Untersuchung der Lichtemission konzentriert sich auf den Prozess der thermischen Aktivierung, welchen die Seltenerdionen bei Ausheilung der Proben erleiden. Der Effekt der Ausheiltemperatur, der Probentemperatur und der Konzentration der Seltenen Erden auf die Intensität der Lichtemission wird mit Anregung von Photonen und Elektronen untersucht. Es wird ein Änderungsratenmodell der Übergänge verwendet, um die globale mit Tb assoziierte Lichtemission der dünnen *a*-SiC:H:Tb^{3+}, Schichten in Abhängigkeit von der Konzentration by verschiedenen Ausheiltemperaturen zu modellieren. Es konnte eine Aktivierungsenergie der thermischen Aktivierung bestimmt werden. Zuletzt beobachtet man im Falle von *a*-SiC:H:Tb^{3+} eine Verminderung der Unterdrückung der Konzentration, welches ein Hinweis darauf ist, dass ein zusätzlicher Mechanismus für die Erhöhung der Lichtemission mit der Tb Konzentration verantwortlich ist.

Abstract (English)

In the present thesis the optical properties and light emission features of Tb-doped amorphous AlN, SiN and SiC:H thin films are assessed. The optical characterization is focused in the determination of the bandgap, Urbach energy and Urbach focus from optical measurements. A model, based on thermal band-fluctuations, to describe the fundamental absorption overlapped with Urbach tails is developed. Thenceforth, an analysis of the existence and meaning of the Urbach focus is performed and contrasted with the latter model. One of the main results in this part is the capability of aforementioned model to distinguish the Urbach and Tauc regions of the absorption coefficient. In this matter, *a*-SiC:H thin films grown with distinct hydrogen dilution conditions exhibited an uncorrelated bandgap with the Urbach energy when using this model, contrary to what is typically observed after applying the Tauc model. The light emission features analysis is concerned with the thermal activation process that rare earth ions suffer when annealing the samples. The effect of the annealing temperature, sample temperature and rare earth concentration on the light emission intensity is assessed under photon and electron excitation sources. A rate equation model is used to fit the overall Tb-related intensity of *a*-SiC:H:Tb^{3+} versus the Tb concentration after different annealing temperatures. An activation energy associated to the thermal activation is recovered. Finally, in the case of *a*-SiC:H:Tb^{3+} a diminution of the concentration quenching effect is observed suggesting an additional mechanism to enhance the Tb-related light emission intensity.

Tesis publicada con autorización del autor
No olvide citar esta tesis
ET LUX IN TENEBRIS LUCET MCMXVII PUCP

Resumen (Español)

En la presente tesis se evalúan las propiedades ópticas y las características de emisión de luz de películas delgadas amorfas de AlN, SiN y SiC:H dopadas con Tb. La caracterización óptica se centra en la determinación del ancho de banda, la energía de Urbach y el foco de Urbach a partir de mediciones ópticas. Se desarrolla un modelo, basado en fluctuaciones térmicas de la banda, para describir la absorción fundamental sobrepuesta con las colas de Urbach. Luego, se realiza un análisis de la existencia y significado del foco de Urbach y se contrasta con modelo anterior. Uno de los principales resultados en esta parte es la capacidad del modelo antes mencionado para distinguir las regiones de Urbach y Tauc del coeficiente de absorción. En este caso, películas delgadas de *a*-SiC:H depositadas en distintas condiciones de dilución de hidrógeno exhibieron un ancho de banda no correlacionado con la energía de Urbach al usar este modelo, en contraste a lo que se observa típicamente después de utilizar el modelo de Tauc. El análisis de características de emisión de luz se centra al proceso de activación térmica que sufren los iones de tierras raras cuando se calientan las muestras. El efecto de la temperatura de recocido, temperatura de la muestra y concentración de tierras raras en la intensidad de la emisión de luz se evalúa bajo fuentes de excitación de fotones y electrones. Se utiliza un modelo de tasa de transiciones para ajustar la intensidad de luz global asociada al Tb en películas delgadas de *a*-SiC:H:Tb^{3+} frente a la concentración de Tb después de diferentes temperaturas de recocido. Se recupera una energía de activación asociada a la activación térmica. Finalmente, en el caso de *a*-SiC: H: Tb^{3+}, se observa una disminución del efecto de enfriamiento de la concentración, lo que sugiere un mecanismo adicional para aumentar la intensidad de emisión de luz relacionada con Tb.

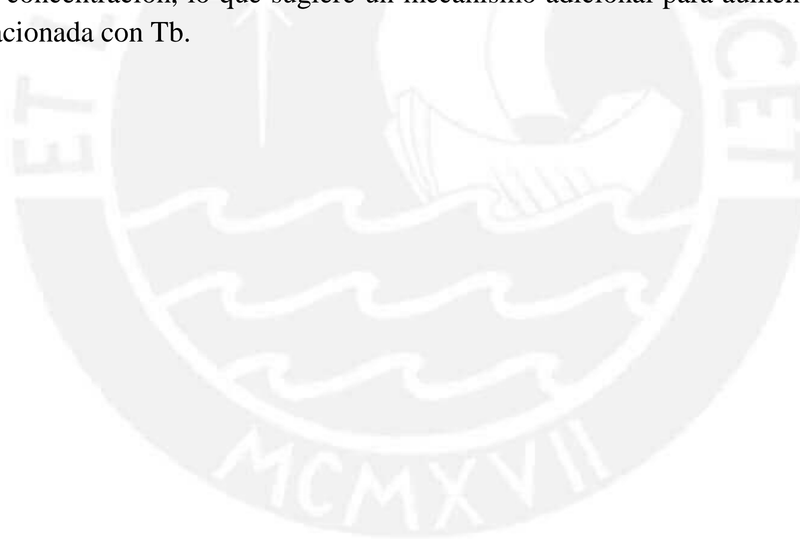

Tesis publicada con autorización del autor
No olvide citar esta tesis
PUCP

to my family

Tesis publicada con autorización del autor
No olvide citar esta tesis

PUCP

Acknowledgments

I wish to thank my advisors, Prof. Dr. Albrecht Winnacker (FAU) and Prof. Dr. Roland Weingärtner (PUCP) for their constant support and advice and for introducing me in the exciting subject of materials science, especially in the topics which constitute this thesis work. I would like to mention the efforts invested by my advisors to initiate the successful collaboration between the PUCP and the University of Erlangen since 2005. This collaboration is being continued by Dr. Miroslav Batentschuk. My doctorate was developed within the framework of this collaboration.

The research conducted in this work was founded by the Research Management Office (DGI) of the Pontificia Universidad Católica del Perú (PUCP) and by the PhD scholarship Huiracocha. Additional support has been provided by the German Academic Exchange Service (DAAD) under the contract number A13-93251. I am indebted to Prof. Dr. F. Alvarez (UNICAMP, Brazil) for opening his lab in order to perform the XPS measurements on the SiC:H:Tb samples, to Prof. Dr. A. R. Zanatta (IFSC-USP, Brazil) for his valuable collaboration and for providing access to his lab in order to perform the PL measurements of the SiC:H:Tb samples and to the late Prof. Dr. H.P Strunk (Stuttgart-University, Germany) for his collaboration and for helping us with the PLE and TEM measurements and for providing us with the polycrystalline AlN samples. I also thank Prof. Dr. M. Bickermann, Prof. Dr. M. Albrecht, Dr. K. Irmscher, and Dr. T. Schulz (IKZ, Germany) for receiving me and providing access to their labs, where I performed the temperature-dependent CL and PL measurements and further feedback. My thanks go also to all other colleagues, collaborators and students that are currently working in related topics.

Tesis publicada con autorización del autor
No olvide citar esta tesis
ET LUX IN TENEBRIS LUCET MCMXVII PUCP

DEDICATORY 1

ACKNOWLEDGMENTS 2

INTRODUCTION 5

GENERAL BACKGROUND 7

2.1 SPUTTERING PRINCIPLES 7
2.2 OPTICAL PROPERTIES OF THIN FILMS 8
2.3 DETERMINATION OF THE OPTICAL CONSTANTS OF THIN FILMS 10
2.4 RARE EARTH DOPED MATERIALS 16

FUNDAMENTAL THEORY 20

3.1 OPTICAL PROPERTIES OF AMORPHOUS SEMICONDUCTORS 20
ELECTRONIC DENSITY OF STATES 21
DEFECT STATES IN AMORPHOUS SEMICONDUCTORS 23
FUNDAMENTAL ABSORPTION IN AMORPHOUS SEMICONDUCTORS 27
THE URBACH EDGE 30
ON THE ORIGIN OF THE URBACH RULE AND THE URBACH FOCUS 32
3.2 LUMINESCENT PROPERTIES OF RE DOPED MATERIALS 44
ELEMENTARY FEATURES 46
HAMILTONIAN OF A RE ION IN A SOLID 51
CRYSTAL FIELD INTERACTION 55
INDUCED ELECTRIC DIPOLE TRANSITIONS AND RADIATIVE LIFETIMES 60
NON-RADIATIVE DECAY 66
ENERGY TRANSFER PROCESSES 70

EXPERIMENTAL DETAILS 78

4.1 DEPOSITION 78
4.2 OPTICAL CHARACTERIZATION TECHNIQUES 79
UV-VIS TRANSMITTANCE 79
LIGHT EMISSION CHARACTERIZATION 80
INFRARED ABSORPTION BY FOURIER TRANSFORM SPECTROSCOPY (FTIR) 80
4.3 ANNEALING TREATMENTS 82
4.4 TERBIUM CONCENTRATION DETERMINATION 82

RESULTS AND DISCUSSION 87

Tesis publicada con autorización del autor
No olvide citar esta tesis
PUCP

5.1 Optical characterization of the amorphous AlN, SiN and SiC:H_x thin films **87**
Bandgap and Urbach energy 88
The Urbach focus and the Orapunt & O'Leary analysis 101
5.2 Tb^{3+} doped SiN, AlN and SiC:H light emission properties **110**
The emission 111
Concentration quenching 121
Thermal activation 127
Temperature dependent measurements 133

SUMMARY AND CONCLUDING REMARKS **141**

The optical bandgap and the Urbach focus 141
Rare earth thermal activation 143
Temperature dependent luminescence 144

APPENDIX **146**

A.1 Optical constants and thickness determination of dielectric thin films from single optical transmittance measurements **146**
The thin film assembly 147
The envelope method and our improvements 148
Simulation of the transmittance curve 152
Recovery of the simulated transmittance and comparison of the three methods 153
Confidence analysis 156
Final remarks 159
A.2 Multiphonon transitions **161**
A.3 Up-conversion **163**
A.4 On the conversion of atomic concentration of RE into average ion interdistance **164**
On the conversion of the atomic concentration of REs into number density 164
Distribution of the nearest neighbor in a random distribution of particles 166

REFERENCES **170**

Tesis publicada con autorización del autor
No olvide citar esta tesis
PUCP

Introduction

The interest on new light sources especially the study of the light emission from rare-earth (RE) ions has been on a steady growth during the past decades. The trends for this are twofold. First, the increasing demand for optical sources and amplifiers operating at wavelengths compatible with fiber communications technology has been driving most of the research in past years. This is mainly due to the fortunate coincidence between the Er^{3+} emission band at 1535 nm and the principal low-loss spectral region in the optical absorption of aluminosilicate optical fiber [Ken02, Zav03, Ste99, Abe11]. However, the technological interest on RE luminescence reaches applications in displays, laser materials, radiation detection and medical applications [Wan09]. Second, there is currently a tremendous concern in the application of RE doped materials for solar energy conversion. This is owing to the fact that the RE-host and RE-RE interaction opens the possibility to processes known as photon up-conversion and photon down-conversion. In the latter to low energy photon are absorbed by a single RE to emit a single higher energy photon. In the down-conversion case, a high energy photon is absorbed to produce two low energy photons. RE doped luminescent materials exhibit unique down-conversion and up-conversion properties. They offer the effective use of high-energy photons without energy loss upon thermalization and sub-bandgap energy photons that are otherwise lost in solar cells. In this way opening the possibility to increase the spectral efficiency of silicon based solar cells [Sha07, Wan11, Lia13, Wan14]. In this context, a deeper understanding of the activation process, the connection between the thermal activation and the effect of the host matrix in the overall efficiency is necessary.

RE elements possess unique optical and electronic properties due to their electronic structure. For instance, their light emission spectra do not depend on the host material. This fact makes RE-doped materials suitable candidates for light emission applications as an alternative to direct electronic transitions devices [Ste99, Ric02, Lee03, Ada07, Wak08]. Additionally, wide-bandgap semiconductors are transparent to visible light and thus allow the output of the RE emission which can cover the colors blue (Tm), green

Tesis publicada con autorización del autor
No olvide citar esta tesis
PUCP

(Tb), and red (Eu). Moreover, conventional semiconductors like silicon are known to quench any RE emission at room temperature, and thus are not suitable for technical applications. Wide-bandgap semiconductors are known to overcome the latter problem [Zan03]. However, a new channel of light intensity loss is introduced when using RE doped semiconductors, the concentration quenching effect. The more close-packed the RE ions are, the higher the chance to lose the energy by a non-radiative electronic transition. On the other hand, the RE light emission intensity can be enhanced through post thermal annealing treatments and/or by bandgap engineering of the host matrix [Wei06, Abe11, Gue15]. Concerning the latter matter, the effect of thermal annealing treatments on the activation mechanism of RE doped wide-bandgap semiconductors is still under discussion [Jan07, Zan09, Abe11, Gue13].

The present work is divided in two main subjects. The optical properties of amorphous SiC:H, AlN and SiN thin films, and the light emission properties of the Tb doped versions of the same materials. In the first part, the mayor concern of the study of the optical properties is the calculation of the optical bandgap of these three materials in amorphous state. The structural dependent and independent parameters such as the Urbach energy and Urbach focus are identified in the three materials under study. We try to shed some light on the meaning of the Urbach focus and the definition of the bandgap of amorphous materials. In order to do so, a new model for the fundamental absorption of amorphous semiconductors is proposed. From this model is possible to recover the Urbach rule and the Tauc models merged in a single equation. The second mayor part is focused on the light emission properties of the Tb^{3+} when embedded in the aforementioned materials. The concentration quenching and thermal activation are the main interest. The effect of thermal annealing treatments on the optical activation of Tb ions is evaluated. Further temperature dependent analysis is presented upon CL and PL excitation means in order to develop some insights concerning the principal excitation process.

Tesis publicada con autorización del autor
No olvide citar esta tesis
ET LUX IN TENEBRIS LUCET MCMXVII PUCP

General background

2.1 Sputtering principles

Sputtering is a physical process in which a material called target is bombarded with accelerated ions in order to rip off atoms and molecules from its surface. These ripped particles called sputtered particles usually retain the chemical and physical properties of the target. The sputtered particles are subsequently thrown to a different surface called substrate growing a thin film made of the target's material. The process can be compared to shooting steel balls to a concrete wall which acts as a target. Upon impact, the balls tear apart fragments of concrete. On a continuous process, surfaces in the vicinity of the impact are covered with a layer of concrete powder. This dust is equivalent in some extent to the deposited film.

The sputtering process takes place in an evacuated chamber with a continuous flow of argon (and/or nitrogen) which is then ionized. The typical pressures during the deposition process range from 10^{-3} to 10^{-1} mbar. The target is kept at negative potential (cathode) relative to the charged ions from the ionized gas. When the ions with a high kinetic energy strike the cathode, the collisions sputter material from the target. The basic principle of this technique is the momentum transfer from the accelerated ions to the target's surface (see figure 2.1.1). The ions generally do not become implanted in the target, but they slam onto it and then return to the chamber atmosphere. The released material settles on any surface in the chamber. The plasma is ignited between the cathode and anode caused by a high voltage which can be either direct (DC) or alternate (radio frequency, RF). Furthermore, a magnetic field (magnetron sputtering) can be used to densify the plasma near the target in order to increase the deposition rate. The main asset of the RF sputtering over the DC sputtering is the possibility to sputter insulating targets. This feature is owned to the fact that in RF sputtering the positive charge build up on the target (cathode) is avoided by the alternating potential, whereas in the DC case the charge build up reduce considerably the sputtering rate.

Tesis publicada con autorización del autor
No olvide citar esta tesis
ET LUX IN TENEBRIS LUCET MCMXVII PUCP

Additionally, the gas ions can react with the target's atoms to form a new compound different from the target's material. For instance, if we use Si, Ga, or Al as targets and nitrogen as ionized gas, we are able to grow Si_3N_4, GaN or AlN. The structure and stoichiometry of the subsequent thin film will depend besides of the target material, on the substrate's temperature, gas mixtures, gasses partial pressures and sputtering power. Finally, sputtering two targets at the same time (co-sputtering) allow for other compounds possibilities or even doping (see figure 2.1.1).

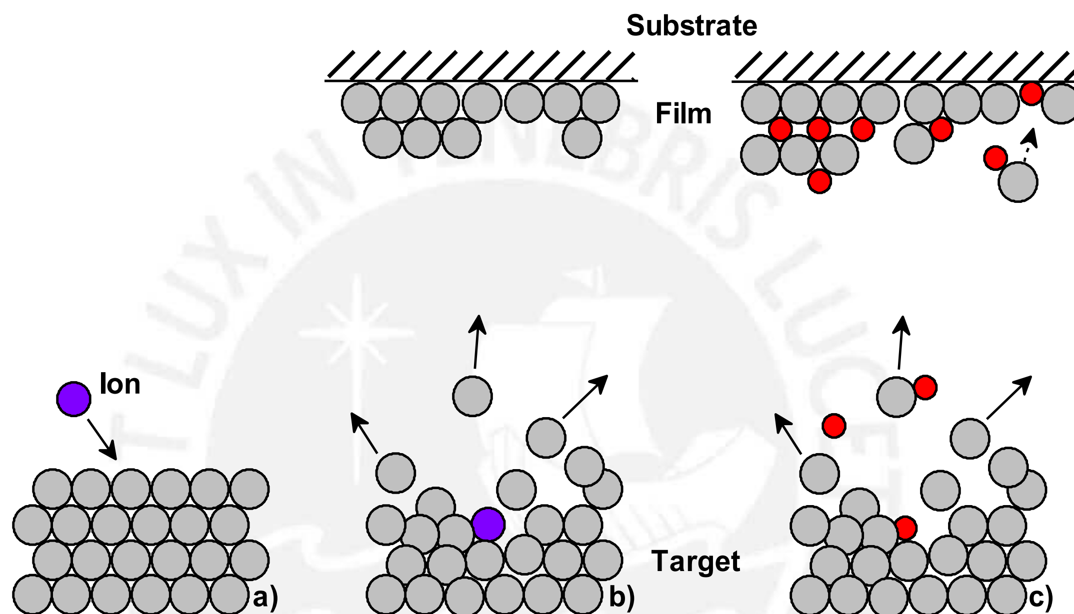

Figure 2.1.1. An ion (e.g. Ar^+) carrying kinetic energy is directed towards the target's surface (a). The impact transfers momentum to the target and releases material that settles on a substrate (b). The sputtering process can be reactive if the ionized gas (e.g. N^+) bonds to the target's atoms, thus forming a different compound (c).

2.2 Optical properties of thin films

In general, the optical properties of thin films are of substantial importance. The wide use of thin films in optics, and in the case of semiconductor thin films in opto-electronic devices entails a good understanding of their optical properties. The main macroscopic interaction phenomena are reflection, absorption and transmission of the incident light onto the layer. When light propagates from one medium

Tesis publicada con autorización del autor
No olvide citar esta tesis
ET LUX IN TENEBRIS LUCET MCMXVII PUCP

into another i.e. to a medium with a different refractive index, a portion of the light intensity is reflected, another part is absorbed by the medium and finally some of the light radiation is transmitted (see figure 2.2.1). During these processes the light polarization states may also vary. By the principle of energy conservation and ignoring light dispersion due to the surface roughness or other micro defects (grains, fractures, etc.) in the material, the relation between the mentioned intensities can be written as shown in the equation 2.2.1. Following the definition of the coefficients $R = I_R/I_0$ for reflectance, $A = I_A/I_0$ for absorbance and $T = I_T/I_0$ for transmittance the equation 2.2.1 can be rewritten as shown in the equation 2.2.2.

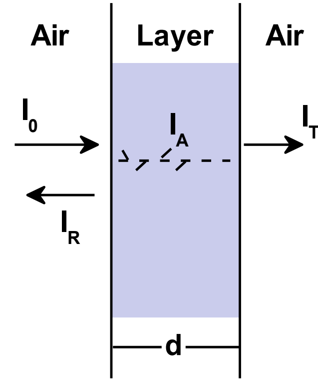

Figure 2.2.1. Part of the incident light intensity I_0 is reflected I_R, absorbed I_A and transmitted I_T by and through the layer, respectively. d denotes a finite thickness of the layer.

$$I_0 = I_R + I_A + I_T \quad (2.2.1)$$

$$R + A + T = 1 \quad (2.2.2)$$

The optical processes within a material involve the interaction of photons with electrons. In the ultraviolet (UV) and visible (VIS) light spectral regions the photons interact directly with the electrons in the material allowing the characterization of electronic energy bands. Whilst in the infrared (IR) light spectral region the interaction of photons with the polarization of molecules are dominating, allowing the characterization of distinct vibrational states. The optical properties of a material, concerning the light absorption and emission can be expounded in terms of the electronic band structure which is the result of the assembly of a large number of atoms bonded to form a solid.

For a comprehensive study of the optical behavior of a thin film, knowledge concerning the structure of the film's material is necessary. The layers may found to exhibit for instance mono-crystalline, poly-crystalline, amorphous, nano- and/or micro-crystalline

Tesis publicada con autorización del autor
No olvide citar esta tesis
PUCP

aggregates embedded in an amorphous matrix, etc. The optical properties depend considerably on the particular structure of the layer.

2.3 Determination of the optical constants of thin films

The refractive index $n(\lambda)$ and the extinction coefficient $k(\lambda)$ are the most important macroscopic optical constants of any material. They are the respective real and imaginary parts of the complex refractive index $\tilde{n}(\lambda)$ and the latter is the square of the complex dielectric constant. From the fundamental and technological point of view, knowledge of their dependency with the photon wavelength (λ) is of great interest. For instance, on the one hand the refractive index is necessary for the design of optical components like coatings and interference filters. Whilst, on the other hand, the extinction coefficient, which is linked to the absorption coefficient by $\alpha(\lambda) = 4\pi k(\lambda)/\lambda$, contains essential information of the electronic density of states (DOS) of insulators and semiconductors and therefore of the optical energy bandgap.

Consequently, the accurate determination of the optical constants of thin films has been an issue for years. Several contributions concerning the improvement of numerical methods and models to apply in techniques such as spectroscopic ellipsometry, optical transmittance and/or reflectance have been developed [Swa83, Cha97, Cha98, Poe03]. In the present work we deal with the determination of the optical constants of dielectric thin films grown on transparent substrates by single optical transmittance measurements. For this matter we review some features concerning this method.

Spectrophotometry techniques are quite simple because nowadays they are available in any material science laboratory. Although their capacity to measure accurately optical constants is very well known, the effort in extraction of materials parameters like the optical bandgap has been often underestimated. Notwithstanding, they compound an effective tool to obtain crucial information of the optical properties of thin films when used properly. Now, in order to determine the optical constants from transmittance and/or reflectance measurements, it is necessary to know precisely the geometry of the sample, and accordingly, adopt a model. We simplify the system by assuming an isotropic,

Tesis publicada con autorización del autor
No olvide citar esta tesis
PUCP

homogeneous, plane-parallel layer which in our case is sufficiently achieved. For instance, for normal incidence, the transmittance and reflectance of the system depicted in figure 2.2.1 is well described by the following equations in the spectral range of interest:

$$T = \frac{(1-R_1)^2 x}{R_1^2 x^2 - 2R_1 \cos(\phi) x + 1} \quad (2.3.1)$$

$$R = \frac{R_1[1+(1-2R_1)x^2]}{R_1^2 x^2 - 2R_1 \cos(\phi) x + 1} \quad (2.3.2)$$

Here, R_1 is the Fresnel coefficient corresponding to the air-film interface and is defined as $R_1 = (n-1)^2/(n+1)^2$. x is the absorbance of the layer and is defined by $x = \exp(-\alpha d)$. ϕ is the phase shift of the light due to its propagation through the thin film taking into account the interference of the multiple reflections inside the layer. It is defined as $\phi = 4\pi n d/\lambda$.

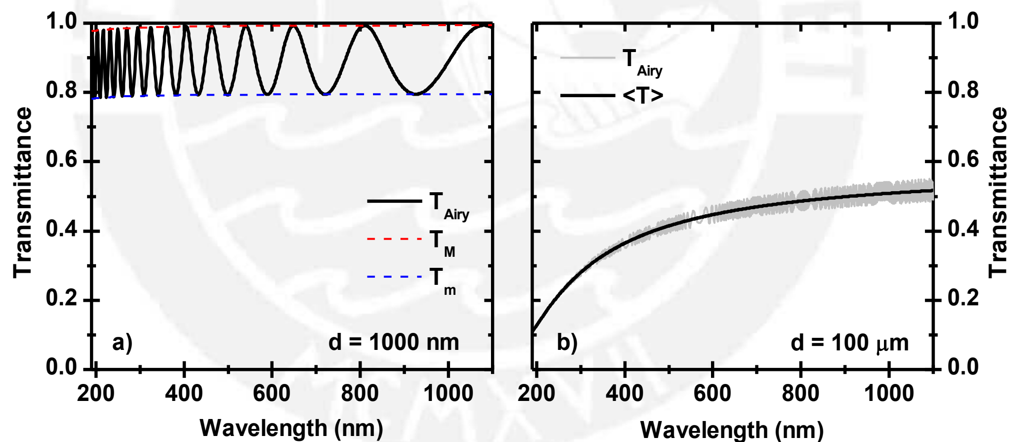

Figure 2.3.1. Simulated transmittance using Airy's equation for a slightly absorbing layer with 1000 nm thickness (a) and 100 μm thickness (b). A conventional spectrophotometer is not able to resolve the rapid oscillations in the transmittance of thick layers, thus it measures the average $\langle T \rangle$ instead of the T_{Airy}. T_M and T_m denote the upper and lower envelopes in the legend.

The equation 2.3.1 is known as Airy's equation for the case of normal incidence [Kuz09]. Both equations can be obtained for instance using the matrix description of optical systems [Mac86]. It is important to note that these equations describe the transmittance

Tesis publicada con autorización del autor
No olvide citar esta tesis
ET LUX IN TENEBRIS LUCET MCMXVII PUCP

and reflectance coefficients taking into account the light interference effect due to the multiple reflections inside the layer. This effect typically results in oscillations in both the transmittance T and reflectance R versus the wavelength. When the layer is thick enough the mentioned oscillations become too dense comparing to the spectrometer resolution and thus an average is measured (see figure 2.3.1). This average is performed in equation 2.3.3, where $\widehat{\omega}(\lambda - \lambda')$ is the weighting function (typically a Gaussian curve can be used as good approximation). Unfortunately, there is no analytical solution for the integral in equation 2.3.3. Nonetheless, a good approximation can be reached by averaging over the phase ϕ, as shown in equation 2.3.4. The analytical result of this average over the transmittance and reflectance is given in the equations 2.3.5 and 2.3.6. The latter expressions are commonly used for describing the transmittance and reflectance of bulk samples [Mac86, Gon02].

$$\langle T \rangle = \int_{-\infty}^{\infty} T(\lambda')\widehat{\omega}(\lambda - \lambda')d\lambda' \tag{2.3.3}$$

$$\langle T \rangle \approx \frac{1}{2\pi}\int_{0}^{2\pi} T(\lambda)d\phi \tag{2.3.4}$$

$$\langle T \rangle = \frac{(1 - R_1)^2 x}{1 - R_1^2 x^2} \tag{2.3.5}$$

$$\langle R \rangle = \frac{R_1[1 + (1 - 2R_1)x^2]}{1 - R_1^2 x^2} \tag{2.3.6}$$

Notice that the transmittance and reflectance are functions of the wavelength, the refractive index, the absorption coefficient and the layer thickness. That is $T = T(\lambda; n(\lambda), \alpha(\lambda), d)$ and $R = R(\lambda; n(\lambda), \alpha(\lambda), d)$. Therefore, assuming it is possible to obtain the layer thickness by an alternative method, the calculation of $n(\lambda)$ and $\alpha(\lambda)$ follows by solving either the system of equations 2.3.5 and 2.3.6 for the case of layers with a thickness of several hundreds of µm or the equations system 2.3.1 and 2.3.2 for the case of a thickness in the order of nm or tens of micrometers. Therefore two spectroscopic measurements (besides the thickness measurement) are necessary to obtain

Tesis publicada con autorización del autor
No olvide citar esta tesis
PUCP

the wavelength dependency of the refractive index and absorption coefficient. However, measuring the reflectance at normal incidence could be a difficult task, thus another approach is desirable. For instance measuring the transmittance at two different incident angles is a possibility. In this way two independent measurements are obtained from which the equations system can be solved [Poe03].

Here we use and discuss the method to estimate the optical constants of a thin film from a single transmittance spectrum by taking advantage of the interference fringes appearing due to the multiple reflections inside the layer. In order to do this we must define the envelopes that contain the maxima (T_M) and minima (T_m) extremes of the transmittance. From the Airy's equation (equation 2.3.1) these are defined by:

$$T_{m/M} = \frac{(1-R_1)^2 x}{R_1^2 x^2 \pm 2R_1 x + 1} \quad (2.3.7)$$

From the envelopes, the *finesse* (*f*) of the interference is calculated (see equation 2.3.8). *f* is independent from the absorbance and thickness, and therefore the refractive index can be calculated straightforward following the equations 2.3.9 and 2.3.10.

$$f = \frac{1}{T_m} - \frac{1}{T_M} = \frac{4R_1}{(1-R_1)^2} \quad (2.3.8)$$

$$R_1 = 1 + 2f - \sqrt{(1+2f)^2 - 1} \quad (2.3.9)$$

$$n = \frac{1+\sqrt{R_1}}{1-\sqrt{R_1}} \quad (2.3.10)$$

The layer thickness can then be estimated from the fact that the phase shift difference $\Delta\phi$ between two extremes is always 2π (see equation 2.3.11). By knowing the layer's refractive index and the thickness, the absorption coefficient can be calculated directly by solving for instance the equation 2.3.1. Note that in this approach, two virtual measurements (the constructed envelopes) were used in order to complete the equations system.

Tesis publicada con autorización del autor
No olvide citar esta tesis
ET LUX IN TENEBRIS LUCET MCMXVII PUCP

$$\Delta\phi = 2\pi = 4\pi d\left(\frac{n_2}{\lambda_2} - \frac{n_1}{\lambda_1}\right)$$

$$\xrightarrow{yields} d = \frac{1}{2}\left(\frac{\lambda_1\lambda_2}{n_2\lambda_1 - n_1\lambda_2}\right) \tag{2.3.11}$$

Typically, a film is grown on a substrate and in order to perform spectro-photometric transmittance measurements the substrate must exhibit certain transparency in the wavelength range of interest. If the goal is to obtain the fundamental absorption from such measurements, then the optical bandgap of the substrate must be larger than that of the film. In this sense, the optical properties of the substrate must be taken into account.

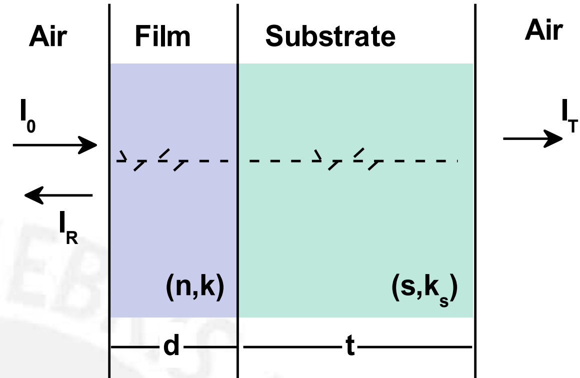

Figure 2.3.2. Film substrate system. Typically the film thickness is in the order of hundreds of nanometers, while the substrate thickness is in the order of millimeters.

The equation for the transmittance in this case varies from that of the system shown in the figure 2.2.1. Nonetheless, in order to retrieve the optical constants we can apply the previously described approaches. The corresponding equation that describes in a good approximation the system depicted in the figure 2.3.2 is shown in the equation 2.3.12. This equation is obtained after performing and average like in equation 2.34 but for the substrate induced phase shift only. The use of envelopes described above in this case is named the envelope or Swanepoel method [Swa83].

$$T = \frac{(1-R_1)(1-R_2)(1-R_3)x}{(R_1R_2 - R_1R_3 - R_2R_3)x^2 - 2\sqrt{R_1R_2}\,\cos(\phi)x + 1} \tag{2.3.12}$$

$$T_{m/M} = \frac{(1-R_1)(1-R_2)(1-R_3)x}{(R_1R_2 - R_1R_3 - R_2R_3)x^2 \pm 2\sqrt{R_1R_2}\,x + 1} \tag{2.3.13}$$

Tesis publicada con autorización del autor
No olvide citar esta tesis
ET LUX IN TENEBRIS LUCET MCMXVII PUCP

$$f = \frac{1}{T_m} - \frac{1}{T_M} = \frac{4\sqrt{R_1 R_2}}{(1-R_1)(1-R_2)(1-R_3)} \tag{2.3.14}$$

$$n = \left(N + (N^2 - s^2)^{1/2}\right)^{1/2} \tag{2.3.15}$$

The envelopes are defined by the equation 2.3.13. From the envelopes the finess f is calculated and related to the layer and substrate refractive indexes (see the equation 2.3.14). Subsequently, the refractive index $n(\lambda)$ can be found (see the equation 2.3.15, here $N = 2sf + (s^2 + 1)/2$) and the film thickness can be calculated by using the relation 2.3.11. Finally, by knowing the refractive index and the film thickness the system is solved for the absorption coefficient.

The envelope method was developed based on the approach proposed by Manifacier [Man76]. The envelope method is a simple straightforward technique that allows for the optical constants determination of thin films grown on transparent substrates. An extension of the method to work with slightly absorbing substrates has been proposed before in [Gon02]. Nonetheless, the method presents some critical drawbacks. First, there is no proper way to define and build up the envelopes between the interference extremes using only the transmittance spectrum. Second, the envelopes should ideally be constructed from the tangent points of the transmittance curve and not from the interference extremes. This effect becomes more appreciable in the region where the absorption of the film increases dramatically. Third, a large number of interference fringe extremes are necessary in order to construct the envelopes and apply the method. This condition is only met for films with a sufficient thickness. On the other hand, in order to be able to measure the fundamental absorption of the film, the film thickness must be sufficiently small leading typically in only a few fringes decreasing the applicability of the method [Poe03, Gue10t].

Aiming to overcome the latter mentioned drawbacks we modified the envelope method. In this modification, the refractive index is modeled, whilst the absorption coefficient behavior is retrieved by fitting the transmittance spectrum. Further details on this

Tesis publicada con autorización del autor
No olvide citar esta tesis
PUCP

approach and a confident analysis in comparison with the Swanepoel method and the PUMA method, which is another well-known technique to obtain optical constants from single optical transmittance spectra, can be found in the appendix A1.

2.4 Rare Earth doped materials

During the last four decades, the interest and applications of RE ions have increased significantly. For instance, RE doped materials have found place for applications in sensors, waveguides, solid-state lasers, energy-efficient luminescent materials, dopant stabilizers for fuel cells, photon up-conversion coatings for improving solar cells spectral efficiency, nano-particles radiation and photodynamic therapy for cancer treatment, medical imaging, etc. Albeit their potential use, RE commercial applications are still limited due to their high price which is comparable to gold. The main reason is that REs can be isolated only by using ion-exchange separation techniques which are difficult to apply in larger scales. Notwithstanding, RE doped materials continue to be an interesting field of study, for instance from the fundamental point of view. In some materials there is still not a consensus on what the activation processes for optical emission are. What is the role of the host matrix in enhancing or quenching the emission intensity? And finally, what excitation mechanisms are the most probable? Altogether, in order to improve the light emission intensity, different studies on RE doped semiconductors, isolators and other systems have been realized [Gue13q, Ben12, Mir11, Che10, ODo10, Zan09, Loz07, Jan03, Lu02].

The RE luminescence arises from radiative intra-4f electron transitions of the triply ionized lanthanides (RE^{3+}) doped in host matrices like semiconductors. For instance, Tb^0 has an electronic configuration $[Xe]4f^9 6s^2$, whereas Tb^{3+} has an electronic configuration $[Xe]4f^8$. The 4f shell remains partially filled, which means that intra f-shell transitions are potentially possible, albeit they don’t belong to the outermost shell. Furthermore, notice that in REs the 5s and 5p shells shield the 4f electrons from the 6s bonding electrons (see figure 2.4.1). The mixing with the 4f electrons is then very low,

Tesis publicada con autorización del autor
No olvide citar esta tesis
ET LUX IN TENEBRIS LUCET MCMXVII PUCP

and thus the effect on the 4f energy levels due to the RE bonding with the host matrix atoms is weak. Therefore, the weak interaction between the 4f electrons and the ion environment allows energy levels that are relatively insensitive to the host environment, and thus narrow spectral lines, and long fluorescence lifetimes are expected. In other words, the light emission spectra of REs are well defined and does not dramatically depend on the host matrix.

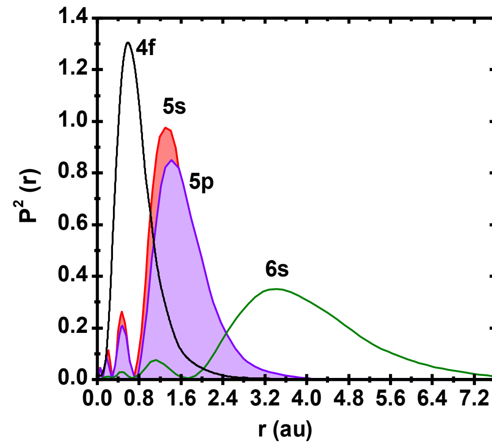

Figure 2.4.1. Electron orbitals radial distribution $P^2(r)$ for the 4f, 5s, 5p and 6s electrons of Gd^+ [Fre62].

The optical active transitions under study are parity-forbidden in free ions due to the angular momentum conservation $\Delta l = 0$ (Laporte's selection rule). Owing to the local crystal field when the ion is surrounded by the host matrix the selection rules of free atoms no longer can be applied [Jud62, Ofe62, Hüf78]. In other words, thanks to the interaction with the surrounding atoms, the RE observed emission is possible with the particular fact that the spectra is practically unaffected by the host. This crystal field must be non-centrosymmetric at the equilibrium position in order to have a coupling between even and odd wavefunction parity states. Historically, in the 60's with the independent contributions of Judd and Ofelt [Jud62, Ofe62] the understanding of the atomic emission spectra of RE in solids started to be finally understood. Before, the RE emission spectra was well known but the understanding behind it presented a puzzle that took about 30 years to be solved [Vle37]. Later on, the race to design light emitting devices using various hosts and REs encounter its first drawback. In the early 80's only semiconductors with a small bandgap were available, therefore the applications were limited to infra-red light emitting devices. The application was then focused on the infrared emission of Er^{3+} since the emission corresponding to the ${}^4I_{13/2} \rightarrow {}^4I_{15/2}$ transition (see figure 2.4.2) matches the most pronounced absorption minimum of SiO_2 based optical fibers. In fact, the study of Er compiles most of the contributions up to day. The light emission quenching due to thermal effects drove disappointing results. Nevertheless, the quantum

Tesis publicada con autorización del autor
No olvide citar esta tesis
ET LUX IN TENEBRIS LUCET MCMXVII PUCP

efficiency of these systems was somewhat large, opening new and promising research paths in the field.

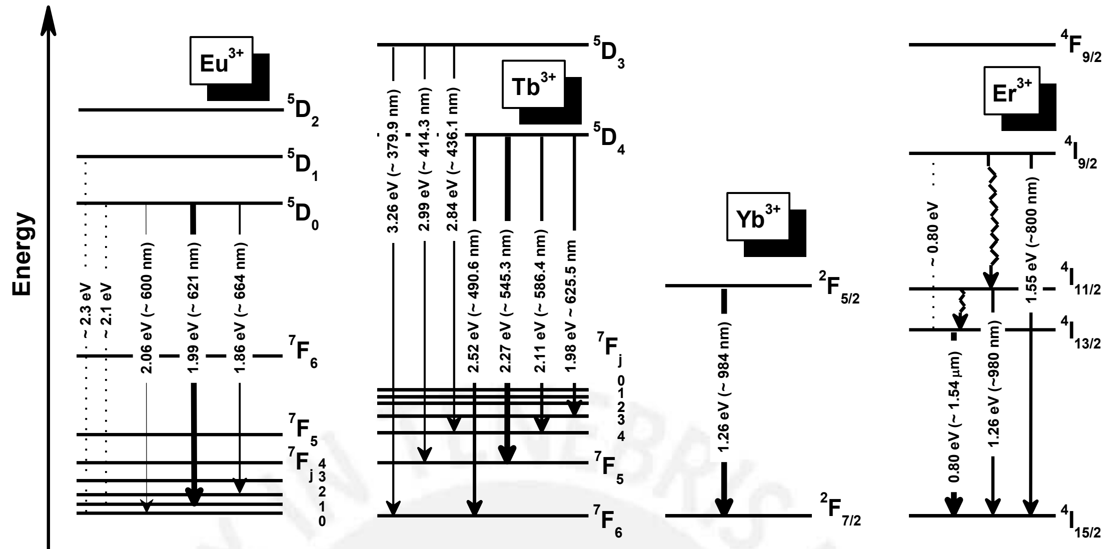

Figure 2.4.2. Energy level diagrams of Eu^{3+}, Tb^{3+}, Yb^{3+} and Er^{3+}. It has been already reported that interaction between Eu^{3+}, Tb^{3+} and Yb^{3+} allows cooperative up-conversion and down-conversion [Sal03, Kir06]. In the case of Er^{3+} cooperative up-conversion between ions of Er^{3+} allows the emission in the red [Ken02].

It was not until the early 90's that wide bandgap semiconductors become sufficiently available opening the field for visible light emitting devices based on REs. Moreover, due to the large bandgap of these hosts the phonon energy threshold was sufficiently large to avoid the thermal quenching of the luminescence at room temperature [Ste99, Ken02, Zan03]. These features, plus the property that REs can interact with each other, open the possibility to produce materials which could shift the excitation wavelength to higher or lower energies, known as up and down conversion (see figure 2.4.2). In summary, different REs exhibit a particular well

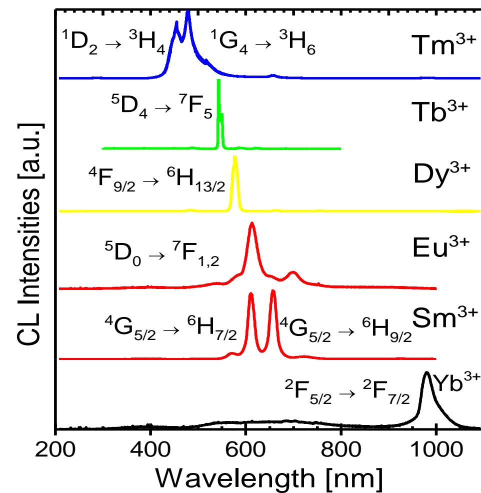

Figure 2.4.3. CL emission spectra of a/nc-AlN doped with different REs Covering the basic colors [Wei06].

Tesis publicada con autorización del autor
No olvide citar esta tesis
PUCP

defined and spectrally sharp luminescence (see figure 2.4.3). Covering for instance the basic colors green (Tb^{3+}), red (Eu^{3+} or Sm^{3+}) and blue (Tm^{3+}). The RE light emission spectral energy does not depend strongly on the host matrix. However the light emission intensity can be enhanced or quenched by the host matrix thus making RE doped materials suitable candidates for applications in several fields.

Tesis publicada con autorización del autor
No olvide citar esta tesis
PUCP

3.1 Optical properties of amorphous semiconductors

The determination of the optical properties of amorphous semiconductors is of great interest for technology development and fundamental characterization. This is owing to the fact that optical properties are related to structural and electronic properties of any solid. Now, the description of the electronic properties of amorphous semiconductors begins with the energy distribution of electronic states. In amorphous materials due to the absence of long-range order the electronic states are broadened compared to the crystalline counterpart and form band-tails at the band edge. Band-tails are also observed in the crystalline case with increasing temperature of the material, caused by the phonon interaction and broadening of electronic states due to the atomic thermal vibrations. Furthermore, there is a complete loss of momentum conservation in the electronic transitions in the amorphous case. The effect of these features on the optical properties can be evaluated in the analysis of the absorption coefficient and the corresponding effect on the optical bandgap. A schematic shape of the absorption coefficient encountered in amorphous semiconductors is depicted in figure 3.1.1. Three regions are typically assigned and as we will see later, these regions are connected deeply with features of the electronic density of states.

In the following sections we will review first the electronic density of states of amorphous semiconductors in contrast with the crystalline counterpart in the free electron approximation near the band-edges. Second, the defect states that amorphous semiconductors experience is revised. Subsequently, we proceed to perform the traditional calculation of the fundamental absorption in the one electron approximation at cero Kelvin temperature. The Urbach edge is studied and the Urbach focus defined. Finally, we develop a model for the absorption coefficient based in thermal fluctuations and motivated in the Kubo-Greenwodd formula which takes into account an ensemble of electrons at finite temperatures. The consequences of this final calculation are considered and contrasted with the Urbach rule and the Urbach focus.

Tesis publicada con autorización del autor
No olvide citar esta tesis

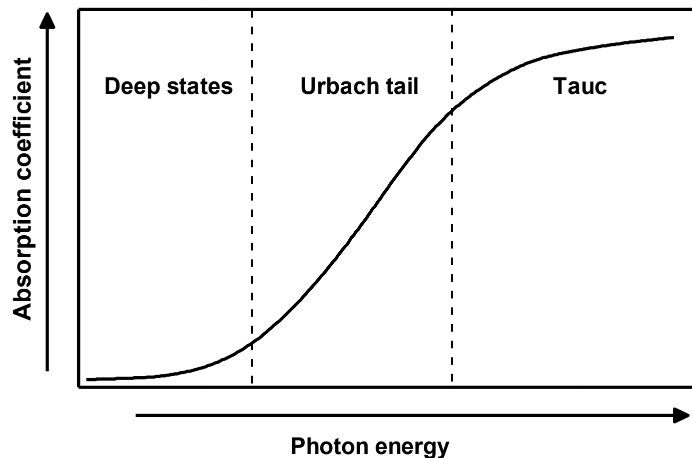

Figure 3.1.1. Schematic plot of the typical shape of the absorption coefficient in logarithmic scale of amorphous semiconductors in the UV-VIS-NIR spectral region. Three zones can be identified: the deep band tail states, the Urbach tail region, and the Tauc region corresponding to the fundamental absorption.

Electronic density of states

In amorphous semiconductors, it is not possible to define an energy-momentum band structure. Due to the lack of translational symmetry the Bloch theorem is not applicable. Therefore, the quasi-momentum conservation for transitions (phonon decay, phonon-photon interaction, etc.) involving reciprocal lattice vectors is no longer valid. Instead of using an energy band structure like in the crystalline semiconductor case, we start our description with the energy-dependent density of states distribution $D(E)$. The concept of electronic density of states is independent of translational symmetry and therefore applicable to amorphous semiconductors [Str91, YuC04]. Furthermore, it has been shown that in the amorphous case an energy gap opens. An energy gap is not only related to translational symmetry but related to the atomic bonding [Str91]. In summary, amorphous semiconductors exhibit electronic states and an energy gap forbidden for the electrons.

According to the physical origin, the electronic density of states separates into three different energy regions (see i, ii, and iii in figure 3.1.2). First, the conduction and valence extended states that are limited by the band edges (or mobility edges) denoted by E_c and E_v for the conduction and valence regions, respectively. As the name indicates the

Tesis publicada con autorización del autor
No olvide citar esta tesis
ET LUX IN TENEBRIS LUCET MCMXVII PUCP

states are considered to be extended throughout the solid and play a similar role as the Bloch states in a crystal. Second, the band tails (or Urbach tail) region overlapping the band edges and extending further towards the forbidden gap which represents localized electron states, i.e. electrons which cannot contribute to mobility. And finally, the defect states region right inside the forbidden gap.

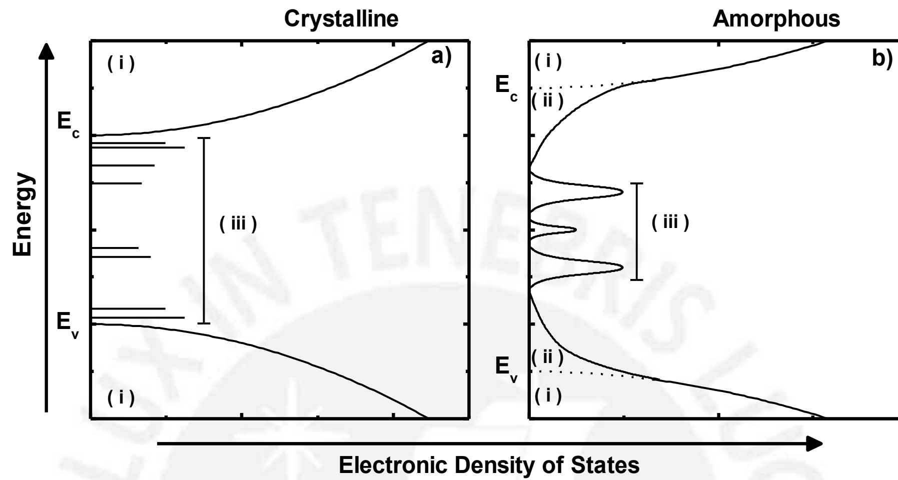

Figure 3.1.2. Scheme of the electronic density of states (DOS) of crystalline (a) and amorphous (b) semiconductors. The DOS can be separated in three regions: the conduction and valence bands region (i), the band tail states (ii) and the defect states region (iii).

In the crystalline case, the energy band tails are pretty small compared to those observed in the amorphous counterpart and are therefore considered absent. The nature of these tails is completely thermal and will be explained later. What can be seen from figure 3.1.2 is that the mobility edges which correspond to the bandgap in the crystalline solid do not show up in the density of states of the amorphous solid. The functional behavior from the extended states to the localized states (Urbach tail) is rather continuous. These features make difficult to define the optical bandgap of an amorphous semiconductor. There exist several approaches to define the optical bandgap energy value. What we can actually learn from these models and/or definitions may not be an absolute bandgap value but rather a representation whose behavior is expected to be similar to that of the real bandgap. For instance, when altered by the modification of the Urbach tails or mobility edges through thermal annealing treatments and/or passivation of dangling bonds by hydrogen or further dilution of nitrogen/oxygen.

Tesis publicada con autorización del autor
No olvide citar esta tesis
ET LUX IN TENEBRIS LUCET
MCMXVII
PUCP

Defect states in amorphous semiconductors

Defect states in the forbidden gap influence the electronic properties of the material, owing to the fact that their electron occupancy is changed by doping or by trapping charge carriers. The energy levels of any defect depend on the local environment. In the crystalline case any divergence from the crystalline lattice is a defect, which in fact there exist a large amount of defect types in crystalline structures. On the other hand, the disorder of a random lattice is an integral part of the amorphous semiconductor, thus thinking of the amorphous lattice as a collection of defects is not helpful at all. Hence a different definition of defect states is necessary for amorphous materials.

Taking the analogy of the crystalline case, that any departure from the perfect lattice is a defect, we can define a defect in an amorphous material as any departure from the ideal random network [Str91, Mor99, Sad99, Sin03]. The ideal random network would be a continuous and uniform lattice. Understanding by 'continuous lattice' that all the bonds are saturated in the random network and by 'uniform lattice' that there is no actual segregation of the species (on the large scale) but the atoms are homogenously distributed and therefore a compound and not a composite is formed.

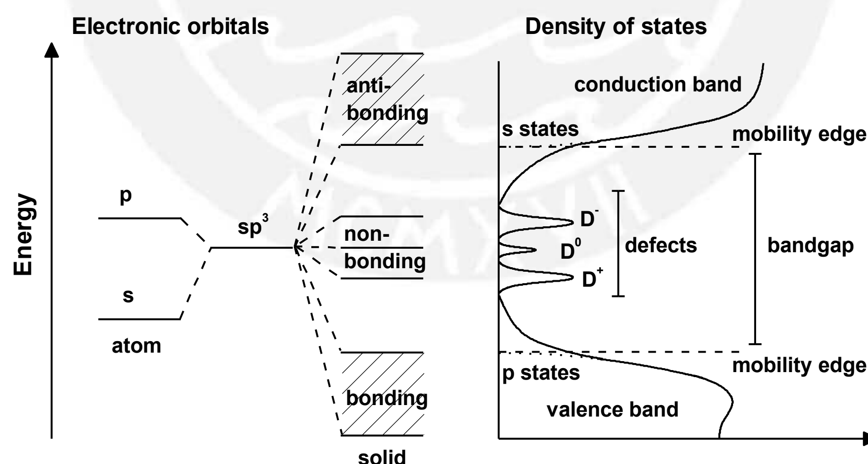

Figure 3.1.3. Schematic representation of the molecular orbit model of the electronic structure of amorphous silicon and the corresponding density of states [Str91, Mor99, Sad99].

Tesis publicada con autorización del autor
No olvide citar esta tesis
ET LUX IN TENEBRIS LUCET MCMXVII PUCP

This approach immediately leads to the idea of a coordination defect in which an atom lacks forming a bond [Str91]. Let's take for instance the case of amorphous silicon (a-Si). The s and p orbital states combine to form the sp^3 hybrid orbital states for the tetrahedral bonding. So in a solid formed by an ideal random network of Si atoms, all the atoms are tetrahedral coordinated. The sp^3 orbital states split forming the anti-bonding and bonding states which become the valence and conduction bands, respectively in a solid. However, in fact not all the sp^3 orbital states find a neighboring orbital pair to form a bond in an amorphous solid. Any non-bonding orbital is not split by the bonding interaction and thus give rise to localized states in the gap (see figure 3.1.3). This type of defect is called dangling bond and in this particular example is a three-fold coordinated silicon dangling bond.

Now, all the electrons in an ideal random network are paired in bonding states. However if the local coordination of an atom is one less (or greater) than the ideal, then the neutral state of the atom has an unpaired electron forming the dangling bond. The addition of one electron into the dangling bond results in paired electrons and a net charge. Therefore, this non-bonding state has actually three possible charge states: two electrons D^-, one electron D^0 and no electron D^+. The electronic energies of these defects are not the same due to the electron-electron interactions. The two electrons (holes) repel each other with a Coulomb interaction which is absent in the singly occupied state. Thus the energy levels split by the correlation energy U_c [Str91].

$$U_c = \frac{e^2}{4\pi\epsilon\epsilon_0}\frac{1}{r} \tag{3.1.1}$$

Here r is the effective separation of the two electrons. Consequently, it is roughly the localization length of the defect wave-function. It is difficult to calculate the energy value exactly, because the wave-function is not known accurately. Nonetheless, a rough estimate in the case of amorphous hydrogenated silicon gives $U_c = 130\text{ meV}$ for $r = 10\text{ A°}$ [Str91]. Notice that the correlation energy is an important fraction of the bandgap energy in a-Si:H ($E_g \approx 1.75$ eV).

Tesis publicada con autorización del autor
No olvide citar esta tesis
ET LUX IN TENEBRIS LUCET MCMXVII PUCP

The electron-phonon coupling between the bonding electrons and the gap-state electrons causes the defect structure and energy to depend further on the charge state. This effect is called lattice relaxation and is generally described by a configurational coordinate diagram of the type shown in figure 3.1.4. This model describes the effect of the electronic excitation and the local distortions of the bonding. For instance, let's consider the trapping of an electron from the conduction band onto a defect. The potential energy of the upper state consists of two terms. One of which is the energy E_c of the electron at the bottom of the conduction band and the second term is the additional energy of lattice vibrations. These are considered to be single vibrational mode described by a configurational coordinate q. For the simple harmonic oscillator approximation, it gives and energy $E(q)$ by:

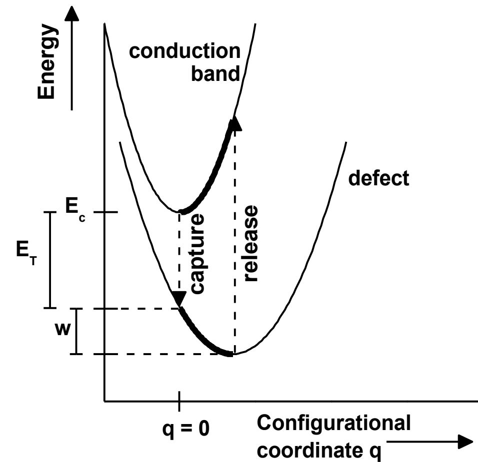

Figure 3.1.4. Configuration coordinate diagram describing the capture and release of an electron from the conduction band into a defect state.

$$E(q) = E_c + Fq^2 \quad (3.1.2)$$

F is the strength of the network vibrations and the equilibrium state take place at $q = 0$. The solution (quantum mechanical) of the harmonic oscillator gives the phonon energies $(n + 1/2\,)\hbar\omega$ with the frequency $\omega = (2F/m)^{1/2}$. This model includes more than one vibrational mode. The trapping of an electron releases an energy E_T and without any electron-phonon interaction the energy of the state E_T is below the upper energy sate. The phonon interaction introduces an additional term which couples the energy to the configuration coordinate q. At first order this linear coupling results in an energy $E(q)$ given by:

$$^{defect}E(q) \;= E_c - E_T + Fq^2 - Gq \quad (3.1.3)$$

Tesis publicada con autorización del autor
No olvide citar esta tesis
PUCP

Here G is the local deformation potential. This solution shows that the defect state has a potential minimum at $q = G/2F$, rather than at $q = 0$. The minimum energy of the defect is $E_c - E_T - w$, where $w = G^2/4F$. The potential well is depicted in the figure 3.1.4. The electron-phonon coupling causes the lattice to relax to a new equilibrium configuration at a lower energy. The main outcome of the lattice relaxation is that the transition energy between two electronic states depends on excitation and relaxation process. Thermal excitation requires an energy $E_T + w$, which is the energy difference of the potential minima depicted in figure 3.1.4, where there is no change of configuration but leaves the upper vibrational state excited. The electron then relaxes to the equilibrium state by emitting phonons. The dominant transition from the upper to lower states is also vertical and leaves the lower vibrational state excited. Consequently, defect electronic transitions are characterized by three energies, E_T, $E_T + w$ and $E_T + 2w$. The first and third correspond to optical transitions, whilst the second to thermal excitation [Str91].

In summary, in the amorphous material, small differences in local structure which fall within the disorder of the ideal network cannot be meaningfully defined as a defect. Thus one expects, contrary to the crystalline case, a few separated classes of defects, but with their energy levels broadened by the disorder as illustrated in the figures 3.1.2 and 3.1.3. There exist different types of defects in random networks, here we have reviewed some features of the dangling bond states which have a well-defined character in the sense that they can be separated from the ideal random network. For instance, dangling bonds have the distinctive characteristic of either a paramagnetic spin or an electric charge, which puts it apart from the electronic states of an ideal random network. Other type of defects are possible, nevertheless they have a less well-defined character. For instance a hydrogen void in a-Si:H certainly is a defect in the sense that it has a local structure different from the rest of the amorphous network. However, from the atomic coordination point of view, it is difficult to distinguish a void from the ideal network. If the atoms around the void have similar distribution of bonding disorder, then the electronic states probably fall within the ensemble of bulk states and are indistinguishable from those of the bulk [Str91]. Similar arguments apply to impurity states. Any impurity which is

Tesis publicada con autorización del autor
No olvide citar esta tesis
ET LUX IN TENEBRIS LUCET MCMXVII PUCP

bonded with its optimum valency is expected to form part of the ideal random network and contribute only to the conduction and valence bands.

Fundamental absorption in amorphous semiconductors

Electronic transitions between the conduction and valence extended states are responsible for the main absorption and are the measure of the optical bandgap energy. The optical data contains information of the DOS, thus of the band tail density of states and the optical bandgap. Notwithstanding, the absorption coefficient depends on the convolution of conduction and valence band densities of states and also on the transition matrix elements and these cannot be separated by optical absorption measurements only.

The absorption coefficient α is related to the electronic transition rate per unit volume R_{cv} due to optical excitation between the extended valence states $|v\rangle$ and conduction states $|c\rangle$ by equation 3.1.4. Here *c* is the speed of light, *n* the index of refraction, ϵ_0 the electric permittivity constant in vacuum and $|\mathbf{E}|$ the electric field amplitude [YuC04]. This equation is found after equaling the energy density rate per unit volume absorbed by the material $W_M = R_{cv}\hbar\omega$ and the energy density rate per unit volume delivered by the electromagnetic radiation $W_R = -d\langle U\rangle/dt$.

$$\alpha \frac{c\, n\, \epsilon_0}{2} |\mathbf{E}|^2 = R_{cv}\hbar\omega \quad (3.1.4)$$

The electronic transition rate R_{cv} between the valence and conduction bands in crystals and in the one electron approximation due to the optical excitation of Bloch electrons can be written from the Fermi's Golden Rule as presented in the equation 3.1.5. Here m_e is the electron mass, e the electron charge, ω the photon frequency, $E_{c/v}$ and $\boldsymbol{k_{c/v}}$ are the electron energy and the electron wave vector, respectively at the conduction (*c*) and valence states (*v*). $|M_{cv}|$ is the transition matrix element in the dipole approximation given by $|M_{cv}|e/m_e = \langle c|H_{eR}|v\rangle$, with $H_{eR} = e\,\boldsymbol{p}\cdot\boldsymbol{A}/m_e$ the interaction of the electromagnetic radiation with the electrons in the solid [YuC04].

$$R_{cv} = \frac{2\pi}{\hbar}\left(\frac{\mathbf{E}\, e}{2\omega m_e}\right)^2 \sum_{k_c, k_v} |M_{cv}|^2 \delta(E_c - E_v - \hbar\omega)\delta_{k_c, k_v} \quad (3.1.5)$$

Tesis publicada con autorización del autor
No olvide citar esta tesis
PUCP

$$\alpha = \frac{\hbar}{4\pi\epsilon_0 nc}\left(\frac{2\pi e}{m_e}\right)^2 \frac{1}{\hbar\omega}\sum_{k_c,k_v} |M_{cv}|^2 \delta(E_c - E_v - \hbar\omega)\delta_{k_c,k_v} \quad (3.1.6)$$

From equations 3.1.4 and 3.1.5 the absorption coefficient can be written as shown in equation 3.1.6 where naturally both quantities energy and momentum between the valence and conduction states are conserved. In general, depending on the band structure of the crystalline solid, the electronic transitions with highest probability can be direct or indirect. That is, between energy levels with the same electron wave vector k (direct) or different wave vectors $\boldsymbol{k_c} = \boldsymbol{k_v} \pm \boldsymbol{k_\phi}$ (indirect). In the latter case, the remaining momentum to maintain the $\boldsymbol{k}$ conservation is delivered by a third interacting particle, i.e. phonons, here denoted by $(\boldsymbol{k_\phi}, E_\phi)$. The electronic transition rate per unit volume R_{cv} in such case must be calculated using the Fermi's Golden Rule for three interacting particles. In this sense the band structure allows the discrimination between two categories of crystalline materials, indirect materials and direct materials.

$$^{ind}\alpha = \frac{\alpha_0}{\hbar\omega}\int_{E_c(0)}^{\hbar\omega + E_v(0)} \int_{E_c - \hbar\omega}^{E_v(0)} D_c(E_c) D_v(E_v)\delta\left(E_c - E_v - \hbar\omega \pm E_\phi\right) dE_v dE_c \quad (3.1.7)$$

$$^{dir}\alpha = \frac{{\alpha_0}'}{\hbar\omega}\int_{E_{cv}(0)}^{\hbar\omega} D_{cv}(E_{cv})\delta(E_{cv} - \hbar\omega) dE_{cv} \quad (3.1.8)$$

The absorption coefficient can be then written as a function of the valence $D_c(E_c)$ and conduction $D_v(E_v)$ electronic density of states for the case of indirect materials as shown in the equation 3.1.7. Or for the case of direct materials as shown in the equation 3.1.8, where the $D_{cv}(E_{cv})$ is the density of combined states (or joint density of states) defined from the direct transitions energy difference $E_{cv} \equiv E_c - E_v$. In both cases, the transition matrix elements $|M_{cv}|$ are assumed to change slowly with the energy in the fundamental absorption region and therefore it is absorbed along with the rest of the constants in the coefficient α_0.

Tesis publicada con autorización del autor
No olvide citar esta tesis
PUCP

In the amorphous case the picture is quite different. First, in the free electron approximation, the energy bands can be written by:

$$E_c \approx E_c(0) + \frac{\hbar}{2m_e^*}k_c^2$$
$$E_v \approx E_v(0) + \frac{\hbar}{2m_h^*}k_v^2 \qquad (3.1.9)$$

Here, m_e^* is the electron effective mass, m_h^* is the hole effective mass. However this approach is no longer applicable in amorphous materials since $\boldsymbol{k}$ is no longer a good quantum number. Thenceforth, by taking advantage that the electronic density of states is still an applicable concept, from the equation 3.1.6 we can write the absorption coefficient in the following form:

$$^{amorph}\alpha = \frac{\alpha_0}{\hbar\omega}\int\int D_c(E_c)D_v(E_v)\delta(E_c - E_v - \hbar\omega)dE_v dE_c \qquad (3.1.10)$$

Here, the conservation of momentum $\boldsymbol{k}$ is relaxed completely so a joint density of states cannot be defined. Nonetheless we can assume a shape for the valence and conduction electronic density of states. For instance, we can take the shape from the free electron approximation obtained from the energy bands in equation 3.1.9 (see equations 3.1.11).

$$D_c(E_c) = \sqrt{2}\frac{{m_e^*}^{3/2}}{\pi^2\hbar^3}\left(E_c - E(0)\right)^{1/2}$$
$$D_v(E_v) = \sqrt{2}\frac{{m_h^*}^{3/2}}{\pi^2\hbar^3}(E_v(0) - E_v)^{1/2} \qquad (3.1.11)$$

This was the approach proposed by Tauc [Tau68]. By doing so and solving the integral in equation 3.1.10 the absorption coefficient can be written as follows:

$$\alpha_{Tauc} = M_{Tauc}^2\frac{(\hbar\omega - E_{Tauc})^2}{\hbar\omega} \qquad (3.1.12)$$

Notice, that it actually looks pretty similar to the solution found after solving the integral in the equation 3.1.7 for indirect materials (see equations 3.1.13). Nonetheless, the result 3.1.12 is fundamentally distinct from the one of the indirect transitions. In the former the

Tesis publicada con autorización del autor
No olvide citar esta tesis
PUCP

transitions are assisted by phonons. And even when in both cases the bandgap is defined as the separation between the mobility edges in the former these are defined by the assumption taken for the electronic density of states in first hand.

$$
\begin{aligned}
{}^{ind}\alpha &= M_{ind}^{2}\frac{\left(\hbar\omega - E_g \pm E_\phi\right)^2}{\hbar\omega} \\
{}^{dir}\alpha &= M_{dir}^{1/2}\frac{\left(\hbar\omega - E_g\right)^{1/2}}{\hbar\omega}
\end{aligned}
\tag{3.1.13}
$$

Furthermore, the mobility edges in the amorphous case are well merged into the band tails and these were not taken into account in the preceding calculation. As we have shortly mentioned before, the band tails play an important role on the optical and electronic properties of the material and in fact they exhibit a strong influence in the optical bandgap calculated by the equation 3.1.12. In this sense, the Tauc-gap is used typically as a representative value of the 'true' gap. Currently, there is still not an adequate formulation of the fundamental absorption in amorphous materials besides the Tauc's approach [Dun83, Dun85, OLe95a, OLe98, Gue13m].

The Urbach edge

Localized states have been predicted in the early studies of amorphous semiconductors by the Anderson localization theory. Almost sixty years have passed since the publication of Anderson in 1958 [And58]. The aforementioned band-tails present in the electronic density of states are certainly localized states [Str91]. The influence of electronic localized states becomes perceptible in doping, electrical transport, recombination, etc. properties of the material. Therefore they establish the main differences between amorphous materials and their crystalline counterparts. The origin of the band-tail states and how they merge into the extended conduction and valence band states is a complicated issue. Most experiments suggest that the band-tails are at least approximately exponential. However the underlying reason for this shape is less clear. A modest model for random disorder energies is expected to have a Gaussian distribution of disorder energies and therefore Gaussian band-tails [Str91, OLe95a, OLe95b, Toy81, Sou84, Saj86]. Several attempts have been realized to explain the exponential shape of

Tesis publicada con autorización del autor
No olvide citar esta tesis
ET LUX IN TENEBRIS LUCET MCMXVII PUCP

the band tails. Taking advantage that the shape of the absorption coefficient is closely related to the shape of the DOS some models are even specific to the optical absorption since it also presents an exponential edge below the mobility edge.

Typically, the band-tail observed in the absorption coefficient can be described empirically by an exponential energy dependence in the vicinity of the bandgap energy (equation 3.1.14),

$$\alpha(E) = \alpha_F \exp\left(\frac{E - E_F}{E_u}\right) \quad (3.1.14)$$

where the Urbach energy E_u ranges regularly from ~10 meV to ~200 meV. The exponential tail is also known as Urbach edge or Urbach tail after its first observation in alakali halide crystals [Urb53] and is found in all amorphous semiconductors. From there the name of Urbach rule. Furthermore, E_F and α_F denote the Urbach focus coordinate [Cod81]. This constant has been reported already in a series of materials, e.g. a-Ge [Cod05], LnSe [Aba99], a-SiC [Zha92, Gue11, Guer13m, Mon13], and a-AlN [Gue11, Gue13m] and its origin is less clear.

The theoretical approaches of the origin of the nearly universal exponential shape of the Urbach tail have gone through a complete transformation over the years. First, the possibility that the shape was given by the joint density of states was largely discounted in favor of explanations in terms of the energy dependence of the matrix elements [Mot79]. This approach was supported by the fact that the similarity of the slope in all amorphous semiconductors seemed an unlikely coincidence if it represented the density of states. The observation of an Urbach edge in alkali halide crystals is obviously not a density of states effect [Str91, Sad99]. The most promising of various models was of an exciton transition broadened by random internal fields arising from the disorder [Dow71]. This model is able to account for the exponential slope with internal fields which are reasonably consistent with the disorder of the amorphous semiconductors. This explanation of the Urbach absorption edge has been largely discarded in favor of one in

Tesis publicada con autorización del autor
No olvide citar esta tesis
ET LUX IN TENEBRIS LUCET MCMXVII PUCP

which the shape is simply given by the joint density of states and so reflects the disorder broadening of the bands [Sin03].

Other models attribute the band edge broadening to electron-phonon interactions and/or thermodynamic equilibrium occupancy of different possible configurations. Nevertheless, despite these theories, the precise relation between structural disorder and the band-tails shape remains unclear [Str91]. For instance the Toyazawa's group [Toy71, Toy81] introduced the static disorder effect assuming a Gaussian distribution for thereby random site energies into the electronic Hamiltonian, achieving the exponential behavior of the band edges. Other contributions, such as the work of Dunstan [Dun83, Dun85], Soukoulis, Sajeev, Cohen and Economou [Sou84, Saj86] and later on the contribution of the group of O'Leary on understanding and modeling the electronic properties of amorphous materials [OLe95a, OLe95b, OLe98, OLe02, OLe04], introduced the effect of thermal fluctuations in the band edge (or the band edge fluctuations due to static disorder) and calculated the average absorption coefficient obtaining an expression at both the Tauc and Urbach regimes [OLe95a].

Now, since the slope E_u of the Urbach absorption edge reflects the shape of valence band tails, it follows that E_u varies with the structural disorder. For instance, one measure of the disorder is the average bond angle variation, which can be measured from the width of vibrational spectra using Raman spectroscopy [Lan82, Lan84] or infrared absorption spectroscopy [Mus97]. The defect density is another measure of disorder and it also increases along with the band tail slope [Stu89, Jan03, Let10].

On the origin of the Urbach rule and the Urbach focus

It is well established that whilst the universally observed exponential shape of the band-tails is not properly explained yet, its origin lay in the topological disorder and thermal vibrations [Toy71, Toy81, Dun83, Sou84, Saj86, OLe95a, OLe95b, Sin03]. The latter is normally small and insignificant at low temperatures. However, the fact that both have the same functional behavior provides the possibility to model both effects by thermal vibrations alone. The physical reason lays in the assumption that a disordered material

Tesis publicada con autorización del autor
No olvide citar esta tesis
PUCP

may be considered as an ordered one at a high (fictive) temperature in which molecules are frozen in time (i.e. frozen phonon model). In order to calculate the absorption coefficient in such systems we need to calculate the average electronic transition rate R_{cv} between the conduction and valence bands due to the optical absorption process of an ensemble of electrons in a fictive heat bath. This can be achieved by extending the one electron approximation considering the electronic occupation degree in the valence band and the available states in the conduction band by using $D_c \rightarrow D_c(E_c) \times (1 - f(E_c))$ and $D_v \rightarrow D_v(E_v) \times f(E_v)$ and taking into account the stimulated relaxation process in the Fermi's Goden rule (see equation 3.1.15 and figure 3.1.5).

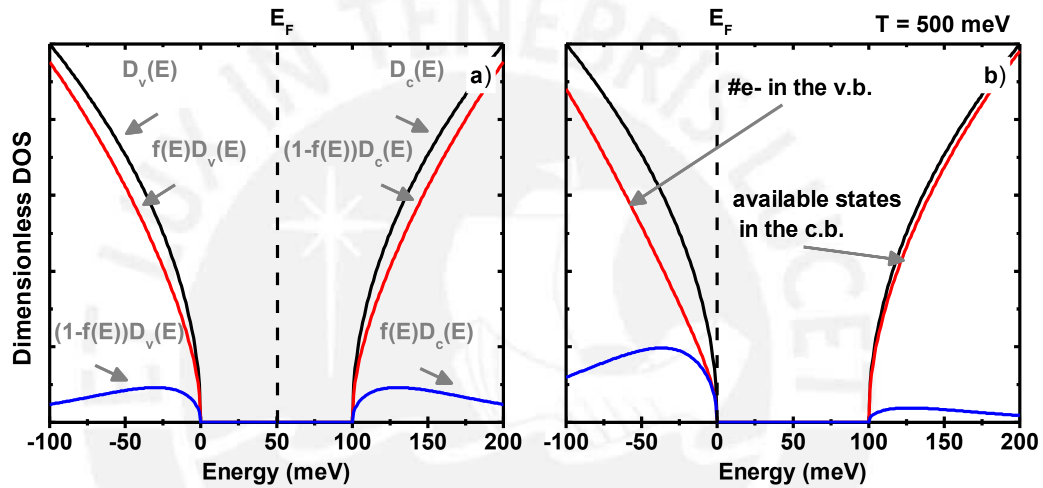

Figure 3.1.5. Electronic density of states at cero kelvin (black line). Electronic occupation degree in the valence band and available states in the conduction band at a finite temperature (red line). Unoccupied states in the valence band and occupied states in the conduction band (blue line). Graphs (a) and (b) are presented for two different Fermi levels.

$$R_{cv} = \frac{2\pi}{\hbar}\left(\frac{\tilde{E}e}{2\omega m_e}\right)^2 \sum_{k_c,k_v} |M_{cv}|^2 \,[f(E_v)]\{\ \delta(E_c - E_v - \hbar\omega) \\ -\delta(E_c - E_v + \hbar\omega)\ \}[1 - f(E_c)]\delta_{k_c,k_v} \tag{3.1.15}$$

Here, $\tilde{E}$ is the electric field of the incident. M_{cv} is the electronic transition matrix element between the conduction and valence bands. $f(E)$ is the Fermi distribution. m_e is the free electron mass, and e is the electron charge. Equation 3.1.15 can be further reduced to the equation 3.1.16. The latter is known as the Kubo-Greenwood formula, commonly used to

Tesis publicada con autorización del autor
No olvide citar esta tesis
PUCP

describe the temperature dependence of the electrical conductivity of semiconductors. The proof can be found by following the approach of Moseley [Mos78]. Here, the Kubgo-Greenwood formula defines de average electronic transition rate versus the temperature (see equation 3.1.17) [Mot79].

$$R_{cv}(\hbar\omega) = \frac{2\pi}{\hbar}\left(\frac{\tilde{E}e}{2\omega m_e}\right)^2 \sum_{k_c,k_v} |M_{cv}|^2 \{f(E_v) - f(E_c)\}\delta(E_c - E_v - \hbar\omega) \quad (3.1.16)$$

$$\langle R_{cv}\rangle(T) = \int R_{cv}(\hbar\omega)|_{T=0}\{-df(\hbar\omega)/d\hbar\omega\}d\hbar\omega \quad (3.1.17)$$

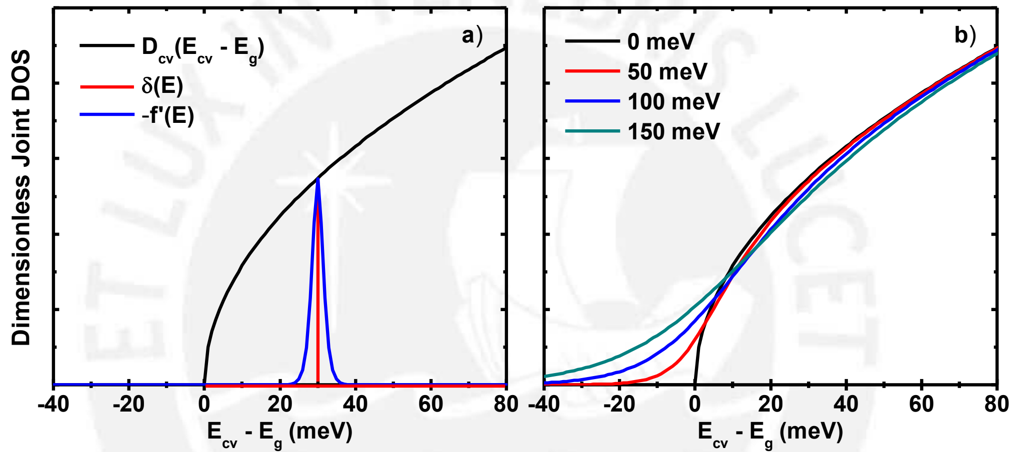

Figure 3.1.6. Electronic Joint Density of States (D_{cv}) at cero Kelvin (a) and after the proposed average at different temperatures (b).

In order to calculate the average electronic transition rate versus the photon energy $\hbar\omega$ and at different temperatures lets proceed with the following approach. S. K. O'Leary proposed to average the Local Joint Density of States $\left({}^{local}D_{cv}(E_{cv})\right)$ with a Gaussian distribution so as to account for the thermal fluctuations [OLe95a, OLe95b]. Now, motivated by the equation 3.1.17, we see that the transition rate is being averaged with $-f'(\hbar\omega) = -df(\hbar\omega)/d\hbar\omega$ as weighting function. Furthermore $-f'(\hbar\omega)$ behaves quite similarly to a Gaussian type distribution and $\lim_{T\to 0} -f'(\hbar\omega, T) = \delta(\hbar\omega)$. In this sense we propose the average of the Joint Density of States as presented in the equation 3.1.18.

Tesis publicada con autorización del autor
No olvide citar esta tesis
PUCP

The average will look as depicted in figure 3.1.6 producing tails below the bandgap energy value.

$$\langle D_{cv}\rangle(E_{cv}) = \int_{-\infty}^{\infty} -f'(\epsilon - E_{cv}) D_{cv}(\epsilon) d\epsilon \qquad (3.1.18)$$

Therefore the average transition rate $\langle R_{cv}\rangle$ under direct transitions (i.e $k_c = k_v$) can be written as shown in the equation 3.1.19. After integrating (see eq. 3.1.20) and writing the $\langle D_{cv}\rangle$ in its integral form we are lead to the equation 3.1.21.

$$\langle R_{cv}\rangle = \frac{2\pi}{\hbar}\left(\frac{\tilde{E}e}{2\omega m_e}\right)^2 \int_{E_{cv}(0)}^{\infty} |M_{cv}|^2 \langle D_{cv}\rangle(E_{cv}) \delta(E_{cv} - \hbar\omega) dE_{cv} \qquad (3.1.19)$$

$$\langle R_{cv}\rangle = \frac{2\pi}{\hbar}\left(\frac{\tilde{E}e}{2\omega m_e}\right)^2 \langle D_{cv}\rangle(\hbar\omega) \qquad (3.1.20)$$

$$\langle R_{cv}\rangle(\hbar\omega, T) = \frac{2\pi}{\hbar}\left(\frac{\tilde{E}e}{2\omega m_e}\right)^2 \int_{E_{cv}(0)}^{\infty} |M_{cv}|^2 D_{cv}(E_{cv}) \{-f'(E_{cv} - \hbar\omega)\} dE_{cv} \qquad (3.1.21)$$

Notice that equation 3.1.21 is identical to the electronic transition rate at cero Kelvin for direct transitions except for the Dirac Delta function term that ended up been replaced by the Fermi distribution derivative (see equation 3.1.5). We propose to extend this average directly to the electronic transition rate R_{cv} by relaxing the energy conservation term. That is by replacing $\delta(E_c - E_v - \hbar\omega) \rightarrow -f'(E_c - E_v - \hbar\omega)$ either for direct or indirect transitions.

From this point on, we follow Tauc's calculation for amorphous semiconductors, i.e., relaxing the conservation of $\boldsymbol{k}$ and write $\langle R_{cv}\rangle$ in its integral form, by using the valence $D_v(E_v)$ and conduction $D_c(E_c)$ electronic density of states in the free electron approximation. The absorption coefficient is then obtained as shown in equation 3.1.22, where the energy reference is taken so that $E_c(0) = E_g$ and $E_v(0) = 0$.

Tesis publicada con autorización del autor
No olvide citar esta tesis
PUCP

$$\alpha(\hbar\omega, T) = \frac{\alpha_0}{\hbar\omega}\int\int\sqrt{E_c - E_g}\sqrt{-E_v}\ \{-f'(E_c - E_v - \hbar\omega)\ \}dE_v dE_c \qquad (3.1.22)$$

with

$$\alpha_0 \ = \frac{2}{cn\epsilon_0}\left(\frac{e}{m_e}\right)^2 \frac{(m_e^* m_h^*)^{3/2}}{\pi^3\hbar^5}|M_{cv}|^2$$

Finally, equation 3.1.22 can be written more compactly as presented in the equation 3.1.23. Here $\mathrm{Li}_2(x)$ is the Di-Logarithm function of *x*:

$$\alpha(\hbar\omega) = -\frac{\pi}{4}\frac{\alpha_0}{\beta^2\hbar\omega}\mathrm{Li}_2\left(-e^{\beta(\hbar\omega - E_0)}\right) \qquad (3.1.23)$$

E_0 is defined as $E_0 = E_g - \mu_f$, and μ_f plays the role of a pseudo-chemical potential that depends for instance on the matrix doping. $\beta = 1/(k_B T)$ is the definition of the Urbach slope. Notice that μ_f enters only as a shift of the bandgap and therefore it can be interpreted as the bandgap shift due to the doping effect or other mechanisms that may vary the band edges.

$$\alpha(\hbar\omega) = \frac{\pi}{8}\frac{\alpha_0}{\hbar\omega}\begin{cases} \frac{2}{\beta^2}e^{\beta(\hbar\omega - E_0)} & , \quad \hbar\omega \ll E_0 \\ (\hbar\omega - E_0)^2 + \frac{\pi}{\beta^2} & , \quad \hbar\omega \gg E_0 \end{cases} \qquad (3.1.24)$$

Asymptotic analysis of equation 3.1.23 leads to the Urbach and Tauc expressions, here on called extended Urbach and Tauc equations, respectively as shown in equation 3.1.24. At cero Kelvin (or 0 meV Urbach energy) the extended Tauc expression is reduced to the traditional Tauc model as expected. On the other hand, the extended Urbach rule behaves just like the Urbach rule except for the factor $1/\beta^2$ which becomes evident when comparing the absorption coefficient with different slopes. Furthermore, we obtain mathematically the same coefficient α_0 in both regimes. Notwithstanding, physically we may allow different coefficients in order to account for the variation of the matrix elements $|M_{cv}|$ with the photon energy in both regimens. This result is very similar to the obtained by S. K. O'Leary [OLe95a, OLe95b, OLe04]. The main difference lays in the

Tesis publicada con autorización del autor
No olvide citar esta tesis
ET LUX IN TENEBRIS LUCET MCMXVII PUCP

weighting function or the assumption of exponential tails directly in the band edges [OLe04]. Here we average the JDOS (D_{cv}) with the Fermi distribution derivative and recover analytically the exponential behavior of the band tails afterwards.

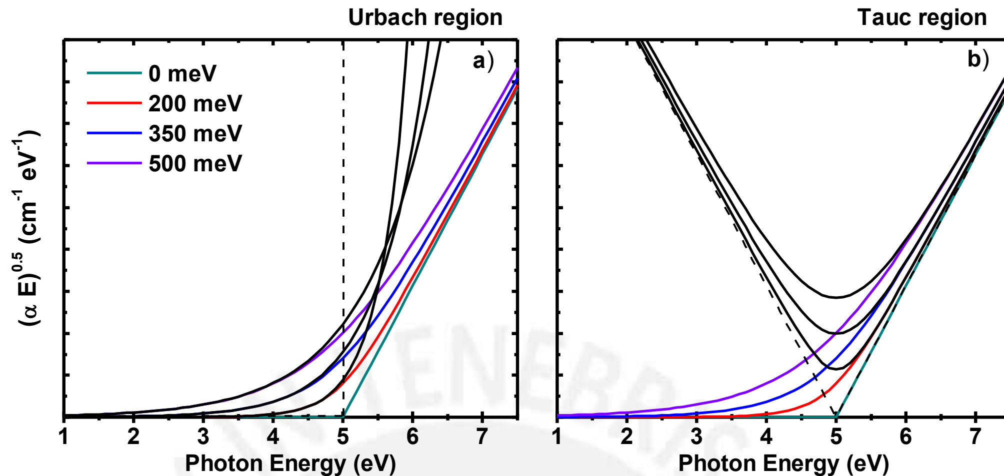

Figure 3.1.7. Tauc plot of equation 3.1.23 for a $E_0 = 5$ eV and $1/\beta$ = 200, 350 and 500 meV. The black lines correspond to the function in the asymptotic regimen of the Urbach (a) and Tauc (b) regions i.e. equation 3.1.24.

The approach here presented predicts and models both the Urbach tail region of the optical absorption and the fundamental absorption region. Additionally, by assuming a constant $|M_{cv}|$ it also models de transition between the Urbach and Tauc regions. In contrast to other approaches, it provides a simple an analytical tool which we believe to prove of use to the experimentalist since a fit with the equation 3.1.23 is possible. The asset of this equation lays in the fact that both Urbach and Tauc regions are merged into one single and simple analytical expression relating the bandgap in the absence of disorder E_0 with the Urbach energy $E_u = 1/\beta$ in both regimens [Gue16].

Let us now asses the implications of the equation 3.1.23 and its asymptotic behavior (equation 3.1.24). Two features are to be noted. First, the extended Urbach rule does not actually predict an Urbach focus. The Urbach focus is a constant typically observed as intersection of the absorption coefficients when extrapolating the exponential behavior of the Urbach region towards higher photon energies upon different Urbach slopes (see figure 3.1.8). The Urbach energy can be modified after thermal annealing treatments or

Tesis publicada con autorización del autor
No olvide citar esta tesis
ET LUX IN TENEBRIS LUCET MCMXVII PUCP

upon different sample temperatures. The nature of the Urbach focus seems to be related to the bandgap in the absence of disorder since it is a constant of the material. Nevertheless it is calculated using the equation 3.1.14 and therefore assuming its existence beforehand [Gue11]. The extended Urbach rule (i.e the equation 3.1.24 for energies below E_0) predicts the existence of a constant different than the Urbach focus. Furthermore, this equation actually predicts a region where the Urbach focus falls depending on the dispersion of the Urbach slopes values (see figure 3.1.8.a). An analysis to test the existence of the Urbach focus has been developed by F. Orapunt and S. K. O'leary [Ora04]. In section 5.1, we perform the aforementioned analysis and extend it to the equation 3.1.24 for the materials here under study (i.e. SiN, AlN and SiC:H_x).

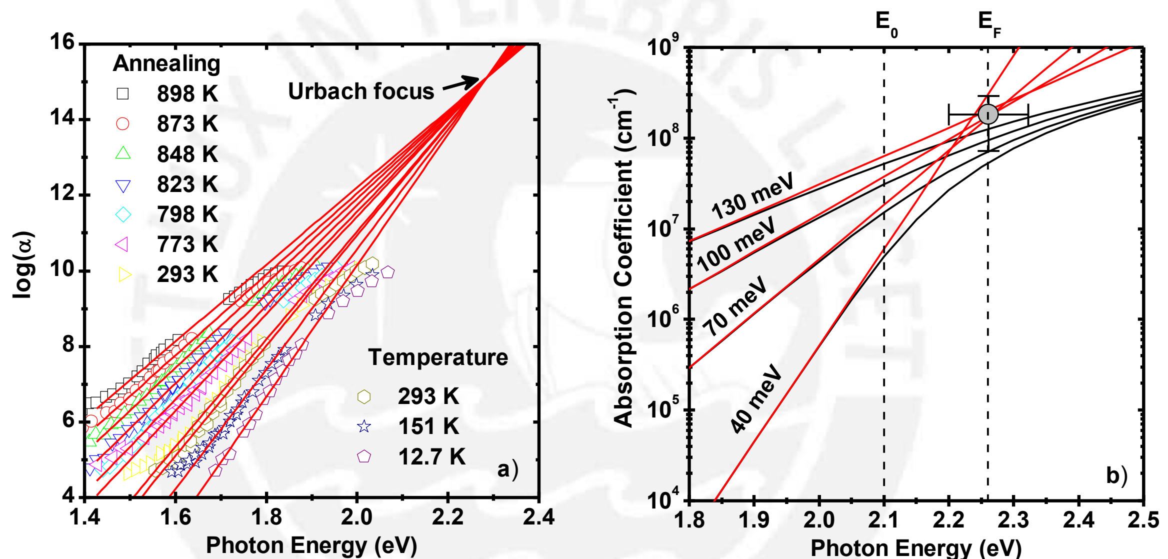

Figure 3.1.8. Absorption coefficient of amorphous Si:H exhibiting the Urbach focus at $E_F = 2.21 \pm 0.06$ eV close to the value in the literature that surrounds 2.12 eV [Cod81]. The fits are performed using the equation 3.1.14 sharing the parameters E_F and α_F (a). Absorption coefficient generated using the equation 3.1.23 (black lines) and their respective asymptotic curves in the Urbach region (red curves), in this plot E_0= 2.1 eV was used. Notice that the extended Urbach rule does not merge in a single point but a region (b).

Second, what will we obtain if we fit the common models to the equation 3.1.23. That is the Urbach rule (eq. 3.1.14) and the Tauc model (eq. 3.1.12). For this let us generate the absorption coefficient by 3.1.23. Such simulation is depicted in the figure 3.1.9 along with the corresponding fits for each region.

Tesis publicada con autorización del autor
No olvide citar esta tesis
ET LUX IN TENEBRIS LUCET
MCMXVII
PUCP

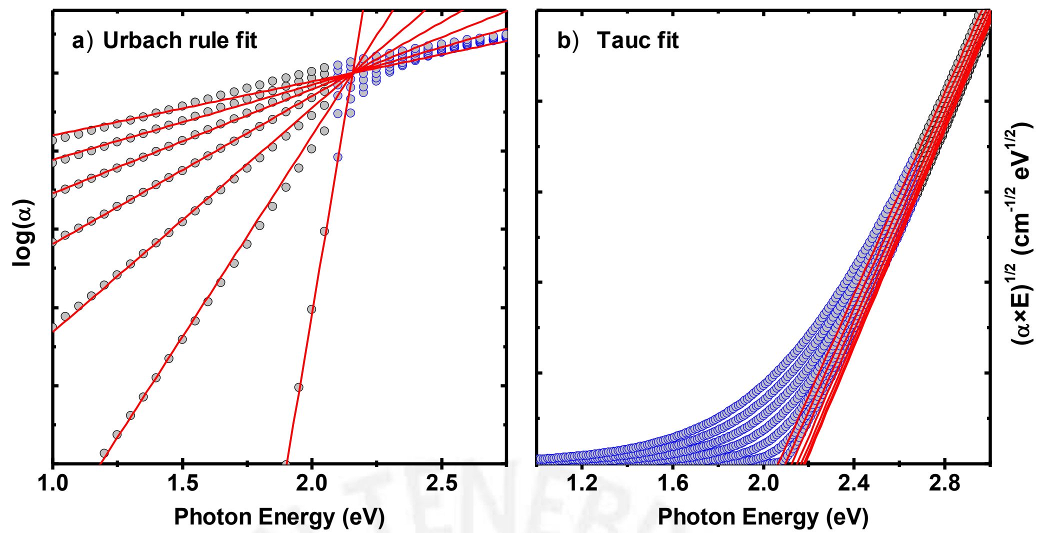

Figure 3.1.9. Absorption coefficient under two representations: logarithm-scale (a) and Tauc-plot (b) of equation 3.1.23 for $E_0 = 2.1$ eV and $1/\beta$ from 10 meV to 190 meV. The red lines correspond to fits using the Urbach rule (a) and the Tauc model (b). The Urbach rule fit was performed by sharing the parameters E_F and α_F for all the curves. The blue circles denote the masked (not-considered) data in each fitting procedure. The Urbach focus energy ordinate was found at $E_F = 2.156 \pm 0.0016$ eV.

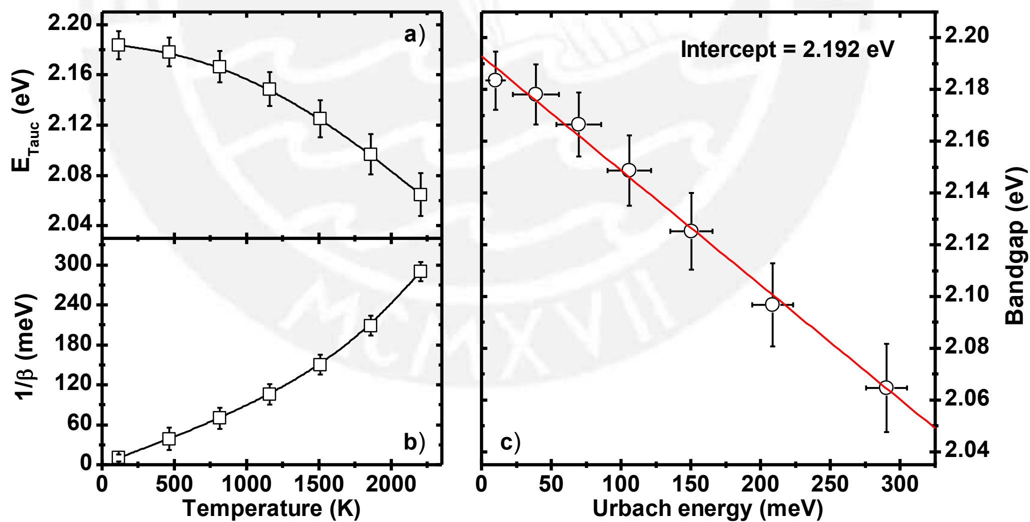

Figure 3.1.10. Tauc-gap versus the sample temperature (a). Urbach energy versus the sample temperature (b). And Tauc-gap versus the Urbach energy (c). These parameters were obtained from the simulation shown in figure 3.1.9. Notice that the intercept in (c) matches closely to the Urbach focus energy value.

Tesis publicada con autorización del autor
No olvide citar esta tesis
PUCP

The Tauc-gap and Urbach energy corresponding to the latter fits are depicted in figure 3.1.10. Here we recover a known behavior: the bandgap shrinking and the Urbach energy enhancement due to the increase of the thermal vibrations with the temperature. Both parameters seem to follow a linear correlation just as predicted by Cody et al [Cod81] (see figure 3.1.10).

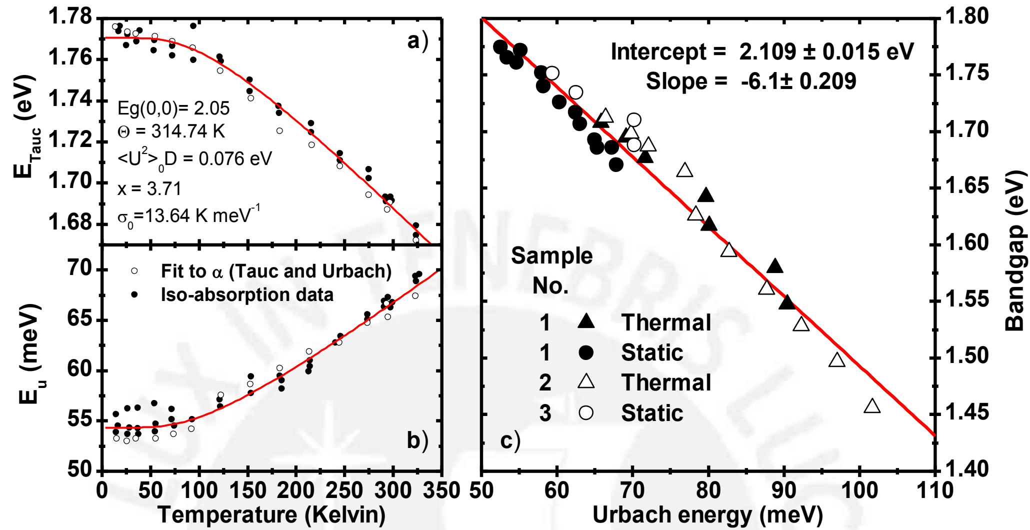

Figure 3.1.11. Tauc-gap versus the sample temperature (a). Urbach energy versus the sample temperature (b). Tauc-gap versus the Urbach energy of *a*-Si:H samples were the parameters were obtained after varying the disorder through thermal annealing treatments (static disorder variation) and changing the sample temperature (thermal disorder variation) (c) [Cod81]. The red lines correspond to fits performed with the equations 3.1.30 (a), 3.1.26 (b) and 3.1.31 (c).

The frozen phonon model approach relates the thermal and static disorder to the optical absorption spectra through the Urbach energy [Cod81]. For instance, the family of absorption curves presented in figure 3.1.8 was obtained at different sample temperatures and after different thermal annealing temperatures. As we already mentioned the thermal annealing treatments causes fundamentally a variation on the structure of the material, by delivering energy to the atoms and therefore allowing them to move sufficiently to reduce bond stress and static disorder. In the case of *a*-Si:H, evidence shows that the Urbach energy is enhanced by the hydrogen out-diffusion [Str91, Cod81]. Other hydrogenated exhibit a similar behavior [Jan03, Gue16]. Now then, the observation of a single family of curves describing the two types of disorder (static and thermal) is indication that both types of disorder are alike in terms of their effect in the optical absorption process. That

Tesis publicada con autorización del autor
No olvide citar esta tesis
ET LUX IN TENEBRIS LUCET MCMXVII PUCP

is, increasing the disorder (thermal or static nature) causes the bandgap to decrease and Urbach energy to increase. The latter behavior is observed in the experimental bandgap and Urbach energy data of a-Si:H depicted in figure 3.1.11.

Standard treatments of the Urbach edge in crystalline semiconductors [Toy71], conclude that the Urbach energy E_u is proportional to $\langle U^2 \rangle_T$, thermal average of the square of the displacement U of the atoms from their equilibrium positions: $E_u(T) = K\langle U^2 \rangle_T$. Thus, in order to include the effect of the topological (static) disorder in E_u, we make the plausible generalization that

$$E_u(T,X) = K\left\{ \langle U^2 \rangle_T + \langle U^2 \rangle_x \right\}, \tag{3.1.25}$$

where $\langle U^2 \rangle_x$ is the contribution of the static disorder to the mean-square deviation of the atomic positions from a perfectly ordered configuration [Cod81]. In order to justify this central hypothesis, the dynamic phonon disorder and static topological disorder, in the adiabatic approximation, should have similar effects on the electronic band energy levels. The temperature dependence of E_u can be estimated by approximating the phonon spectrum of the material by an Einstein oscillator with a characteristic temperature Θ [Cod81, Str91]. Here, the Einstein model is a good approximation to a Debye phonon spectrum with a Debye temperature $\Theta_D = 4/3\ \Theta$. Thus, in this model the equation 3.1.25 can be expressed as

$$E_u(T,X) = \frac{\Theta}{\sigma_0}\left(\frac{1+X}{2} + \frac{1}{\exp(\Theta/T) - 1}\right) \tag{3.1.26}$$

The condition that $E_u(T,X) \to T/\sigma_0$ while $T \to \infty$ is imposed and therefore the constant K from equation 3.1.25 is absorbed in σ_0, the latter being an Urbach edge parameter of order unity. In equation 3.1.26, $X = \langle U^2 \rangle_x / \langle U^2 \rangle_0$ is a measure of the structural disorder normalized to the zero-point uncertainty in the atomic positions $\langle U^2 \rangle_0$.

Now, in order to relate the temperature dependence of $E_u(T,X)$ to the bandgap $E_g(T)$ we separate the temperature dependence of the bandgap in two different components as

Tesis publicada con autorización del autor
No olvide citar esta tesis
ET LUX IN TENEBRIS LUCET MCMXVII PUCP

shown in the equation 3.1.27 [Str91, Cod81, All81]. The first term in the right hand side is the explicit temperature dependence of the bandgap which originates from the electron-phonon interaction through a deformation potential (here named D), whilst the second term is the implicit temperature dependence due to the thermal expansion of the network. γ is the thermal expansion coefficient and κ is the material's compressibility. From the known values of γ and κ, the second term contributes only about 2% to the measured temperature dependence setting the explicit temperature dependence as the dominant contribution for the temperature dependence of the bandgap [Str91].

$$\left(\frac{dE_g}{dT}\right)_P = \left(\frac{dE_g}{dT}\right)_V - \frac{\gamma}{\kappa}\left(\frac{dE_g}{dT}\right)_T \qquad (3.1.27)$$

The electron-phonon interaction on the temperature dependence of the bandgap in crystalline semiconductors can be written as shown in the equation 3.1.28, where $E_g(0)$ is the zero-temperature optical bandgap and D the second-order deformation potential. Analogously to the equation 3.1.25, equation 3.1.28 can be generalized to the case of amorphous materials by introducing the contribution of static disorder as shown in the equation 3.1.29. Finally, the mean square lattice displacements in equation 3.1.29 can be expressed in terms of the $E_u(T,X)$ by using the equation 3.1.25. This result is presented in the equation 3.1.30.

$$E_g(T) = E_g(0) - D\left\{ \langle U^2\rangle_T - \langle U^2\rangle_0 \right\} \qquad (3.1.28)$$

$$E_g(T,X) = E_g(0,0) - D\left\{ \langle U^2\rangle_T + \langle U^2\rangle_x - \langle U^2\rangle_0 \right\} \qquad (3.1.29)$$

$$E_g(T,X) = E_g(0,0) - \langle U^2\rangle_0 D\left(\frac{E_u(T,X)}{E_u(0,0)} - 1\right) \qquad (3.1.30)$$

The above model provides a consistent picture of the effects of static and thermal disorder on the bandgap energy and the Urbach tail slope. Moreover, the relation between

Tesis publicada con autorización del autor
No olvide citar esta tesis
ET LUX IN TENEBRIS LUCET MCMXVII PUCP

the bandgap and the Urbach energy are in good agreement with the experimental data of a-Si:H. For instance the solid curves in figure 3.1.11 are fits[1] performed with equations 3.1.30 and 3.1.26. The best fitted parameters (see figure 3.1.11) are close to the values obtained in [Cod81, Str91].

This result suggest that the optical bandgap of a-Si:H is determined by the degree of disorder in the lattice, rather than by the hydrogen content, as it was commonly assumed [Str91]. In this model, the hydrogen affects the bandgap only indirectly through its ability to relieve strain in the lattice. This result proofs sufficiently that thermal and topological disorder affects the bandgap and Urbach energy in the same way [Cod81]. Therefore since the Urbach edge represent the JDOS near the mobility edge it is plausible to treat the effect of the disorder on the optical absorption by thermal effects only but considering that a fictive temperature is also present in order to account for the static disorder. This statement establishes the basis of the frozen-phonon approach used previously and explains the fact that figures 3.1.10 and 3.1.11 are so similar. In this context, from the linear relation between the bandgap and the Urbach energy observed in equation 3.1.30 and assuming that the relation depicted in equation 3.1.31 is correct, the Urbach focus becomes the addition of the bangap in absence of disorder plus a term proportional to the deformation potential $E_F = E_g(0,0) + \langle U^2 \rangle_0 D$ [Cod05]. So the affirmation that the Urbach focus is a constant is valid only as far as $\langle U^2 \rangle_0 D$ is a disorder independent constant. Additionally, from equation 3.1.30, the slope of the aforementioned linear relation is defined by $G = \langle U^2 \rangle_0 D / E_u(0,0)$. A linear fit of the bandgap versus the Urbach energy in the case of a-Si:H is also depicted in figure 3.1.11. The Urbach focus found through this linear fit matches indeed with the value obtained directly by a global fit of the set absorption coefficients measured at different annealing stages and sample temperatures.

$$E_g(T, X) = E_F + G E_u(T, X) \tag{3.1.31}$$

[1]More precisely in the present thesis, a single fit of both data sets simultaneously sharing the same parameters in both equations achieved by the minimization of the sum of the estimator χ^2 of both models and data sets.

Tesis publicada con autorización del autor
No olvide citar esta tesis
PUCP

Finally, the above approach allowed us to relate the Urbach focus with the bandgap in the absence of disorder. This relation was somehow also observed by the proposed model in equation 3.1.23. Nevertheless, in the latter model the Urbach focus is actually a small region than a true constant. The proposed model for the absorption coefficient provides a simple equation that describes fully both the Urbach and the fundamental absorption regions. In section 5.1 a test to proof the validity of traditional approaches and the early proposed equation 3.1.23 is performed for *a*-Si:H and the materials that compound the main study of this thesis (AlN, SiN and SiC:H).

3.2 Luminescent properties of RE doped materials

When considering the optical emission within a single ion (or group of ions) embedded in a solid, it is appropriate to treat an optical transition with a localized model rather than a band model. In fact, most phosphors present localized luminescent centers and contain a far larger variety of ions than delocalized centers [Yen07]. A luminescent center is a localized electronic state capable to produce luminescence after suitable excitation. In crystals, luminescence centers arise from defects, such as positive and negative ion vacancies or interstitial atoms, or from activators which are specially introduced atoms or ions. The most important types of luminescent centers are transition metal ions (TMI) and rare earth ions (REI) that have been intentionally doped into a material. The luminescence features of these systems depend on the dopant and the host matrix. These states are also known as color centers. The host materials for localized, optically active centers are usually large bandgap solids. The large gap bestows transparency in the visible region to the host, and also prevents electrons from bridging the gap thermally.

As we have shortly reviewed in section 2.4, RE luminescence arises from radiative electronic transitions within the 4f-shell of triply ionized lanthanides. This luminescence presents remarkable features. First, its occurrence solely is already noteworthy. It was first reported by J. Becquerel in 1907 [Bec07], and afterwards it was found that the nature of this luminescence is of electric-dipole character. Such discovery was in contrast with what electrodynamics predict. More precisely, electrodynamics requires the change of parity between the initial and final states of the electron system with a spherically

Tesis publicada con autorización del autor
No olvide citar esta tesis
PUCP

symmetric potential. This requirement is known as Laporte's selection rule and it presented a Puzzle that took about 30 years to be solved [Vle37, Jud62, Ofe62] (see table 3.2.1). It was not until the independent and almost simultaneous publications of B. R. Judd [Jud62] and S. Ofelt [Ofe62] that a solution was found: the admixture of states of opposite parity through a crystal field, thus granting radiative electric-dipole transitions within the 4f-shell. Since the elaboration of this theory vast efforts have been realized to develop a powerful theory based on numerous spectroscopic experiments. This theory allows the calculation of transition probabilities and its development has been progressing for more than 40 years already. The main reason is that triply ionized lanthanides could always contribute to modern research demands. Despite their interesting magnetic properties (the most widespread commercial use of RE solids at present is the production of super-strong permanent magnets containing Neodymium), the application of REs in the field of light emitting devices plays a very important role. For instance, an extensive use of Neodymium is the Nd:YAG laser, widely used both at its fundamental wavelength of 1064 nm (infra-red) or in the visible when the frequency is doubled.

Table 3.2.1. Multipole operators and selection rules. ***P*** electric dipole, ***M*** magnetic dipole and ***Q*** quadrupole operators. ***M*** radiation can account for some RE transitions however it represents just a special case. ***Q*** radiation accounts for all the RE transitions, yet the probability is too low to account for the observed intensities. Therefore, ***P*** radiation is the only reasonable channel to explain the observed RE luminescence intensity. This solution implied a variation of the electronic motion due to crystalline fields. Such theory is known as Judd-Ofelt theory.

Operator	S	L	J ($J = 0 \rightarrow J = 0$, not allowed)	Parity
$\bar{P} = -e\sum_i \bar{r}_i$	$\Delta S = 0$	$\Delta L = 0, \pm 1$	$\Delta J = 0, \pm 1$	opposite
$\bar{M} = -\frac{e\hbar}{2mc}\sum_i \bar{l}_i + 2\bar{s}_i$	$\Delta S = 0$	$\Delta L = 0$	$\Delta J = 0, \pm 1$	same
$\bar{Q} = \frac{1}{2}\sum_i (\bar{k} \cdot \bar{r}_i)\bar{r}_i$	$\Delta S = 0$	$\Delta L = 0, \pm 1, \pm 2$	$\Delta J = 0, \pm 1, \pm 2$	same

The most remarkable feature of RE spectra is their sharp luminescence lines similar to the spectra observed in the case of free ions. This behavior is consequence of the fact that the

Tesis publicada con autorización del autor
No olvide citar esta tesis
ET LUX IN TENEBRIS LUCET MCMXVII PUCP

4f electrons are partially shielded from surrounding crystal fields due to the outer filled 5s and 5p shells (see figure 2.4.1). Owing to this shielding, the energy levels of the 4f electron systems are almost unaltered, and the spectral line-widths are to some extent often only a bit broadened. However the influence of the crystal field on the dynamical processes is profound. The crystal field is responsible for the radiative transitions between 4f states (i.e. relaxing the Laporte's selection rules). Additionally it drives the non-radiative processes that allow the energy exchange between the host matrix and the ion. In the following sections we will develop a condensed approach to the theory up to the final solution. This will be done only to certain degree due to its large volume. The formal treatment of intensity and energy levels calculations are based on group theory (detailed calculations can be found in [Jud97] and [Wyb65]). The subsequent description is based in the following references [Gör98, ODo10, Vij06, Hüf78].

Elementary features

Partially filled shells are observed usually in transition metal groups which comprise the 3d iron group, the 4d palladium group, the 4f lanthanide group, and the 5f actinide group. In a crystal, luminescent center ions are by no means free but surrounded by a cage of ligand atoms. The ligand atoms interact with the luminescent center ions, producing the so called crystal field. The small crystal field interaction entails that the RE ions are not very sensitive to the motion of the lattice. Consequently $f \rightarrow f$ transitions are characterized by sharp lines, with typical linewidths around 1 cm^{-1} at low temperatures. The energy associated with this interaction varies around 1 to 1000 meV. This energy can exceed the spin-orbit interaction, and in some cases the electrostatic interaction with other electrons. Thus the crystal field is an additional interaction in an already complicated problem. A perturbation approach is necessary in which terms are considered in suitable order, for instance by decreasing interaction energy. The crystal field interaction is introduced at the appropriate point relative to the sequence of interactions internal to the luminescent ion (see figure 3.2.1). In decreasing interaction energy order these are [Vij06]:

Tesis publicada con autorización del autor
No olvide citar esta tesis
PUCP

(i) The interaction of an electron with the Coulomb field of the nucleus, modified by the repulsion field of the other electrons. With an appropriate mean electronic field with central symmetry this interaction ends in the electronic levels grouped in configurations. For instance, the ground configuration of Cr^{3+} is $3d^3$, which is about 10 000 meV below the first excited configuration $3d^2 4s$.

(ii) The residual mutual electrostatic repulsion of the electrons $H_c = -e^2 \sum_{ij} 1/r_{ij}$, not represented by a central field. The Hamiltonian of this interaction is partially simplified in the LS-coupling scheme (this scheme is also known as Russel-Saunders for $H_c \gg H_{so}$). Where a suitable basis is chosen in order to diagonalize the spin orbit coupling in which the orbital angular momentum and the electron spin are coupled and give rise to the total angular momentum L and total spin S. This coupling produces energy splittings separated about 1000 meV between terms of different quantum numbers L and S associated with a determined configuration. For example, the ground term of a $3d^3$ configuration is (according to the Hund's rule) ^4F, with $S = 3/2$ and $L = 3$, around 1000 meV below ^4P term, with $S = 3/2$ and $L = 1$ which belongs to the same $3d^3$ configuration.

(iii) The spin-orbit coupling, $H_{SO} = \lambda L \cdot S$, with $J = L \pm S$ being a good quantum number. With the upper and lower sign suitable to electron shells being more or less than half-filled, respectively. This interaction splits a given term into a multiplet of levels with different J. The components of the multiplets are split by about 1000 meV for 4f electrons while about 10meV for 3d electrons.

Tesis publicada con autorización del autor
No olvide citar esta tesis
ET LUX IN TENEBRIS LUCET MCMXVII PUCP

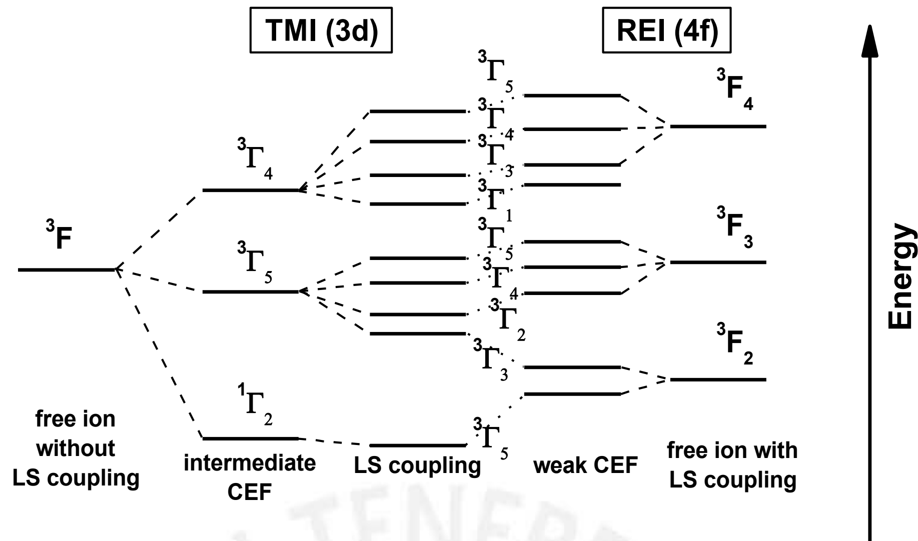

Figure 3.2.1. Crystal field interaction of an ion with $L = 3$ and $S = 1$ for intermediate and weak crystal field strength [Pur90].

The magnitude of the crystal field interaction (CF) relative to the interactions enumerated above is different for the various transition groups. This magnitude might conveniently be grouped as follows:

(i) Strong crystal field, i.e. CF > LS-coupling. For example the 4d and 5d electron systems.

(ii) Intermediate crystal field, i.e. CF ≈ LS-coupling > spin-orbit coupling. Typically case found in 3d electron systems.

(iii) Weak crystal field, i.e. CF < spin-orbit coupling. The 4f electron systems exhibit this behavior.

Figure 3.2.1 depicts an example of the crystal field interaction effect on the energy level scheme of an ion with $L = 3$ and $S = 1$. The weak (iii) and intermediate (ii) cases are shown in the right and left hand, respectively [Pur90].

Tesis publicada con autorización del autor
No olvide citar esta tesis
PUCP

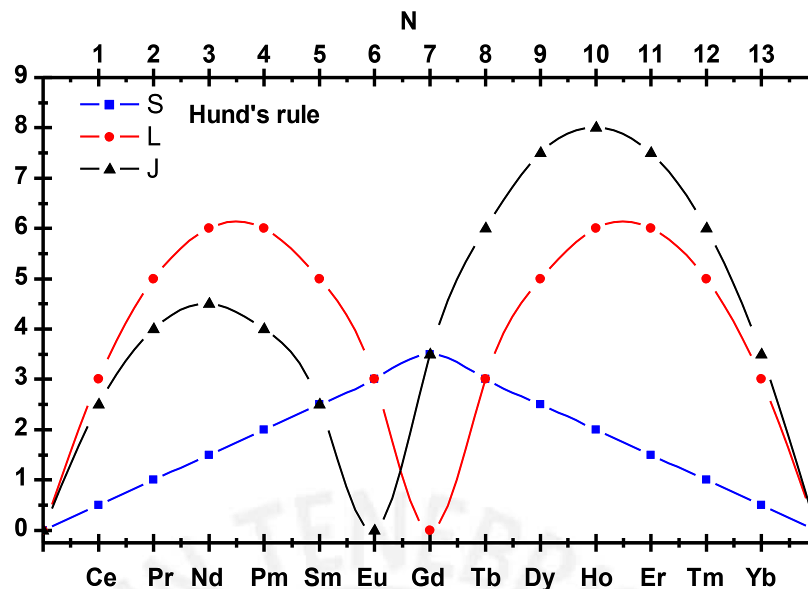

Figure 3.2.2. Application of the Hund's rule to trivalent RE ions, here depicted by increasing the number of electrons in the *f* shell.

Besides gadolinium, neutral REs exhibit an electron configuration $4f^N 5s^2 5p^6 s^2$, where the number *N* of electrons ranges from 2 for Ce^0 up to 14 for Yb^0. The typical oxidation state REs are found is 3+, though 2+ is found in some compounds. In the triply ionized state the electron configuration becomes $4f^N 5s^2 5p^6$ having the number *N* of electrons ranging from 1 for Ce^{3+} to 13 for Yb^{3+}. The Hund's rule describes the filling of the 4*f* shell. It establishes that the term with the highest quantum number *S* has the lowest energy. In the case of several terms with the same *S*, the one with the highest angular momentum quantum number *L* has the lowest energy. Additionally, due to the spin-orbit coupling, the terms ${}^{2S+1}L$ are split into levels $J = L + S, L + S - 1, \dots, |L - S|$, where for less than half filled shells the term with the smallest J lies lowest in energy. Otherwise the term with the largest J has the lowest energy (see figure 3.2.2). In this way it is possible to predict the ground state $\boldsymbol{{}^{2S+1}L_J}$ of RE ions, as it is shown in the table 3.2.2 [Hua10].

A noteworthy feature of REI is the observed decrease in both the ionic and covalent radii and the increase of the Pauling's electronegativity with increasing the atomic number *Z*. This might be attributed to the poor shielding capabilities of the $4f$ electrons causing the subsequent shrinking of the radial integrals of the outer $5s$ and $5p$ electrons with

Tesis publicada con autorización del autor
No olvide citar esta tesis
ET LUX IN TENEBRIS LUCET MCMXVII PUCP

increasing the nuclear charge [Hua10]. This effect is the main reason of the slightly different chemistry found in compounds throughout the lanthanide series [Dor13]. Additionally, the different ionic radii may also have an impact on the symmetry at which REI are found. For instance, the symmetry of Tb^{3+} implanted GaN is different from the observed in Pr^{3+} and Sm^{3+}[Gru01,Gru02, Gru02a]. Triply ionized REs are found with a large amount of possible coordination numbers, leading to a large number of possible symmetries [Gör98, Hua10]. Typically coordination numbers up to 8 and 9 are found, nonetheless higher coordination numbers are also possible. This feature is in contrast to the limited amount of coordination numbers found in TMI [Vij06].

Table 3.2.2. Filling of the $4f$ shells of RE ions and predicted ground state according to the Hund's rule [Hua10].

$S = |\sum m_s|$, with $m_s = \pm 1/2$.

$L = |\sum m_l|$

$J = |L - S|$ (less than half-filled sheld), $J = L + S$ (otherwise)

		m_l	-3	-2	-1	0	1	2	3	S	L	J	$^{2S+1}L_J$
Ce^{3+}	$4f^1$		↓							1/2	3	5/2	$^2F_{5/2}$
Pr^{3+}	$4f^2$		↓	↓						1	5		$^3H_4$
Nd^{3+}	$4f^3$		↓	↓	↓					3/2	6	9/2	$^4I_{9/2}$
Pm^{3+}	$4f^4$		↓	↓	↓	↓				2	6	4	$^5I_4$
Sm^{3+}	$4f^5$		↓	↓	↓	↓	↓			5/2	5	5/2	$^6H_{5/2}$
Eu^{3+}	$4f^6$		↓	↓	↓	↓	↓	↓		3	3	0	$^7F_0$
Gd^{3+}	$4f^7$		↓	↓	↓	↓	↓	↓	↓	7/2	0	7/2	$^8S_{7/2}$
Tb^{3+}	$4f^8$		↓↑	↓	↓	↓	↓	↓	↓	3	3	6	$^7F_6$
Dy^{3+}	$4f^9$		↓↑	↓↑	↓	↓	↓	↓	↓	5/2	5	15/2	$^6H_{15/2}$
Ho^{3+}	$4f^{10}$		↓↑	↓↑	↓↑	↓	↓	↓	↓	2	6	8	$^5I_8$
Er^{3+}	$4f^{11}$		↓↑	↓↑	↓↑	↓↑	↓	↓	↓	3/2	6	15/2	$^4I_{15/2}$
Tm^{3+}	$4f^{12}$		↓↑	↓↑	↓↑	↓↑	↓↑	↓	↓	1	5	6	$^3H_6$
Yb^{3+}	$4f^{13}$		↓↑	↓↑	↓↑	↓↑	↓↑	↓↑	↓	1/2	3	7/2	$^2F_{7/2}$

Tesis publicada con autorización del autor
No olvide citar esta tesis
ET LUX IN TENEBRIS LUCET MCMXVII PUCP

Hamiltonian of a RE ion in a solid

The treatment of triply ionized lanthanides in solids is dealt according to the Schrödinger equation. The Hamiltonian of an optically active RE ion in a solid can be written as shown in the equation 3.2.1. Here the H_{FI}, H_{CF} and H_L are the Hamiltonians for the free ion, static crystal field interaction and lattice (electron-phonon) interaction, respectively.

$$H = H_{FI} + H_{CF} + H_L \tag{3.2.1}$$

The free ion Hamiltonian H_{FI} includes all electric and magnetic interaction in the ion. For many-electron atoms this Hamiltonian is quite burdensome. Extensive treatments on the various interaction contained in H_{FI} can be found in [Die68, Mor82]. Now, considering only the most relevant interactions, H_{FI} can be expressed in the following form:

$$H_{FI} = H_0 + H_C + H_{SO}. \tag{3.2.2}$$

Here, H_0 contains the kinetic energy of the electrons H_K, and the electrostatic interaction of each electron with an average potential due to the nucleus and the other electrons H_P (see equation 3.2.3). This potential and the kinetic energy have typically a spherical symmetry. The sum in equation 3.2.3 runs all over the 4f electrons and Z represents the atomic potentials screened by the inner electrons.

$$H_0 = H_K + H_P = -\frac{\hbar^2}{2m}\sum_{i=1}^{N}\nabla_i^2 - \sum_{i=1}^{N}\frac{Ze^2}{r_i} \tag{3.2.3}$$

Solving the Schrödinger equation at this point leads to the approximate solutions $|n, l, m_{l,} m_s\rangle$ characterized by the quantum numbers n, l, m_l, m_s shown in equation 3.2.4.

$$\psi_{n,l,m_l,m_s}(r,\theta,\phi) = \frac{1}{r}R_{n,l}(r)Y_{l,m_l}(\theta,\phi)\chi_{m_s} \tag{3.2.4}$$

The eigenstates of H_0 corresponding to a particular configuration $(4f^N)$ are degenerate. The perturbations are responsible partially for the removal of the degeneracy of the levels encountered in equation 3.2.3.

Tesis publicada con autorización del autor
No olvide citar esta tesis
ET LUX IN TENEBRIS LUCET MCMXVII PUCP

H_C on the other hand accounts for the electrostatic interaction between electrons in the unfilled shell. The electrostatic interaction is expanded into Legendre polynomials and the spherical-harmonic addition theorem is applied, thus writing H_C in tensor-operator form [Sob72]:

$$\begin{aligned} H_C &= -e^2 \sum_i \sum_{j>i} \frac{1}{|r_j - r_i|} \\ &= -e^2 \sum_i \sum_{j>i} \sum_{k=0}^{\infty} \frac{r_<^k}{r_>^{k+1}} P_k\big(\cos(r_i, r_j)\big) \\ &= -e^2 \sum_i \sum_{j>i} \sum_{k=0}^{\infty} \frac{r_<^k}{r_>^{k+1}} \sum_{q=-k}^{k} \frac{4\pi}{2k+1} (-1)^q Y_k^q(\theta_i, \phi_i) Y_k^{-q}(\theta_j, \phi_j) \\ &\equiv -e^2 \sum_i \sum_{j>i} \sum_{q=-k}^{k} \frac{r_<^k}{r_>^{k+1}} (-1)^q C_{-q}^{(k)}(i) C_q^{(k)}(j) \equiv -e^2 \sum_i \sum_{j>i} \frac{r_<^k}{r_>^{k+1}} C_i^{(k)} C_j^{(k)} \end{aligned} \tag{3.2.5}$$

with the $C_q^{(k)}$ defined by

$$C_q^{(k)}(i) \equiv \sqrt{\frac{4\pi}{2k+1}} Y_k^q(\theta_i, \phi_i)$$

Rewriting equation 3.2.5 in a more convenient form [Jud97]:

$$\begin{aligned} H_C &= -e^2 \sum_i \sum_{j>i} \frac{r_<^k}{r_>^{k+1}} \left(u_i^{(k)} u_j^{(k)}\right) \langle f \| C^{(k)} \| f \rangle \\ &\equiv e^2 \sum_{k=0,2,4,6} f_k F^k \end{aligned} \tag{3.2.6}$$

Here f_k are the operators and F^k are the Slater integrals

$$F^k \equiv e^2 \iint_0^{\infty} \frac{r_<^k}{r_>^{k+1}} R^2(r_i) R^2(r_j) dr_i dr_j \tag{3.2.7}$$

This interaction splits the ground configuration into different terms. This terms share common values of S and L and are identified by the ^{2S+1}L notation. H_C commute with the

Tesis publicada con autorización del autor
No olvide citar esta tesis
ET LUX IN TENEBRIS LUCET MCMXVII PUCP

L^2, S^2, L_z and S_z operators and thus the corresponding quantum numbers L, S, M_L and M_S, respectively are valid. The energy of each state is independent of M_L and M_S, and therefore exhibit a degenerance of $(2L+1)(2S+1)$. It is not difficult to show that the parameter F^0 produced a shift to the whole $4f$ configuration energy levels, but with no effect on the relative energetic positions. Thus, this parameter is excluded and along with other shifting contributions summed up in a parameter here on named H_{AVE} (see equation 3.2.10).

Lastly, the spin-orbit term is denoted by H_{SO} in the free ion Hamiltonian (equation 3.2.2). For RE ions it is the next most significant interaction followed by the crystal field interaction H_{CF}. This case is known as the weak crystal field scheme. Nonetheless, for TM ions H_{CF} is larger than H_{SO}, so either the medium or strong field scheme is relevant (see figure 3.2.2). It describes the interaction between the spin of the electron and its magnetic moment. The Hamiltonian term H_{SO} is obtained from the non-relativistic form of the Dirac equation and takes a known form in the case of spherically symmetric electrostatic potential [Sob72].

$$H_{SO} = \sum_i \xi_i \mathbf{s}_i \cdot \mathbf{l}_i \quad (3.2.8)$$

Again, the sum in equation 3.2.8 runs over all $4f$ electrons. Furthermore, equation 3.2.8 can be written similarly to the equation 3.2.6 [Jud97]:

$$H_{SO} = -e^2 \sum_i \left(u_i^{(1)} u_j^{(1)}\right) \langle f \| \mathbf{s} \| f \rangle \langle f \| \mathbf{l} \| f \rangle \quad (3.2.9)$$

Tesis publicada con autorización del autor
No olvide citar esta tesis
ET LUX IN TENEBRIS LUCET MCMXVII PUCP

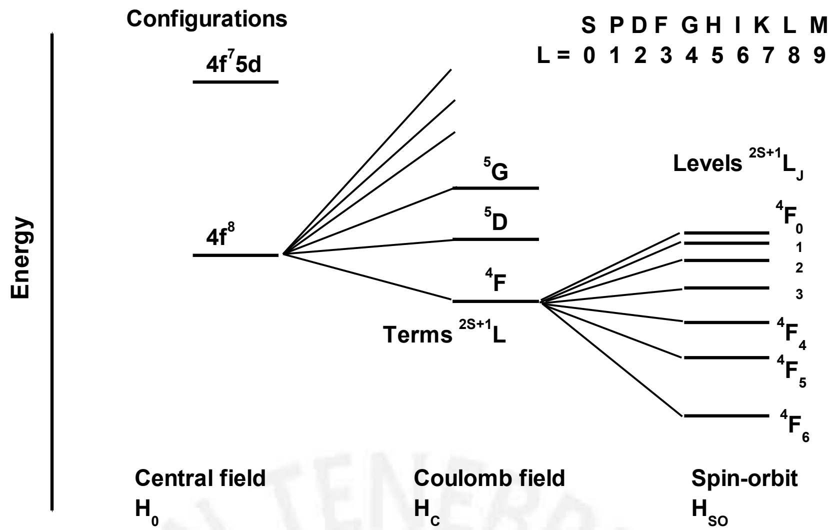

Figure 3.2.3. Schematic representation of the energy levels splitting due to the distinct interactions included in the free RE ion Hamiltonian (equation 3.2.2). H_0 represents the central field interaction, that is the electrons in the field of the nucleus. H_C denotes the mutual repulsion of electrons solely. H_{SO} accounts for the coupling between spin and orbital angular momentum. This is scheme is known as the LS-coupling scheme in which the Coulomb interaction is greater than the spin-orbit interaction.

When including the spin-orbit interaction, the free ion energy levels can no longer be categorized by the quantum numbers S and L. In fact this interaction splits each spectral term into different levels. These levels are called J-multiplets (or J-manifolds) since H_{SO} commutes with $J = L + S$ and not with S and L separately. See figure 3.2.3 in which the labeling of the states changes from ${}^{2S+1}L$ to ${}^{2S+1}L_J$ after the spin orbit interaction.

The Hamiltonian of the free ion H_{FI} can be written in the following way:

$$H_{FI} = H_{AVE} - \frac{\hbar^2}{2m}\sum_i \nabla_i^2 - \sum_i \frac{Ze^2}{r_i} + e^2 \sum_{k=2,4,6} f_k F^k + \sum_i \xi_i \mathbf{s}_i \cdot \mathbf{l}_i \qquad (3.2.10)$$

Further corrections to the interactions can be included. For instance, a correction to the two-particle Coulomb interaction has been proposed by Rajnak and Wybourne [Raj63]. This interaction is named linear configuration interaction H_{LC} and is parameterized using three parameters α, β and γ in the form shown in equation 3.2.11 where L is the total

Tesis publicada con autorización del autor
No olvide citar esta tesis
PUCP

angular momentum operator, $G(G_2)$ and $G(R_7)$ are Casimir's operators for the corresponding groups G_2 and G_7. Another correction that can be taken into account besides the aforementioned linear configuration is for the case of more than 12 electrons in the 4f shell. It is named non-linear three-particle configuration interaction [Jud66]. Notwithstanding these corrections will not alter very much the energy levels calculated by solving the Schrödinger equation with the shown H_{FI} Hamiltonian in the equation 3.2.10.

$$H_{LC} = \alpha L(L+1) + \beta G(G_2) + \gamma G(R_7) \tag{3.2.11}$$

Crystal field interaction

Up to this point, in the Hamiltonian of equation 3.2.10 we have only considered the ion as free. However as mentioned earlier, RE ions inserted into a crystal matrix experience another contribution to the Hamiltonian due to the interaction of the 4f electrons with the surrounding crystal field H_{CF}. For an overview of the calculation of the crystal field with the 4f electrons the *Crystal field Handbook* [New00] is a good alternative among others like [Gör98], [Vij06] and [Hüf78]. As we already remarked before, in the free atom there is a spherical symmetry and each level is reduced to $2J+1$ degeneracy. Notwithstanding, when the ion is placed in a crystal environment the spherical symmetry is broken and each level splits. In fact the spherical symmetry is reduced to the point symmetry at the ion location. The degree to which the $2J+1$ degeneracy is removed will depend on the symmetry surrounding the ion. These features will become clear shortly.

From now on we will follow with the point-charge description. In this scheme point charges Z_j will produce a potential V_i at a distance R_j.

$$V(r_i) = -e \sum_j \frac{Z_j}{|R_j - r_i|} d\tau \tag{3.2.12}$$

The potential $V(r_i)$ written in the equation 3.1.12 is the potential from all point charges j within the lattice at a position r_i of the ith 4f electron [Gör98, Vij06]. Since the

Tesis publicada con autorización del autor
No olvide citar esta tesis

eigenfunctions of the free Hamiltonian possess complete spherical symmetry and can be expressed in terms of spherical harmonics we then expand the equation 3.2.12 in spherical harmonics as shown in the equation 3.2.13. This procedure is performed by expanding the term $|R_j - r_i|^{-1}$ into Legendre polynomials, where $r_<$ is the smaller and $r_>$ the larger distance of (R, r_i). The angle ω between R and r_i is expressed in the polar angles θ and ϕ, applying the so called spherical harmonic addition theorem.

$$\begin{aligned} V(r_i) &= -e\sum_j \frac{Z_j}{|R_j - r_i|} d\tau \\ &= -e\sum_j Z_j \sum_{k=0}^{\infty} \frac{r_<^k}{r_>^{k+1}} P_k(\cos(R, r_i)) \\ &= -e\sum_j Z_j \sum_{k=0}^{\infty} \frac{r_<^k}{r_>^{k+1}} \sum_{q=-k}^{k} \frac{4\pi}{2k+1}(-1)^q Y_k^q(\theta_i, \phi_i) Y_k^{-q}(\theta, \phi) \\ &= -e\sum_j Z_j \sum_{k=0}^{\infty} \sum_{q=-k}^{k} B_q^{(k)} C_q^{(k)}(i) \end{aligned} \tag{3.2.13}$$

$C_q^{(k)}$ and $B_q^{(k)}$ are defined by

$$\begin{aligned} C_q^{(k)}(i) &= \sqrt{\frac{4\pi}{2k+1}} Y_k^q(\theta_i, \phi_i) \\ B_q^{(k)} &= -e\sum_{k=0}^{\infty} Z_j (-1)^q C_k^{-q}(\theta, \phi) \frac{r_<^k}{r_>^{k+1}} \end{aligned} \tag{3.2.14}$$

Since $B_q^{(k)}$ (see equation 3.2.14) does not act on the $4f$ wavefunctions whilst the $C_q^{(k)}(i)$ term does the $B_q^{(k)}$ operators can be taken outside the crystal field matrix element as shown in equation 3.2.15 [Hüf78].

$$\left\langle 4f^N \gamma\, S\, L\, J\, M \middle| \sum_i C_q^{(k)}(i) \middle| 4f\wedge N\gamma' S' L' J' M' \right\rangle$$

Tesis publicada con autorización del autor
No olvide citar esta tesis
PUCP

$$
\begin{aligned}
&= \left\langle 4f^N\gamma\, S\, L\, J\, M \middle| U_q^{(k)} \middle| 4f\,^\wedge N\gamma' S' L' J' M' \right\rangle \left\langle 3 \left\| C^{(k)} \right\| 3 \right\rangle \\
&= \sqrt{49}(-1)^{2J-M+S+k+l}[[J][J']]^{1/2} \\
&\qquad \times \begin{pmatrix} 3 & k & 3 \\ 0 & 0 & 0 \end{pmatrix} \begin{pmatrix} J & k & J' \\ -M & q & M' \end{pmatrix} \begin{Bmatrix} J & J' & k \\ L' & L & S \end{Bmatrix} \\
&\qquad \times \left\langle 4f^N\gamma\, S\, L\, J \left\| U_q^{(k)} \right\| 4f\,^\wedge N\gamma' S' L' J' \right\rangle
\end{aligned} \tag{3.2.15}
$$

Notice that when $-M + q + M' = 0$ is satisfied the second 3j-symbol term in the equation 3.2.15 is different from zero. This is actually a general selection rule for transitions between different crystal field levels. Additionally, the triangle conditions of the 3j-symbols require that $J + J' \geq k$. The first 3j-symbol is different to zero only if $k + 6$ is even, thus only with an even k. Furthermore, the triangle conditions require $k \leq 6$. Consequently only the $C_q^{(k)}$ with an even k between 0 and 6 are responsible for splitting the crystal field levels. In this sense, only the even part of the crystal field potential is responsible for the splitting of the ${}^{2S+1}L_J$ levels, while the odd part of the crystal field potential is responsible for the intensities of the induced electric dipole transitions. The latter features were shown by Judd and Ofelt and will be discussed shortly.

Now, if we separate the spherical harmonic by real and imaginary parts, the potential can be written as [Hüf78, Gör98, Vij06]:

$$
\begin{aligned}
V(r_i) = \sum_{k=0}^{7} \Bigg[\; B_0^{(k)} C_0^{(k)}(i) + \sum_{q=1}^{k} \bigg(& B_q^{(k)} \left(C_{-q}^{(k)}(i) + (-1)^q C_k^{(q)}(i) \right) \\
& + B'^{(k)}_q \left(C_{-q}^{(k)}(i) - (-1)^q C_k^{(q)}(i) \right) \bigg) \; \Bigg]
\end{aligned} \tag{3.2.16}
$$

with the $B_q^{(k)}$ rewritten as follows,

$$
B_0^{(k)} = \sqrt{\frac{4\pi}{2k+1}} Y_k^0 \sum_j (-Ze) \frac{r^k}{R_j^{k+1}} \tag{3.2.17}
$$

Tesis publicada con autorización del autor
No olvide citar esta tesis
ET LUX IN TENEBRIS LUCET MCMXVII PUCP

$$B_q^{(k)} = \sqrt{\frac{4\pi}{2k+1}}(-1)^q \operatorname{Re} Y_k^q \sum_j (-Ze) \frac{r^k}{R_j^{k+1}}$$

$$B_q'^{(k)} = \sqrt{\frac{4\pi}{2k+1}}(-1)^q \operatorname{Im} Y_k^q \sum_j (-Ze) \frac{r^k}{R_j^{k+1}}$$

Due to the fact that the crystal field Hamiltonian is invariant under all symmetry operations of the point group the $B_q^{(k)}$ parameters become further restricted. This means that only the $B_q^{(k)}$ for a specified symmetry will be nonzero and the corresponding $Y_k^{(q)}$ will contain the symmetry elements of the point group. These $B_q^{(k)}$ terms are typically determined experimentally by fitting the measured energy levels to the ones calculated theoretically. More specifically, as soon as the point symmetry and the appropriate form of the crystal field are known, the crystal field energy matrix is constructed and then diagonalized using an estimate set of $B_q^{(k)}$ starting parameters. The resultant set of theoretical energy levels is compared to the set of experimental levels and then by an iterative fitting procedure the $B_q^{(k)}$ parameters are adjusted to obtain the best overall fit to the experiment [Hüf78].

The crystallographic point groups can be divided into four general symmetry classes [Run56]:

i. Cubic: O_h, O, T_d, T_h, T
ii. Hexagonal: D_{6h}, D_6, C_{6v}, C_6, D_{3h}, D_{3d}, D_3, C_{3v}, S_6, C_3
iii. Tetragonal: D_{4h}, D_4, C_{4v}, C_4, D_{2d}, S_4
iv. Lower symmetry: D_{2h}, D_2, C_{2v}, C_{2h}, C_2, C_s, S_2, C_1

For instance, for the C_{3v} symmetry, the potential at a 4f electron turns as shown in equation 3.2.18 where only the even part (responsible of the energy level splitting) of the crystal field is written [Gör98]. In this case we have six fitting parameters.

Tesis publicada con autorización del autor
No olvide citar esta tesis
PUCP

$$V_{C_{3v}}^{even} = B_0^{(2)}C_0^{(2)} + B_0^{(4)}C_0^{(4)} + B_3^{(4)}\left(C_3^{(4)}C_{-3}^{(4)}\right) + B_0^{(6)}C_0^{(6)} + B_3^{(6)}\left(C_3^{(6)}C_{-3}^{(6)}\right) + B_6^{(6)}\left(C_6^{(6)}C_{-6}^{(6)}\right) \quad (3.2.18)$$

On the other hand, the even part of the potential for a 4f electron in the case of D_{3h} symmetry looks as shown in the equation 3.2.19 where four fitting parameters are necessary [Hüf78].

$$V_{D_{3h}}^{even} = B_0^{(2)}C_0^{(2)} + B_0^{(4)}C_0^{(4)} + B_0^{(6)}C_0^{(6)} + B_6^{(6)}\left(C_6^{(6)} + C_{-6}^{(6)}\right) \quad (3.2.19)$$

In summary, the positions of the electronic energy levels arise from a combination of the Coulomb, spin-orbit and crystal field interactions. The electrostatic interaction leads to the ^{2S+1}L splitting with an energy separation about 10^4cm^{-1}. Then the spin-orbit interaction splits further the levels into $^{2S+1}L_J$ states putting them apart about 10^3cm^{-1}. Subsequently, the even part of the crystal field potential removes (partially) the degeneracy in J producing an energy level separation of about 10^2 cm^{-1}. The magnitude of this separation depends on the crystal field strength. The values for k and q are limited by the point symmetry. That is, the number of nonzero terms in the H_{CF} Hamiltonian depends on the point symmetry and thus the crystal field must exhibit the same symmetry of the ion. Notwithstanding at present is almost impossible to determine the $B_q^{(k)}$ parameters, therefore the Hamiltonian in equation 3.2.16 is used to parameterize the observed crystal field energy levels in terms of the parameters $B_q^{(k)}$. If a large number of crystal field energy levels have been determined experimentally, these energy levels are examined by evaluating the matrix elements of $C_q^{(k)}$ and treating the $B_q^{(k)}$ as fitting parameters [Wyb65, Hüf78]. On the other hand, the nonzero terms corresponding to the odd-order of the H_{CF} Hamiltonian (defined by $k = 1, 3, 5$) play a key role in the Judd-Ofelt theory for induced dipole transitions which we will review shortly. Additionally the terms with $k = 0$ and $q = 0$ are spherically symmetric and affect all energy levels by a uniform shift in the configuration.

Tesis publicada con autorización del autor
No olvide citar esta tesis
PUCP

Finally, the local environment of a RE ion is roughly the same as that in a crystal, giving rise to the known spectrum. However, since the far field is different for every RE ion in an amorphous host the spectral lines exhibit a large inhomogeneous broadening, typically of the order of 100 cm^{-1}. This feature makes the spectra much less useful for an investigation of the crystal field features in glasses. Therefore most investigations of the optical emission properties of RE-doped glasses deal with the determination of lifetimes and oscillator strength [Hüf78].

Induced electric dipole transitions and radiative lifetimes

Up to now we have developed the theory of the energy levels of RE ions in solids based on the static, free-ion and single configuration approximations. That is, the central ion is affected by the surrounding host ions via a static crystal field. This field acts on the free ion Hamiltonian and is treated as a perturbation. Finally in the single configuration model, the interaction of electrons between configurations is neglected. Now we would like to know what happens to the electronic transitions selection rules when incorporating the crystal field. For this let us start by the electric multipole tensor operator $-eD_\rho^{(l)}$ (see equation 3.2.20) where the index l denotes the multipolarity of the radiation i.e. $l = 1$ for dipole, $l = 2$ for quadrupole, etc. The sum in equation 3.2.20 runs over all 4f electrons and $\boldsymbol{r}_\rho$ is the position operator of the ith electron.

$$-eD_\rho^{(l)} = -e\sum_i \boldsymbol{r}_\rho^{(l)}(r_i, \theta_i, \phi_i) \qquad (3.2.20)$$

For the initial $\langle m|$ and final $|n\rangle$ states the matrix element for an electric dipole transition fulfills the condition depicted in equation 3.2.21 only if $\langle n|$ and $|m\rangle$ have opposite parities. Notice that the parity operator $\boldsymbol{\pi}_\rho$ does not commute with $\boldsymbol{r}_\rho$. Now, we know that the lanthanide ions are characterized by the shielded $4f$ shell (where the atomic like transitions take place). Since the $4f$ states all have the same parity, i.e $\pi = (-1)^{\sum_i l_i}$ with $l = 3$ for lanthanides the probability of this transitions is negligible. Notwithstanding, the occurrence of electric dipole transitions can be explained by the admixture of states of opposite parity due to the crystal field [Gör98, Jud62, Ofe62]. Here we will follow a brief description.

Tesis publicada con autorización del autor
No olvide citar esta tesis
PUCP

$$\langle n|\boldsymbol{r}_{\boldsymbol{\rho}}|m\rangle = \langle n|\boldsymbol{\pi}_{\boldsymbol{\rho}}^{\dagger}\boldsymbol{\pi}_{\boldsymbol{\rho}}\boldsymbol{r}_{\boldsymbol{\rho}}\boldsymbol{\pi}_{\boldsymbol{\rho}}^{\dagger}\boldsymbol{\pi}_{\boldsymbol{\rho}}|m\rangle = -\epsilon_i\epsilon_f\langle n|\boldsymbol{r}_{\boldsymbol{\rho}}|m\rangle \tag{3.2.21}$$

Let us start with an arbitrary initial level $\langle\psi_a|$:

$$\langle\psi_a| \equiv \sum_M a_M\langle l^N\gamma M| \tag{3.2.22}$$

Where a_M are expansion coefficients. γ stands for all necessary quantum numbers. In first-order perturbation theory, the state $\langle\psi_a|$ becomes the state $\langle\psi_b|$:

$$\langle\psi_b| = \sum_M a_M\langle 4f^N\gamma M| + \sum_K b(n'l'\gamma''M'')\langle 4f^{N-1}(n'l')\gamma''M''| \tag{3.2.23}$$

with

$$b(n'l'\gamma''M'') = \frac{1}{E(\gamma) - E(n'l'\gamma'')}\sum_M a_M\langle 4f^N\gamma M|V_{odd}|4f^{N-1}(n'l')\gamma''M''\rangle$$

Here, $n'l'$ are from other configurations and not from the $4f$ shell. Equation 3.2.23 remarks the fact that an admixture of states is not possible if the odd part of the crystal field potential V_{odd} is zero and in fact this is actually the case of symmetries with an inversion center. In the same way the final state $|\psi_b{}'\rangle$ is expressed as:

$$|\psi_b{}'\rangle = \sum_{M'} a'_{M'}|4f^N\gamma'M'\rangle + \sum_K b'(n'l'\gamma''M'')|4f^{N-1}(n'l')\gamma''M''\rangle \tag{3.2.24}$$

with

$$b'(n'l'\gamma''M'') = \frac{1}{E(\gamma') - E(n'l'\gamma'')}\sum_{M'} a'_{M'}\langle 4f^N\gamma'M'|V_{odd}|4f^{N-1}(n'l')\gamma''M''\rangle$$

Tesis publicada con autorización del autor
No olvide citar esta tesis
PUCP

Combining the initial $\langle\psi_b|$ and final $|\psi_b{}'\rangle$ states about the electric dipole operator, it is clear that the terms $\left\langle\psi_a\middle|D_\rho^{(1)}\middle|\psi_a{}'\right\rangle$ and $\left\langle 4f^{N-1}(n'l')\gamma''M''\middle|D_\rho^{(1)}\middle|4f^{N-1}(n'l')\gamma''M''\right\rangle$ are equal to cero since dipole transitions are forbidden between states of the same parity. The expression for the electric dipole matrix element D is reduced to:

$$\left\langle\psi_b\middle|D_\rho^{(1)}\middle|\psi_b{}'\right\rangle =$$

$$\sum_{K,M,M',k,q} a_M a'_{M'} A_{kq} \frac{\left\langle 4f^N\gamma M\middle|D_\rho^{(1)}\middle|4f^N\gamma'M'\right\rangle\left\langle 4f^{N-1}(n'l')\gamma''M''\middle|D_\rho^{(k)}\middle|4f^N\gamma'M'\right\rangle}{E(\gamma')-E(n'l'\gamma')}$$
$$+\sum_{K,M,M',k,q} a_M a'_{M'} A_{kq} \frac{\left\langle 4f^N\gamma M\middle|D_\rho^{(k)}\middle|4f^N\gamma'M'\right\rangle\left\langle 4f^{N-1}(n'l')\gamma''M''\middle|D_\rho^{(k)}\middle|4f^N\gamma'M'\right\rangle}{E(\gamma)-E(n'l'\gamma')} \tag{3.2.25}$$

The final expression for a single transition between to individual levels is (see [Gör98] for more details):

$$\left\langle\psi_b\middle|D_\rho^{(l)}\middle|\psi_b{}'\right\rangle =$$

$$\sum_{k,q}\sum_{\lambda=even}(2\lambda+1)(-1)^{q+\rho}A_{kq}\begin{pmatrix}1 & \lambda & k\\ \rho & -(q+\rho) & q\end{pmatrix}\left\langle\psi_a\middle|U_{q+\rho}^{(\lambda)}\middle|\psi'_a\right\rangle\Xi(k,\lambda) \tag{3.2.26}$$

with

$$\Xi(k,\lambda) = 14\sum_{n',l'}(2l'+1)(-1)^{3+l'}$$
$$\times\begin{Bmatrix}1 & \lambda & k\\ 3 & l' & 3\end{Bmatrix}\begin{pmatrix}3 & 1 & l'\\ 0 & 0 & 0\end{pmatrix}\begin{pmatrix}l' & k & 3\\ 0 & 0 & 0\end{pmatrix}$$
$$\times\frac{\langle 4f|\boldsymbol{r}|n'l'\rangle\left\langle 4f\middle|\boldsymbol{r}^{(k)}\middle|n'l'\right\rangle}{\Delta(n'l')}$$

Here A_{kq} are the crystal field parameters and are related to the crystal field B_k parameters by:

Tesis publicada con autorización del autor
No olvide citar esta tesis
ET LUX IN TENEBRIS LUCET MCMXVII PUCP

$$B_k = \sum_q \left|A_{kq}\right|^2 \frac{1}{(2k+1)^2} \tag{3.2.27}$$

Additionally the equation 3.2.26 can be further reduced after taking into account the orthogonality condition of the M components depicted in equation 3.2.28.

$$\sum_{M,K,M',K'} a_M a_K a'_{M'} a_{K'} = \delta_{MK} \delta_{M'K'} \tag{3.2.28}$$

On the other hand, magnetic dipole transitions are parity-allowed within the $4f$ shell and moreover they can occur under inversion symmetry. These can be derived in the same way as above. For this, let us introduce the magnetic dipole operator $\mu_\rho^{(1)}$ defined as:

$$\mu_\rho^{(1)} = -\frac{e\hbar}{2m_e c} (\boldsymbol{L} + g_e \boldsymbol{S})_\rho^{(1)} \tag{3.2.29}$$

Here $\boldsymbol{S}$ and $\boldsymbol{L}$ are the total spin and total orbital angular momentum operators, respectively. g_e is the electron g-factor. Just like before, the matrix element can be solved in the following way.

$$\begin{aligned} &\langle 4f^N \gamma SLJM_J \left| (\boldsymbol{L} + g_e \boldsymbol{S})^{(1)} \right| 4f^N \gamma' S' L' J' M_J' \rangle = \\ &\qquad (-1)^{J-M} \begin{pmatrix} J & J & S \\ J' & L & 1 \end{pmatrix} \langle 4f^N \gamma SLJ \left|\left| (\boldsymbol{L} + g_e \boldsymbol{S})^{(1)} \right|\right| 4f^N \gamma' S' L' J' \rangle \end{aligned} \tag{3.2.30}$$

The reduced matrix element in equation 3.2.30 can be further reduced by splitting the independent terms of $\boldsymbol{L}$ and $\boldsymbol{S}$ and for the case of $J = J'$ it becomes:

$$\langle J \left|\left| (\boldsymbol{L} + 2\boldsymbol{S})^{(1)} \right|\right| J \rangle = g\sqrt{[J(J+1)[J]]} \tag{3.2.31}$$

Here g is the Landé factor. Notice that magnetic dipole transitions are allowed within the $4f$ shell although they are about one order of magnitude smaller than induced electric dipole transitions. From the above expression of induced electric dipole and magnetic dipole transitions the transitions selection rules can be derived. A summary is given in table 3.2.3. It is important to remark that these selection rules are applicable only if the

Tesis publicada con autorización del autor
No olvide citar esta tesis
ET LUX IN TENEBRIS LUCET MCMXVII PUCP

corresponding quantum numbers are good enough. For instance, the selection rules on M and S break down in the intermediate coupling scheme, whilst the selection rules of J breaks down in the case of J-mixing.

Table 3.2.3. Selection rules for induced electric dipole (ED) and magnetic dipole (MD) transitions [Gör98]

	ED	MD
ΔJ	$\lvert\Delta J\rvert \leq 6$ $\lvert\Delta J\rvert = 2, 4, 6$ with $J = 0$ or $J' = 0$	$\Delta J = 0, \pm 1$ $0 \leftrightarrow 0$ forbidden
$\Delta \mathrm{M}$	$-(q+\rho)$	$-\rho(\rho = \pm 1)$
ΔL	$\lvert\Delta L\rvert \leq 6$	0
ΔS	0	0
$\Delta \tau$	0	0
Δl	± 1	-

While magnetic dipole transitions can be calculated without any further parameterization, induced electric dipole transitions are parametrized mainly because *ab initio* calculations do not yield reliable results. The dipole strength is calculated as the absolute square of the matrix element of the dipole operator.

$$D = \left|\left\langle \psi_b \middle| \boldsymbol{D}_\rho^{(1)} \middle| \psi_b' \right\rangle\right|^2 = \left|\boldsymbol{D}_{\rho,\psi\rightarrow\psi'}^{(1)}\right|^2 \tag{3.2.32}$$

From there the dipole oscillator strength can be calculated by:

$$f^{osc} = \frac{8\pi^2 mc}{3he^2}\bar{\nu}D \tag{3.2.33}$$

The total oscillator strength, i.e. including both electric and magnetic dipole transitions can be expressed in the following form:

$$f_{J\rightarrow J'} = \frac{8\pi^2 m\bar{\nu}}{3h(2J+1)e^2}\left[\ \chi_{ED}S_{ED}(J;J') + \chi_{MD}S_{MD}(J;J')\ \right] \tag{3.2.34}$$

Tesis publicada con autorización del autor
No olvide citar esta tesis
PUCP

Here, m and e are the mass and charge of the electron. c is the speed of light, $\bar{\nu}$ is the average frequency at which the transition occur, h the Plack constant and n the refractive index. $\chi_{ED} = n(n+2)^2/9$ and $\chi_{MD} = n^3$ are the Lorentz correction factors, which correct the effective field at an active center in a solid, the latter correction is introduced because the electric field acting on an impurity in a solid is different from that in vacuum owing to the effect of the polarization of the surrounding atoms. S_{ED} and S_{MD} are the electric and magnetic dipole line strength both defined in the equations 3.2.35 and 3.2.36.

$$S_{ED}(J;J') = e^2 \sum_{\lambda=2,4,6} \Omega_\lambda \left| \langle f^N[SL]J \| U^{(\lambda)} \| f^N[S'L']J' \rangle \right|^2 \tag{3.2.35}$$

$$S_{MD}(J;J') = \frac{e^2 h^2}{16\,\pi^2\, m^2\, c^2} |\langle f^N[SL]J \| \boldsymbol{L} + 2\boldsymbol{S} \| f^N[S'L']J' \rangle|^2 \tag{3.2.36}$$

Equation 3.2.35 is known as the Judd parameterization scheme for lanthanides in a solution [Jud62]. $U^{(\lambda)}$ are the unitarian tensor operators and Ω_λ are known as the Judd-Ofelt parameters. Judd was the first to relate the experimental spectra to the parameters Ω_λ. This equation was derived for a randomly oriented system and without considereing transitions between individual Stark levels, i.e. only transitions between *LSJ* multiples are taken into account [Gör98].

Since the electric dipole transitions arise from small crystal field perturbations, the matrix elements in equation 3.2.35 are not highly dependent on the host material. A large portion of the book "Spectroscopic coefficients of the pn, dn, and fn configurations" by Nielson and Koster [Nie63] is dedicated to tabulating matrix elements in the LS-coupling scheme. Further efforts must be provided on converting these wavefunctions to the intermediate coupling case applicable to RE ions.

The radiative emission probability is given by the Einstein's coefficient A for spontaneous emission and it can be calculated from the oscillator strength as shown in the equation 3.2.37, $\tau_{JJ'}$ denotes the transition time from the excited initial state to a final

Tesis publicada con autorización del autor
No olvide citar esta tesis
PUCP

state. Additionally, the absorption cross-section is related to the oscillator strength by the equation 3.2.38. The correction factors for the effective field at the ion in the solid are already included in the oscillator strength (see equation 3.2.34) however in the case of the absorption cross-section an additional $1/n^2$ factor must be included [Yen07].

$$\tau_{JJ'}^{-1} = A_{J\to J'} = \frac{8\pi^2 e^2 \bar{\nu}^2}{(4\pi\varepsilon_0)mc^3} f_{J\to J'} \tag{3.2.37}$$

$$\sigma_{J\to J'} = \frac{2\pi e^2}{(4\pi\varepsilon_0)mc}\frac{1}{n^2} f_{J\to J'} \tag{3.2.38}$$

Finally the Einstein's coefficient can be written as follows:

$$A(J;J') = \frac{64\pi^4\nu^3}{(4\pi\varepsilon_0)3h(2J+1)c^3}\left[\ \chi_{ED}S_{ED}(J;J') + \chi_{MD}S_{MD}(J;J')\ \right] \tag{3.2.40}$$

Now taking into account all possible radiative channels through which a populated level may decay, the lifetime is defines by:

$$\tau_J = \frac{1}{\sum_{J'} A(J;J')} \tag{3.2.41}$$

Nonetheless, it is typically found that the experimental lifetimes are smaller than the calculated ones. This discrepancy is attributed to non-radiative processes such as energy migration between lanthanide ions or energy transfer to the lattice host. Thus the ratio between the experimental and calculated lifetime is defined as the quantum efficiency.

Non-radiative decay

The classical approach describes a non-radiative transition as a process in which an excited state relaxes to the ground state by crossing over the intersection of the configuration coordinate curve through thermal excitation or other means (see figure 3.2.4). Let's recall that the configurational coordinate model is often used to explain the effect of lattice vibrations on the optical properties of a localized center. In this model the

Tesis publicada con autorización del autor
No olvide citar esta tesis
PUCP

large amount of actual vibrational modes of the lattice are approximated by a small combination of specific coordinates.

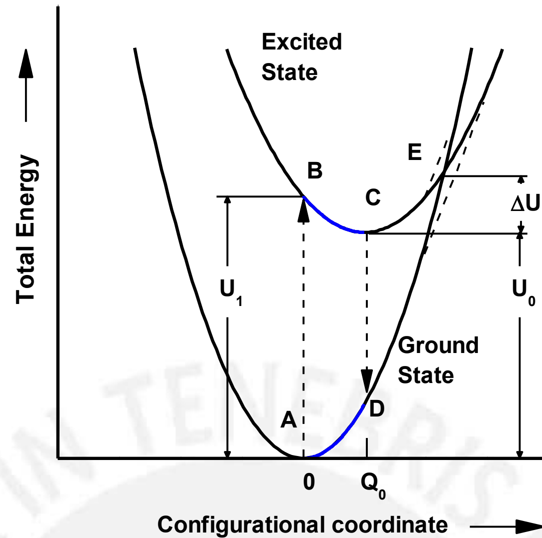

Figure 3.2.4. A schematic illustration of the configurational coordinate model. The two curves are modified by repulsion near the intersection (point E). Vertical broken arrows A⇋B and C⇋D indicate the absorption and emission of light, respectively. After thermal assistance, and excited state can relax to the ground state by generating lattice vibrations without an optical emission through the point E. The blue region of the potential curves denotes the path followed by the electron after losing energy.

Following the path of the optical transition illustrated in figure 3.2.4, we can assume that the bonding force between the luminescent ion and the nearest-neighbor ion is expressed by the Hooke's law. The deviation from the equilibrium position of the ions is taken as the configurational coordinate Q. The total energy of the ground state, U_g, and the total energy of the excited states, U_e, are given by the equation 3.2.42 and 3.2.43, respectively.

$$U_g = K_g \frac{Q^2}{2} \tag{3.2.42}$$

$$U_e = U_0 + K_e \frac{(Q - Q_0)^2}{2} \tag{3.2.43}$$

Here K_e and K_g are the force constants of the chemical bond, Q_0 is the interatomic distance from the equilibrium of the ground states, and U_0 is the total energy at $Q = Q_0$.

Tesis publicada con autorización del autor
No olvide citar esta tesis
PUCP

Naturally, the spatial distribution of an electron orbital is different between the ground and excited states thus giving rise to a difference in the electron wavefunction overlap with neighboring ions. In figure 3.2.4, optical absorption and emission processes are indicated by vertical broken arrows. In this approach the nucleus of an emitting ion stays approximately at the same position throughout the optical processes. This is known as the Franck-Condon principle. The latter approximation is quite reasonable since an atomic nucleus is heavier than an electron by 10^3 to 10^5 times. At 0 Kelvin, the optical absorption proceed from the equilibrium position of the ground state, as indicated by the arrow A → B. The probability for an excited electron to lose energy by emitting phonons is about $10^{12}\ \mathrm{s}^{-1}$, whilst the probability for light emission is at most $10^9\ \mathrm{s}^{-1}$. Therefore, an electron in the state B relaxes to the equilibrium position C before it emits a photon. Then the emission process C → D and the relaxation process D → A are followed.

Electron states oscillate around the equilibrium position along the configurational coordinate curve up to $k_B T$. The amplitude of this oscillation produces the spectral widening of the absorption transition. The intersection of two configuration coordinate curves shown in the figure 3.2.4, allows an electron in the excited state to cross the intersection assisted by thermal energy and thus reaching the ground sate non-radiatively, i.e. a non-radiative relaxation process with an activation energy ΔU, and a transition probability N given by the equation 3.2.44 can be assumed. Here s is the product of the transition probability between the ground and excited states and a frequency at which the excited state reaches the intersection E. The latter quantity can be treated as a constant and is called frequency factor usually in the order of $10^{13}\mathrm{s}^{-1}$.

$$N = s \exp\left(-\frac{\Delta U}{k_B T}\right) \quad (3.2.44)$$

However, it is typically observed that the experimentally determined activation energy of a non-radiative process depends on the temperature. This problem has a quantum mechanical explanation. An optical transition accompanied by absorption or emission of $m - n$ phonons can take place when and n^{th} vibrational level of the excited state and an mth vibrational level of the ground state are located at the same energy. The probability

Tesis publicada con autorización del autor
No olvide citar esta tesis
ET LUX IN TENEBRIS LUCET MCMXVII PUCP

of such transition is also proportional to a product of the Franck-Condon coefficient and thermal distribution of population in ground state, giving the required temperature dependent probability. In such case, the non-radiative relaxation probability is given by [Yen07]:

$$N_p = N_{eg}\exp\left(-S(2\langle n\rangle + 1)\right)\sum_{j=0}^{\infty}\frac{(S\langle n\rangle)^j\{S(1+\langle n\rangle)\}^{p+j}}{\left(j!\,(p+j)\right)!} \tag{3.2.45}$$

Here, $p \equiv m - n$, $\langle n\rangle$ is the mean number of vibrational quanta n at the temperature T expressed by $\langle n\rangle^{-1} = \exp(\hbar\omega/k_bT) - 1$, S is defined by $S = \frac{1}{2}\frac{K}{\hbar\omega}(Q - Q_0)^2$. The notation N_{eg} stands for the overlap integral of the electron wavefunctions. Notice that the temperature dependence of N_p is included in $\langle n\rangle$. Clearly equation 3.2.45 does not have a form characterized by a single activation energy. If we write it in a form such as $N_p \propto \exp\left(-E_p/k_BT\right)$ one gets:

$$E_p = \left(\langle n\rangle_p + \langle n\rangle\right)\hbar\omega \tag{3.2.46}$$

where $\langle n\rangle_p\hbar\omega$ is the mean energy of the excited state subject to the non-radiative process. E_p increases with temperature and at sufficiently low temperatures $E_p < \Delta U$.

In the case that $S < 1/4$ or in other words the electron-phonon interactions is small enough, equation 3.2.45 can be further simplified by neglecting all the terms but $j = 0$. That is:

$$N_p = N_{eg}\exp\{-S(2\langle n\rangle + 1)\}\{-S(1+\langle n\rangle)\}^p/p! \tag{3.2.47}$$

In the case of RE ions, the dominating non-radiative relaxation process is the multiphonon emission (see appendix A.2). If ΔE is the energy separation between two levels, the non-radiative relaxation probability between these levels is given by Kiel [Kie65, Yen07]:

$$N_p = A_K\epsilon^p(1+\langle n\rangle)^p \tag{3.2.48}$$

Tesis publicada con autorización del autor
No olvide citar esta tesis
PUCP

$$p\hbar\omega = \Delta E \quad (3.2.49)$$

where A_K is a rate constant and ϵ is a coupling constant.

Equation 3.2.47 can be shaped to the same form as equation 3.2.48 by the conditions $S \approx 0$, $\exp\{-S(1+\langle n \rangle)\} \approx 1, S^p/p! \approx \epsilon^p$ and $A_K = N_{eg}$, notwithstanding equation 3.2.47 was derived independently of the configuration coordinate model. If two potential curves in the configurational model have the same curvature and the same equilibrium positions they will not cross and there is no relaxation process by thermal activation between the two in the framework of the classical theory. Nevertheless, thermal quenching of luminescence can be explained for such a case by taking phonon-emission relaxation into account, as predicted by Kiel's equation.

Energy transfer processes

When more than one optically active center is existent, an excited color center my transfer all or part of its energy to a nearby center. This energy transfer process can happen radiatively or non-radiatively (see figure 3.2.5). The ion from which the energy is being transferred is called sensitizer (S) whilst the ion to which the energy is transferred is named activator (A). In the radiative process, the excited ion emits a photon and another ion absorbs that photon before it leaves the host matrix. This process has a low effect in the lifetime of the radiating state. On the other hand, the most well-known non-radiative energy transfer process is the Förster Resonant Energy Transfer (FRET). This mechanism was first invoked to describe the energy transfer between organic molecules in the dipole approximation [För48]. It was further generalized to higher-order interactions between dopant ions in inorganic solids by Dexter [Dex53]. There are further possibilities in the non-radiative energy transfer process. We will consider three cases: resonant, phonon-assisted and cross-relaxation (see figure 3.2.5).

Tesis publicada con autorización del autor
No olvide citar esta tesis
ET LUX IN TENEBRIS LUCET MCMXVII PUCP

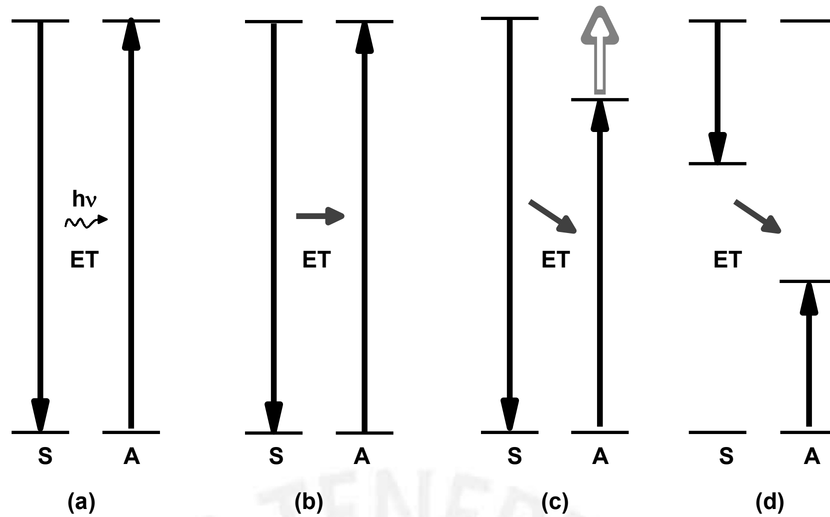

Figure 3.2.5. Energy transfer processes: radiative (a), resonant non-radiative (b), phonon-assisted (c), and non-radiative cross-relaxation (d).

In the resonant case, the initial state of the system is an excited sensitizer and an activator in the ground state. The final sate of the system is a sensitizer in the ground state and an activator in excited state. The Hamiltonian is the coulombic interaction between the electrons of the sensitizer and those of the activator. Forster [Zim61] and Dexter [Spa90] developed an equation to describe the resonant energy migration rate W_{SA} between S and A (see equation 3.2.50) [Vij06].

$$W_{SA} = K\frac{Q_A}{R^n \tau_S}\int \frac{g_S(E)g_A(E)}{E^4}dE \qquad (3.2.50)$$

In equation 3.2.50, K is a constant, Q_A is the area under the absorption band of the activator, τ_s is the lifetime of the sensitizer and R is the distance between the sensitizer and the activator. g_S and g_A are the normalized shape function of the emission bands of the sensitirzer and the absorption bands of the activator, respectively. The integral includes the overlap of these two functions, and is mainly a conservation of energy statement. The R^n factor is determined by the multipole interaction between S and A. Most cases, dipole-dipole ($n = 6$) is the dominant mechanism. However, in cases where the dipole-dipole term vanishes due to symmetry, the dipole-quadrupole ($n = 8$) or quadrupole-quadrupole ($n = 10$) terms may dominate. This exchange interaction may

Tesis publicada con autorización del autor
No olvide citar esta tesis
ET LUX IN TENEBRIS LUCET MCMXVII PUCP

drive the energy transfer, but only when S and A are close to one another [Vij06]. Phonon-assisted energy transfer highlights because the overlap integral in the equation 3.2.50 is close to zero, and the energy different between the emission of S and the absorption of A must be compensated by the absorption or emission of one or more phonons. Two features can be remarked. First, the energy transfer obeys an exponential energy gap law if the gap is much larger than the phonon energy. In other words, if more than one phonon is required the transition rate decreases exponentially. This situation is usually found in RE ions. Second, if W_{SA} is much larger than the decay rate of the upper levels of both S and A, the two levels become thermalized according to Boltzmann distribution. Additionally it has been commonly observed that the energy transfer rate generally increases with temperature for TM ions. However in the case of RE ions, the rate may increase or decreases with temperature depending on the energy levels involved [Gal68].

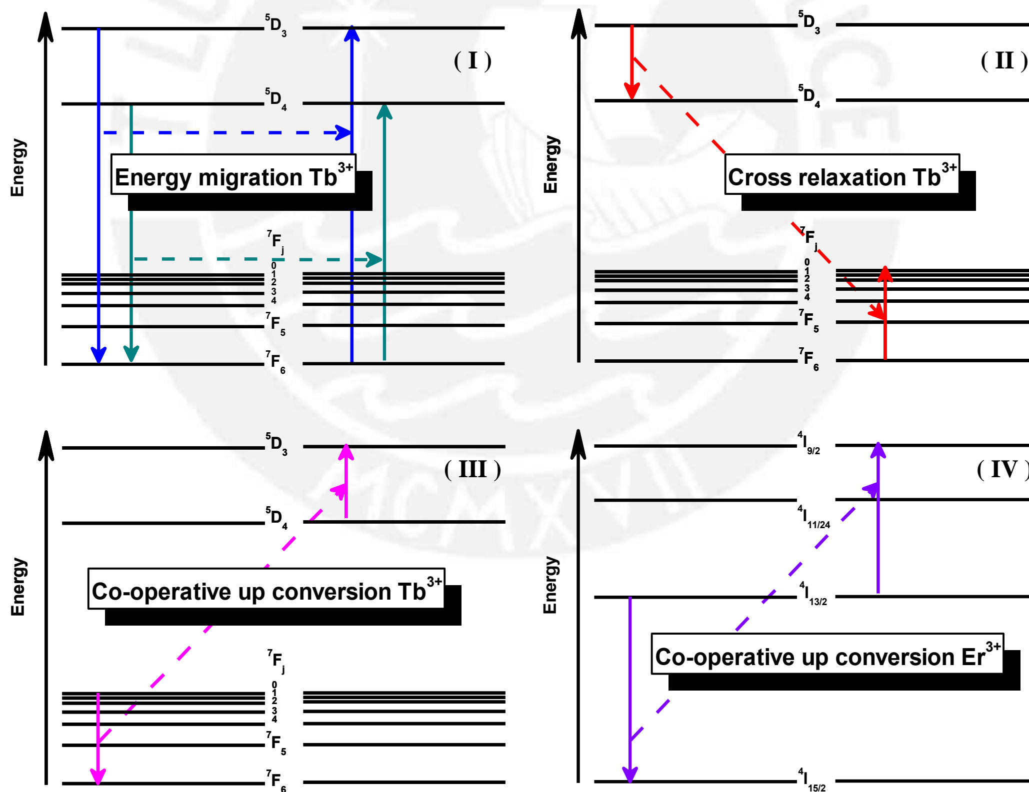

Figure 3.2.6. Energy transfer processes in Tb^{3+}. Non-radiative resonant energy migration (I), cross relaxation (II). Co-operative up-conversion in Tb^{3+}. Co-operative up-conversion in Er^{3+} (IV).

Tesis publicada con autorización del autor
No olvide citar esta tesis
PUCP

Energy transfer by cross-relaxation (or self-quenching) is also a coulombic interaction phenomenon. However in this case the sensitizer and the activator are two identical ions in which the first one relaxes to a lower energy state but not the ground state and the activator is excited to an intermediate state. The energy between the intermediate and ground states of the activator must be equal to the energy between the excited state and the lower energy state of the sensitizer.

The energy transfer mechanisms reviewed above open a large amount of possible channels for energy migration exhibiting interesting properties. One of this is the possibility for energy up-conversion. More details on this feature can be found in the appendix A.3. Figure 3.2.6 depicts the possible energy transfer pathways in Tb^{3+}. First the resonant energy migration between the $^5D_3/^5D_4$ states to the ground $^7F_6$ state which is possible and very likely due to the fact that the energy gap between sates is large enough to avoid multiphonon emission before the former process could occur. Second, the cross-relaxation process is also very likely. It occurs by the electronic transition from the $^5D_3$ to the $^5D_4$ level in the sensitizer and from the $^7F_6$ to the $^7F_0$ in the activator, the energy of this transition rounds about ~0.72 eV. Subsequently, the electron in the $^7F_0$ state relax non-radiatively increasing therefore the overall population in the $^5D_4$ level. On the other hand the opposite process to the cross-relaxation, namely cooperative up-conversion is also possible, however is pretty unlikely due to the fact that the energy gap between the ^7F_J sates is in the order of 100 meV and therefore multi-phonon decay becomes the dominant relaxation process from the $^7F_0$ to the $^7F_6$ energy levels, additionally in order to have two ions excited one $^7F_0$ and other in the $^5D_4$ two different excitation sources are necessary. Notwithstanding, this behavior has been observed and extensively studied in Er^{3+} in which a single excitation wavelength (1550 nm) can excite two nearby Er^{3+} ions to the $^4I_{13/2}$ state. Thenceforth, in that case the co-operative energy up conversion is possible with a higher probability by transferring the energy of one of the Er ions to the other excited one and thus reaching the $^4I_{9/2}$ level [Auz04].

Tesis publicada con autorización del autor
No olvide citar esta tesis
ET LUX IN TENEBRIS LUCET MCMXVII PUCP

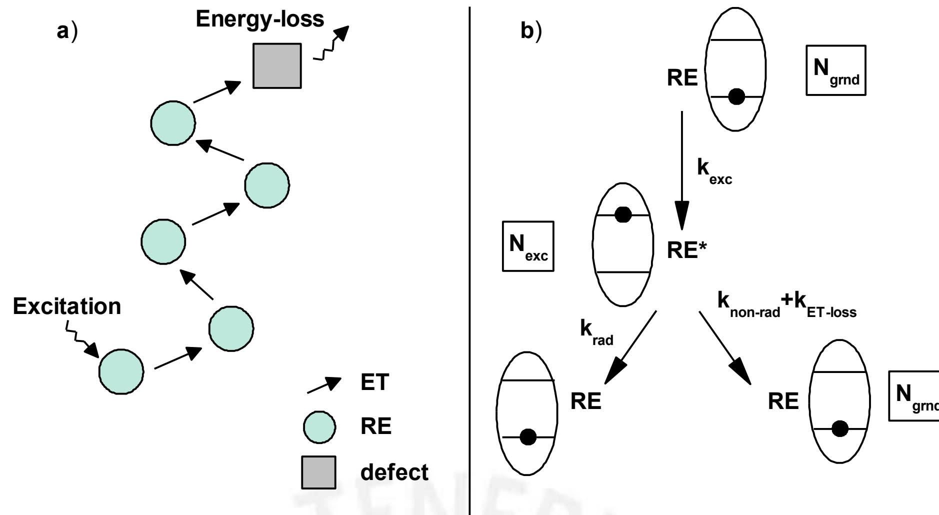

Figure 3.2.7. After the excitation of a RE ion, the energy can migrate to a nearby RE ion successively thus increasing the probability to reach a non-radiative recombination channel (a). An excited RE ion can relax radiatively and non radiatively. Taking into account the population variation due to the excitation (k_{exc}) and relaxation rates ($k_{rad}, k_{non-rad}, k_{ET-loss}$) we are able to write the equation 3.2.57.

Lastly a particular feature and consequence of the energy migration between RE ions that will be further studied and characterized in the present work is the concentration quenching effect. It consists in the self-quenching of the RE luminescence by enhancing the energy loss probability through non-radiative channels due to the increase of the energy transfer probability between these ions, see figure 3.2.7. In other words, the increase of the probability of an energy transfer between ions, for instance due to the reduction of the ion interspace, enhance the possibility of the energy to reach an ion which is close to a non-radiative decay channel, for instance a defect. Processes of this nature are typically modeled by phenomenological rate equations which describe the time dynamics of population densities of RE ions excited in different energy states. If we restrict the model to only two states, let's say for instance in Tb^{3+} the main representative energy transfer mechanism being the cross-relaxation process pointed out lines above (see figure 3.2.6), the corresponding rate equation and therefore the variation of the intensity can be modeled in the following way:

Tesis publicada con autorización del autor
No olvide citar esta tesis
PUCP

Let N_{exc} and N_{grnd} be the population of the excited and ground states, respectively. Since the total number of active centers is constant, $N = N_{exc} + N_{grnd}$, the variation of the excited state population should match the variation of the ground state population as shown in equation 3.2.51.

$$\frac{d}{dt}N_{exc} = -\frac{d}{dt}N_{grnd} \tag{3.2.51}$$

The ground state is continuously excited with an excitation rate k_{exc} thus reducing its population in $-k_{exc}N_{grnd}$, while simultaneously growing in population due to the relaxation of ions in the excited state. This relaxation can be either radiative or non-radiative. The radiative decay is characterized by the transition rate k_{rad} (equivalent to the corresponding Einstein's coefficient A in s^{-1}) while the non-radiative decay is described by the addition of the transition rate of two processes. First the non-radiative decay rate $k_{non-rad}$ due to the energy migration from the excited RE to a non-radiative recombination center (e.g. a defect). Second the self-quenching transition rate $k_{ET-loss}$ due to the successive energy transfer between RE ions and thus the subsequent energy loss into a non-radiative recombination center (see figure 3.2.7). These last two transition rates contribute to the light emission quenching. The variation of the ground state population then follows as:

$$\frac{d}{dt}N_{grnd} = -k_{exc}N_{grnd} + k_{rad}N_{exc} + (k_{non-rad} + k_{ET-loss})N_{exc} \tag{3.2.52}$$

From this point, the population of the excited state can be solved as function of the aforementioned transition rates by solving the corresponding differential equation as shown in the equation 3.2.53. Additionally, the light emission intensity is proportional to $N_{exc} \times k_{rad}$. Considering only the steady solution after a sufficient long time we obtain an equation for the light emission intensity versus the number of active centers (see equation 3.2.54).

$$\begin{gathered}\frac{d}{dt}N_{grnd} = -k_{exc}(N - N_{exc}) + k_{rad}N_{exc} + (k_{non-rad} + k_{ET-loss})N_{exc} \\ \Rightarrow \frac{d}{dt}N_{exc} = k_{exc}N - (k_{exc} + k_{rad} + k_{non-rad} + k_{ET-loss})N_{exc}\end{gathered} \tag{3.2.53}$$

Tesis publicada con autorización del autor
No olvide citar esta tesis
PUCP

$$\Rightarrow N_{exc} = \frac{k_{exc}N}{k_{exc} + k_{rad} + k_{non-rad} + k_{ET-loss}} + C\exp[-t\sum k]$$

$$I \propto \frac{k_{rad}k_{exc}N}{k_{exc} + k_{rad} + k_{non-rad} + k_{ET-loss}} \quad (3.2.54)$$

On the other hand, the $k_{ET-loss}$ depends on the distance between the RE ions. There are two approaches to describe the energy transfer probability. The approach of Förster [För59] based on classical electrostatic interaction (multipole-multipole interaction) and the approach of Dexter [Dex53] based on a quantum mechanical exchange interaction. Both dependencies are summarized in the equation 3.2.55.

$$\begin{aligned} p_{ET}^{Dexter}(r) &\propto \exp\left(-\frac{r}{r_0}\right) \\ p_{ET}^{Förster}(r) &\propto \left(\frac{r}{r_0}\right)^{-m} \end{aligned} \quad (3.2.55)$$

Here r is the distance between the RE ions, $m = 6, 8, 10$ corresponding to the dipole-dipole, dipole-quadrupole and quadrupole-quadropole interactions, respectively and r_0 a characteristic size threshold of the ions. In order to model the distance dependent luminescence intensity the interspace distance average can be used (see equation 3.2.56). Nonetheless and average of the $\langle k_{ET-loss}\rangle$ can also be used. More details can be found in [Ben13, Hub79, Spe75].

$$k_{ET-loss} = k_{loss} \times p_{ET}(\langle r\rangle) \quad (3.2.56)$$

Finally, the overall intensity can be written as a function of the RE concentration η_{RE} and the mean RE interdistance r_{RE} (see equation 3.2.57). Notice that these two quantities are actually related. For a random distribution of REs in a solid it is possible to directly calculate the average ion interdistance from the ion concentration. Details on these calculations can be found in appendix A.4. In any case equation 3.2.57 has the shape similar to a sigmoidal function multiplied by a line with intercept in the origin. So for low concentrations (thus large average ion interdistance) the RE related intensity increases

Tesis publicada con autorización del autor
No olvide citar esta tesis
PUCP

linearly with the concentration. Whilst for larger concentrations the self-quenching becomes relevant thus reducing the light emission intensity. Figure 3.2.8 depicts this behavior for Tb doped Y_2O_3 [Mue07, Wan10].

$$I(\eta_{RE}) = \frac{A\,\eta_{RE}}{1 + \beta \times p_{ET}(r_{RE})} \tag{3.2.57}$$

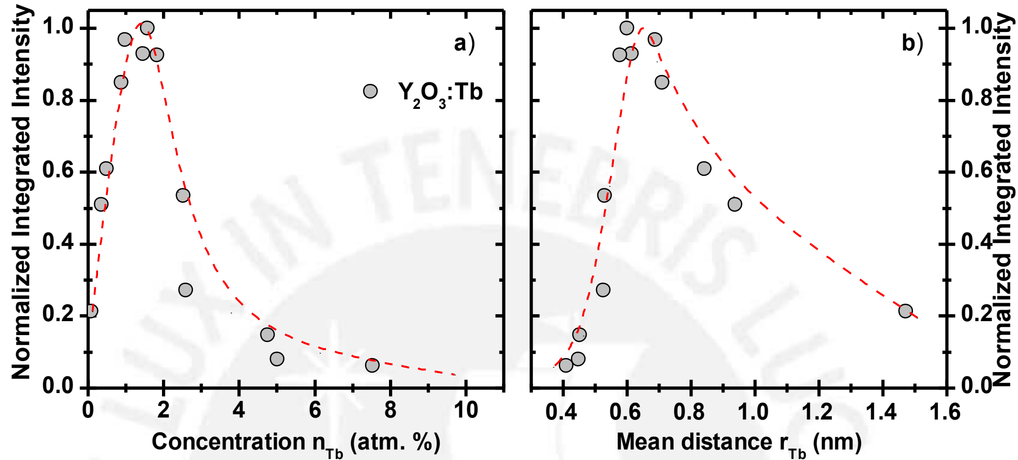

Figure 3.2.8. Normalized PL integrated intensity of Tb doped Y_2O_3 versus the Tb concentration (a) and mean ion interdistance (b). Here the ion mean interdistance is calculated following the procedure from the appendix A.4. The data was taken and normalized from two different references [Mue07, Wan10]. Notice that the integrated intentsity increases till a critical concentration value and then the energy transfer between REs becomes more likely thus quenching the light emission intensity.

Tesis publicada con autorización del autor
No olvide citar esta tesis
ET LUX IN TENEBRIS LUCET MCMXVII PUCP

4.1 Deposition

All films were grown on two side polished crystalline calcium fluoride (CaF_2) and polished silicon (Si) substrates by radio frequency magnetron sputtering. The pressure before the deposition process was lower than 4×10^{-6} mbar. The distance between the target and the substrate was fixed to 55 mm. The copper substrate holder and thus the substrates were cooled down with a constant water flux at 12°C to ensure the amorphous structure of the layers. In the case of the SiC films the deposition was performed in an argon-hydrogen atmosphere mixture using a high purity SiC target. This target's dominant impurity was nitrogen with a concentration smaller than 10 ppm wt. The AlN and SiN films were grown in an argon-nitrogen atmosphere mixture using high purity AlN and Si targets, respectively. The dominating impurity of the AlN target was oxygen with a concentration below 90 ppm wt. The doping with Tb was performed during the deposition process by using a Tb target attached to a second magnetron. The purity of the Tb target was 99.9%. The typical power used to get a suitable amount of Tb in the layer, ranged from 1 to 5 Watts. In the case of the *a*-SiC:H:Tb grown with different Tb amounts, a single process was performed in which the magnetrons were hold in such position to achieve a gradient in the composition (see figure 4.1.1). The deposition conditions for each material are listed in table 4.1.1.

Table 4.1.1. Deposition conditions

Sample	Ar flow (sccm)	H_2 flow (sccm)	N_2 flow (sccm)	Power (Watts)	Time (min)	Pressure (mbar)
SiC	50	0	-	120	143	1.5 E-02
SiC:H(a)	50	5	-	120	270	9 E-03
SiC:H(b)	35	15	-	120	330	1.2 E-02
AlN	25	-	25	100	480	9 E-03
SiN	40	-	10	100	140	1.0 E-02

Tesis publicada con autorización del autor
No olvide citar esta tesis
ET LUX IN TENEBRIS LUCET MCMXVII PUCP

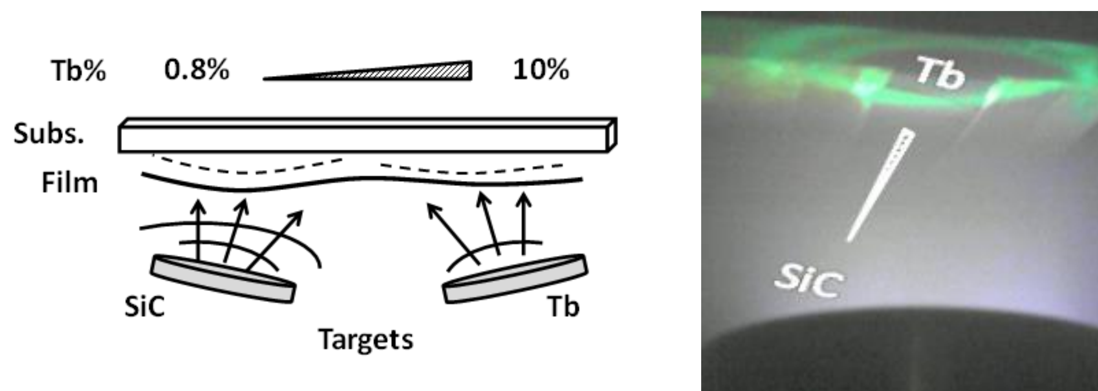

Figure 4.1.1. Magnetrons arrangement in order to obtain a gradient of the Tb in the SiC:H films (left). Photography of the substrate holder exhibiting the Tb characteristic green emission during the deposition process of SiC:H:Tb (right). Notice that the region with a larger Tb amount doesn't exhibit any emission due to the concentration quenching effect.

The poly-crystalline AlN samples were grown by reactive DC sputtering from two high purity Al targets, each constantly powered with 150 Watts. In order to achieve different Tb dopant concentrations the DC power of a Tb target was adjusted between 2 and 44 Watts. These processes were performed in an argon-nitrogen atmosphere mixture at 6×10^{-3} mbar. These last samples were grown and provided by the group of Prof. Dr. H. P. Strunk in the University of Stuttgart, Germany [Ben13].

4.2 Optical characterization techniques

UV-VIS transmittance

The optical characterization was performed through optical transmittance measurements, using a double beam photo-spectrometer model Lambda 2 UV/VIS/NIR from the company Perkin Elmer. The transmittance spectra were measured in the wavelength range from 190 nm to 1100 nm. In order to obtain the absorption coefficient, the refractive index and the film thickness from transmittance data, we applied a slightly improved self-consistent method of Swanepoel. The errors obtained for the film thickness were less than 5% and were mainly caused by film inhomogeneities and low number of interference fringes in the transmission spectra which are crucial for this method in order to determine the thickness accurately. For more details concerning this method please consult appendix A.1.

Tesis publicada con autorización del autor
No olvide citar esta tesis
PUCP

Light emission characterization

The light emission characterization of the films was performed upon two types of excitation sources, photons (PL) and electrons (CL). Two distinct setups were used in the PL case.

In the PL case the samples excited upon 488 nm excitation wavelength were measured in a commercial micro-Raman system. Two systems were actually used, one of the company Ranishaw model InVia and another of the company Horiba model LabRAM-HR. The PL spectrum was taken in a reflection setup and the excitation source was an argon laser. Additionally, monochromatized light from a xenon lamp attached to a monochromator was used to excite the samples at different wavelengths. From this setup PLE and PL were performed. In the case of PLE (Photoluminescence excitation spectroscopy) the spectral bandwidth of the monitored emission line was set to 4 nm.

The CL was performed using two systems: a Triax Monochromator, Jobin Yvon attached to a SEM and a monoCL system of Gatan attached also to a SEM. The CCD camera of both systems is capable to cover the wavelength range from 200 nm to 1000 nm. Typical size of the excitation area was 200µm×200µm. Suitable beam currents were used and the acceleration voltage was kept typically at 20kV.

Infrared absorption by Fourier transform spectroscopy (FTIR)

Infrared transmittance measurements taken on the amorphous films were carried by using an infrared spectrometer FTIR model Spectrum 1000 from the company Perkin Elmer with a resolution of 8 cm^{-1}. These spectra were recorded in the spectral region from 400 cm^{-1} to 4000 cm^{-1} and were corrected for the silicon substrate absorption. Additionally, in order to increase the reproducibility of the measurements and to avoid further effects due to the films inhomogeneity an aluminum sample holder allowing a light spot of only 2 mm diameter was used.

It is important to note that due to the film thickness an interference effect is observed in the IR spectra. However the transmittance obtained using a silicon substrate as reference exhibits values above 100%. This is cause by the higher refractive index of the Si

Tesis publicada con autorización del autor
No olvide citar esta tesis

substrate (~3) in comparison to the film refractive index (~2). This problem is well known in the literature and since these values lack of physical meaning an additional base line correction is necessary [Raj03]. In order to do so, a polynomial fit of order five is performed. Nevertheless a different approach has been taken in [Gue16] for *a*-SiC:H. Subsequently, the absorbance is calculated by applying the Lambert-Beer's law to the corrected transmittance as shown in the figure 4.2.1.

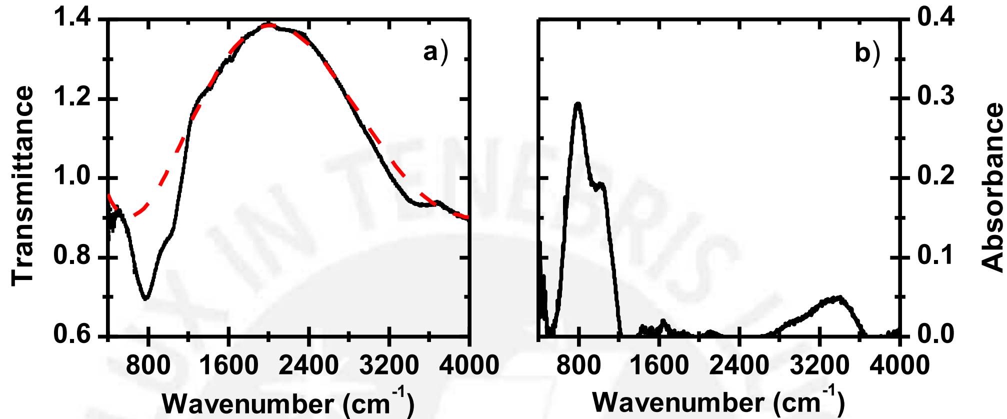

Figure 4.2.1. Measured IR transmittance of *a*-SiC:H grown on a polished silicon substrate. Due to the procedure in the FTIR measurements in which a reference beam is measured and the refractive index of the substrate which is higher than of the film, the transmittance exceeds 100% (a). A baseline is calculated trough a fit using a polynomial fit of order five. The absorbance is then calculated through the Lambert-Beer's Law (b).

Lambert-Beer's Law can be written as shown in the equation 4.2.1, where $\alpha(\nu)$ is the absorption coefficient versus the wavenumber ν, T is the transmittance related to the absorption due to the distinct vibrational modes encountered in the material while T_0 is the zero absorption transmittance or base line. The number of bonds N related to the observed absorption peak can be estimated through the equation 4.2.2 knowing the corresponding inverse absorption cross section for each vibrational mode [Kuz09]. In this way it is possible to monitor the variation of the amount of the distinct bonds after for instance annealing treatments at different temperatures on the same sample.

$$\alpha(\nu) = \log\left(\frac{T}{T_0}\right)/d \qquad (4.2.1)$$

Tesis publicada con autorización del autor
No olvide citar esta tesis
ET LUX IN TENEBRIS LUCET MCMXVII PUCP

$$N \propto \int \frac{\alpha(\nu)}{\nu} d\nu \qquad (4.2.2)$$

4.3 Annealing treatments

The annealing treatments were performed at different temperatures and took place in a quartz tube inside a tube oven which could be heated up to 1200 °C. In the case of the u undoped samples, the quartz tube was first evacuated down to 10^{-6} mbar and then filled with a constant flux of high purity (5N) nitrogen or argon up to a pressure of 10^{-2} mbar. The AlN and SiN samples were annealed in a nitrogen atmosphere while the SiC ones were annealed in an argon atmosphere. After the operating temperature was reached, the quartz tube with the samples under treatment was moved rapidly inside the oven (shock tempering). On the other hand, the doped samples were annealed at 1bar pressure and under the respective atmospheres. The annealing time for each annealing step was 30 min and the same samples were used for the next annealing steps (isochronical annealing).

4.4 Terbium concentration determination

In order to estimate the Tb concentration of the amorphous hydrogenated SiC thin films we cut the sample in 6 equal parts along the Tb amount gradient as it was described earlier in section 4.1. Then we label 3 positions equally spaced in each sample piece thus making a total of 18 distinct positions in which the Tb amount increase along one direction. We performed X-ray photon scattering (XPS) measurements in order to determine the Tb concentration of the first 4 pieces. We only measure these 4 sample pieces due to resources limitations. An example of the spectrum obtained is depicted in figure 4.4.1 and table 4.4.1. Notice the presence of oxygen, mainly due to the affinity of Tb to oxidize. The oxygen content is also observed in the FTIR spectra as Si-O bonds around 1070 cm^{-1}.

Additionally, notice from figure 4.4.2 that the overall IR absorbance spectra of the samples decreases along the direction of increasing Tb. This decrease is mainly attributed to the reduction of Si-C and Si-O bonds with increasing the dilution of Tb in the host

Tesis publicada con autorización del autor
No olvide citar esta tesis
PUCP

matrix. We take advantage of this fact to calibrate the Tb concentration of the samples in the distinct positions with the area below the curve of the FTIR spectra as shown in figure 4.4.3.

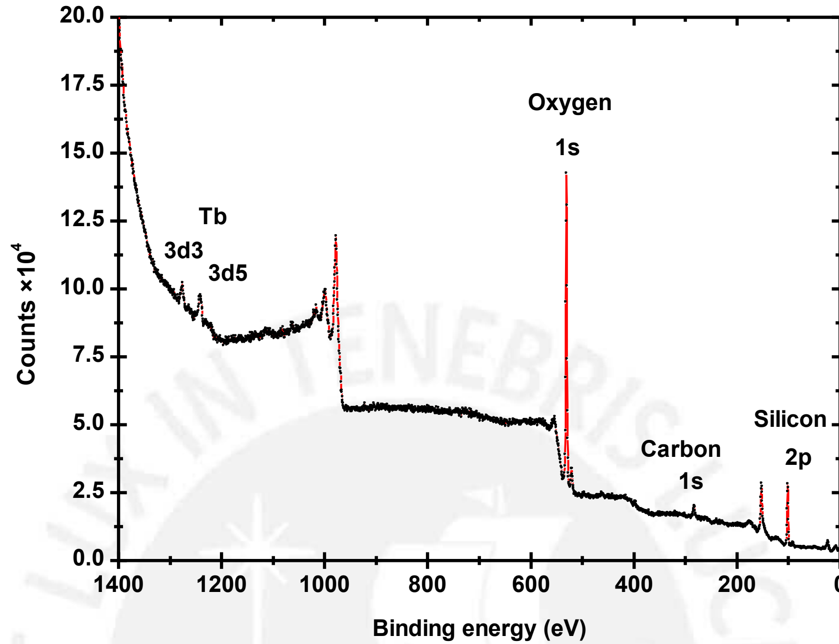

Figure 4.4.1. XPS spectra of Tb doped amorphous hydrogenated SiC. The spectrum of the 4th sample piece is shown corresponding to the sample position number 5. The obtained Tb concentration is obtained after correcting the base line of the electronic orbitals of each element and then fitting a Gaussian peak. In this case the value is of 3.89 at. % of Tb, see table 4.4.1.

Table. 4.4.1. Peak information corresponding to the XPS spectra shown in figure 4.4.1. The total terbium amount is calculated by adding the contributions of the distinct binding states. In this case the 3d3 and the 3d5.

Name	Start (eV)	Peak (eV)	End (eV)	Height (Counts)	FWHM (eV)	At. %
Tb 3d3	1285.64	1279.16	1272.13	2691.72	5.75	**1.81**
Tb 3d5	1256.05	1244.74	1238.64	3573	7.34	**2.08**
C 1s	292.21	286.03	278.5	1585.55	3.8	**24.14**
Si 2p	110.32	104.53	100.5	7240.99	2.57	**71.98**

Notice, that these measurements were performed after the samples were annealed at 1050°C following the procedure described in section 4.3. When taking a close look to the variation of the shape of IR absorbance spectra after the thermal annealing it is possible

Tesis publicada con autorización del autor
No olvide citar esta tesis
PUCP

to realize a sharpening of the Si-O related vibrational modes at 454 cm^{-1} and 1070 cm^{-1}, see figure 4.4.2. Furthermore, this sharpening becomes more prominent for concentrations above 1.55 at.%. This effect could be attributed to a RE induced crystallization which is not uncommon to occur in these systems.

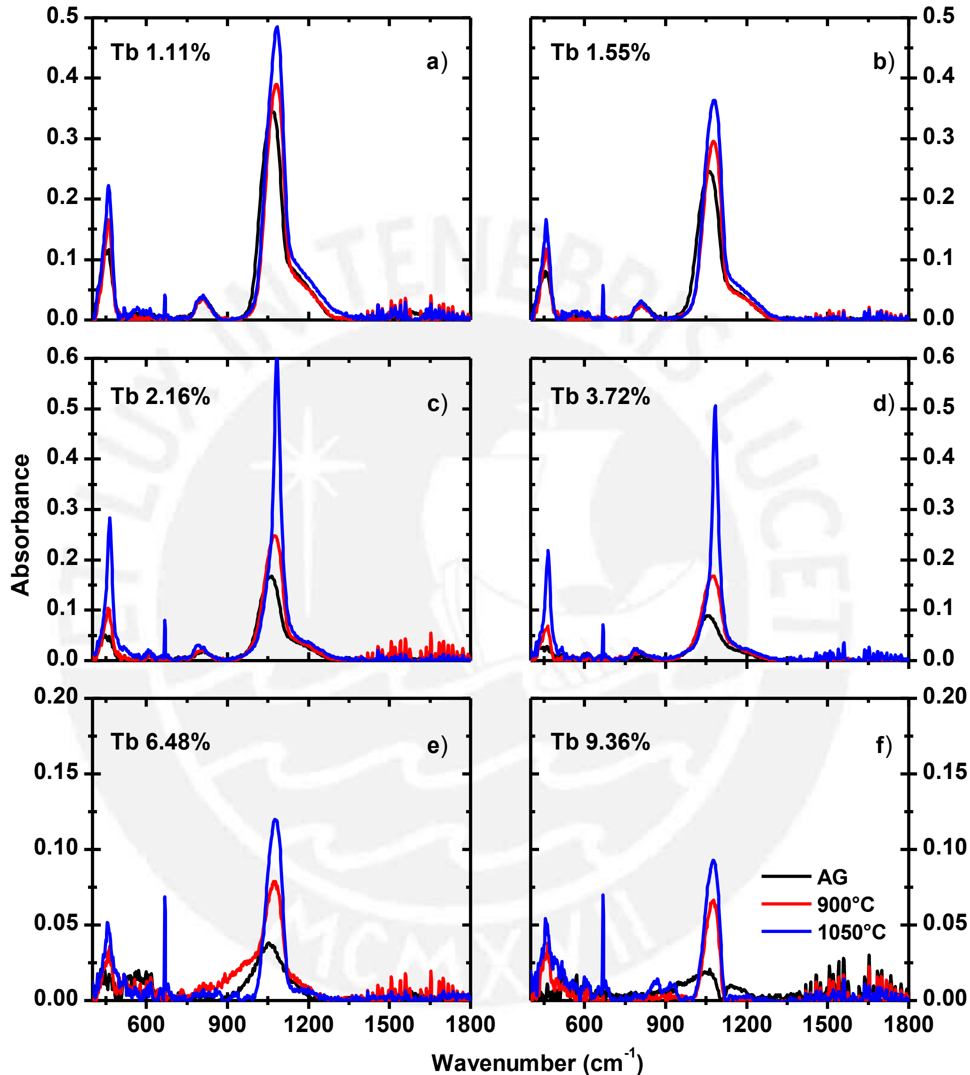

Figure 4.4.2. FTIR spectra of the six sample pieces. Two distinct annealing temperatures are shown. AG stands for the as gown case. TEM revealed that *a*-SiC:H will become polycrystalline after an annealing treatment at 1000°C [Ben13]. The crystallization process seems to be enhanced with increasing the Tb amount up to 3.72 at.% since the corresponding absorption peaks become sharper.

It is important to remark that the calibration described in figure 4.4.3 above introduces systematical errors. First, the films in each sample piece are not homogeneous thus

Tesis publicada con autorización del autor
No olvide citar esta tesis
PUCP

introducing an error not taken into account when using the area of the absorbance and not of the absorption coefficient. Additionally, since we had to extrapolate the concentration values for the last 2 sample pieces, that is for the positions 12 to 18, the calibration was not performed through a linear fit of the measured Tb concentration versus the inverse of the IR absorbance area (see figure 4.4.3), but through an averaged accomplished by rescaling the inverse of the IR absorbance area to match each of the 4 measured Tb concentration values independently. The four rescaled curves are then averaged. The red line depicted in the frame (b) of figure 4.4.3 is the result of this average.

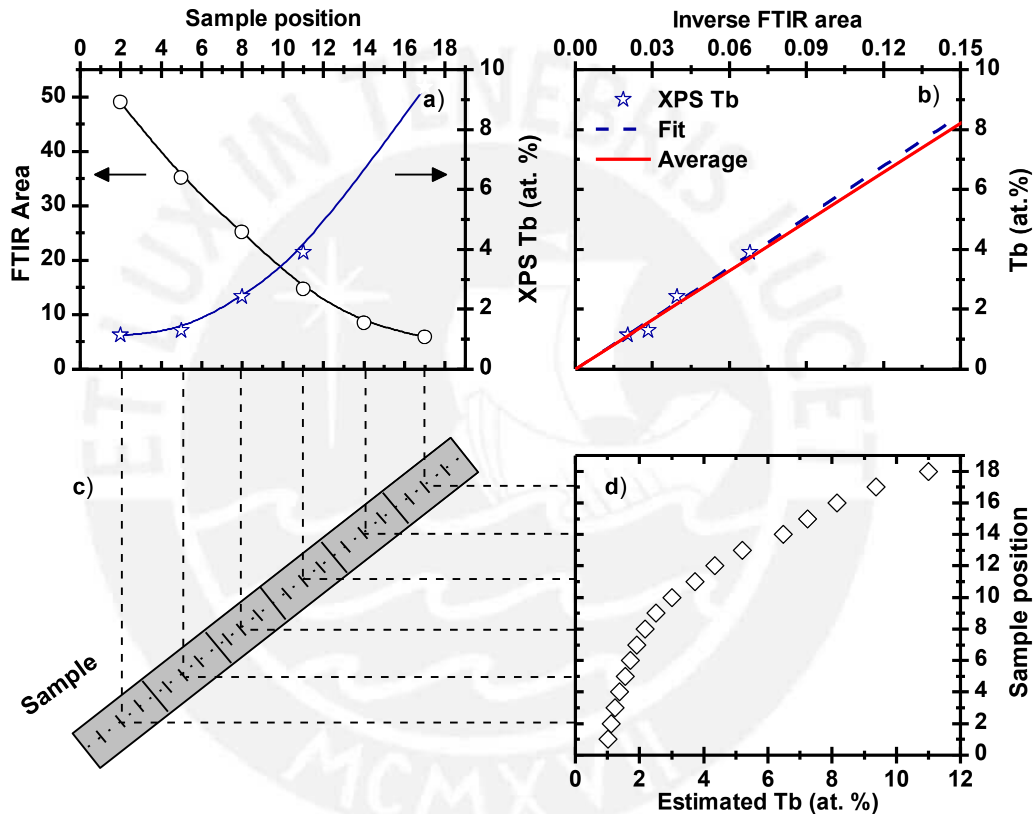

Figure 4.4.3. The IR absorption area are obtained after integrating from 400 cm^{-1} to 1400 cm^{-1} the spectra shown in the figure 4.4.2, these areas are plotted along with the measured Tb concentration determined by XPS versus the sample position (a). The calibration is performed between the inverse of the aforementioned areas and the measured Tb concentration. The blue dashed line is a linear fit with the intercept fixed in the origin, while the red line is calculated after averaging the curves obtained after scaling the inverse of the IR absorbance area with each measured Tb concentration (b). Schematic of the SiC sample positions (c). Resulting estimated Tb concentration for each sample position after the calibration (d). The interpolation and extrapolation values are performed linearly.

Tesis publicada con autorización del autor
No olvide citar esta tesis
PUCP

Finally, concerning the Tb concentration values corresponding to the polycrystalline AlN grown in the University of Stuttgart, these were determined by a combination of XPS measurements and inductively coupled plasma optical emission spectroscopy (ICP-OES), the latter sensible to the metal elements only, while the former renders the concentration of all the constituents. It was found that the main impurity was oxygen homogeneously distributed in the films [Ben13].

Tesis publicada con autorización del autor
No olvide citar esta tesis
PUCP

Results and discussion

The experimental results presented here can be organized in two main groups. One part treats, the optical characterization, which accounts for the optical bandgap determination of the three materials under study, the modification of the bandgap upon iscochronical annealing treatments and the relation between the bandgap and the Urbach energy. Additionally, the Urbach focus is reported for the three materials and the tailoring of the bandgap and the Urbach focus of *a*-SiC:H under different hydrogen dilution degrees is also presented [Gue13m, Gue16]. Finally, the models developed in the section 3.1 are brought and tested.

The other main topic treats the Tb light emission properties, in which features of the Tb-related spectra are examined upon electron band-to-band excitation and photon sub-bandgap excitation for the three materials under study. Furthermore, the concentration quenching effect is examined for the SiC:H and AlN host matrices upon the two aforementioned excitation sources. The thermal activation of the light emission of the Tb ions is examined and contrasted with the variation of the optical bandgap and Urbach energies after different annealing temperatures. This thermal activation is evaluated profoundly in the case of *a*-SiC:H for the Tb concentration range from ~0.5 at.% to 10 at.% and has been first reported here revealing valuable information concerning the activation process. For instance, the interaction probability between Tb ions seems to be quenched with the annealing temperature. Finally, since different host matrices affect the RE ions differently by enhancing or quenching the RE-related emission, temperature dependent measurements are performed in order to shed light on the possible excitation mechanisms that take place.

5.1 Optical characterization of the amorphous AlN, SiN and SiC:H$_x$ thin films

One important aspect of amorphous semiconductors is the wavelength dependent absorption coefficient in the fundamental and adjacent region. The Tauc region describes the extended states related transitions, whilst the Urbach region accounts for localized

Tesis publicada con autorización del autor
No olvide citar esta tesis
ET LUX IN TENEBRIS LUCET MCMXVII PUCP

states related transitions, observed as the so called exponential tail in the absorption coefficient. The set of three materials (*a*-AlN, *a*-SiN, *a*-SiC:H_x) were characterized by means of optical transmittance spectroscopy in order to measure the optical parameters such as the refractive index and the absorption coefficient. Details concerning the used method to extract the aforementioned optical parameters along with an analysis of its accuracy can be found in the appendix A.1. Here we will focus on the fundamental absorption and Urbach tail regions of the absorption coefficient. We measure the optical bandgap, the Urbach energy and the Urbach focus. Furthermore, the bandgap dependency with the annealing treatments and the Urbach Energy is presented. Finally, the variation of the Urbach focus of *a*-SiC:H_x with increasing the hydrogen dilution during the deposition process is reported [Gue16].

Bandgap and Urbach energy

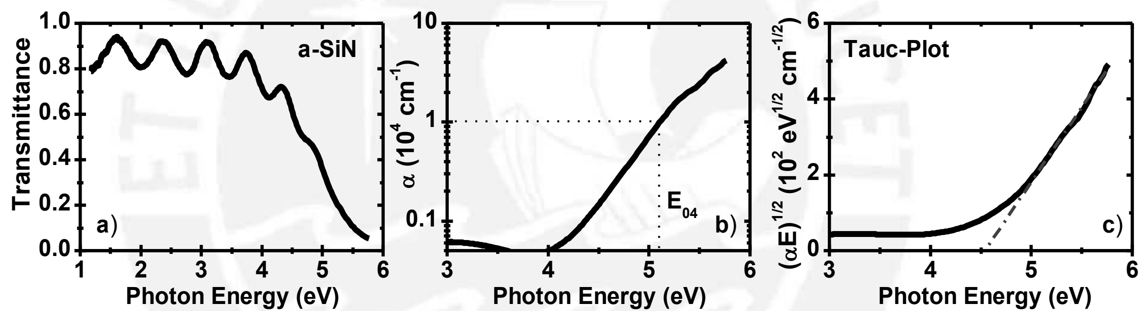

Figure 5.1.1. UV/VIS/NIR transmittance spectra in the wavelength range 200-1100 nm of *a*-SiN grown on quartz. The layer thickness is 420 nm (a). Absorption coefficient in logarithm scale along with the E_{04} energy value (b). Tauc-plot showing a good linear relation in the high energy region (c).

It is important to remark that the optical bandgap can be solely calculated from the region of the fundamental absorption of the absorption coefficient. In the case of thin films, this region can only be observed in sufficiently thin samples [Gue10t] (see appendix A.1). Furthermore, there is actually no proper model to accurately determine the optical bandgap of amorphous semiconductors from their fundamental absorption spectrum (see section 3.1). Nevertheless, the values obtained with the existing models give information of the relative behavior of the bandgap. Here we use the E_{04} iso-absorption gap, the Tauc gap (E_{Tauc}) and the Urbach focus minus the Urbach energy ($E_{UG} = E_F - E_u$) [Gue11,

Tesis publicada con autorización del autor
No olvide citar esta tesis
PUCP

Dun83, Dun85] as representative values of the true bandgap of an amorphous semiconductor. The Urbach focus determination is discussed in detail in the succeeding section.

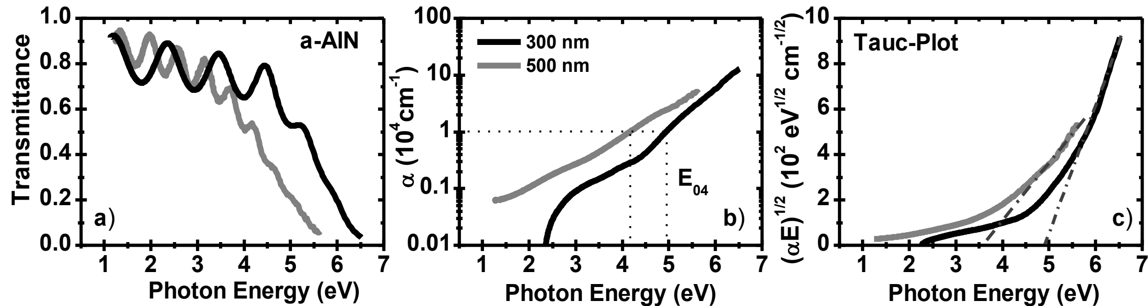

Figure 5.1.2. UV/VIS/NIR transmittance spectra in the wavelength range 190-1100 nm of *a*-AlN grown on CaF_2. Two samples were grown, one of 500 nm thickness by sputtering an Al target in a nitrogen atmosphere and another of 300 nm thickness by sputtering a single-crystal bulk AlN target in a nitrogen-argon atmosphere mixture (a). Absorption coefficient in logarithm scale along with the E_{04} energy value (b). Tauc-plot showing a good linear relation in the high energy region for the thinner sample (c).

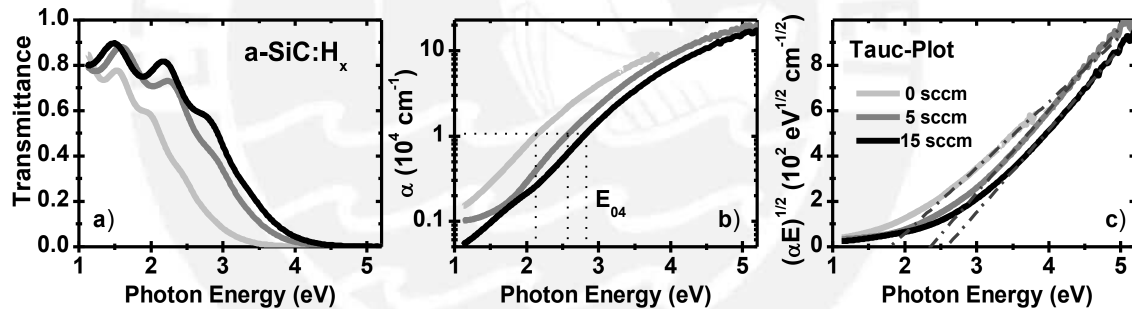

Figure 5.1.3. UV/VIS/NIR transmittance spectra in the wavelength range 190-1100 nm of *a*-SiC and *a*-SiC:H grown on CaF_2. The layers thicknesses are 652 nm (without H_2), 411 nm (with 5 sccm H_2 flux) and 435 nm (with 15 sccm H_2 flux) (a). Absorption coefficient in logarithm scale along with the E_{04} energy value (b). Tauc-plot showing a good linear relation in the high energy region (c).

Figures 5.1.1, 5.1.2 and 5.1.3 depict the UV/VIS/NIR transmittance (a), absorption coefficient in logarithm scale (b) and the Tauc-plot (c) of the as grown amorphous thin films of SiN, AlN and SiC:H_x, respectively. Notice the good linear relationship of the absorption coefficient in the Tauc-plot representation. In the AlN case, films with a thickness around or below 300 nm are necessary to be able to observe the fundamental absorption region in the Tauc representation [Gue10t].

Tesis publicada con autorización del autor
No olvide citar esta tesis
ET LUX IN TENEBRIS LUCET MCMXVII PUCP

After the isochronical thermal annealing treatments at different temperatures, a reduction of the Urbach energy is observed in the SiN and AlN samples. That is, the diminution of the band tail states near the band edge due to the disorder relaxation of the matrix [Str91, Ada04]. This effect is also reflected in the optical bandgap as an increase with the annealing temperature. In the case of SiC:H$_x$ the bandgap shrinks after reaching a critical annealing temperature. We will treat the latter behavior as a separated case. Figures 5.1.4 and 5.1.5 depict the bandgap, obtained with the aforementioned models, versus the annealing temperature and versus the Urbach energy for the a-SiN and a-AlN films, respectively. In the case of the AlN sample a linear relation is observed between the Tauc-gap and the inverse of the Tauc-slope ($1/m_{\mathrm{Tauc}}$), which is known as a measure of the disorder degree [Mor99].

As it was already presented in the section 3.1, the linear relation between the bandgap (Tauc-gap) and the Urbach energy can be explained by the frozen phonon model [Str91, Ada04, Cod81]. From the intercept of such relation the bandgap in the absence of disorder can be calculated, here named ${}^{(Tauc)}E_F$. From the analysis of several absorption coefficients data of a-Si:H, Cody suggested that this intercept value and the Urbach focus are actually the same parameter [Cod81]. This linear dependency is not always met. Nevertheless, other linear relations between the optical bandgap and a disorder related parameter can be expected depending on the position of the Urbach focus, wherever it falls in the Urbach tail region or in the fundamental absorption region. Here, we present three linear relations which connect the Urbach focus (E_F) with the bandgap. First, the equation 5.1.1 which accounts for the frozen phonon model and relates the Tauc-gap with the Urbach energy (see equation 3.1.31). Second, the linear relation depicted by equation 5.1.2, consequence of the empirical Urbach rule and the definition of the E_{04} iso-absorption gap. And third the equation 5.1.3, resulting from the case of the Urbach focus energy value E_F falling in the fundamental absorption region and then modeling the fundamental absorption with the Tauc approach [Gue11]. The left upper label denotes the origin of the constant E_F.

Tesis publicada con autorización del autor
No olvide citar esta tesis
ET LUX IN TENEBRIS LUCET MCMXVII PUCP

$$E_{Tauc} = {}^{(Tauc)}E_F - \frac{1}{\beta} G_{Cody} \qquad (5.1.1)$$

$$E_{04} = {}^{(04)}E_F - \frac{1}{\beta} \log(10^{-4}\alpha_F) \qquad (5.1.2)$$

$$E_{Tauc} = {}^{(m_{Tauc})}E_F - \frac{1}{m_{Tauc}} (\alpha_F E_F)^{1/2} \qquad (5.1.3)$$

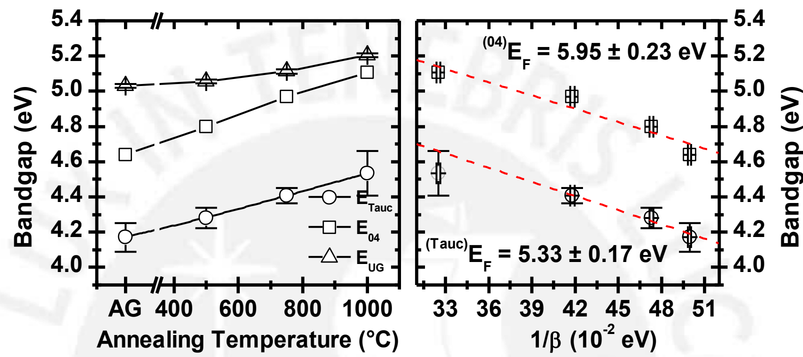

Figure 5.1.4. E_{Tauc}, E_{04} and E_{UG} of the *a*-SiN films after different isochronical annealing temperatures (a). E_{Tauc} and E_{04} versus the Urbach energy (b), the red dashed lines are fits using the equations 5.1.1 and 5.1.2.

By using the equations 5.1.1 and 5.1.2, two distinct values of the Urbach focus energy E_F are found for *a*-SiN, see figure 5.1.4. The obtained ${}^{(04)}E_F$ using the E_{04} iso-absorption gap match pretty well with the Urbach focus obtained through a global fit of the absorption coefficients (see next sub-section), while the obtained ${}^{(Tauc)}E_F$ using the E_{Tauc} does not. Notwithstanding, the ${}^{(Tauc)}E_F$ match pretty well the value obtained for the bandgap in the absence of disorder obtained using an extension of the Urbach rule proposed here [Gue13m, Gue16] (see section 3.1). In the AlN case though, the constant E_F obtained with the equations 5.1.1, 5.1.2 and 5.1.3 are pretty close to each other (see figure 5.1.5). These values are also close to the one obtained by a global fit of the absorption coefficient (see next sub-section).

Tesis publicada con autorización del autor
No olvide citar esta tesis
PUCP

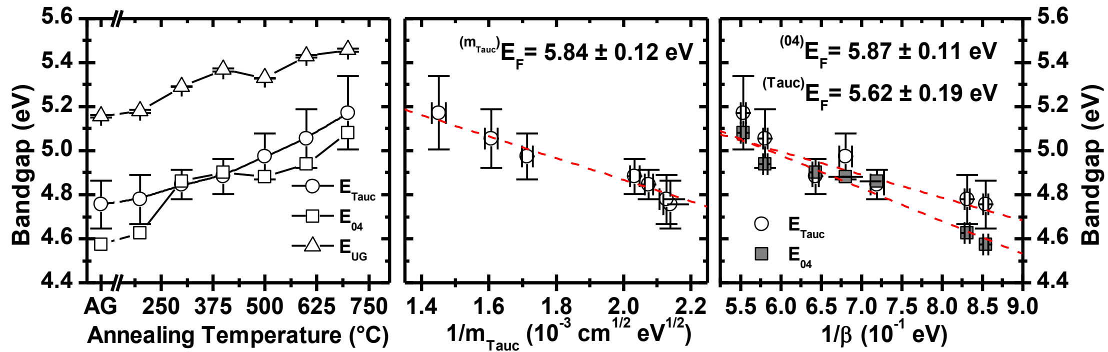

Figure 5.1.5. E_{Tauc}, E_{04} and E_{UG} of the a-AlN films after different isochronical annealing temperatures (a). E_{Tauc} versus the inverse of the Tauc slope (b). E_{Tauc} and E_{04} versus the Urbach energy (c).

Whilst in the SiN and AlN cases the bandgap increases with the annealing temperature, in the SiC:H_x case it increases till a critical annealing temperature and then it decreases (see figures 5.1.6). This differing behavior is typically attributed to the induced effusion of hydrogen from the SiC matrix during the thermal treatments [Mon13, Zha92]. The quenching of the bandgap of an hydrogenated amorphous semiconductor with the annealing temperature has been observed before in a-Si:H [Str91, Mor99] and for SiC:H [Mon13, Tes95]. Notwithstanding, we report this behavior also for the non-hydrogenated sample, thus exhibiting that the shrinking effect cannot be attributed to the hydrogen out-diffusion alone.

We examine the latter features in detail for a-SiC:H with different hydrogen dilution contents by changing the hydrogen flux during the deposition process. Three samples were grown, one without any hydrogen flux (0 sccm), which serves as our reference sample, another with 5 sccm hydrogen flux and a last one with 15 sccm hydrogen flux during the deposition process. The bandgap versus the annealing temperature of these samples are depicted in the figure 5.1.6. The E_{04} iso-absorption gap was the only parameter that exhibited a well-defined linear relationship with the Urbach energy. The corresponding plots are shown in the figure 5.1.7.

Tesis publicada con autorización del autor
No olvide citar esta tesis

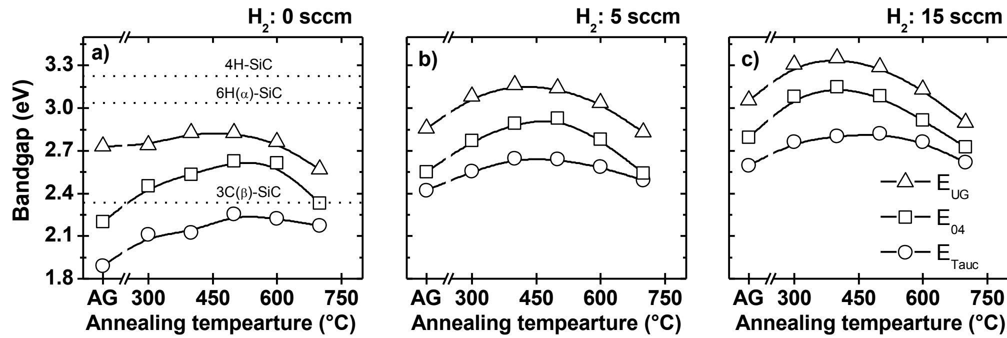

Figure 5.1.6. E_{Tauc}, E_{04} and E_{UG} of the *a*-SiC (a), *a*-SiC:H grown with 5 sccm H_2 flux (b) and *a*-SiC:H grown with 15 sccm H_2 flux (c), after different annealing temperatures. The doted lines, denote the bandgap of the three main poltypes of SiC.

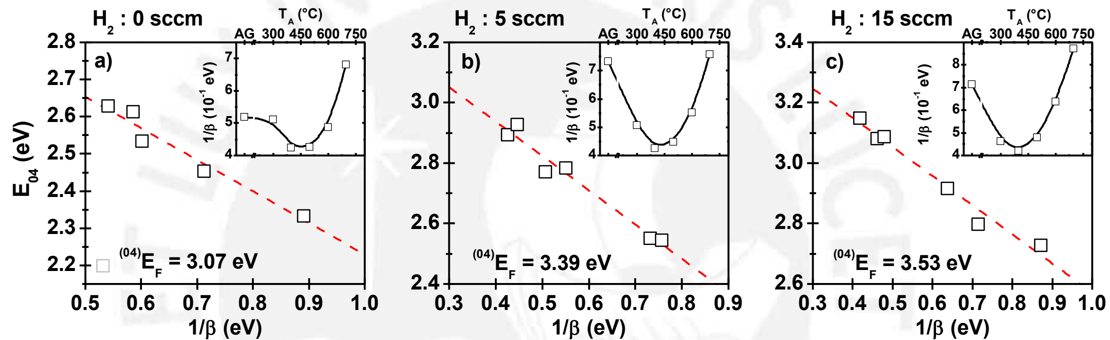

Figure 5.1.7. E_{04} iso-absorption gap versus the Urbach energy for *a*-SiC (a), *a*-SiC:H grown with 5 sccm H_2 flux (b) and *a*-SiC:H grown with 15 sccm H_2 flux (c). The increase of the parameter $^{(04)}E_F$ with the hydrogen dilution content suggests an increase of the energy separation between the mobility edges. Inset graphs include the variation of the Urbach energy with the annealing temperature.

Two major features are noted. First, the bandgap increases with the amount of hydrogen used during the deposition process, and this difference is kept after the annealing treatments independently of the model used for the bandgap calculation (see figure 5.1.6). Furthermore, this difference is also observed in the increase of the Urbach focus energy E_F with the hydrogen incorporation, see figure 5.1.7. Second, the bandgap is quenched after an annealing temperature around 450°C for all the three samples including the non-hydrogenated one. In the following paragraphs we'll try to elucidate the possible mechanisms behind the latter behavior.

Tesis publicada con autorización del autor
No olvide citar esta tesis
PUCP

The thermal induced out diffusion of hydrogen from the matrix can be translated in the depletion of hydrogen related bonds. Therefore, like in the case of *a*-Si:H an increase of the Urbach energy is expected reducing the bandgap [Str91, Bul87, Mor99]. This depletion of hydrogen related bonds can be followed through IR absorption spectroscopy [Sum04]. IR absorbance measurements of the three samples were performed, see figure 5.1.8. The IR absorption spectra of the samples in the range of 400-4000 cm^{-1} consist of four main absorption bands at ~790 cm^{-1}, ~1000 cm^{-1}, ~2100 cm^{-1} and ~2900 cm^{-1} for the hydrogenated samples and three bands at ~790 cm^{-1}, ~1065 cm^{-1} and ~1190 cm^{-1} for the non-hydrogenated one. The bands at 2100 cm^{-1} and 2900 cm^{-1} are attributed to the stretching vibration modes of Si-H_n and C(sp^3)-H_n, respectively [Bul87]. These bands decay with increasing the annealing temperature as shown in figures 5.1.9 and 5.1.10.

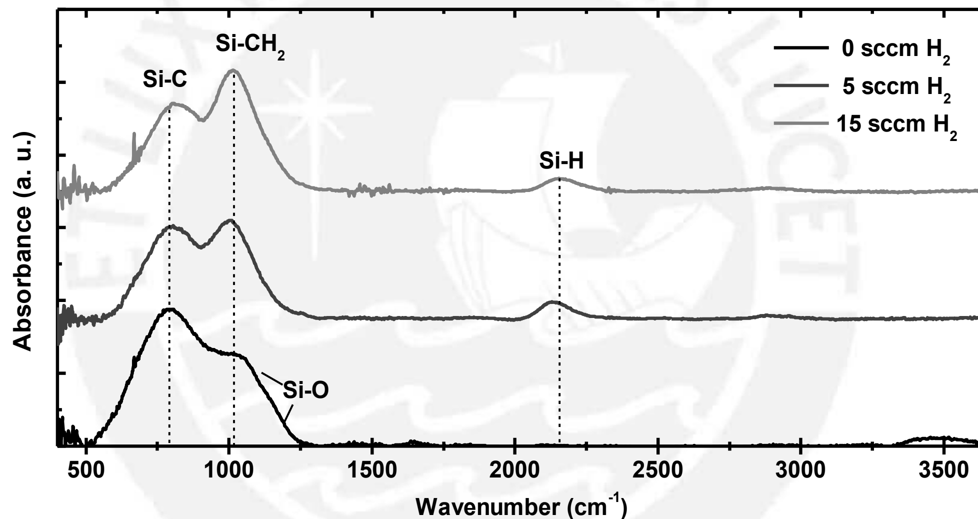

Figure 5.1.8. IR absorbance spectra of the three as grown *a*-SiC:H_x thin films with different hydrogen fluxes during the deposition process. Three main bands are to be noted. The Si-C stretching mode at 790, the Si-CH_n 1100 cm^{-1} and the Si-H stretching mode at 2100 cm^{-1}.

The Si-H_n IR absorption band disappeared completely at 600°C in agreement with [Vas11]. The bands at 790 cm^{-1} and 1000 cm^{-1} correspond to the Si-C stretching vibration mode and Si-CH_2 rocking/waging modes [Bul87], respectively. Nevertheless, sub-stoichiometric SiO_x ($x < 2$) structural fragments are known to present a broad absorption band at around 1100 cm^{-1} [Kan05]. This band is actually composed by 4 bands from which only and average resulting in two peaks at 1065 cm^{-1} and 1190 cm^{-1} are resolved.

Tesis publicada con autorización del autor
No olvide citar esta tesis
PUCP

After annealing at 700°C a Si-O bond related absorption band at 450 cm^{-1} increase slowly with the annealing temperature in the non-hydrogenated sample. This band appears after 800°C annealing in the hydrogenated samples, suggesting that the Si-O stretching modes contribute in absorption near 1000 cm^{-1} since residual oxygen contamination is considerable during the annealing procedure (see figure 5.1.9). Nevertheless, this contribution is very low compared to the main Si-C and Si-CH_n absorption peaks.

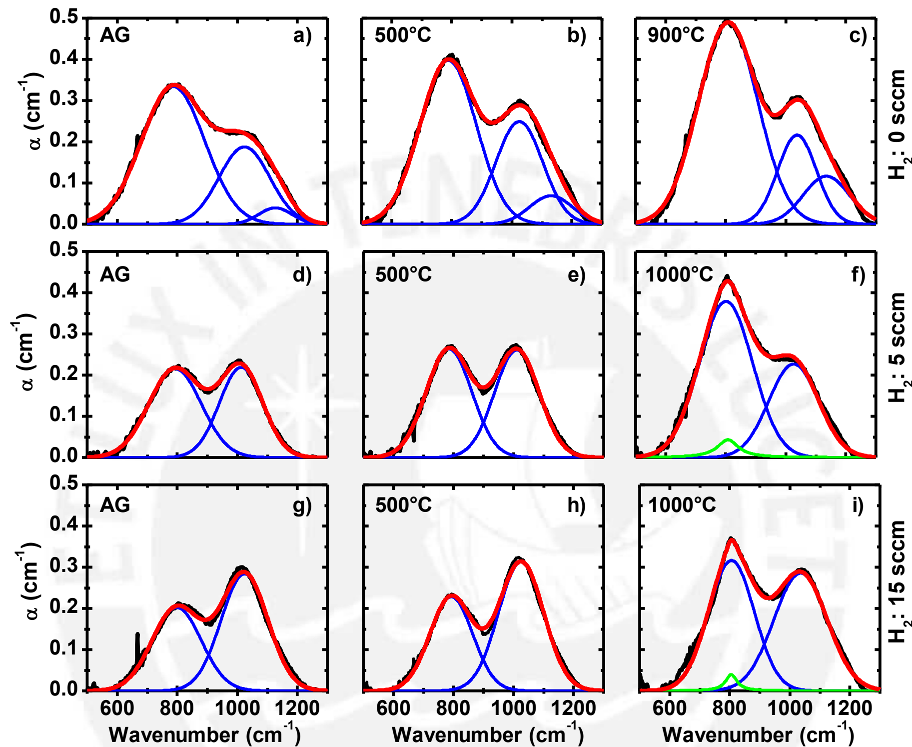

Figure 5.1.9. Effect of the annealing temperature on the shape of the different absorption peaks in the IR spectra of the three SiC:H_x thin films. The blue peaks are Gaussian fits of the corresponding vibrational modes while the green curves denote Lorentzian peaks corresponding to the crystallization of SiC. The red curves denote the peak sum. Notice the increase of a shoulder at 1190 cm^{-1} in the non-hydrogenated case. This shoulder does not appear in the hydrogenated samples, suggesting that the presence of oxygen contamination is not measurable by this mean in the hydrogenated samples but in the non-hydrogenated one.

It is well known that the area of the IR absorption peaks is directly related to the amount of corresponding bonds in the sample [Kuz09]. In order to assess the above mentioned variations on the vibrational modes and therefore on the chemical composition of the samples under study, the bond density is calculated and plotted versus the annealing

Tesis publicada con autorización del autor
No olvide citar esta tesis
ET LUX IN TENEBRIS LUCET MCMXVII PUCP

temperature as shown in the figure 5.1.10. This calculation is performed by $\rho \int \alpha(\nu)/\nu\, d\nu$ where ρ is the inverse absorption cross-section. The absorption coefficient α is obtained from the Lambert's law and the peaks fits shown in figure 5.1.9. The analysis reveals for instance that after the Si-H_n bonds are completely depleted at 600°C, the Si-CH_n bonds are quenched with the annealing temperature, whilst the Si-C bonds increase [Gue16].

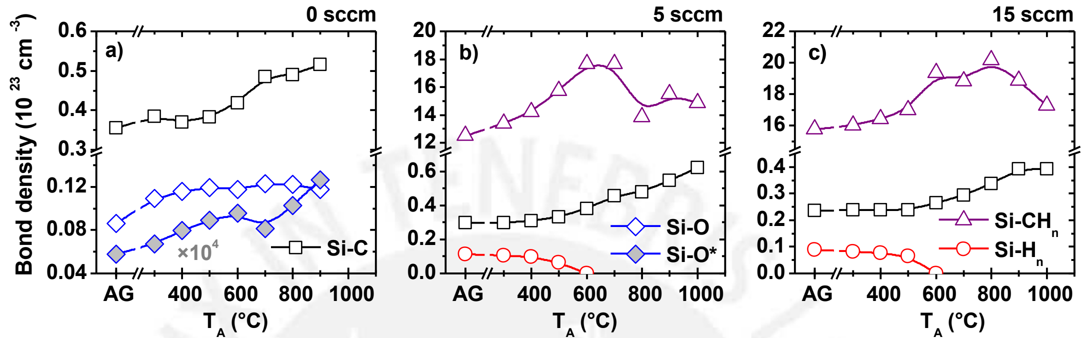

Figure 5.1.10. Calculated bond densities for each absorption peak obtained from the FTIR measurements of the *a*-SiC:H grown on *c*-Si with 0 sccm (a), 5 sccm (b), and 15 sccm (c) hydrogen flux during the deposition process. The bond density corresponding to the Si-O vibrational mode centered at 1190 cm^{-1} has been multiplied by 10^4 (filled blue diamonds) for viewing reasons (a). Note the depletion of hydrogen related bond with the annealing temperature.

In the case of the hydrogen doped samples, the bandgap reaches its maximum value at around the same annealing temperature for which the Si-H bonds are depleted. The bandgap starts decreasing when the Si-CH_2 bonds decrease and consequently the amount of Si-C bonds increase. This correlation may account for the bangap quenching of *a*-SiC:H due to the out-diffusion of hydrogen and therefore the increase of Si-Si and Si-C bonds. However, in the case of the non-hydrogenated sample no significant correlation can be observed between the bandgap and the vibrational modes area. Note that we cannot see Si'H correlated peak either. Therefore, we can assume the trend of at least two different processes which quench the bandgap after a critical temperature in amorphous hydrogenated SiC. The effect of the hydrogen related bonds depletion, and the bandgap shrinking related to structural features of the material which are triggered with the thermal annealing treatments. According to Kityk *et al*, the latter behavior is observed in amorphous SiC [Kit00]. Kityk proposed and supported by ab initio simulations that the

Tesis publicada con autorización del autor
No olvide citar esta tesis
ET LUX IN TENEBRIS LUCET MCMXVII PUCP

bandgap is affected by the formation of nano-composites clusters in the SiC matrix, which occurrence are not uncommon. The bandgap is then crystallite and cluster size dependent [Kit00]. Furthermore, Kityk calculated the bandgap versus the crystallite size and versus the cluster size, predicting an increase and then, after a critical crystallite size, a shrinking of the bandgap. Alternatively, the formation of Si-Si and C-C bonds is also a common feature in these amorphous systems [Cui01, Lee00]. In fact, Raman analysis on RF sputtered a-SiC and a-SiC:H revealed two features. First, a decrease and after a critical temperature an increase of the disorder with the annealing temperature, observed by measuring the FWHM of the Si-C related vibrational modes [Vas11]. Second, the increase of C-C bonds with the annealing temperature in both hydrogenated and non-hydrogenated a-SiC, reported by Vasin *et al* [Vas11]. In summary, these effects contribute exhibiting the observed features in the bandgap versus the annealing temperature.

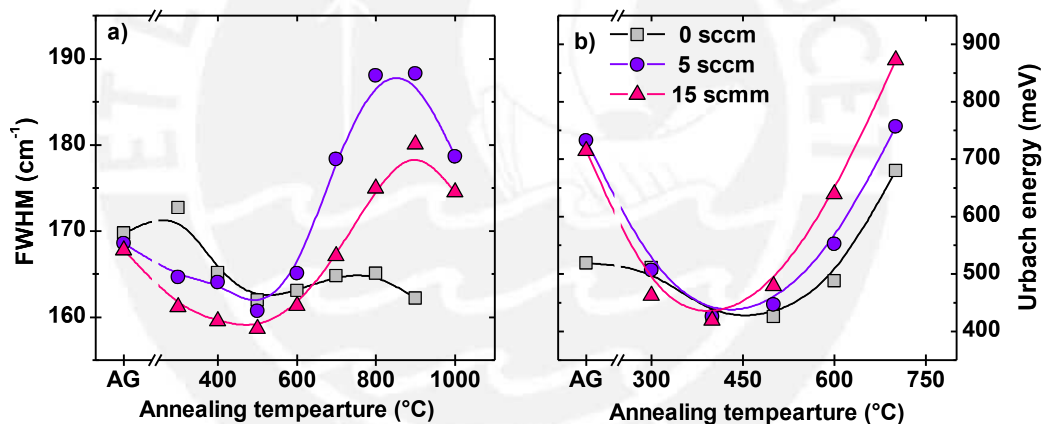

Figure 5.1.11. Average FWHM of the Si-C, Si-CH$_n$ and Si-O bond related IR peaks of the three SiC:H$_x$ samples versus the annealing temperature (a). Urbach energy of the same samples versus the annealing temperature (b). Notice the good correspondence of both parameters. Additionally, the Urbach energy of the three samples is quite similar, thus the bandgap enhancement due to the hydrogen incorporation cannot be attributed to the Urbach energy but to the increase of the energy separation of the mobility edges.

In agreement with the results reported by A. V. Vasin [Vas11], the disorder of the SiC:H samples studied here is reduced with the annealing treatments till a critical temperature, and then an increase is observed. This effect has been measured by the Urbach energy $1/\beta$ and by the average FWHM of the absorption peaks observed in the IR absorbance

Tesis publicada con autorización del autor
No olvide citar esta tesis
ET LUX IN TENEBRIS LUCET MCMXVII PUCP

spectra (see figure 5.1.11). However, the fact that the Tauc-gap and the iso-absorption gap exhibit a correlated behavior with the Urbach energy may actually be a consequence of their definition. For instance, the E_{04} energy value in this case falls inside the Urbach region, thus E_{04} is subjected to the Urbach energy through the equation 5.1.2, and any increase of the Urbach energy causes a decrease of the bandgap and vice versa. Furthermore, the shift observed on the E_{04} gap due to the hydrogen incorporation can be translated to an increase of the constant ${}^{(04)}E_F$. Notice, that the disorder, or tails depth, is pretty much the same in all three SiC:H samples. On the other hand, it is important to emphasis that the Tauc model does not take into account the band tails (tail to tail and band to tail transitions), nonetheless the band tails overlap considerably with the so called Tauc-region. So even when the relations depicted by the equations 5.1.1 and 5.1.3 are not met, any variation of the Urbach energy will affect the Tauc-gap value as well (see figure 3.1.9).

The shift in the bandgap observed in figure 5.1.6 is band-edge rather than band-tail related. This fact is supported by the shift of the constant ${}^{(04)}E_F$ depicted in figure 5.1.7. The Tauc-gap and the E_{04} iso-absorption gap are subjected to two distinct physical parameters: the mobility edges energy gap and the Urbach energy. The former can be estimated by the parameter E_0 in the equation 3.1.23. Figure 5.1.12 depicts and compares the parameters obtained through the Tauc model and the model depicted by the equation 3.1.13 (DiLog, band-fluctuations based model, which derivation was explained in chapter 3). The parameters E_0, α_0 and β were estimated by single fits of each absorption coefficient using the DiLog model. The main advantage of the latter model is that no discrimination must be done between the Urbach and Tauc regions i.e. the admixture region is also part of the fitting input. Notice from figure 5.1.12 that contrary to the Tauc-gap, E_0 is not correlated to the Urbach energy.

Tesis publicada con autorización del autor
No olvide citar esta tesis
ET LUX IN TENEBRIS LUCET MCMXVII PUCP

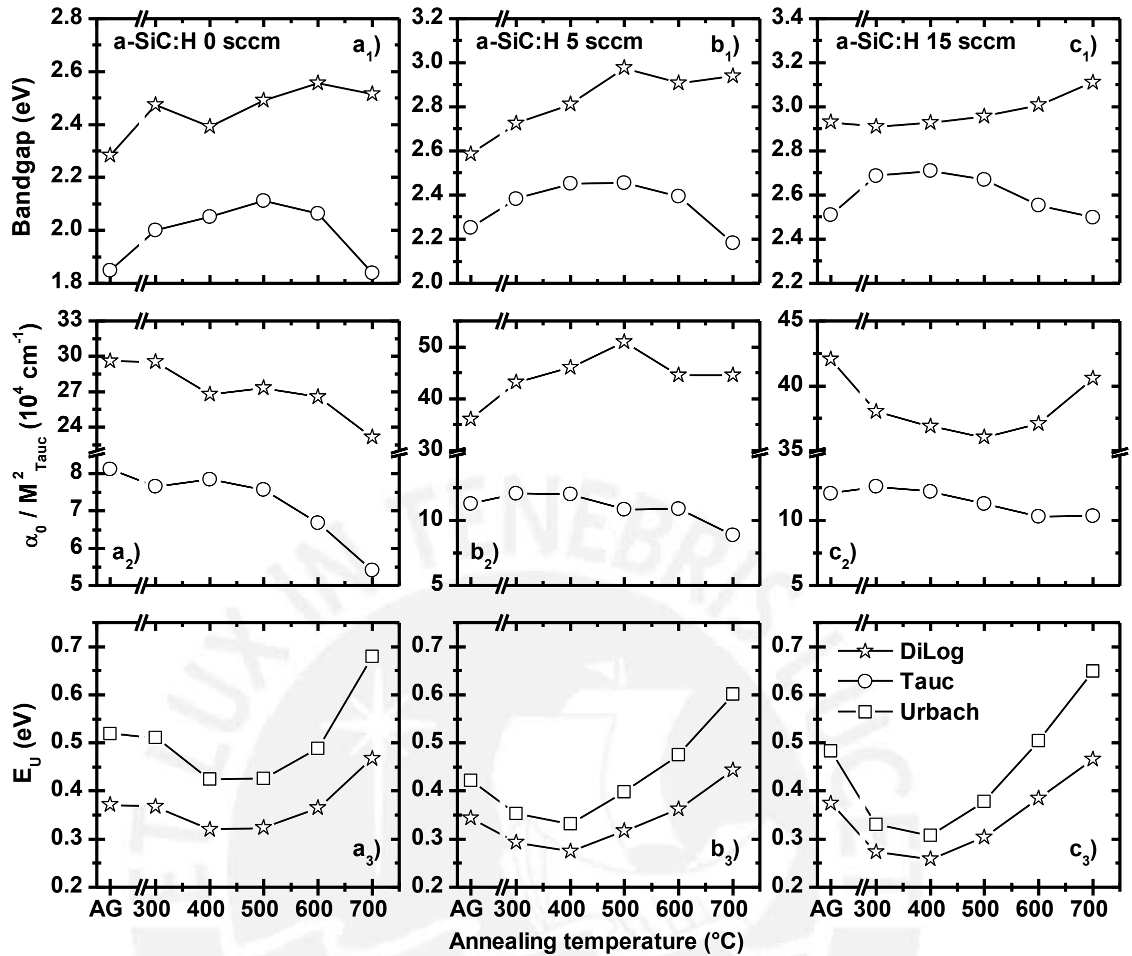

Figure 5.1.12. Bandgaps E_0 and E_{Tauc} (a), scale factors α_0 and M_{Tauc}^2 (b) and Urbach energy (c), for the SiC:H_x samples grown with 0 sccm, 5 sccm and 15 sccm hydrogen flux during the deposition process. Notice that the bandgap calculated with the DiLog model has no correlation with the Urbach energy. Additional information concerning the electronic transition matrix element is recovered through α_0.

In summary, the effect of the isochronical thermal annealing treatments on the bandgap of *a*-SiN, *a*-AlN and *a*-SiC:H_x has been examined. A reduction of the disorder with the annealing temperature is observed by the decrease of the Urbach energy and increase of the optical bandgap of the amorphous SiN and AlN matrices due to a thermal induced structural relaxation of the matrices. The hydrogenated SiC case is treated separately since the bandgap increases till a critical annealing temperature from which afterwards is quenched with further annealing treatments at higher temperatures. The matrix relaxation solely cannot account for such behavior nor the H_2 effusion from the matrix since the behavior is also reported in the non-hydrogenated case. The Urbach focus energy E_F is

Tesis publicada con autorización del autor
No olvide citar esta tesis
PUCP

found by the different linear relations presented. However, not all the linear relations are met by the three materials. The bandgap of a-SiC:H increased with the amount of diluted hydrogen, suggesting the effective passivation of dangling bonds and therefore the widening of the band edges reflected in the increase of the Urbach focus energy E_F. The latter behavior can be understood by taking into account the shrinking of the average lattice constant due to the passivation of the dangling bonds by hydrogen atoms which occupy a smaller volume [Bul87].

The approach to explain the quenching of the bandgap of a-SiC:H turned differently to what is typically found in the literature [Zha92, Kal94, Cui01]. First the behavior observed in E_{Tauc} and E_{04} versus the annealing temperature is attributed to the behavior of the Urbach energy. While the increase of the bandgap with the annealing temperature is mainly due to the matrix relaxation, disorder reduction and hence the reduction of electronic band tails states, the decrease of the bandgap (increase of the Urbach energy) cannot be only due to the hydrogen effusion but probably also related to the formation of crystalline clusters in the matrix with the thermal annealing treatments [Lee00, Kit00, Raj03]. In fact TEM and electron diffraction revealed that up to 600°C annealing temperature the SiC:H matrix is predominantly amorphous, while after 1000°C annealing temperature it becomes a polycrystalline structure embedded in an amorphous matrix (see figure 5.1.13). Furthermore, the formation of C-C and Si-Si clusters is also a common in these disordered systems therefore influencing the bandgap. As reported already by Vasin an increase of C-C clusters with the annealing treatment could be a precursor of the bandgap quenching [Vas11]. This latter effect has also been reported and characterized by Bullot [Bul87].

Tesis publicada con autorización del autor
No olvide citar esta tesis
ET LUX IN TENEBRIS LUCET MCMXVII PUCP

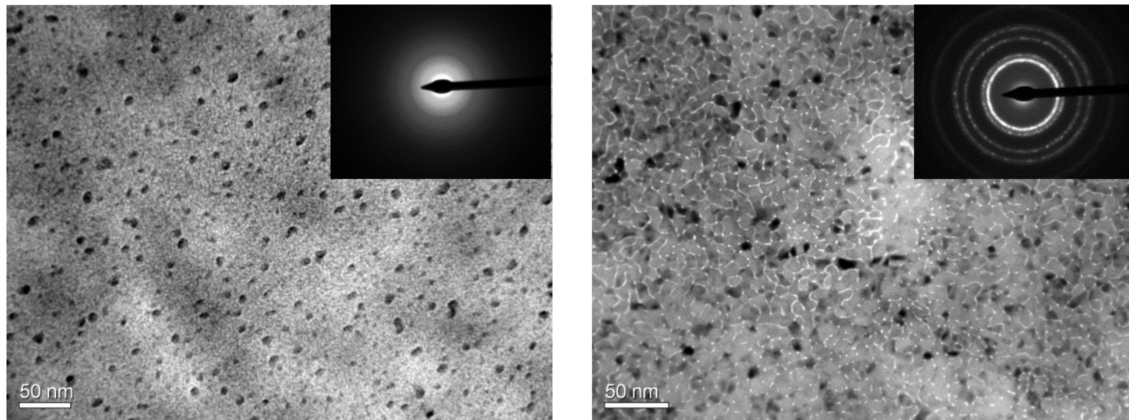

Figure 5.1.13. TEM images and electron diffraction patterns of a-SiC:H annealed at 600°C (a) and 1000°C (b). After 600°C the samples are still amorphous, whilst after 1000°C a polycrystalline structure embedded in an amorphous matrix is observed.

The Urbach focus and the Orapunt & O'Leary analysis

As we have already reviewed and discussed in section 3.1, the optical absorption of an amorphous material shows a near universal exponential energy dependence in the vicinity of the bandgap energy, known as Urbach tail. The current agreement is that this region is a measure of the shape of the electronic density of states near the band edge and the nature of this broadening is closely related to the disorder of the material (see section 3.1) [Str91, Ada04, Mor99]. The simple an empirical Urbach rule (equation. 3.1.14, here renumbered as equation 5.1.4) describes very well this region.

$$\alpha_{\mu}(E) = \alpha_F \exp\left(\frac{E - E_F}{E_u}\right) \tag{5.1.4}$$

Here E_u is the Urbach energy, α_F and E_F are both constants which will denote the Urbach focus coordinate (E_F, α_F). The Urbach focus has been observed in several amorphous materials already. In this work, the Urbach focus is reported in the three materials under study SiC:H_x, AlN, SiN. In order to test the existence of the Urbach focus, in other words: to prove that the Urbach focus existence is not biased by the Urbach rule itself, we will follow up with the analysis proposed by Orapunt and O'Leary [Ora04]. Furthermore, we will extend this analysis introducing also the equation 3.1.24 obtained previously in section 3.1, which predicts the non-existence of the Urbach focus, but of another constant with a lower energy value [Gue13m, Gue16].

Tesis publicada con autorización del autor
No olvide citar esta tesis
ET LUX IN TENEBRIS LUCET MCMXVII PUCP

In order to find the Urbach focus (E_F, α_F), a global linear fit of the equation 5.1.4 in logarithm scale is performed using various absorption coefficients of the same material at different temperatures or treated at different annealing temperatures so as to vary the electronic band tails. In this fit the parameters E_F and α_F are shared while E_u is left independent. Notwithstanding, sharing the parameters (E_F, α_F) may introduce a numerical bias. For instance, three parallel lines can be easily fitted to 3 lines pivoted in a common point and predict a fictive focus [Gue13m]. Therefore, to avoid the above mentioned problem in this analysis, linear independent fits per absorption coefficient spectrum are performed. The Urbach slope $\beta = 1/E_u$ and the intercept $\log(\psi_\beta)$, are calculated for each absorption coefficient independently using the equation 5.1.5, thus avoiding any enforcing of the Urbach focus.

$$\log(\alpha_\mu) = \log(\psi_\beta) + \beta E \qquad (5.1.5)$$

$$\log(\psi_\beta) = \log(\alpha_F) - \beta E_F \qquad (5.1.6)$$

Subsequently, the Urbach focus can be recovered from the linear relation between the intercept $\log(\psi_\beta)$ and Urbach slope β. In order words, if and only if the Urbach focus exists, the linear relation in equation 5.1.6 must hold. This asseveration is valid as long as the Urbach rule is valid. That is, it is possible to isolate an exponential region of the absorption coefficient.

In summary, the simple analysis proposed by Orapunt and O'Leary lead to a straightforward calculation of the Urbach focus trough a linear fit of $\log(\psi_\beta)$ versus β. The Urbach focus is then obtained directly from the slope and intercept of the equation 5.1.6. Although in the original paper the fits are actually performed without taking the logarithm of the Urbach rule (linear scale), the results do not vary dramatically. Now let us introduce the equation 3.1.24 here renumbered as 5.1.7 for the Urbach tail region only. This equation is a semi-empirical result (see section 3.1). It is an extension of the calculation of the fundamental absorption of amorphous materials obtained after averaging the thermal fluctuations in the electronic density of states and then relaxing the

Tesis publicada con autorización del autor
No olvide citar esta tesis
PUCP

conservation of the wave vector $\boldsymbol{k}$. While this equation does not predict an Urbach focus it does predict the disorder independent constants E_0 and α_0.

$$\alpha_\Omega = \frac{\pi}{4}\frac{E_u^2}{E}\alpha_0 \exp\left(\frac{E - E_0}{E_u}\right) \quad (5.1.7)$$

In order to perform the same previous analysis, independent fits of the absorption coefficient in the Urbach region are performed using the equation 5.1.8 which is the logarithm of equation 5.1.7. In this case we write $\log(\psi_\beta) = \log(\alpha_0) - \beta E_0$. Note, that the independent fits to acquire $\log(\psi_\beta)$ and β are not truly linear.

$$\log(\alpha_\Omega) = \log(\psi_\beta) + \beta E - 2\log(\beta) - \log\left(\frac{4}{\pi}E\right) \quad (5.1.8)$$

After the fitting, again if the linear relation between $\log(\psi_\beta)$ and β holds, it is thus likely that the constants E_0 and α_0 exist within the error of the fit of the equation 5.1.9.

$$\log(\psi_\beta) = \log(\alpha_0) - \beta E_0 \quad (5.1.9)$$

In this way, we have shown that the Orapunt and O'Leary analysis can be applied to both the Urbach rule and the extended Urbach rule proposed before. The former predicting the disorder independent Urbach focus, while the latter predicts no Urbach focus but the constants E_0 and α_0.

Now, before continuing on performing the Orapunt and O'Leary analysis on the materials under study, lets first apply it to the case of *a*-Si:H, reproducing the previous results of Orapunt and O'Leary [Ora04]. We take the data of the absorption coefficient of *a*-Si:H at several different annealing temperatures and for various temperatures published by Cody [Cod81]. The global fits are performed minimizing the total Chi square $\chi^2(\beta_1, \dots, \beta_N, \alpha_{F/0}, E_{F/0})$ defined as the sum of the Chi square of each absorption curve $\sum_i \chi^2(\beta_i, \alpha_{F/0}, E_{F/0})$.

Tesis publicada con autorización del autor
No olvide citar esta tesis
PUCP

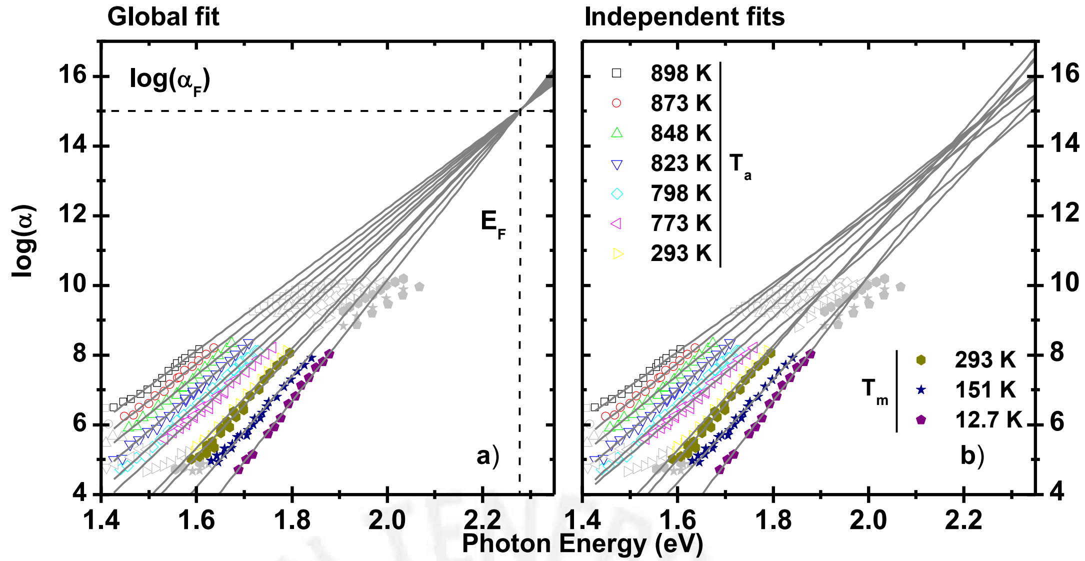

Figure 5.1.14. Optical absorption edge of a-Si:H measured at a couple sample temperatures T_m, and measured at room temperature after several annealing temperatures T_a. Global fit (a) and independent fits (b) using the equation 5.1.5. In the former case (a), the parameters E_F and α_F are shared and distinct slopes β are retrieved for each absorption coefficient. Whilst in the in independent fits case (b) the Urbach slope β and the intercept $\log(\psi_\beta)$ are obtained per each absorption coefficient curve.

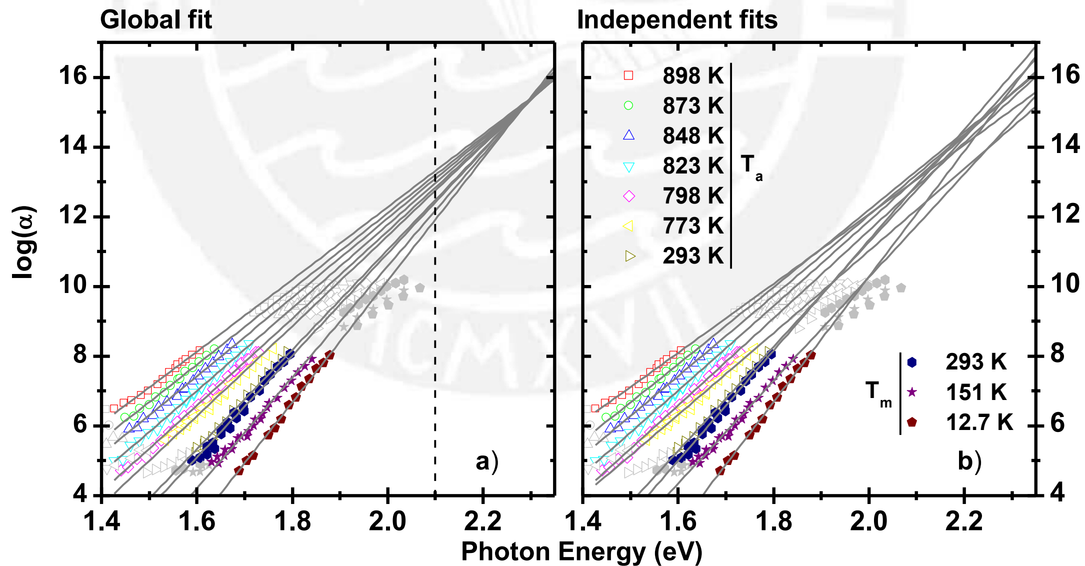

Figure 5.1.15. Optical absorption edge of a-Si:H measured at a couple sample temperatures T_m, and measured at room temperature after several annealing temperatures T_a. Global fit (a) and independent fits (b) using the equation 5.1.8. In the former case (a), the parameters E_0 and α_0 are shared and distinct slopes β are retrieved for each absorption coefficient. Whilst in the in independent fits case (b) the Urbach slope β and the intercept $\log(\psi_\beta)$ are obtained per each absorption coefficient curve.

Tesis publicada con autorización del autor
No olvide citar esta tesis
PUCP

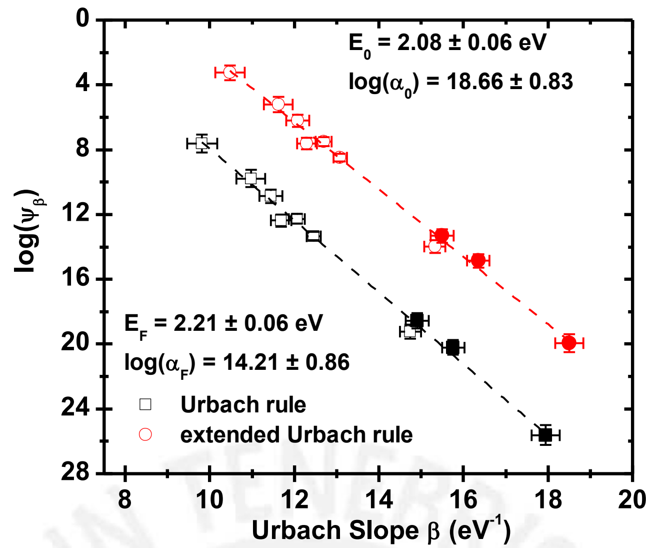

Figure 5.1.16. Intercept $\log(\psi_\beta)$ versus the Urbach slope β for both the Urbach rule and the extended Urbach rule of the absorption coefficient of a-Si:H after different annealing temperatures (open symbols) and for various temperatures (filled symbols).

Table 5.1.1: Urbach focus (E_F, α_F) and (E_0, α_0) for a-Si:H obtained through a global fit and the independent fits of the Urbach region in the absorption coefficient.

a-Si:H		**Global fit**	**Independent fits**
Urbach rule	$\log(\alpha_F)$	15.12 ± 0.40	14.21 ± 0.86
	E_F	2.28 ± 0.03 eV	2.21 ± 0.06 eV
Extended Urbach rule	$\log(\alpha_0)$	19.69 ± 0.43	18.66 ± 0.83
	E_0	2.15 ± 0.03 eV	2.08 ± 0.06 eV

The global and independent fits are depicted in the figures 5.1.13 and 5.1.14 for the Urbach rule and the extended Urbach rule, respectively in logarithm scale. The resulting fitted curves are pretty similar in both cases. Two main features are observed. First, whilst the global fit shows a convergence point, no convergence point (no focus) is noticeable in the independent fits. Second, even when the extended Urbach rule does not predict an Urbach focus, the global fit shows that the curves seem to converge in a single point or small region (see figure 5.2.15.a). Subsequently, the plots of the intercept $\log(\psi_\beta)$ versus the Urbach slope β are presented in the figure 5.1.16 for both the Urbach rule and the extended Urbach rule. Notice the good linear relation in both cases

Tesis publicada con autorización del autor
No olvide citar esta tesis
ET LUX IN TENEBRIS LUCET MCMXVII PUCP

predicting the not biased constants E_0 and E_F. The recovered Urbach focus (E_F, α_F) and the constants (E_0, α_0) are summarized in the table 5.1.1.

We have reproduced the results of Orapunt and O'Leary [Ora04] using the Urbach slope instead of the Urbach energy in order to obtain a simple linear fit. The analysis concludes that the Urbach focus of *a*-Si:H does exist and is not biased by the Urbach rule itself. Nevertheless, we have also performed the same analysis using the extended Urbach rule, which does not predict the Urbach focus mathematically, resulting also in a good agreement with the existence of the constants E_0 and α_0. It is important to remark that the linear fits depicted in figure 5.1.16 actually predict an Urbach focus within a small region defined by the confidence of the fitting procedure. Therefore the extended Urbach rule allows the existence of the Urbach focus defined in such way. Before driving any further conclusions let us apply the same analysis on the materials studied here.

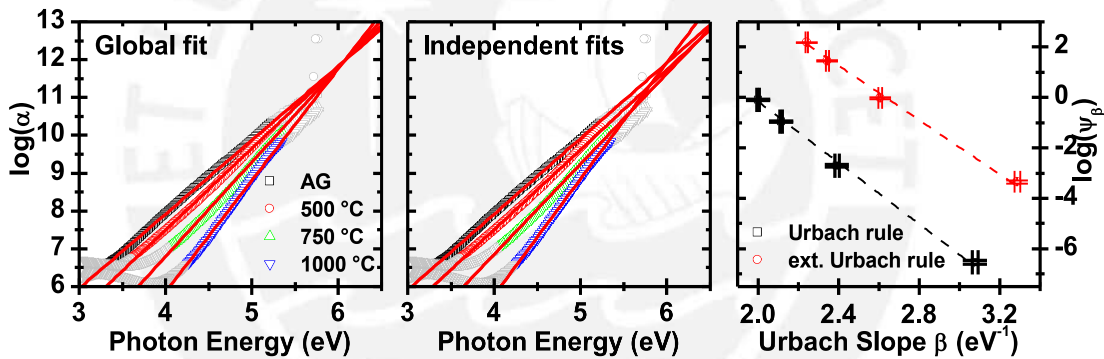

Figure 5.1.17. Global fit (a), linear independent fits (b) and linear relation between the intercept $\log(\psi_\beta)$ versus the Urbach slope β (c) of the *a*-SiN thin film after various annealing temperatures. The colored regions are the ones used for the fit.

Table 5.1.2: Urbach focus (E_F, α_F) and (E_0, α_0) obtained through a global fit and the independent fits of the Urbach region in the absorption coefficient of *a*-SiN.

a-SiN		**Global fit**	**Independent fits**
Urbach rule	$\log(\alpha_F)$	11.97 ± 0.06	12.01 ± 0.60
	E_F	6.07 ± 0.02 eV	6.08 ± 0.28 eV
Extended Urbach rule	$\log(\alpha_0)$	14.03 ± 0.06	14.22 ± 0.69
	E_0	5.33 ± 0.02 eV	5.40 ± 0.29 eV

Tesis publicada con autorización del autor
No olvide citar esta tesis
PUCP

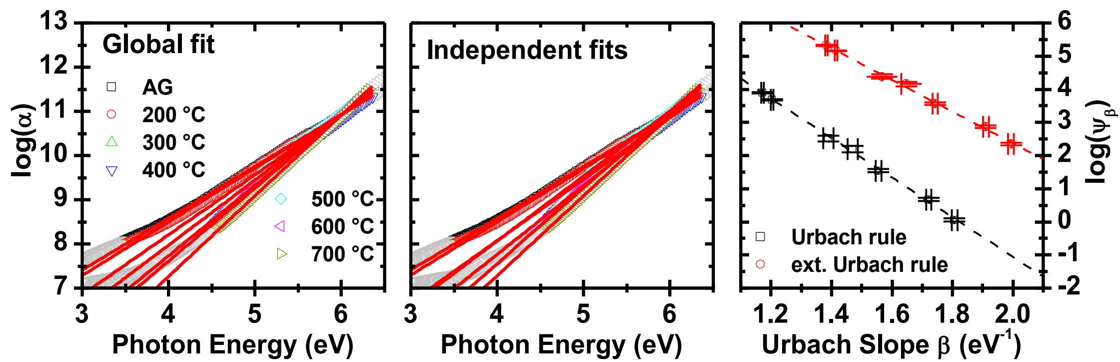

Figure 5.1.18. Global fit (a), linear independent fits (b) and linear relation between the intercept $\log(\psi_\beta)$ versus the Urbach slope β (c) of the a-AlN thin film after various annealing temperatures. The colored regions are the ones used for the fit.

Table 5.1.3: Urbach focus (E_F, α_F) and (E_0, α_0) obtained through a global fit and the independent fits of the Urbach region in the absorption coefficient of a-AlN.

a-AlN		**Global fit**	**Independent fits**
Urbach rule	$\log(\alpha_F)$	10.94 ± 0.02	10.87 ± 0.08
	E_F	6.01 ± 0.01 eV	5.97 ± 0.06 eV
Extended Urbach rule	$\log(\alpha_0)$	12.03 ± 0.02	11.92 ± 0.09
	E_0	4.84 ± 0.01 eV	4.77 ± 0.06 eV

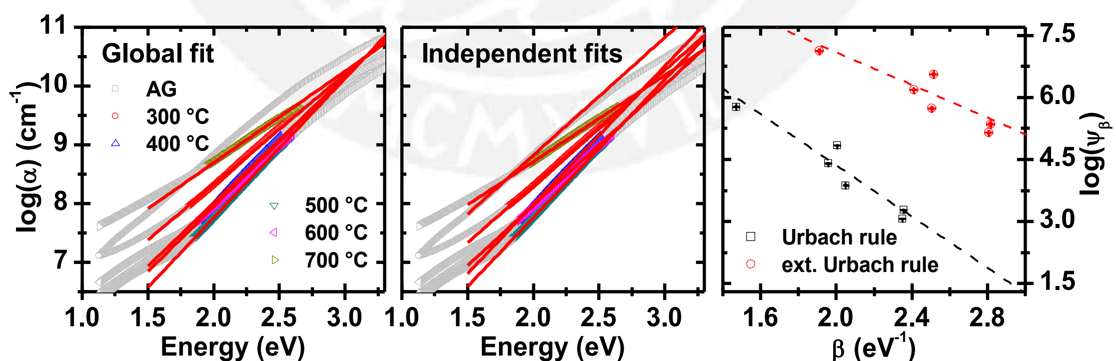

Figure 5.1.19. Global fit (a), linear independent fits (b) and linear relation between the intercept $\log(\psi_\beta)$ versus the Urbach slope β of a-SiC thin film after various annealing temperatures. The colored regions are the ones used for the fit.

Tesis publicada con autorización del autor
No olvide citar esta tesis
ET LUX IN TENEBRIS LUCET MCMXVII PUCP

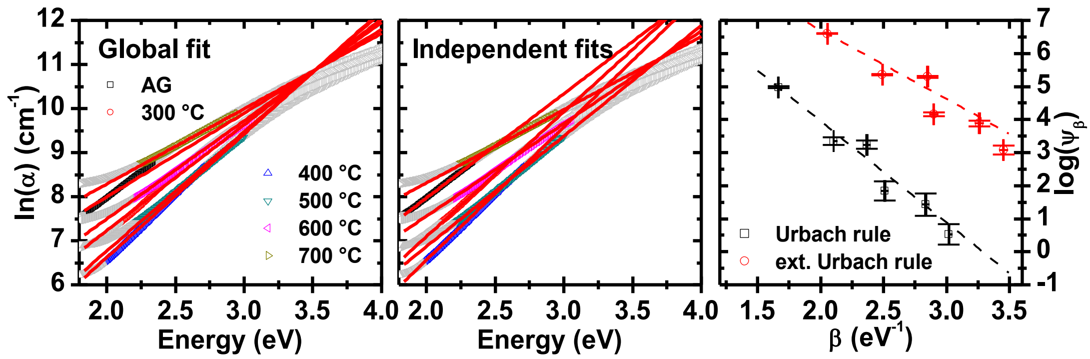

Figure 5.1.20. Global fit (a), linear independent fits (b) and linear relation between the intercept $\log(\psi_\beta)$ versus the Urbach slope β of the *a*-SiC:H thin film grown with 5 sccm H_2 during the deposition process after various annealing temperatures. The colored regions are the ones used for the fit.

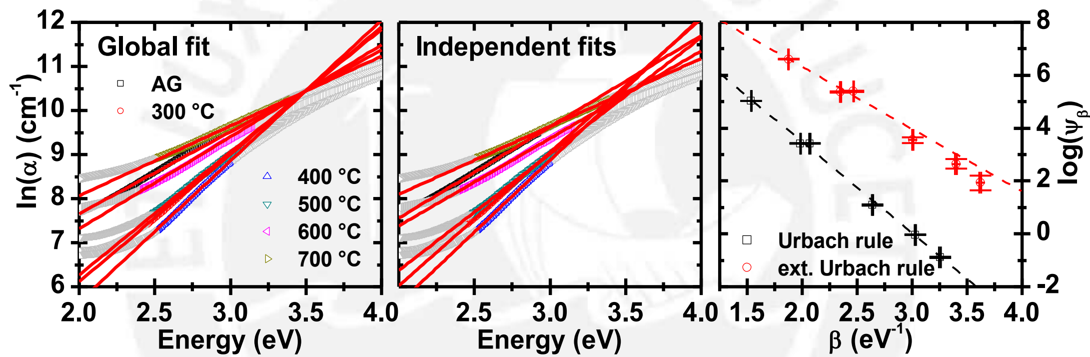

Figure 5.1.21. Global fit (a), linear independent fits (b) and linear relation between the intercept $\log(\psi_\beta)$ versus the Urbach slope β of the *a*-SiC:H thin film grown with 15 sccm H_2 during the deposition process after various annealing temperatures. The colored regions are the ones used for the fit.

Figures 5.1.17 and 5.1.18 depict the aforementioned analysis using the Urbach rule and the extended Urbach rule, for the *a*-SiN and *a*-AlN thin films, respectively. The results from the global an independent fits are listed in the tables 5.1.2 and 5.1.3 for these two materials. The analysis of *a*-SiC:H_x was performed for the 0 sccm, 5 sccm and 15 sccm hydrogen flux cases. This analysis is depicted in the figures 5.1.19, 5.1.20 and 5.1.21 and the results from the global and independent fits are listed in the table 5.1.4 for each case. Since the fits using the Urbach rule and the extended Urbach rule look very alike only the

Tesis publicada con autorización del autor
No olvide citar esta tesis
ET LUX IN TENEBRIS LUCET MCMXVII PUCP

former case is plotted. The linear relation between the intercept ψ_β and the Urbach slope β is plotted for both models.

Table 5.1.4: Urbach focus (E_F, α_F) and (E_0, α_0) for a-SiC:H$_x$ obtained through a global fit and the independent fits of the Urbach region of the absorption coefficient. The light grayed cells highlight the increase of E_0 with the hydrogen incorporation.

a-SiC:H$_x$		Global fit			Independent fits		
	H_2 flux	0 sccm	5 sccm	15 sccm	0 sccm	5 sccm	15 sccm
Urbach rule	$\log(\alpha_F)$	10.48 $\pm$ 0.02	10.89 $\pm$ 0.05	10.43 $\pm$ 0.01	10.55 $\pm$ 1.17	10.08 $\pm$ 0.47	10.38 $\pm$ 0.27
	E_F	3.15 $\pm$ 0.01 eV	3.52 $\pm$ 0.02 eV	3.49 $\pm$ 0.01 eV	3.09 $\pm$ 0.57 eV	3.06 $\pm$ 0.26 eV	3.45 $\pm$ 0.12 eV
Ext. Urbach rule	$\log(\alpha_0)$	11.72 $\pm$ 0.04	12.34 $\pm$ 0.02	11.83 $\pm$ 0.02	11.05 $\pm$ 1.54	10.88 $\pm$ 0.65	11.02 $\pm$ 0.32
	E_0	2.33 $\pm$ 0.01 eV	2.75 $\pm$ 0.02 eV	2.73 $\pm$ 0.01 eV	1.98 $\pm$ 0.62 eV	2.09 $\pm$ 0.29 eV	2.35 $\pm$ 0.16 eV

As observed from the above results, the E_0 energy value is fundamentally smaller than the Urbach focus energy coordinate E_F as expected after a close inspection of both models. In the case of a-SiN and a-AlN, the parameters (E_F, α_F) and (E_0, α_0) don't vary considerably when retrieving them either by using the global fit or the independent fits. On the other hand, in the particular case of a-SiC:H$_x$ notice that hydrogen incorporation has a measureable effect on these parameters. For instance the hydrogen incorporation increases the energy of E_0, see table 5.1.4. This effect accounts for the increase of the optical bandgap calculated previously as depicted in the figure 5.1.6. Furthermore, the fact that E_0 increases with the hydrogen incorporation strongly suggests the increase of the valence and conduction mobility edges separation. Such increase is a consequence of the passivation of localized states by hydrogen, resulting in a reduction of their occupation volume and has no effect on the Urbach tails as typically stated for this material [Zha92, Mag98, Kim02]. This behavior was treated in the previous section.

In summary, both equations the Urbach rule and the extended Urbach rule following the previous analysis predict equally the constant pairs (E_F, α_F) and (E_0, α_0) for the materials presented here without any biasing from the formulas. A plausible explanation

Tesis publicada con autorización del autor
No olvide citar esta tesis
ET LUX IN TENEBRIS LUCET MCMXVII PUCP

of this result is that the extended Urbach rule can be reduced to the Urbach rule always and only if there is a low dispersion of the Urbach slope and thus the Urbach focus region becomes sufficient small. The latter condition is found in most of the cases here shown. Therefore, the Urbach focus can be interpreted also as a small region and not necessarily a true constant [Gue13m]. Furthermore, there is actually still no agreement on the meaning of the Urbach focus [Cod05, Gue16]. Nevertheless, it is well accepted that the fundamental absorption and absorption edge contain information regarding the energy separation of the band-edges and the disorder driven band shrinking reflected in the Urbach tails, respectively [Mor99, Str91, Ada04]. Here, the extended Urbach rule provides direct information concerning the band-edges behavior not only through the Urbach energy $1/\beta$ but also through the band-edges gap E_0. For instance, in the case of a-SiC:H_x and increase of E_0 is measured due to the hydrogen dilution. This effect is also reflected in the Urbach focus. Finally, independent fits using the DiLog model provide information of the behavior of the parameters α_0, E_0, β versus annealing temperature as it was shown for the case of a-SiC:H_x, showing that even when the pair (E_0, α_0) are independent of the Urbach energy they are subjected to a thermal-induced modification [Gue16].

5.2 Tb^{3+} doped SiN, AlN and SiC:H light emission properties

The present work studies systematically the optical properties and light emission features of Tb doped SiN, AlN and SiC thin films. The main objective is to correlate the effect of thermal annealing treatments on the optical properties and light emission features when doped with Tb. In the following sections we will review the emission of the Tb doped amorphous SiN, AlN and SiC:H layers at room temperature under band-to-band electron excitation (10 kV) and sub-bandgap photon excitation (488 nm). In order to assess the different excitation pathways involved PLE spectroscopy measurements were performed in the AlN:Tb and SiC:H:Tb samples. Then a systematic analysis of the concentration quenching effect of Tb doped poly-crystalline AlN and SiC:H is presented. In the subsequent section the optical activation of the Tb ions upon isochronical thermal annealing treatments is presented and contrasted with the bandgap and Urbach energy evolution of the host matrix upon similar treatments. Such activation is also evaluated for

Tesis publicada con autorización del autor
No olvide citar esta tesis
ET LUX IN TENEBRIS LUCET MCMXVII PUCP

different concentrations. A systematic study of the thermal activation and its effect on the shape of the concentration quenching curves is reported for the case of the Tb doped amorphous SiC:H thin films. Finally in the last section, temperature dependent PL and CL measurements are presented in order to shed some light on the excitation mechanisms involved in the Tb^{3+} excitation.

The emission

The emission of Tb^{3+} doped amorphous wide bandgap semiconductors like SiN, AlN, SiC, GaN has been studied by different excitation means [Lu02, Nyk06, Wei06, Ada07, Zan07, Zan12]. Features of the emission spectra, e.g. relative intensity of the emission lines and crystal field splitting vary depending on the chemical and structural properties of the host, temperature and excitation means.

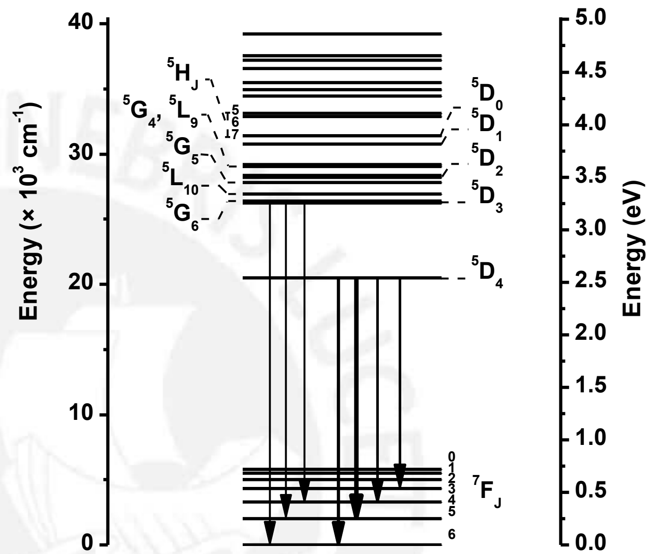

Figure 5.2.1. Electronic transitions typically observed in Tb^{3+} doped materials. The thickness of the arrows corresponds to typical relative transition rate.

Figure 5.2.1 depicts the energy levels configuration of Tb^{3+} and their typical observed emission transitions. The arrows thicknesses account for the relative intensities observed in the materials here studied. The $^5D_4$ to $^7F_5$ transition is the most intense line, as observed in figure 5.2.2. The RE related relative intensity between the different transitions is host and excitation source dependent [Lu02, Nyk06, Wei06, Ada07, Jam11, Ben12, Gue13, Gue15]. For instance, in some cases even a blue emission corresponding to the second excited level decay $^5D_3 \rightarrow {}^7F_{4,5,6}$ is observed with an intensity comparable or even greater than the green emission corresponding to the first excited state decay $^5D_4 \rightarrow {}^7F_{4,5,6}$ upon impact excitation [Ada07, Loz07, Ben12]. Such blue emission may not be observed even upon photon excitation in the same sample [Ben12, Gue13q]. These

Tesis publicada con autorización del autor
No olvide citar esta tesis
PUCP

features for instance make the study of the optical emission properties of Tb doped amorphous wide bandgap semiconductors a difficult task.

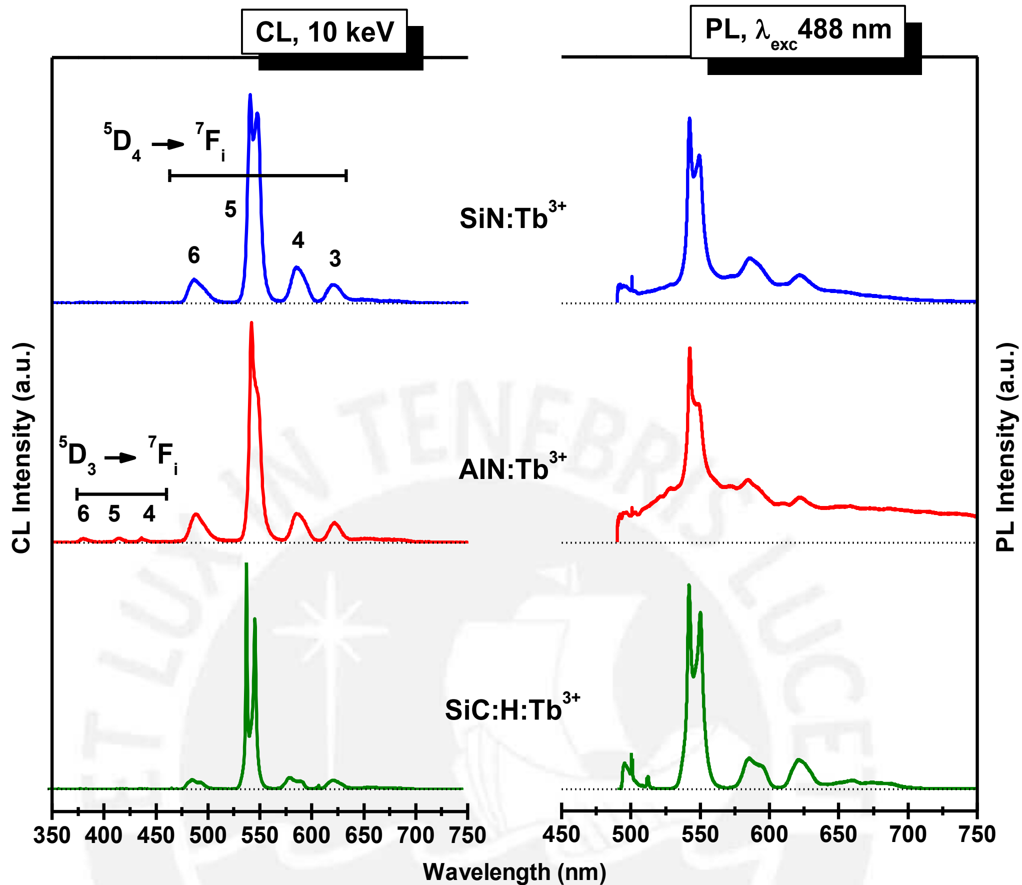

Figure 5.2.2. PL spectra (right) excited upon an Ar laser (488 nm) and CL spectra (left) excited by an electron beam of a SEM (energy 10 keV and current 10 nA) of Tb^{3+} doped SiN, AlN and SiC:H. The measurements were performed at room temperature and after an annealing treatment for 15 min at 900°C in an argon atmosphere.

The recorded spectra of the Tb doped SiN, AlN and SiC:H films exhibit quite similar emission features, see figure 5.2.2. A closer look of the main electronic transition peak ($^5D_4$ to $^7F_5$) reveals a crystal field origin splitting of about 30 meV for the three materials. This splitting becomes more evident at low temperatures since the peaks become sharper due to the freeze out of phonons, see figure 5.2.3. The evolution of the emission and the splitting under different temperatures will be presented in the last subsection of this chapter. In figure 5.2.3 and example of the resolved splitting is shown for the main transition peak in the case of the SiN and AlN samples upon electron excitation.

Tesis publicada con autorización del autor
No olvide citar esta tesis
PUCP

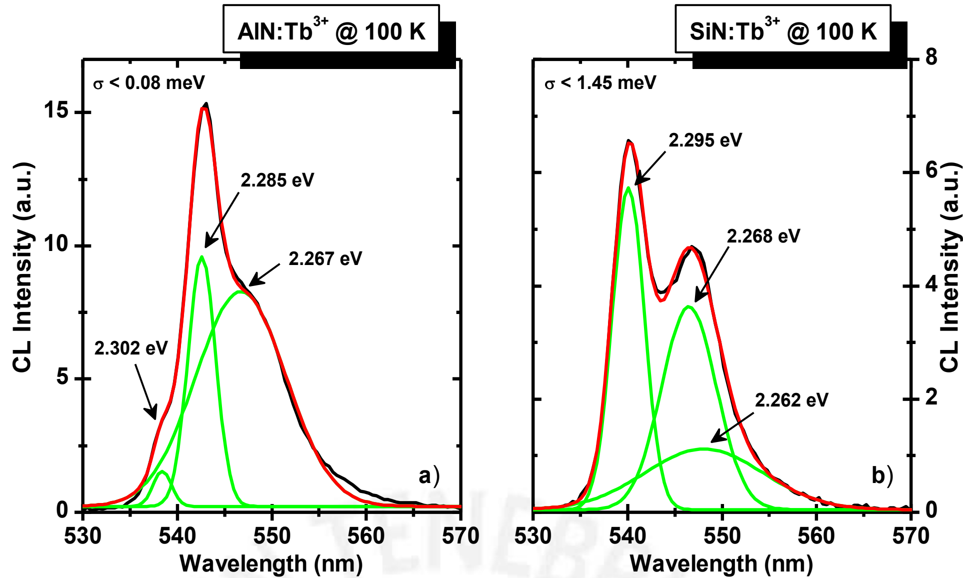

Figure 5.2.3 $^5D_4$ to $^7F_5$ emission line of Tb doped AlN (a) and SiN (b) at 100 Kelvin upon electron excitation. The crystal field splitting intensities exhibit different features for different hosts and temperatures. The peak-widths are lower than 0.08 meV and 1.45 meV in the AlN and SiN samples, respectively.

It can be noted from figure 5.2.2 that upon photon excitation a background emission corresponding to the host matrix is recorded in the SiN and AlN samples with an exception of the SiC:H layers. This background emission is usually attributed to the radiative recombination of electron hole pairs in electronic defects different from the RE. The excitation energy in this case is below the bandgap energy value (λ_{exc} = 488 nm, $E_g \geq 2.54$ eV), so we may actually exciting electronic defects directly. On the other hand, no background emission is recorded upon the electron excitation case (CL), suggesting that a more efficient excitation path takes place. Furthermore, the PL of Tb doped hydrogenated SiC does not exhibit any background emission upon photon excitation even though SiC has a lower bandgap than SiN and AlN. Figure 5.2.4 depicts the PL-spectra of *a*-SiC, *a*-SiC:H and *a*-SiC:H:Tb^{3+} samples annealed at 800°C. As it was reviewed in the last section, the hydrogen dilution on SiC effectively passivates dangling bonds with the additional consequence of the bandgap increase by widening the mobility edges energy separation. Therefore, the 488 nm photons (~2.53 eV) have a higher chance to excite electrons in the bandtails of SiC than of SiC:H. In other words, the *a*-SiC:H seems to be transparent to the 488 nm photons in comparison to the undiluted *a*-SiC.

Tesis publicada con autorización del autor
No olvide citar esta tesis
ET LUX IN TENEBRIS LUCET MCMXVII PUCP

It is widely accepted that RE ions form complexes with defects in the host matrix to which they interact with [Jan03, Loz07, Zan09, Zan12]. For instance, the RE-structured isovalent trap model (RESI) has been thoroughly studied in the crystalline AlN doped with different REs [Loz07]. In the amorphous case different host defect related RE excitation energy transfer mechanisms have been reviewed [För59, Fuh97, Jan03, Che10, Zan12]. Nonetheless, the fact that there is a host matrix emission directly below the transition lines of the Tb^{3+} ions, strongly suggest the possibility of a defect related energy transfer pathway between the Tb ions and electronic defects [Jan03, Nyk06]. Moreover, it is also well accepted that the excitation with 488 nm photons of an Ar-ion laser can excite the Tb ions directly by the resonant excitation of the ground state $^7F_6$ to the first excited level $^5D_4$. Therefore if an energy transfer pathway between the Tb ions and electronic defects exists, a back transfer process is also possible [Jan03, Che10, Zan12, Gue13, Gue15]. This behavior, as we will see in the last section, can be monitored by the effect of the sample temperature on the RE light emission intensity.

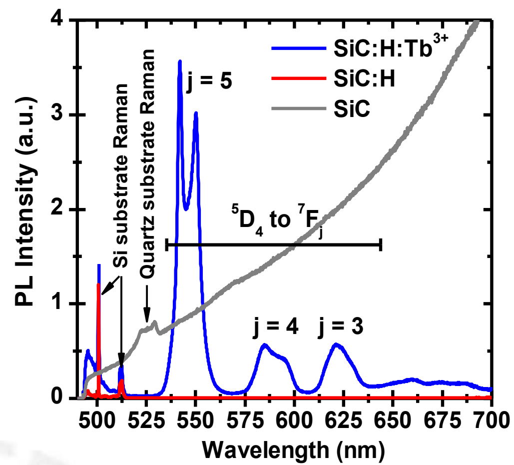

Figure 5.2.4. PL spectra of Tb doped and undoped amorphous SiC:H and a reference SiC thin films annealed at 800°C.

So far, from the shown spectra, some questions arise. First, what suppresses the radiative electronic recombination in a defect and/or increases the probability of a radiative electronic transition in the REs, therefore not exhibiting a background emission with an intensity comparable to the RE as already reported for example in Er^{3+} doped a-SiO_x:H [Jan03]?. Second, why then the Tb doped amorphous SiC:H samples do not show any background even when the SiC:H has a lower bandgap than AlN and SiN?. And last, if there is an energy transfer pathway between electronic defects and the Tb ions, why there is no background emission in the CL spectra?. A glance to the answer of the first question will be given in the last section through temperature dependent measurements analysis.

Tesis publicada con autorización del autor
No olvide citar esta tesis
ET LUX IN TENEBRIS LUCET MCMXVII PUCP

Concerning the second one, the fact that the hydrogen passivates defects seems to be a sufficient explanation, however a systematic characterization and understanding of the relation between the emission intensity and host defect density is still necessary. For the last question, the overall behavior surely is the result of an overlap of different excitation mechanisms, which may compete depending on the excitation and host properties. Before driving any further discussion we first shortly recall the different excitation processes for RE doped materials.

The excitation of RE ions can be generally divided in two categories, direct and indirect excitation mechanisms. The direct excitation process occurs with the selective excitation of $4f^n$ electrons in the core of the RE. This excitation can be resonant, by photons with an energy matching an allowed electronic transition of the RE or by the direct collision with hot electrons, e.g. CL and EL. On the other hand, the indirect excitation process occurs by the energy transfer from host mediated centers to the $4f^n$ electrons. Several non-resonant processes can take place in which the host is excited first. These indirect mechanisms involve the energy transfer of the recombination energy of electron-hole pairs to nearby RE ions. For instance, the excitation of an electronic defect in which the recombination occurs and then the energy is transferred to the RE is not an uncommon process. In the latter case, a defect related Auger effect (DRAE) may well play a key role in some RE doped amorphous semiconductors [Fuhs97]. In general, because of the excess of positive charge, trivalent RE ions (as donors) form with acceptors donor-acceptor pairs (DAP) or larger complexes. Under excitation, an electron is transferred from and orbital localized on the acceptor to an orbital on the RE ion. Afterwards, the DAP recombines transferring the energy to the RE ion [Bra10]. This excitation scheme is the most efficient non-radiative indirect excitation mechanism. The recombination rate and the energy transfer efficiency of the DAP depend on the spatial proximity between the RE and the acceptor and the spectral overlap between the DAP and the RE absorption spectra.

Tesis publicada con autorización del autor
No olvide citar esta tesis
ET LUX IN TENEBRIS LUCET MCMXVII PUCP

Other indirect non-radiative RE excitation paths are possible. These involve the energy transfer of the electron-hole recombination to the RE as bound excitons (BE). Additionally, free carriers can be trapped by the RE or a nearby defect and recombine without the previous formation of an exciton. The RE excitation mediated by BEs is an extensively discussed excitation mechanism in several RE doped semiconductors [Loz07, Bra10]. REs can also be excited by a ligand-to-metal charge transfer (LMCT) changing for a moment the valance state of the RE [Dor03]. The LMCT transition can be described as the promotion of an electron from the valence band to a RE ion changing its valence state RE^{3+} to $RE^{2+} + h$. Even though the hole is delocalized over the ligand, is also bound to the RE^{2+} core forming a charge transfer state (CTS). If the CTS is close in energy to the 4f energy levels of the RE^{3+} an intersystem crossing to the 4f states will happen being followed by the $4f \rightarrow 4f$ emission, see figure 5.2.5. However, in order to this process to be efficient, the excited state of the RE^{3+} ion has to lie below the $RE^{2+} + h$ CTS. Unfortunately, in the case of AlN, GaN and other wide bandgap semiconductors the Tb divalent ground states lie within the conduction band (resonant state), and thus the CTS is not stable since the electron will promptly autoionize in the conduction band [Dor08]. A summary of these distinct excitation mechanisms can be found in [Bra10].

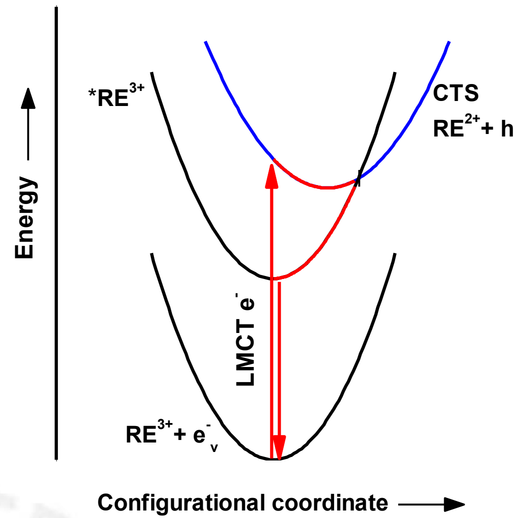

Figure 5.2.5. Configuration coordinate diagram of the excitation by LMCT and CTS. After excitation, an electron from the valence band is promoted into the CTS by a LMCT process. Then a crossover of the CTS with an excited state of the RE^{3+} takes place leading to the subsequent decay.

Tesis publicada con autorización del autor
No olvide citar esta tesis
PUCP

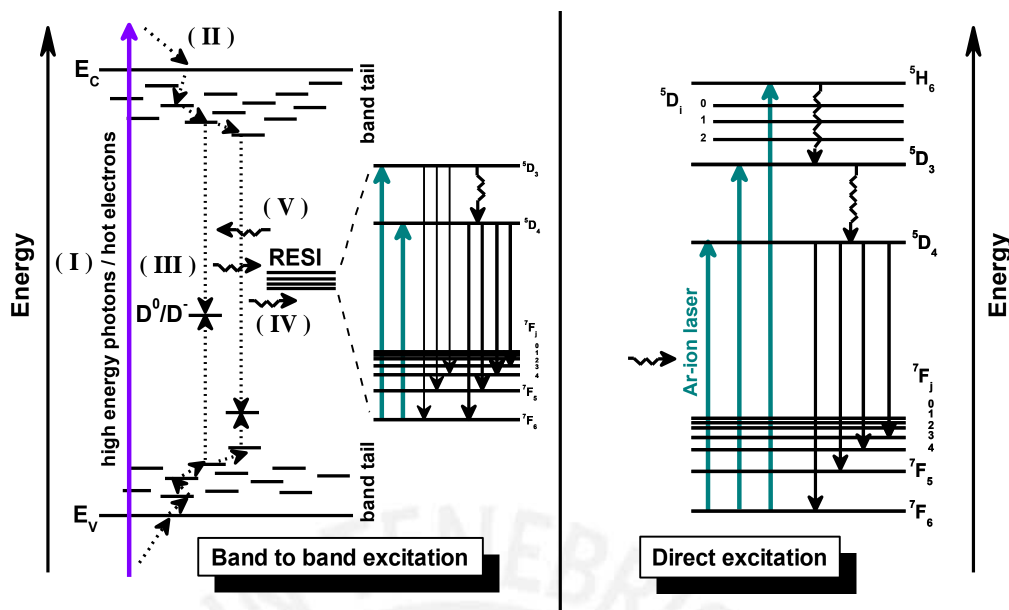

Figure 5.2.6. Possible excitation processes. Left: band to band excitation and generation of electron-hole pairs (I). Thermalization of the charge carriers which end up in the band tails edge (II). An electron from the conduction band-tail is captured by a neutral dangling bond (D^0) and transfers its energy to the RESI (III). Excitation of the RESI by the recombination of an electron-hole pair in deep localized band tail states (IV). Energy back transfer process from the RESI to the host matrix (V). Right: resonant direct excitation of the $^7F_6$ to the $^5D_4$ energy level via an Ar-ion laser, or of the $^7F_6$ to the $^5D_3$ as shown in the PLE spectra of figure 5.2.7. The energy levels depicted here are just a schematic representation. For energy values of these levels please see figure 5.2.1.

As we already discussed in the present work we performed sub-bandgap excitation by using photons with 488 nm wavelength of an Ar-ion laser. The band-to-band excitation was performed by an electron beam with 10keV electrons. While the former excitation source can excite electrons from the $^7F_6$ level to the $^5D_4$ level directly as depicted in the right scale of the figure 5.2.6, the latter excites band-to-band electrons leading to several possible events before the excitation of the RE. The left diagram of figure 5.2.6 depicts these events excluding the direct impact excitation with hot electrons. (I) First, an electron hole pair is formed by the matrix excitation with energy above the necessary threshold to produce the electronic transition. (II) Second, he charge carriers thermalize and lose energy by a cascade of multi-phonon process ending up in the band-tails states. (III) Then it is possible that an electron from the conduction band tail is trapped by a neutral dangling bond and then transfers its energy to the RESI through a DRAE [Jan03,

Tesis publicada con autorización del autor
No olvide citar esta tesis
ET LUX IN TENEBRIS LUCET MCMXVII PUCP

Fuh97]. (IV) Another possibility is that the RE is excited by a dipole mediated resonant energy transfer after the recombination of an electron-hole pair in deep localized band tail states [Jan03, Gue15]. (V) Finally, after the RE excitation, there exist the possibility of an energy back transfer process, which increases the probability of a non-radiative recombination.

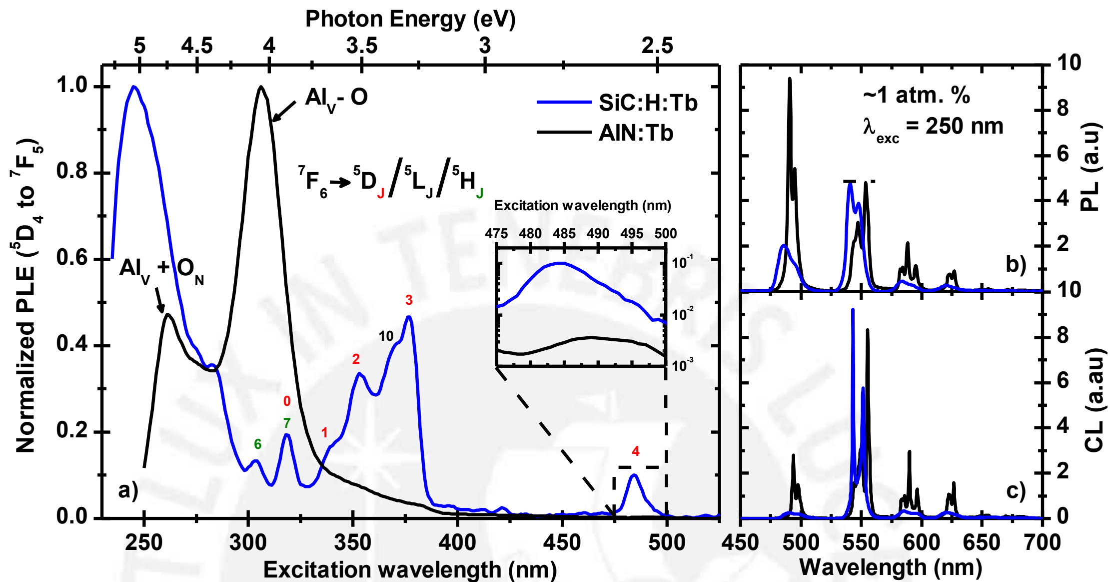

Figure 5.2.7. PLE spectra of Tb doped polycrystalline SiC:H and AlN annealed at 1000°C, λ_{emi} = 545 nm (a). Normalized PL under 250 nm excitation wavelength of the same aforementioned samples (b). Comparable CL at 20 keV excitation energy, 10 nA and 50 nA beam currents for the SiC:H and AlN cases, respectively (c). The distinct Tb related transitions are denoted by the numbers in colors.

In order to have a glance of the possible defect related energy transfer pathways, photo luminescence excitation spectra (PLE) measurements were performed on Tb doped amorphous SiC:H and polycrystalline AlN annealed at 1000°C with about 1 at.% of Tb. Notice that at these annealing temperatures TEM reveals a polycrystalline/amorphous structure in the SiC:H samples (see figure 5.1.13). Figure 5.2.7 depicts the PLE spectra along with the PL and CL spectra of the same samples. Different features are summarized below:

i. The $^5D_4$ to $^7F_6$ transition is stronger than the $^5D_4$ to $^7F_5$ in the PL spectrum of AlN:Tb (λ_{exc} = 250 nm). This is not the case upon electron excitation of the same sample, see figure 5.2.7.

Tesis publicada con autorización del autor
No olvide citar esta tesis
PUCP

ii. The $^7F_6$ to $^5D_4$ direct excitation of the Tb ions is observed as a small peak at around 488 nm for both samples in the PLE spectrum, see the inset graph of figure 5.2.7. This direct selective excitation seems to be much stronger in the SiC:H case than the AlN one.

iii. The SiC:H sample exhibits the $^7F_6$ to $^5D_3$ direct excitation at around 376.5 nm (~3.29 eV) in the PLE spectrum just below the bandgap ~3.33 eV. Whilst the PLE spectrum corresponding to the AlN sample shows just a small shoulder at this wavelength region.

iv. The direct excitation of the $^5L_{10}$, $^5D_{2,1,0}$ and $^5H_{6,7}$ levels are noted in the PLE spectrum of the SiC:H layer and not present in the AlN one. This result reveals the effective excitation of the Tb ions in the SiC:H in contrast to the AlN host.

v. The AlN sample exhibits two dominant peaks in the PLE spectrum. These are observed at 306.1 nm (~4.05 eV) and 260.1 nm (~4.76 eV). Lozykowsky reported the PLE of AlN:Tb monitoring at $\lambda_{emis} = 491$ nm ($^5D_4$ to $^7F_6$ transition) [Loz07], exhibiting the same peaks in agreement with the present result.

Concerning the first feature (i), these relative intensities are typically observed in crystalline and polycrystalline annealed Tb doped AlN upon sub-bangap photo excitation [Lu02, Ada07, Loz07, Ben13] but not in amorphous annealed Tb doped AlN upon the same excitation means [Men06, Wei06, Gue15]. Lozykowsky suggested that this feature may support the exciton mediated energy transfer to the Tb ions [Loz07]. However, under sub-bandgap excitation Tb doped AlN exhibits typically a host related background emission, supporting the lack of an effective energy transfer from the host to the Tb ions.

The direct photon resonant excitation of the $^7F_6 \rightarrow {}^5D_4$ transition with 488 nm photons has actually a very low cross section. Therefore, the light emission efficiency concerning solely this mechanism should be very low. This is observed for instance in the AlN case by the fact that the resonant direct excitation is barely noticeable. In contrast to these observations, SiC:H PLE exhibits the energy corresponding to the $^5D_{4,3,2,10}$, $^5L_{10}$, $^5H_{7,6}$ Tb^{3+} levels, see features (ii), (iii) and (iv). The latter observation suggests that possibly the excitation of the SiC host reaches the Tb ions in some other way (since the direct

Tesis publicada con autorización del autor
No olvide citar esta tesis
ET LUX IN TENEBRIS LUCET MCMXVII PUCP

excitation in the AlN host is not appreciable), perhaps through other electronic defects and not only the resonant direct excitation of the Tb ions. As we will see in the last section this result is supported by temperature dependent measurements.

Regarding the last feature (v), these two peaks have been also reported by Lozykowski et al [Loz07] in Tb doped AlN. Lozykowski argues that these two broad peaks are the result of the creation of bound excitons to different RESI trap clusters. However, these peaks can also be explained by the direct excitation of electronic defects and the subsequent energy transfer to the Tb ions. For instance, these defects could be the aluminum vacancy with one oxygen attached at ~4 eV ($Al_V - O$) [Bas09] and oxygen-vacancy complexes in the range of 4.0 to 4.9 eV ($Al_V + O_N$) [Bic10]. The peak around 4.8 eV is also present in the PLE spectra of AlN doped with Pr^{3+}, Eu^{3+} and Tm^{3+} supporting the host nature of this electronic defect [Loz07].

In summary, the fact that even after the direct excitation of the second excited level $^5D_3$ in the Tb doped SiC:H case, see figure 5.2.7, no comparable emission from the $^5D_3$ level but from the $^5D_4$ is observed, strongly supports the possibility of a non-radiative transition or energy migration from the $^5D_3$ to the $^5D_4$ levels. The energy difference between these energy levels is about 0.75 eV and therefore a multi-phonon process is incapable to explain the observed efficiency. A cross-relaxation between two nearby Tb ions is another possible energy down-conversion mechanism. As depicted in figure 5.2.8, the close energy match between the $^5D_3 \rightarrow {}^5D_4$ and $^7F_6 \rightarrow {}^7F_0$ makes this process highly effective. This would explain why the $^5D_4$ related emission lines are considerably more intense than the $^5D_3$ related ones after exciting with sufficient energy. Additionally, in contrast to the SiC:H case, polycrystalline Tb doped AlN doesn't exhibit a strong resonant excitation of the $^7F_6$ to $^5D_3$ energy levels nor the $^7F_6$ to $^5D_4$ direct excitation in the PLE spectrum. The latter behavior could be attributed to the energy back transfer to deep localized band tail states with a subsequent non-radiative recombination or even simply the lack of host mediated centers that could effectively transfer the energy to the Tb ions. Finally, it is well accepted that at these concentrations the interaction between Tb ions is possible, see figure 5.2.8. The probability of non-radiative transitions after the

Tesis publicada con autorización del autor
No olvide citar esta tesis
ET LUX IN TENEBRIS LUCET MCMXVII PUCP

direct excitation of the $^5D_3$ or $^5D_4$ levels can be enhanced by the energy migration from ion to ion. The host excitation and the subsequent energy transfer to the Tb ions is still efficient enough to produce the observed emission lines in SiC:H.

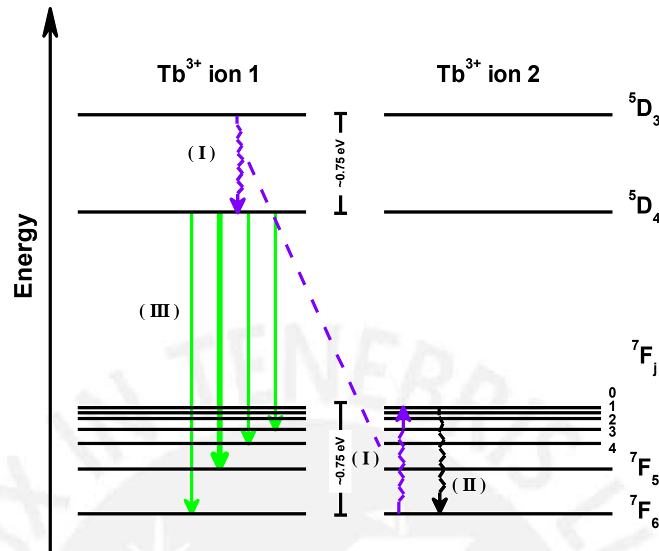

Figure 5.2.8. Cross relaxation process involving two nearby Tb^{3+} ions. An electron in the second excited level $^5D_3$ drops to the first excited energy level $^5D_4$. The energy of such transition is transferred non-radiatively to a nearby Tb^{3+} ion promoting an electron to the $^7F_0$ level (I). The excited electron in the $^7F_0$ level will decay non-radiatively (II). While the electron in the $^5D_4$ level will continue with the process decaying to one of the ^7F_i levels radiatively or transferring its energy to another RE or to the host matrix (III).

Concentration quenching

As we already reviewed in the last section, the ion interactions are a possibility even at atomic concentrations about 1%. The probability of these interactions to happen is proportional to the RE concentration (inverse to the RE interdistance) in the host matrix. Furthermore, RE ions can create pairs and higher clusters. These clusters can be formed between RE ions and other impurities, e.g. oxygen or transition metals [Jan03, Loz07] and they occur more frequently than predicted by a statistical model [Loz07]. The concentration quenching of the light emission of RE doped materials is a result of the tendency of REs to interact with each other. While the light emission quenching by the concentration is well accepted, there are only few characterizations of this process under different excitation sources. Recently, S. Chen et al proposed a suppression of the

Tesis publicada con autorización del autor
No olvide citar esta tesis
PUCP

concentration quenching effect in Er doped GaN through CL upon a high excitation power density [Che10].

In the following section, we report the behavior of the CL and PL spectra of Tb doped SiC:H and AlN thin films under different Tb concentrations. The Terbium concentration was measured through two complementary techniques. In the case of the AlN:Tb films, Inductively Coupled Plasma Optical Emission Spectroscopy (ICP-OES) which detects only the metal elements, and X-ray Photoelectron Spectroscopy (XPS) that renders the concentration of all constituents, were performed[2]. In the case of the Terbium doped SiC:H samples, Fourier Transform Infrared Spectroscopy (FTIR) was used. This technique allows the calibration of the integrated area of the Si-C and Si-C:H_n vibrational modes with various XPS measurements. The PL spectra of the AlN samples in this section were measured using 250 nm excitation wavelength from a monochromatized Xenon lamp. The PL spectra of the SiC:H samples were taken under 488 nm excitation from an argon laser. All the signals were measured in a reflection setup. More details can be found in Chapter 4 and [Ben13].

Figures 5.2.9 and 5.2.10 depict the normalized integrated PL and CL intensities, respectively of the Tb^{3+} doped SiC:H and AlN samples annealed at 1000°C versus different doping concentrations. The calculation of the Tb ions mean distance from the atomic percentage concentration can be found in the appendix A.4. Two regions can be identified in these figures. First, the light emission intensity in the low concentration region increases linearly with the Tb amount. As we will see in the next section, the slope of this linear growth varies with the RE activation degree. Second, the light emission in the high concentration region shows an exponential decay. This decay is attributed to the increased probability of a non-radiative electronic transition due to the interaction between the Tb ions. This interaction becomes stronger when the mean ion inter distance is reduced. The energy transfer probability can be described by an electrostatic dipole-dipole interaction, i.e. Förster's approach [För46]. Dexter generalized the theory to higher-order interactions, including a quantum mechanical exchange interaction [Dex53].

[2] These measurements were performed by the group of Prof. H. P. Strunk of the University of Stutgart in 2012 [Ben13, Gue13].

Tesis publicada con autorización del autor
No olvide citar esta tesis
PUCP

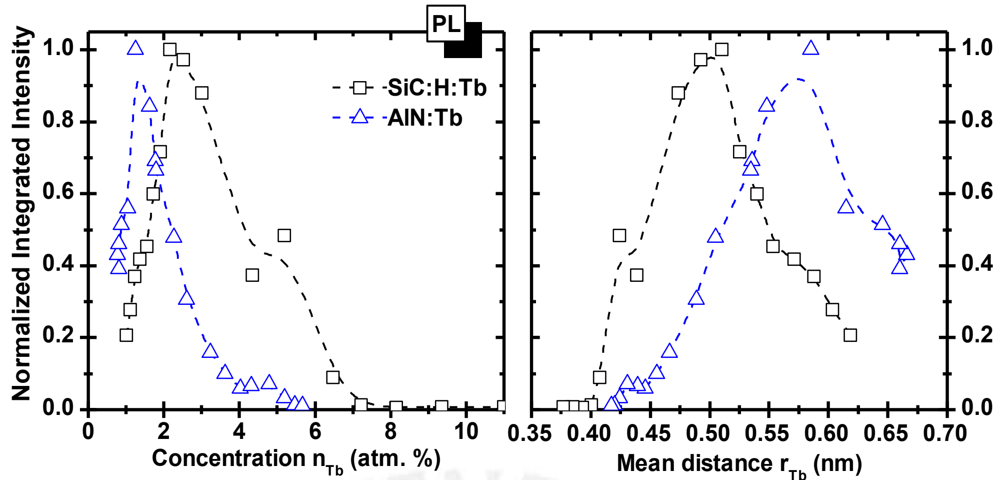

Figure 5.2.9. Normalized integrated PL intensity of the $^5D_4$ to $^7F_6$ emission line of Tb doped SiC:H and AlN thin films versus different doping concentrations (left) and Tb ions mean inter-distance (right).

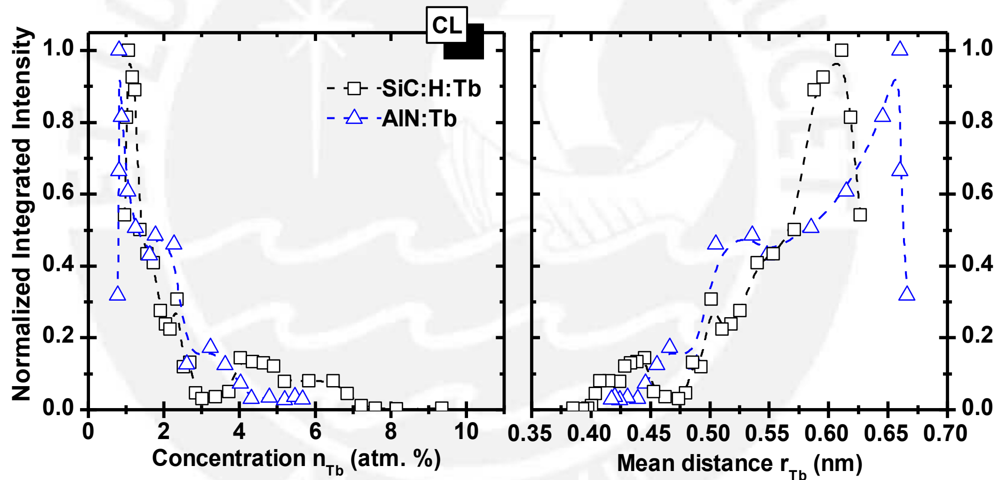

Figure 5.2.10. Normalized integrated CL intensity of the $^5D_4$ to $^7F_6$ emission line of Tb doped SiC:H and AlN thin films versus different doping concentrations (left) and Tb ions mean inter-distance (right).

The maximum observed intensity is shifted to lower concentrations upon electron excitation for both Tb doped AlN and SiC:H samples. From about 3% down to ~1.2% in the SiC:H samples and from ~1.5% to 1% in the AlN samples. The exponential decay rate (x_0) is faster upon electron excitation than upon photon excitation for the SiC:H samples while is slightly slower upon electron excitation than photon excitation in the AlN case (see figure 5.2.11 and table 5.2.1).

Tesis publicada con autorización del autor
No olvide citar esta tesis
ET LUX IN TENEBRIS LUCET MCMXVII PUCP

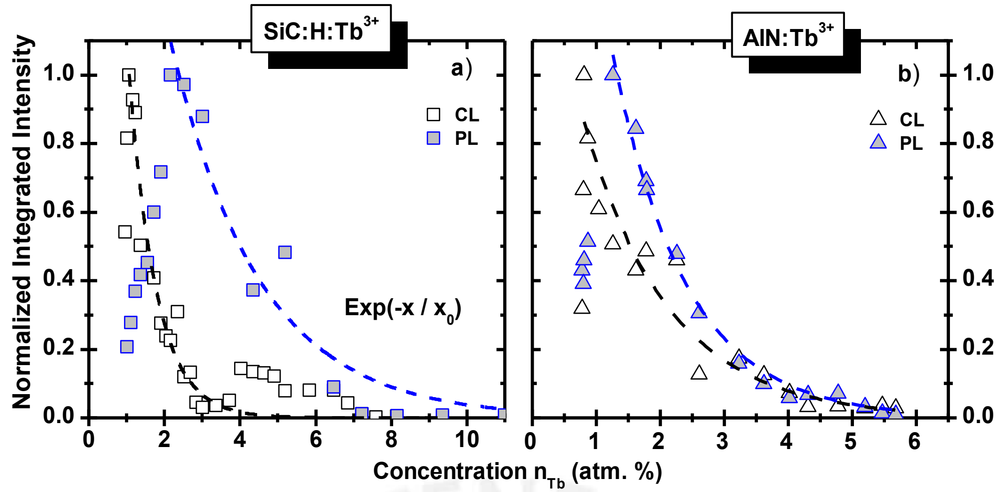

Figure 5.2.11. Normalized integrated CL and PL intensities of Tb doped SiC:H annealed at 1050°C (a). Normalized integrated CL and PL intensities of Tb doped AlN annealed at 1000°C (b). Dashed lines are simple exponential decay fits with decay rates x_0 summarized in table 5.2.1.

Table 5.2.1: decay rates of the PL and CL concentration quenching curves shown in the figure 5.2.9.

Excitation	Host	x_0 (atm. %)
PL	AlN	1.14 ± 0.10
	SiC:H	2.33 ± 0.27
CL	AlN	1.33 ± 0.12
	SiC:H	0.71 ± 0.07

The shape of the curves shown in the figure 5.2.11 can be approximately described by the equation 5.2.1 which is the result of a two levels rate equation model. Here n_{Tb} denotes the Tb atomic concentration. P_{int} is the interaction probability between luminescent centers. A and B are constants that depend on the excitation probability, Einstein coefficient and the non-radiative transitions probability. The derivation of the equation 5.2.1 can be found in section 3.2 (see equation 3.2.57).

$$I(n_{Tb}) = \frac{A \times n_{Tb}}{1 + B \times P_{int}(n_{Tb})} \quad (5.2.1)$$

Even after annealing the samples in similar processes, the activation degree may not be necessarily the same. The average environment of the Tb ions may differ from matrix to

Tesis publicada con autorización del autor
No olvide citar esta tesis
PUCP

matrix. For instance, a simple Monte Carlo simulation can demonstrate how the RE activation degree affects the concentration quenching curves. For this we assume the following:

i) Two interacting REs have a probability to lose the energy by a non-radiative transition. In this simulation the probability of losing the energy after the interaction is one. In this way we neglect the effect of the intrinsic host electronic features. Nonetheless, the simulation can be extended to several energy transfers before reaching a sink.
ii) An optically not active RE is not able to participate in an energy migration process. Therefore, a not active RE not only does not emit light but cannot interact with other REs. If a RE is not optically active, it is reasonable to assume that the electronic transitions involved are parity forbidden due to the lack of the appropriate symmetry.
iii) The host matrix non-radiative paths are the same independently on the RE concentration or activation degree. The quenching is solely influenced by the RE interaction i.e. by the RE concentration and activation degree.

We performed this simulation by distributing the REs randomly in a 2D matrix. Notwithstanding, this simulation can be easily extended to three dimension systems [Ben13p]. For the sake of plainness and minimal computational resources the matrix sizes used were 50 by 50 atomic cell units (c.u.). Thus, the interaction probability at short range distances is given by the equation 5.2.2, obeying the Dexter's approach for the interaction of ions [Dex53]. However, the exponential interaction probability presented in the equation 5.2.2 is normalized to a maximum interaction radii, given by $r_{max} = 25\ \mathrm{c.u.}$ The minimum distance is $r_{min} = 1\ \mathrm{c.u.}$ and the used exponential decay rate was $r_0 = 10\ \mathrm{c.u.}$ Any two REs at the minimum distance interact ($P_i = 1$), while any two REs separated a distance equal or greater than r_{max} do not interact ($P_i = 0$). The simulated intensity is then calculated by counting the number of active and not interacting REs ions in a finite matrix, see figure 5.2.12. The procedure is repeated 500 times for each activation degree and then simply averaged.

Tesis publicada con autorización del autor
No olvide citar esta tesis
ET LUX IN TENEBRIS LUCET MCMXVII PUCP

$$P_i(r) = \frac{e^{-r/r_0} - e^{-r_{max}/r_0}}{e^{r_{min}/r_0} - e^{-r_{max}/r_0}} \qquad (5.2.2)$$

Figure 5.2.12 depicts the variation of the shape of the quenching curves upon different activation degrees according to the above described simulation. Notice the shift of the maximum achievable intensity upon increasing the RE activation degree. The linear slope in the low concentration region increases with the activation degree while the exponential decay becomes sharper. This behavior reflects a competition between the number of active light emitting centers which are also available for interaction and therefore not only enhancing the total light emission but also quenching it after a critical concentration.

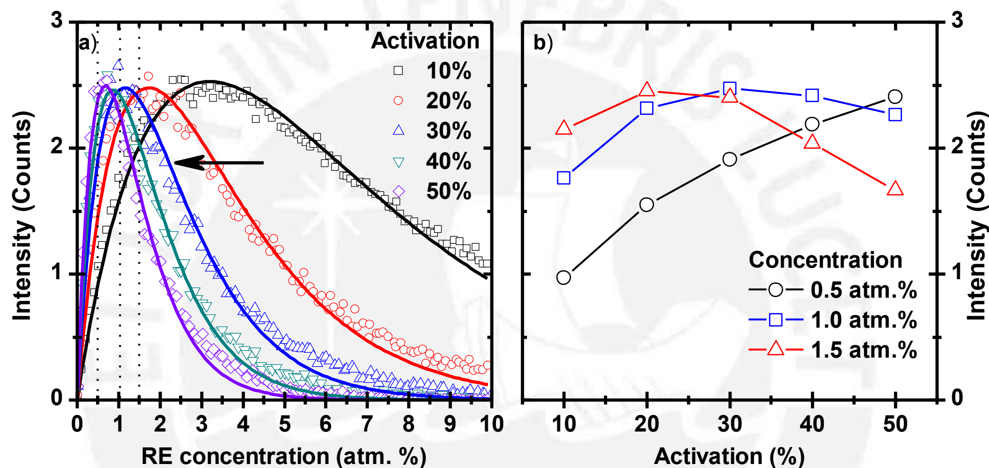

Figure 5.2.12. Simple Monte Carlo simulation of the concentration quenching effect in two dimensions using a normalized interaction probability given by the equation 5.2.2. The solid lines are fits using the equation 5.2.1 with $P_i = \exp(n_{RE}/n_0)$ for simplicity (a). Simulated intensity versus the activation degree for 3 different RE concentrations (b). The curves are not normalized, and the intensities are comparable. Notice the increase of the slope and the sharpness of the exponential decay upon increasing the activation degree.

In summary, the concentration quenching behavior of the light emission of the Tb doped samples here studied exhibit host matrix dependent features, such as the maximum achievable intensity versus the Tb concentration and the quenching exponential decay rate. Therefore displaying the fact that the energy loss mechanisms are mainly host material nature and the probability of a non-radiative transition is enhanced by the RE concentration. The critical concentration value, before the quenching becomes

Tesis publicada con autorización del autor
No olvide citar esta tesis
ET LUX IN TENEBRIS LUCET MCMXVII PUCP

appreciable, is not the same from host to host. These features are also excitation source dependent. After the band-to-band excitation with electrons in both materials, the concentration quenching effect is enhanced demonstrating the new paths for energy loss which are not present after sub-bandgap excitation. That is for instance, reaching Tb ions which are not active upon sub-bandgap excitation but upon band-to-band excitation and therefore explaining the observed shift as depicted in the figure 5.2.12.

Thermal activation

It is well established that not all of the RE ions embedded in a matrix are active for light emission. Furthermore, RE ions can be activated after thermal treatments. However, the mechanisms of this fact are still controversy discussed [Gue13]. For instance, the enhancement of the electronic properties of the host material, i.e. by reducing the electronic defects, upon annealing treatments is a possible mechanism for the light emission boost with the annealing temperature, mainly due to the reduction of non-radiative recombination centers. Likewise, the improvement of the RE surrounding atomic environment, for example by coordinating with oxygen atoms [Jan03], or the rearrangement of the local structure around the RE ions [Men06, Wein06, Zan09] may promote the RE activation. The study of the annealing behavior can provide information concerning the underlying mechanisms for promoting the activation of RE ions in amorphous matrices. However, detailed temperature dependence of the light emission is often overlooked. Particularly, a critical annealing temperature between 400°C and 700°C at which the highest intensity is reached has been reported for Tb doped amorphous/nano-crystalline GaN, AlN and SiC [Wein06, Men06, Zan09, Gue15]. This behavior has been also reported in other RE doped materials. For instance in Er doped amorphous hydrogenated Silica [Jan03], Er_2O_3 sol-gel Silica [Abe11, Ryu95], Er implanted crystalline GaN [ODo10] and Eu doped Al_2O_3 [Ena08].

In this section, we review the variation of the light emission of Tb doped amorphous SiN, AlN and SiC:H upon isochronal thermal annealing treatments. The effect of the annealing temperature on the shape of the so called quenching curves in the case of Tb doped SiC:H is presented and evaluated.

Tesis publicada con autorización del autor
No olvide citar esta tesis
PUCP

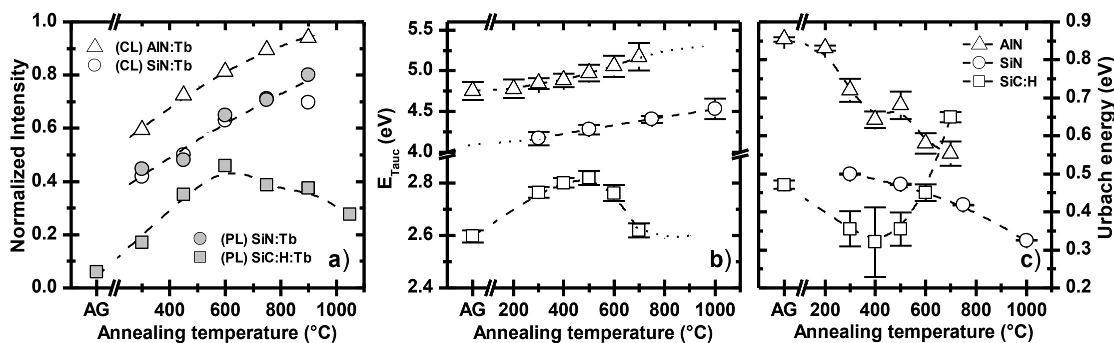

Figure 5.2.13. Normalized integrated CL and PL (λ_{exc} = 488 nm) intensities of Tb doped amorphous SiN, AlN and SiC:H thin films, the curves are shifted for clarity reasons only (a). Optical bandgap (b) and Urbach energy (c) of the undoped amorpous SiN, AlN and SiC:H thin films [Gue15].

The variation of the integrated intensity of the Tb doped samples here under study is depicted in figure 5.2.13. The samples were doped with about ~1 at. % Tb. The emission intensity was taken upon electron and photon excitation. The Tb doped SiN and AlN layers exhibit a monotonically increase of the light emission intensity with the annealing temperature. The optical emission of the Tb doped SiC:H layer exhibited a critical annealing temperature at which the light intensity reaches its highest value before decreasing. If we compare this behavior with the variation of the optical bandgap versus the annealing temperature, a similar shape between the integrated intensity and the Tauc-gap is noted, see figure 5.2.13. This effect displays the fact that the thermal annealing treatments enhance the light emission of REs by reducing electronic defects. Pointing out that the amount of electronic defects, here measured by the Urbach energy, is responsible for the non-radiative paths. Therefore, an increase of the electronic defects which is translated in a decrease of the Tauc-gap, should develop a decrease of the light emission intensity as shown in the SiC:H case. The fact that this correlation between the light emission intensity and the optical bandgap exist, strongly supports that 1 at.% doping concentration is suitable for a low Ion-Ion interaction and that the optical properties of the film are not significantly altered by the doping. At any rate, the RE activation obeys other mechanisms which are not related solely to the increase in efficiency due to the reduction of non-radiative paths. For instance, the formation of RE structured isovalent traps is an extensively well accepted model [Loz07, ODo10]. The formation of such

Tesis publicada con autorización del autor
No olvide citar esta tesis
PUCP

structures can be promoted by the annealing treatments. Additionally, the site a RE occupies in a crystalline matrix and the formation of RE clusters can also influence the activation degree.

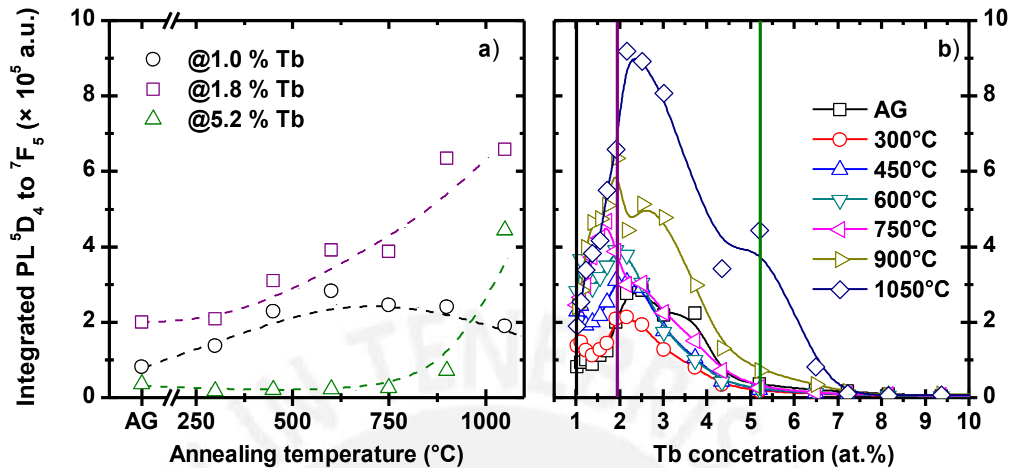

Figure 5.2.14. Thermal activation of Tb doped amorphous SiC:H at different Tb at.% (a). Quenching curves of Tb doped amorphous SiC:H after different annealing temperatures (b). Vertical colored lines in panel (b) correspond to the intensities plotted in panel (a).

The variation of the RE activation degree in the simple simulation presented in the previous subsection showed that the activation behavior of the emission intensity could change completely from one concentration to another, see figure 5.2.12. The simulation aim was to picture the emission intensity sensitivity under different concentrations and activation degrees. Certainly, the considered assumptions do not meet the real case. Notwithstanding, we can still obtain some reliable information such as the slope of the low concentration region which increases with the activation degree. In this frame we study the thermal activation behavior of Tb doped SiC:H at different Tb concentrations. Figure 5.2.12 depicts the variation of the integrated light emission intensity of the Tb doped SiC:H samples at different Tb at.% concentrations versus the annealing temperature. Note that if we increase the Tb concentration the shape of the integrated intensity versus annealing temperature curve changes dramatically. The activation curves lose their correlation with the Tauc-gap (Urbach energy) by increasing slightly the Tb amount, see figures 5.2.12 and 5.2.14. This effect can be attributed to the competition between the recombination in non-radiative centers which in this case after about 600°C

Tesis publicada con autorización del autor
No olvide citar esta tesis
ET LUX IN TENEBRIS LUCET MCMXVII PUCP

annealing temperature increase in number as revealed by the Urbach energy and the new active luminescent centers.

After the thermal annealing treatments, the concentration quenching curves depicted in the figure 5.2.14 still exhibit the previously described behavior: a practically linear increase followed by an exponential decay after a critical concentration. Hence, three main features that can be correlated with the annealing temperature can be recovered from these curves. First, we have the slope of the linear increase in the low concentration region. Second, the critical concentration at which the quenching becomes more significant. And third, the quenching rate of the exponential decay in the high concentration region. In order to extract these parameters we fit the quenching curves using the equation 5.2.1. For the sake of simplicity, we approach the interaction probability to $\exp(n_{Tb}/n_0)$. Thus the decay rate is given by n_0, the slope by A, and the critical concentration by $B' = -\log(B) \times n_0$. The results of these fits are shown in figures 5.2.15, 5.2.16 and table 5.2.2. Additionally, we calculate the slope M_A by a direct linear fit in the low concentration region.

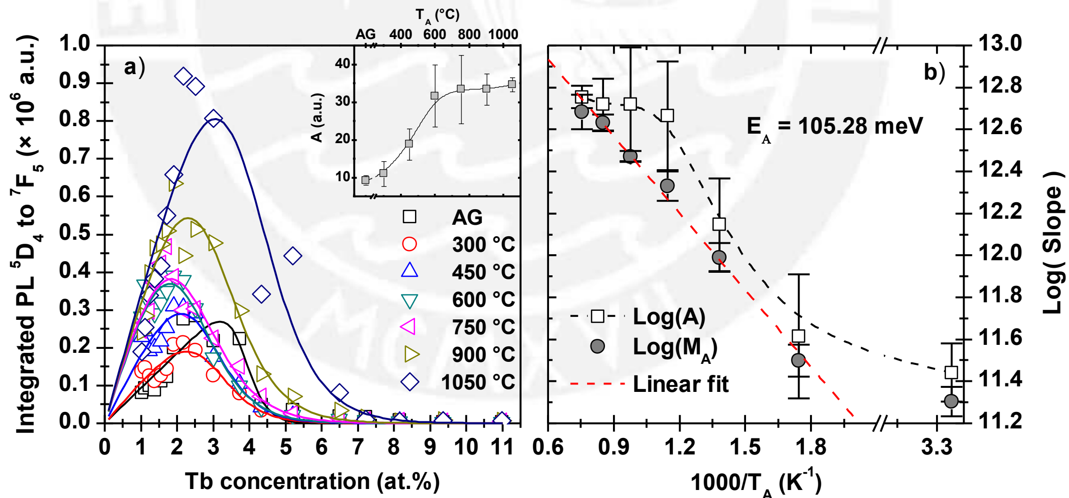

Figure 5.2.15. Integrated PL intensity versus the Tb concentration for different annealing temperatures (a). Solid lines are fitted curves using the equation 5.2.1. Inset graph corresponds to the slope A versus T_A. Arrhenius plot of the slopes M_A and A exhibiting an activation energy of 105.28 meV (b).

Tesis publicada con autorización del autor
No olvide citar esta tesis
PUCP

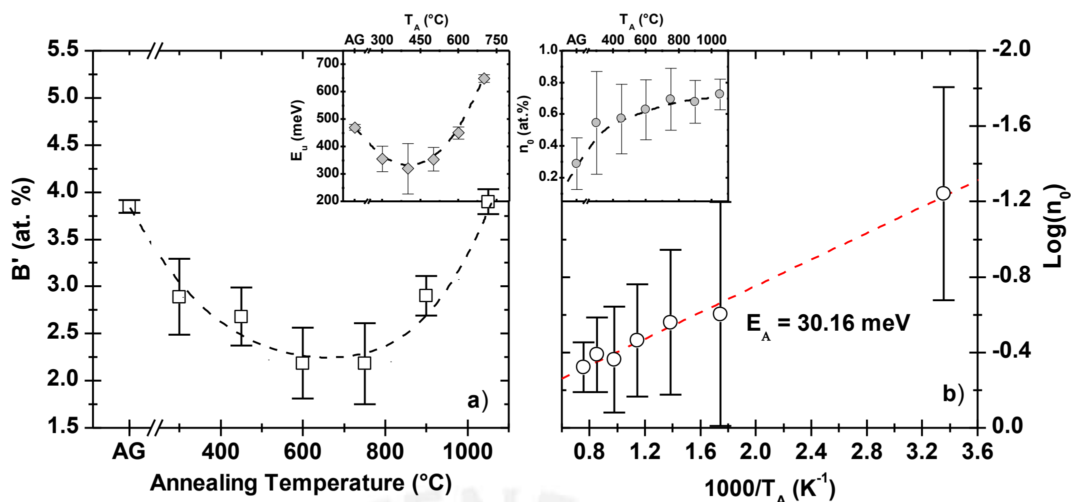

Figure 5.2.16. Effect of the annealing temperature on the parameter *B*', revealing its close relation with the host matrix electronic properties, the inset graph correspond the Urbach energy of SiC:H obtained earlier (a). Arrhenius plot of the exponential decay rate n_0 exhibiting a good linear behavior, the inset graph depicts the decay rate in linear scale versus the annealing temperature (b).

Table 5.2.2. Best fitted parameters using the equation 5.2.1. M_A is the best fitted slope of the linear increase at the low concentration region. $r_{B'}$ and r_0 are the calculated mean distance (nm) based in the values of B' and n_0 (at.%), respectively. Details on the latter calculation procedure can be found in A.4.

T_A (°C)	$M_A \times 10^4$	$A \times 10^4$	B' (at.%)	$r_{B'}$ (nm)	n_0 (at.%)	r_0 (nm)
AG	8.11±0.57	9.31±1.28	3.85 ±0.06	0.44±0.001	0.28 ±0.16	0.89 ±0.11
300	9.86±0.75	11.06±3.27	2.88 ±0.40	0.47 ±0.01	0.54 ±0.32	0.73 ±0.09
450	16.11±1.09	18.83±4.16	2.67 ±0.30	0.48±0.01	0.57 ±0.21	0.72 ±0.06
600	22.66±1.58	31.65±8.19	2.18 ±0.37	0.50±0.02	0.62 ±0.18	0.70 ±0.05
750	26.05±0.68	33.42±9.08	2.18 ±0.42	0.50±0.02	0.69 ±0.19	0.68 ±0.04
900	30.63±1.22	33.41±4.11	2.89 ±0.21	0.47±0.008	0.67 ±0.13	0.69 ±0.03
1050	32.20±2.63	34.62±1.87	3.89 ±0.12	0.44±0.03	0.72 ±0.09	0.67 ±0.02

As described previously, the slope of the linear shape in the low concentration region of these curves is directly proportional to the RE activation degree [Gue13]. Figure 5.2.15 also depicts the Arrhenius plot of the slopes A and M_A for the different annealing temperatures. Notice the good linear relationship for M_A resulting in an activation energy of E_A = 105.3 meV. The slope A exhibits a similar activation energy, however the error is much larger due to the low number of fitting points and a smaller linear region. This is the first report of an activation energy obtained in this way for the activation of a Tb

Tesis publicada con autorización del autor
No olvide citar esta tesis
ET LUX IN TENEBRIS LUCET MCMXVII PUCP

doped wide bandgap semiconductor [Gue13]. The 105.3 meV value is in the order of the optical phonons energy of the host matrix, thus suggesting that the transition process might be phonon-assisted. We will come back to the latter idea in the last section of this chapter.

Concerning the other fitted parameters shown in the table 5.2.2, i.e. B' and n_0, since they have concentration units (at.%), thus their mean distance counterparts $r_{B'}$ and r_0 are also calculated. Figure 5.2.16 depicts the variation of B' and n_0 with the annealing temperature, both exhibiting the following behavior. First, the critical concentration B' exhibits a similar shape to that of the Urbach energy. This behavior, which was already observed in the Tb related integrated light emission intensity at concentrations around 1 at.%, is then recovered in B'. To understand this, let us recall that the parameter is inversely proportional to the probability of a non-radiative recombination as we have seen in section 3.2. That is: $B \propto k_{rad} k_{exc} / (k_{emis} + k_{non_rad})$. Thus B' behaves inversely to B and it is not surprising that it exhibits a similar shape with the Urbach energy of the host matrix. An increase of the Urbach energy is translated into an increase of non-radiative recombination.

Second, the decay rate n_0 presents a different behavior with the annealing temperature. It increases with the annealing temperature reaching a saturation value around ~0.75 at.%, making the quenching exponential decay less sharp with each annealing step. The corresponding Arrhenius plot reveals a process with an activation energy of 30.16 meV. This result shows certainly that the concentration quenching exponential decay becomes slower when increasing the annealing temperature. The exponential decay rate n_0 is directly related to the interaction probability between the Tb ions. Hence in the light of the results presented in the figure 5.2.16, it seems reasonable that the interaction probability is decreasing with the annealing temperature upon resonant PL excitation with 488 nm. However, this result is limited by the rate equation model, and the over-simplified RE interaction probability used to describe the curves.

Tesis publicada con autorización del autor
No olvide citar esta tesis
PUCP

In summary, in this section the thermal activation of Tb doped amorphous SiN, AlN and SiC:H was reported for Tb concentrations around 1 at.% revealing the close relation between the light emission intensity and the Urbach energy. The effect of isochronal thermal annealing treatments on the behavior of the concentration quenching curves was also reported for the case of Tb doped amorphous SiC:H. Three different parameters were recovered and related to the variation of the light emission intensity with thermal annealing treatments: the slope of the linear increase in the low concentration region, the critical concentration $B' = -\log(B) \times n_0$ which denotes the inflexion point in the high concentration regime, and the exponential decay rate n_0. It was established previously that the slope A is proportional to the RE activation degree and B is related to the non-radiative recombination ($k_{non-rad}$) which is in fact associated to localized states. Hence, an activation energy of 105.3 meV was obtained from an Arrhenius plot of the slope M_A, whilst the parameter B' exhibited a similar behavior than the Urbach energy of the host material. The latter behavior is somehow expected since the Urbach energy is also a measure of the amount of non-radiative recombination centers. Finally, the exponential decay rate exhibited a decrease till a saturation point around n_0 = 0.75 at.%, possibly attributed to a diminution of the energy transfer probability between Tb ions upon resonant excitation of the $^5D_4$ energy level, however this behaivor requires additional confirmation.

Temperature dependent measurements

As we have seen already, different atomic environments give rise to slightly different RE-related emission spectra, see figure 5.2.17. Besides the RE activation, thermal annealing treatments can also improve the quality of the electronic properties of the host material enhancing the light emission intensity of the RE by reducing the non-radiative recombination paths. The special case of Tb doped *a*-SiC:H revealed the increase of the Urbach energy and the decrease of the Tb related light emission intensity after a critical annealing temperature. The close relation between the RE-related light emission intensity with the host matrix electronic properties are often overlooked [Abe11, Gue15]. The temperature quenching of the RE-related luminescence intensity has been studied on different matrices and RE ions. For instance, Er-doped compounds exhibit distinct

Tesis publicada con autorización del autor
No olvide citar esta tesis
ET LUX IN TENEBRIS LUCET MCMXVII PUCP

temperature quenching values depending on the host matrix [Zan03, Jan03, Loz07], whilst RE-doped AlN exhibit not only different temperature quenching values but features at temperatures well below thermal quenching [Loz07].

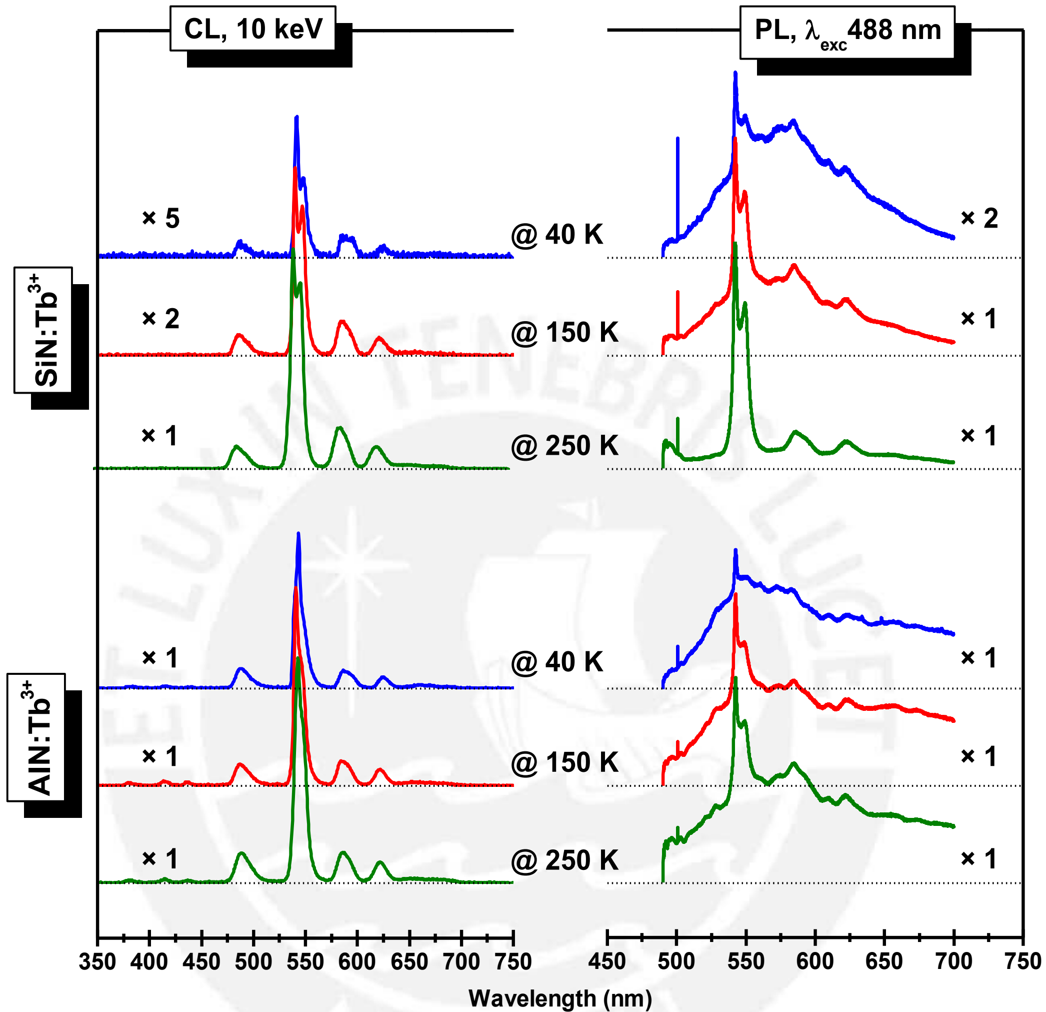

Figure 5.2.17. CL spectra (left) and PL spectra (right) of Tb^{3+} doped SiN (upper group) and AlN (lower group) for three different sample temperatures.

The role amorphous matrices play in the excitation processes can be examined under temperature dependent analysis of the corresponding light emission intensity. Temperature dependent PL and CL have been performed in order to assess the light emission features upon photon sub-bangap and electron band-to-band excitation under conditions where the interaction of the Tb ions with phonons is low. Typically, the decrease of lattice vibrations at low temperatures is expected to enhance the RE-related

Tesis publicada con autorización del autor
No olvide citar esta tesis
ET LUX IN TENEBRIS LUCET MCMXVII PUCP

light emission intensity. This behavior is attributed to the reduction of phonon-assisted processes and therefore the inhibition of the energy migration from the RE ions to the host matrix [Zan03, Zan12].

However, a strong enhancement of the RE-related light emission intensity with the temperature has been reported previously for Sm^{2+}, Tb^{3+}, Tm^{3+} and Ce^{3+}, even after up to 200 degrees above room temperature in different amorphous and crystalline hosts [Spo79a, Spo79b, Loz07, Zan12, Gue15]. For instance, figure 5.2.18 depicts the temperature dependence of the RE related light emission intensity of different RE doped AlN layers in which an exponential increase of the Tb CL intensity is observed [Loz07]. Figure 5.2.17 depicts the Tb^{3+} doped related light emission spectra of the SiN and AlN hosts at three different temperatures, 40, 150 and 250 Kelvin upon sub-bangap photon excitation and band-to-band electron excitation. Some features are noted. First, the Tb-related emission spectra intensity increases with the temperature in both CL and PL measurements. Second, the PL background emission intensity related to the host matrix decreases reciprocally with the temperature, whilst no background emission is recorded in the CL-spectra. Third, both PL- and CL-peaks exhibit a slight variation in the line width of the Tb-related transitions at different temperatures. However, in the PL case this change is not sufficiently substantial or appreciable to be quantified. Nonetheless, an increase of the broadening with the temperature is measured in the CL-spectra in the whole temperature range, with a modification in the relative intensities of the crystal field splitting lines.

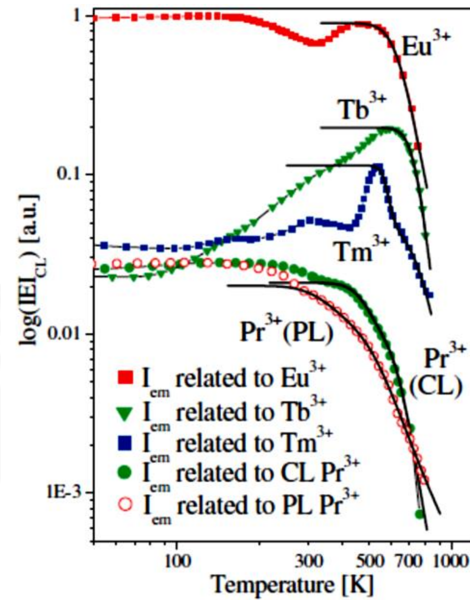

Figure 5.2.18. Temperature dependence of the light emission of AlN doped with Pr^{3+}, Eu^{3+}, Tb^{3+}, and Tm^{3+}, from [Loz07].

In previous sections we have reviewed the different excitation mechanisms of RE-doped amorphous semiconductors. It is important to recall that during the photon and electron

Tesis publicada con autorización del autor
No olvide citar esta tesis
PUCP

excitation we have an overlap of these different excitation processes. The direct photon resonant excitation with 488 nm excitation wavelength of the $^7F_6$ to $^5D_4$ energy levels has actually a very low cross section. Therefore the light efficiency concerning solely this mechanism should be very low in comparison to other excitation paths. Nonetheless, as reported previously, the light emission intensity is rather high upon this excitation source in distinct materials [Wei06, Zan09, Zan12, Gue13, Gue15]. In this sense, other excitation paths beside the direct resonant excitation of the RE must play an important role in the sub-bandgap photon excitation. A summary of the possible excitation paths was presented in figure 5.2.6. Depending on the electronic structure and the energy level location of the RE [Dor08], quasi-resonant energy migration from *e-h* pairs recombination at defects like dangling bond states (path III in figure 5.2.6) or deep band tail states (path IV in figure 5.2.6) to the RE is possible [Jan03]. The former may be achieved by a defect-related Auger effect (DRAE). Nonetheless this process compels the proximity of the REs to dangling-bond defect states [Fuh97]. On the other hand, the energy migration from recombination at deep band tail states can be attained by a dipole-mediated resonant energy transfer, which is efficient for larger distances [För60]. Since the aforementioned processes depend on the host matrix, both may compete with radiative (and non-radiative) recombination at defect sites.

It is likely that the sub-bandgap photon excitation, excites the matrix and depending on the RE and the host matrix i.e. if the RE energy levels match suitable or not with the defect states, it is possible to enhance or decrease the light emission intensity of the RE with the temperature by a phonon-assisted energy migration between defects and RE states [Gue15]. Electron band-to-band excitation would be a more efficient RE excitation source since all the excitation paths are overlapped and thus the probability to excite a RE ion is much higher. This behavior has been reported previously by Lozykowski for *c*-AlN doped with Eu^{3+}, Tb^{3+}, Tm^{3+} and Pr^{3+}, see figure 5.2.18 [Loz07]. In the case presented here, at low temperatures the phonon-assisted energy migration is inhibited, and therefore the direct excitation component and the indirect excitation through bound excitons are present. The former has a very low efficiency due to the low cross section, while the latter is only possible under band-to-band excitation. The host matrix background

Tesis publicada con autorización del autor
No olvide citar esta tesis
ET LUX IN TENEBRIS LUCET MCMXVII PUCP

emission is rather high at these low temperatures due to the fact that even when the RE ions are high efficient recombination centers, the electron-hole pairs recombine in the defects or deep localized band tail states without the possibility to transfer the energy to the Tb ions. Therefore, we can drive the statement that an increase of the Tb-related light emission intensity with the temperature strongly suggests a phonon-assisted energy transfer mechanism between the host matrix and the Tb ions, enhancing the radiative recombination in the latter ones [Gue15].

Figures 5.2.19 and 5.2.20 depict the Arrhenius plot of the CL and PL integrated intensity, respectively versus the sample temperature for the Tb^{3+} doped AlN and SiN thin films. In the CL case, the temperature ranged from 34K to 400K, whilst in the PL case the temperature ranged from 10K to room temperature due to setup limitations. From these plots the activation energies corresponding to the samples annealed at 900°C are extracted and exhibited in the table 5.2.3. Note that the activation energies of the CL case almost doubles that obtained from the PL measurements in both samples.

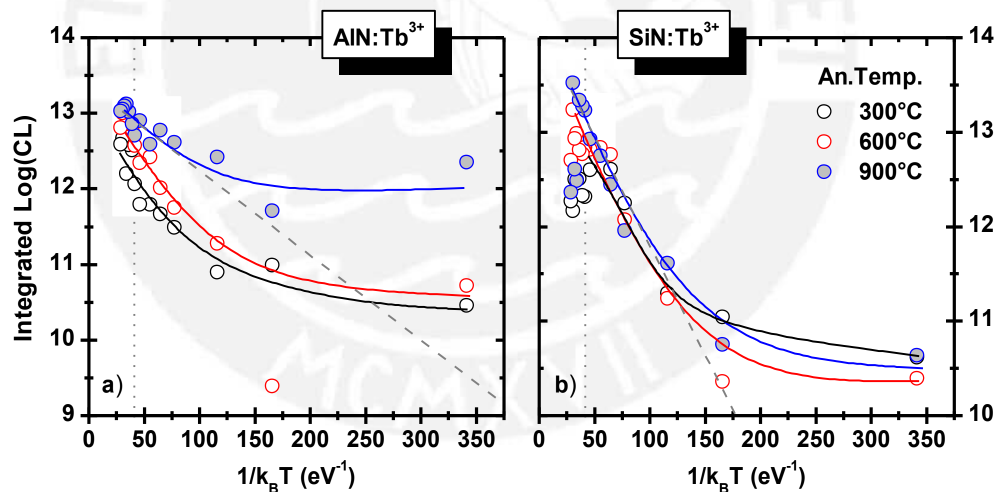

Figure 5.2.19. Integrated CL intensity of Tb doped AlN (a) and Tb doped SiN (b) versus the reciprocal of the temperature after three different annealing temperatures. The dotted vertical lines denote the room temperature at 293.6 K.

Tesis publicada con autorización del autor
No olvide citar esta tesis

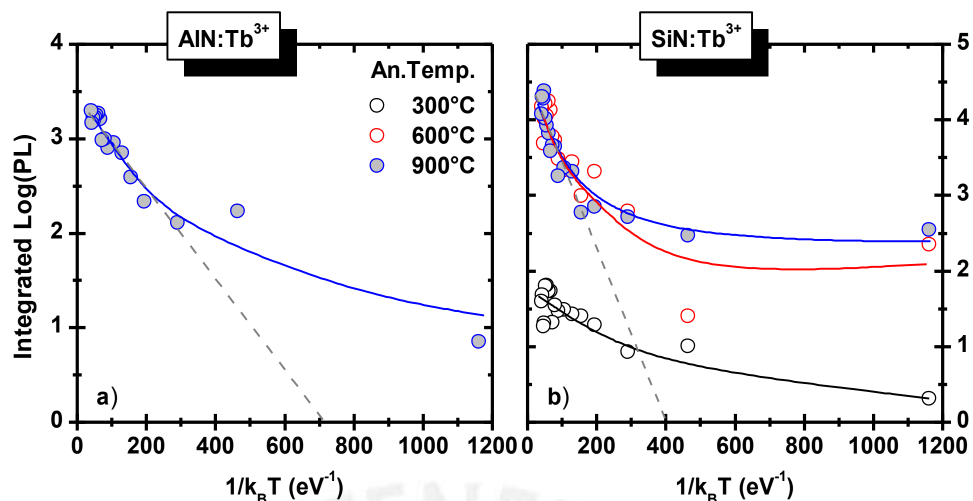

Figure 5.2.20. Integrated PL intensity of Tb doped AlN (a) and Tb doped SiN (b) versus the reciprocal of the temperature after three different annealing temperatures. Unfortunately, below 900°C annealing temperature, the AlN:Tb samples didn't exhibit sufficient signal.

Table 5.2.3. Activation energies after an annealing temperature of 900°C, obtained from the figures 5.2.17 and 5.2.18.

Host	Exc. Source	E_A (meV)
SiN	PL	17.5 ± 2.56
	CL	33.22 ± 1.21
AlN	PL	5.88 ± 0.43
	CL	9.09 ± 0.88

The crystal field at any point in the matrix is the result of the overlap over a large number of neighboring atoms. Nonetheless, the disordered structure of an amorphous material makes the crystal field parameters to vary between sites. These variations give rise to the inhomogeneous spectral broadening observed previously. Furthermore, the energy of the 4f states of RE ions are relatively insensitive to the variation of the site parameters, thus the observed extend of the broadening indicates large fluctuations in the field parameters. In other words, the variation in the site geometry from one RE to another, in an amorphous host matrix, give rise to an inhomogeneous broadening of the RE-related emission spectra [Spe75]. The broadening is then also sensitive to the sample temperature. As we have seen previously in the figure 5.2.3, the emission corresponding

Tesis publicada con autorización del autor
No olvide citar esta tesis
PUCP

to the transition $^5D_4$ to $^7F_6$ is composed by three lines that are resolved at low temperatures only. At higher temperatures, two apparent lines are only visible due to the broadening. Figures 5.2.21 and 5.2.22 depict the emission spectra of the $^5D_4$ to $^7F_6$ transition for five different sample temperatures of the Tb doped SiN and AlN samples, respectively and after an annealing at 900°C. The frame (f) in both figures depicts the width of the first peak (centered at ~539 nm) obtained from fits equivalent to the ones shown in the figure 5.2.3. We take this peak as representative in order to assess the variation of the width with the sample temperature. Moreover, both materials experience the relative increase of the second peak, centered at ~547.5 nm, respect to the first one when increasing the sample temperature.

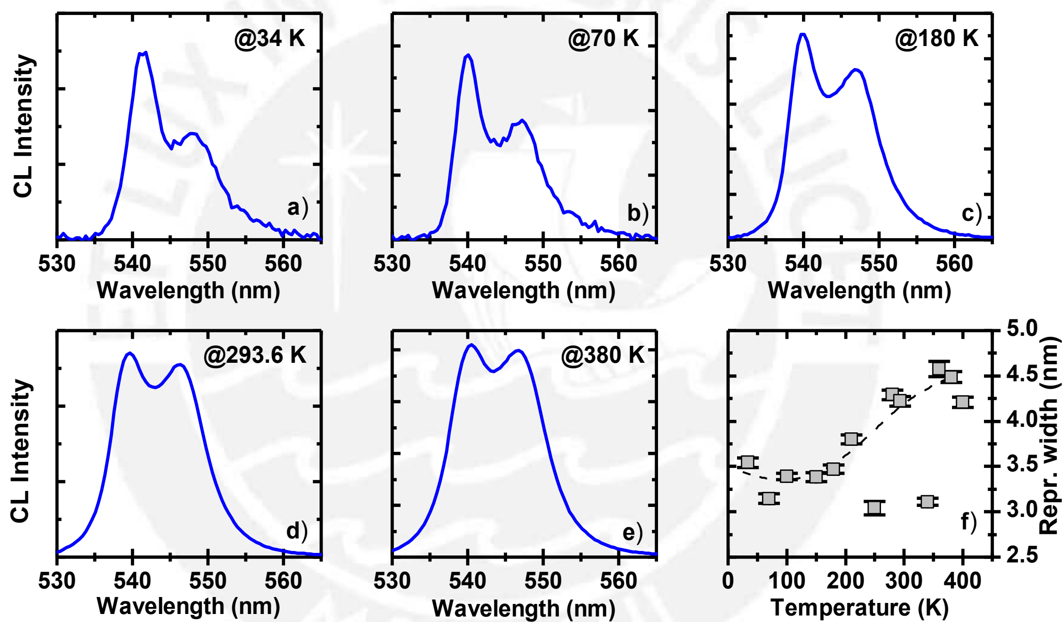

Figure 5.2.19. Variation of the emission peak shape of Tb doped *a*-SiN with the sample temperature (a, b, c, d and e). Peak width versus the sample temperature (f).

Tesis publicada con autorización del autor
No olvide citar esta tesis
ET LUX IN TENEBRIS LUCET MCMXVII PUCP

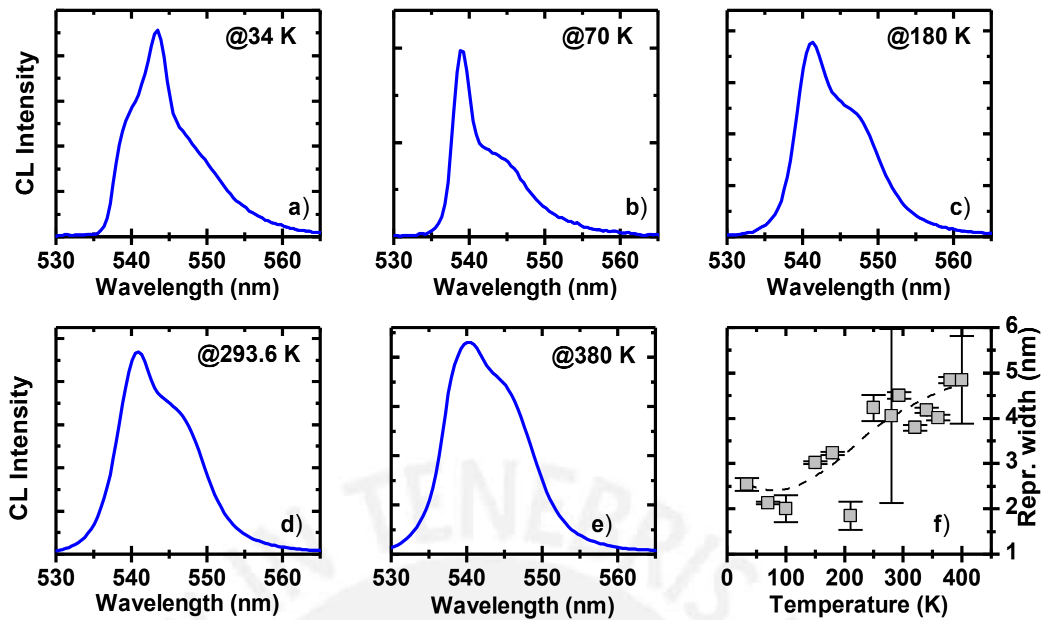

Figure 5.2.20. Variation of the emission peak shape of Tb doped *a*-AlN with the sample temperature (a, b, c, d and e). Peak width versus the sample temperature (f).

In summary, in this section we have reviewed the effect of the sample temperature on the emission spectra of Tb doped SiN and AlN bellow the thermal quenching. The emission was examined upon photon sub-bandgap excitation and electron band-to-band excitation. The results showed that the host matrix plays an important role in the excitation process of the RE ions. We believe that the excitation by 488 nm photons not only excites the Tb ions resonantly but also the matrix which can then transfer the energy to the Tb ions by a phonon-assisted energy migration process. Additionally, electron band-to-band excitation proofs to be a more efficient excitation source than the photon sub-bandgap excitation.

Tesis publicada con autorización del autor
No olvide citar esta tesis
ET LUX IN TENEBRIS LUCET MCMXVII PUCP

Summary and concluding remarks

In this work we have presented a comprehensive study of the effect of thermal annealing treatments on the optical properties and luminescence features of Tb doped amorphous SiN, AlN and SiC:H. In this frame the RE thermal activation process and the effect of temperature on the light emission intensity was evaluated. Furthermore, the concentration quenching effect of Tb doped SiC:H upon different annealing temperatures lead to the discrimination of the effect of the RE activation from the band-tails variation in the Tb related light emission intensity upon thermal annealing treatments. In the present chapter the main results are shortly summarized in three parts.

The optical bandgap and the Urbach focus

The optical bandgap of amorphous systems is typically calculated from optical data by the Tauc-model. This model doesn't take into account band-to-tail and tail-to-tail electronic transitions. On the other hand, the band-tails considerably overlap on the mobility edges becoming a significant and sometimes indistinguishable part of the fundamental absorption in the typical optical measured range. Moreover, the capacity to distinguish a linear region in the Tauc-plot becomes in most cases an arbitrary choice. In this frame we proposed and presented a simple and analytical model based on the previous works of O'Leary and Dunstan [OLe98, Dun83] from which the Urbach energy and the bandgap in the absence of disorder are retrieved from single optical absorption coefficient measurements [Gue13m, Gue16]. The first consequence of this model is related to the Urbach focus constant. As we know, the absorption coefficient around the mobility edges contains two classes of states which overlap, the localized band-tail states and the extended states which start in the mobility edges. The band-tail states effect is reflected in the Urbach energy, while the extended states effect is typically reflected in the Urbach focus. Both contribute to the overall behavior of the Tauc-gap with for instance the annealing temperature. However the meaning of the value delivered by the Urbach focus energy coordinate is still under discussion [Cod05]. The model here proposed reveals that the Urbach focus is actually a small region, and that the true

Tesis publicada con autorización del autor
No olvide citar esta tesis
ET LUX IN TENEBRIS LUCET MCMXVII PUCP

constant is the mobility edges energy gap E_0, thus giving a new meaning to the Urbach focus. In order to test the existence of this constant and contrast it with the Urbach focus, we performed the analysis of Orapunt and O'Learty [Ora04] on amorphous Si:H, SiN, AlN and SiC:H. This analysis was performed using the traditional Urbach rule and the asymptotic behavior of the model proposed here. The results delivered that both equations predicted equally the constants pair (E_F, α_F) and (E_0, α_0) for the materials under study without any biasing from the formulas. A plausible explanation of this result is that the extended Urbach rule can be reduced to the Urbach rule always and only there is a low dispersion of the Urbach slope. In such case the Urbach focus region becomes sufficiently small. Another consequence of this model is the capacity to measure E_0 from single measurements of the absorption coefficient. For instance, the Tauc-gap contains information of both the Urbach energy and the band-edge energy gap, however the latter is implicit and can only be retrieved through the Urbach focus. This fact becomes evident in the case of a-SiC:H_x in which the Urbach energy decreases until a critical annealing temperature to then increase again. In this case E_0 remained nearly constant while E_{Tauc} behaved inversely to E_u [Gue16].

The amorphous SiN and AlN layers exhibited an enhancement of the Tauc-gap followed by a reduction of the Urbach energy with the annealing temperature. Different linear relations between the bandgap E_{Tauc} and E_{04} with the Urbach energy E_u were found. In this case, the constants ${}^{(04)}E_F$, ${}^{(Tauc)}E_F$ and ${}^{(m_{Tauc})}E_F$ were attained with values in agreement with the Urbach focus obtained directly by a global fit of the absorption coefficient and by the analysis of Orapunt and O'Leary of each material. However in the case of a-SiC:H_x only the ${}^{(04)}E_F$ was retrieved. The linear relations between the Tauc-gap and the Urbach energy or the Tauc-slope didn't realize. Nevertheless, the obtained ${}^{(04)}E_F$ values were in agreement with the Urbach focus obtained by the global fit and by the analysis of Orapunt and O'Leary. A shift enhancing the Tauc-gap and E_{04} iso-absorption gap was observed upon increasing the hydrogen content during the deposition process. The Urbach energy remained similar in all SiC:H samples. This shift is mainly attributed to the widening of the band-edges due to the passivation of dangling bonds [Bul87] and is

Tesis publicada con autorización del autor
No olvide citar esta tesis
PUCP

also reflected in the Urbach focus. As expected, this shift was also observed in the E_0 parameter [Gue16].

Finally, the explanation of the quenching of the bandgap of a-SiC:H with the annealing temperature turned differently to what is typically found in the literature [Zha92, Kal94, Cui01] since the behavior is also observed in the non-hydrogenated sample. The increase of the Tauc-gap with the annealing temperature is owing to the matrix relaxation. However, the decrease of the Tauc-gap cannot be attributed to the hydrogen effusion only. It is probably related to the formation of crystalline clusters in the matrix due to thermal annealing treatments that may also increase the Urbach energy [Lee00, Kit00, Raj03]. Additionally, as reported already by Vasin an increase of C-C clusters with the annealing treatment could be also a precursor of the bandgap quenching [Vas11].

Rare earth thermal activation

The study of the annealing behavior can help elucidate the underlying mechanism for producing the optically active Tb centers in the distinct host matrices. It has been reported previously an optimum annealing temperature at which the luminescence intensity reach its highest value. For instance between 400°C and 700°C annealing temperature Tb doped amorphous/nano-crystalline GaN, AlN and SiC reported this behaivor [Wein06, Men06, Zan09, Mon13]. Additionally, around 850°C, Er doped amorphous hydrogenated Silica [Jan03], Er_2O_3 sol-gel Silica [Abe11, Ryu95], Er implanted crystalline GaN [ODo10] and Eu doped Al_2O_3 [Ena08] also exhibit a peak in the integrated intensity. Notwithstanding, the variation of the RE related light emission intensity with thermal annealing treatments not only obeys the increase of luminesce centers by activating more REs in the host matrix. The annealing treatments induce the quench or enhancement of non-radiative recombination paths, thus increasing or reducing the light emission intensity by energy migration between luminescence centers and the host matrix.

In the present work, the thermal activation of Tb doped amorphous SiN, AlN and SiC:H was reported for Tb concentrations around 1 at.% revealing the close relation between the

Tesis publicada con autorización del autor
No olvide citar esta tesis
PUCP

light emission intensity and the Urbach energy. However as described above, it is not possible to discriminate the effect of the RE activation from the electronic enhancement of the material upon thermal annealing treatments only. In this frame, the effect of isochronal thermal annealing treatments on the behavior of the self-quenching curves was presented for the case of Tb doped amorphous SiC:H. We used a two levels simple rate equation to describe the behavior of the curves. Some parameters were recovered and subsequently related to the variation of the integrated light emission intensity with the annealing temperature. First, from the slope of the self-quenching curves in the low Tb concentration regime, an activation energy of 105.28 meV concerning solely to the activation of new luminescence centers is reported [Gue13]. This energy value is close to the phonon energy threshold in SiC and might give some insights concerning the mechanisms involve or necessary conditions for a RE ion to be optically active. Additionally, the non-radiative recombination ($k_{non-rad}$) which is in fact associated to localized states is also recovered and contrasted with the Urbach energy, exhibiting a good correspondence. This type of analysis is the first of its kind and reveals the capability to discriminate both effects.

Temperature dependent luminescence

It is important to remark that during the photon and electron excitation and overlap of distinct excitation processes take place. These processes may or not be phonon-assisted. Furthermore, the direct photon resonant excitation of the $^7F_6 \rightarrow {}^5D_4$ energy levels have a very low cross section and consequently the light efficiency concerning solely this mechanism is limited. However, as reported here and in [Loz07, Zan09, Zan12, Guer13] the light emission intensity upon this excitation source is rather high. In this sense, other excitation paths may play a role in the sub-bandgap photon excitation. PLE analysis reveal the efficient excitation of Tb doped polycrystalline SiC:H under sub-bandgap excitation. However Tb doped polyscrystalline AlN did not exhibit the same behavior. It is possible that the sub-bandgap photon excitation, excites the matrix and depending on the RE and the host matrix, the effective energy transfer between the RE and host mediated centers can enhance or decrease the light emission intensity [Dor13]. Furthermore, temperature dependent analysis of the light emission intensity revealed a

Tesis publicada con autorización del autor
No olvide citar esta tesis
ET LUX IN TENEBRIS LUCET MCMXVII PUCP

phonon-assisted energy migration reaching the Tb ions in Tb doped amorphous SiN and AlN [Gue15]. More precisely, the Tb related light emission intensity is quenched by decreasing the sample temperature. At the same time host related light emission is enhanced. This result evidence that at low temperatures phonon-assisted energy migration is inhibited, and therefore only the direct excitation component is present with a very low efficiency due to its low cross section [Spe75, Spo79b]. The host matrix background PL emission which is rather high at these low temperatures in comparison to the Tb emission follows the recombination of electron-hole pairs in defects and/or deep localized band-tail states without the possibility to transfer the energy to the Tb ions. We believe that an increase of the Tb related light emission intensity with temperature strongly suggest a phonon-assisted energy transfer mechanism between electronic defects and the Tb ions [Spe75, Spo79b, Jan03].

Tesis publicada con autorización del autor
No olvide citar esta tesis

PUCP

Appendix

A.1 Optical constants and thickness determination of dielectric thin films from single optical transmittance measurements

The accurate measure of wavelength dependent optical constants of dielectric thin films is an important issue for research and development of new materials and devices [Mac86, Kiy04]. For instance, the charge carrier concentration of wide band-gap semiconductors, like silicon carbide can be determined [Wei01, Wei02] or their bandgap can be extracted from the region of fundamental absorption. However, the optical constants cannot be measured directly since the geometry of the thin film assembly affects strongly the transmittance spectra. Therefore numerous methods to determine the optical constants have been developed. A comprehensive review can be found in [Poe03].

In the present appendix we develop an improvement of the widely used envelope method to retrieve with high accuracy and from a single transmittance measurement the thickness and optical constants of dielectric thin films. This method has been used in all the UV-VIS transmittance analysis previously presented in this thesis. Our method requires modeling the refractive index with few fitting parameters only, while the absorption coefficient is determined from the transmittance spectrum. The refractive index and absorption coefficient as functions of wavelength can be obtained even from spectra that have few interference fringes. We use the interference free transmittance curve determined from the envelopes, because its construction is highly insensitive to how the envelopes are defined and extracted from the measurement data. We have tested the method against simulated and real data from thin films covering the spectral range of the fundamental absorption. A comparison is made with the methods of Swanepoel [Swa83] and Chambouleyron [Cha97, Cha98], and a confidence analysis is performed to assess precision and accuracy.

Tesis publicada con autorización del autor
No olvide citar esta tesis
ET LUX IN TENEBRIS LUCET MCMXVII PUCP

The thin film assembly

Our starting point is the standard expression of the spectral transmittance of a thin homogeneous film on a thick non-absorbing substrate for normal incident light, considering multiple reflections from the back part of the substrate (see equation A.1.1 and figure A.1.1). Equation A.1.1 is found, for instance using the matrix description of optical filter systems, after averaging the highly oscillatory interference pattern (due to multiple reflections inside a thick substrate) thereby taking into account the finite spectral bandwidth of typical spectrophotometers [Bar10]. We adopt mainly the nomenclature of Swanepoel: the coefficients R_1, R_2 and R_3 in equation A.1.1 are the Fresnel reflection coefficients of the interfaces air-film, film-substrate and substrate-air, respectively. Here, x is the absorbance and ϕ the phase shift of monochromatic light. The refractive index, extinction coefficient and thickness of the film are denoted by n, k and d, respectively. Equation A.1.1 is valid for the case $n \gg k$ [Swa83, Mac86].

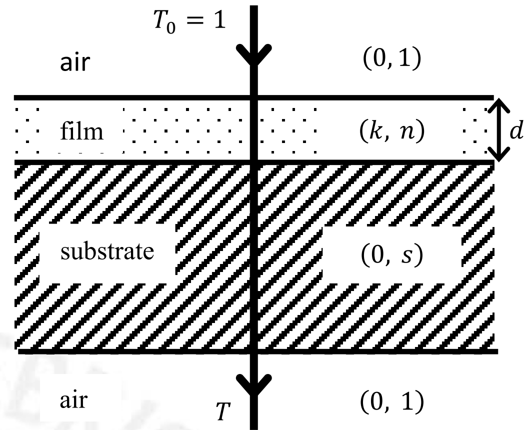

Figure A.1.1. Thin film assembly: The incident beam passes air, film, substrate and air. The transmittance coefficient of the whole assembly is T, normalized to the incident beam T_0. The pair (*, *) indicates the extinction coefficient and refractive index of the respective material in the assembly. The optical constants are the extinction coefficient k and refractive index n of the thin film, the refractive index s of the substrate and the film thickness d.

$$T(\lambda) = \frac{Ax}{B - C\cos\phi\, x + Dx^2} \quad \text{(A.1.1)}$$

The coefficients A, B, C, D, R_1, R_2, R_3, x and ϕ are defined as follows:

$$A = (1 - R_1)(1 - R_2)(1 - R_3)$$

$$B = 1 - R_2R_3$$

Tesis publicada con autorización del autor
No olvide citar esta tesis
ET LUX IN TENEBRIS LUCET MCMXVII PUCP

$$C = 2\sqrt{R_1 R_2}(1 - R_3)$$

$$D = R_1(R_2 - R_3)$$

$$R_1 = \left(\frac{1-n}{1+n}\right)^2, \; R_2 = \left(\frac{n-s}{n+s}\right)^2,$$

$$R_3 = \left(\frac{s-1}{s+1}\right)^2, \; \begin{array}{l} x = exp(-\alpha d) \\ \phi = 4\pi n d/\lambda \end{array}$$

The envelope method and our improvements

In this section we shortly review the envelope method after Swanepoel [Swa83] and then show our improvements.

Step 1. Determination of the refractive index of the substrate: If the refractive index is unknown it can be determined by measuring its transmittance T_s without the thin film. The following well known expression can be used:

$$s = s(\lambda) = \frac{1}{T_s} + \sqrt{\frac{1}{{T_s}^2} - 1}$$

Step 2. Determination of the transmittance coefficient: Measure of the spectral dependency of the transmittance coefficient $T = T(\lambda)$ of the whole assembly (thin film and substrate).

Step 3. Determination of the envelopes and interference free transmittance: The upper (T_+) and lower (T_-) envelopes of the (in step 2) measured transmittance curve are determined (see figure A.1.2). Swanepoel suggests the use of parabolic interpolation between adjutants maxima (minima). This is the weak point of the method: any procedure used to determine the envelopes is intrinsically arbitrary. Although we cannot remove this arbitrariness, we can conveniently modify the procedure. The determination of the envelopes is more accurate even for a low number of extremes using spline interpolation in the energy representation of the transmittance coefficient. The envelope determination

Tesis publicada con autorización del autor
No olvide citar esta tesis
PUCP

plays an essential role in Swanepoel's for determining the refractive index and absorption coefficient. In our method the envelopes are only needed as a preparative step to get a trial function for the fitting procedure.

From the envelopes one calculates the interference free transmittance $T_\alpha = \sqrt{T_+ T_-}$ which can be proved to be exact for our thin film assembly model. It is at this point where our method starts to differ from Swanepoel's. The latter continues with

Step 4. Determination of the refractive index: Using the refractive index of the substrate determined in step 1 and the envelopes determined in step 3, the refractive index of the thin film can be calculated by

$$n = n(\lambda) = \sqrt{N + \sqrt{N^2 - s^2}}$$

with,

$$N = 2s\frac{T_+ - T_-}{T_+ T_-} + \frac{s^2 + 1}{2}$$

Note that in this step the refractive index depends highly on the interpolation procedure of the envelopes.

Step 5. Determination of the thickness: The thickness can be either determined by adjacent maxima or minima (labeled 1 and 2) using

$$d = \frac{\lambda_1 \lambda_2}{2(\lambda_1 n_2 - \lambda_2 n_1)}$$

or by fitting a straight line to the relation of the order number l and the number of maxima m:

$$\frac{l}{2} = 2d\frac{n}{\lambda} - m$$

Tesis publicada con autorización del autor
No olvide citar esta tesis
PUCP

Step 6. Determination of the absorbance and absorption coefficient: The absorbance x can be determined in three ways, assigned here by x_+, x_- and x_α, respectively: from the upper envelope T_+, the lower envelope T_-

$$x_+ = \frac{E_+ - \sqrt{{E_+}^2 - (n^2-1)^3(n^2-s^4)}}{(n-1)^3(n-s^2)}$$

$$E_+ = \frac{8n^2s}{T_+} + (n^2-1)(n^2-s^2),$$

$$x_- = \frac{E_- - \sqrt{{E_-}^2 - (n^2-1)^3(n^2-s^4)}}{(n-1)^3(n-s^2)},$$

$$E_- = \frac{8n^2s}{T_-} + (n^2-1)(n^2-s^2)$$

or from their geometric mean T_α:

$$x_\alpha = \frac{\sqrt{E_\alpha - \sqrt{{E_\alpha}^2 - (n^2-1)^6(n^2-s^4)^2}}}{(n-1)^3(n-s^2)}, \tag{A.1.2}$$

$$E_\alpha = \frac{128n^4s^2}{{T_\alpha}^2} + n^2(n^2-1)^2(n^2-1)^2 + (n^2-1)^2(n^2-s^2)^2$$

Finally, the absorption coefficient is given by

$$\alpha = -\frac{1}{d}\ln(x) \tag{A.1.3}$$

In our method we follow Swanepoels up to step 3 and replace steps 4 to 6 as follows:

Step 4'. Choose a model for the refractive index: In order to prepare a fitting procedure and to overcome the difficulty of solving an underdetermined problem, we have to introduce some constraints. For instance one can choose a model for the refractive index. In our case (thin film of AlN or SiC) it is convenient to choose the Cauchy series

Tesis publicada con autorización del autor
No olvide citar esta tesis
PUCP

$$n = A_0 + \frac{A_2}{\lambda^2} + \frac{A_4}{\lambda^4} + \cdots \tag{A.1.4}$$

instead of a model for the absorption coefficient. This is appropriate since we know that in these materials the Cauchy series are in good agreement with experiment and we are interested in obtaining the absorption coefficient from experiment without modeling it. However, note that this choice is not imperative, depending on the material one can also change the model.

The model of the refractive index in step 4' and the interference free transmittance determined by the envelopes in step 3 are inserted in equation A.1.2 for the absorbance *x*. This absorbance is finally inserted in equation A.1.1 in order to obtain a fitting function for the transmittance:

$$T_{\mathrm{fit}} = T_{\mathrm{fit}}(\lambda, A_0, A_2, A_4, d)$$

Note that this function depends on the wavelength and only four fitting parameters, i. e. A_0, A_2, A_4 and the thickness d.

Step 5'. Fitting procedure: Now we can apply standard fitting procedures as, e.g., Levenberg-Marquardt's to minimize an estimator like the $\chi^2 = \sum \left(T_{\mathrm{measure}}(\lambda) - T_{\mathrm{fit}}(\lambda)\right)^2$ with respect to the fitting parameters A_0, A_2, A_4 and the thickness d.

Step 6'. With the best fitted parameters obtained in step 5', the refractive index and absorption coefficient can be obtained from equations A.1.4 and A.1.3, respectively. Note, that we have objective error bars given by the fitting procedure, which are absent in the Swanepoel method.

In order to test the accuracy of the proposed method we compare it with the method of Swanepoel (SWA) and the widely used method of Chambouleyron, implemented in the software PUMA (Pointwise Unconstrained Minimization Approach) [Cha97, Cha98]. First, the three methods are compared by applying them to a simulated transmittance

Tesis publicada con autorización del autor
No olvide citar esta tesis
ET LUX IN TENEBRIS LUCET MCMXVII PUCP

curve in order to recover the simulated parameters. Second, we repeat this procedure but adding some noise to the simulation in order to test the confidence interval of the recovered parameters. Finally, we also apply the above procedure to real thin to real thin films of the widebandgap materials *a*-SiC, *a*-AlN and the compound *a*-$(SiC)_{0.53}(AlN)_{0.47}$.

Simulation of the transmittance curve

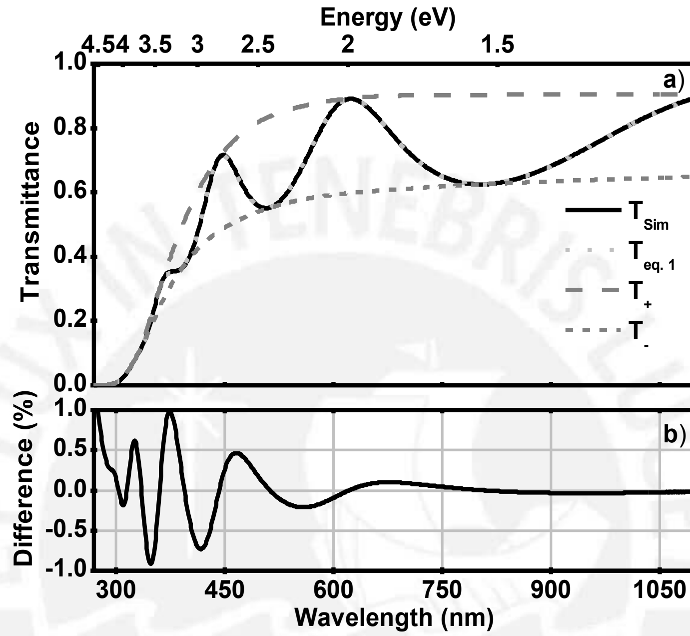

Figure A.1.2. Comparison of a simulation of the optical transmittance of a thin film with 250 nm thickness on a transparent substrate of 0.5 mm thickness measured with a spectral bandwith resolution $\Delta\lambda = 1$ nm (FWHM = 1.77 nm) and the equation A.1.1. The upper and lower envelopes calculated by splines are shown as dashed lines (a). Notice that the difference between the simulation and the equation 1 is lower than 1% (b).

Since we are interested in the fundamental absorption region of amorphous semiconductors we choose the Cauchy-Urbach model as a typical model to simulate the transmittance curve, describing the extinction and absorption coefficient as

$$\kappa = \kappa_0 e^{\beta(E-E_0)}, \;\; \alpha = \alpha_0 E e^{\beta(E-E_0)} \tag{A.1.5}$$

We describe the refractive index using the Sellmeier model to first order

Tesis publicada con autorización del autor
No olvide citar esta tesis
PUCP

$$n^2 = 1 + \frac{p_1 \lambda^2}{\lambda^2 - p_2} \tag{A.1.6}$$

which in addition is expanded as Cauchy series in order to compare the parameters with the recovered values. Notice that, while the simulation is performed using the equation (A.1.6), the fit is carry out describing the refractive index by the Cauchy expansion in order to avoid any possible biasing in the results. The optical parameters of the simulated film-substrate assembly are given in table A.1.1 and the results are shown in figure A.1.2. We chose typical parameters for a UV/VIS transparent glass substrate [Gon02].

Table A.1.1. Selected parameters for the simulation of the thin film substrate assembly.

Substrate	Film		
Cauchy	Cauchy-Urbach	Sellmeier	Cauchy expansion
$A_0 = 1.49$	$\alpha_0 = 1.2 \times 10^4$ $\text{cm}^{-1}\text{eV}^{-1}$	$p_1 = 1.49$	$A_0 = 2.34$
$A_2 = 0\ \text{nm}^2$	$E_0 = 3.5\ \text{eV}$	$p_2 = 5 \times 10^4\ \text{nm}^2$	$A_2 = 4.79 \times 10^4\ \text{nm}^2$
$A_4 = 10^9\ \text{nm}^4$	$\beta = 2\ \text{eV}^{-1}$	-	$A_4 = 2.15 \times 10^9\ \text{nm}^4$

Recovery of the simulated transmittance and comparison of the three methods

The Swanepoel (SWA), the Chambouleyron (PUMA) and the here proposed methods are applied to the simulation depicted in figure A.1.2. In order to apply the Swanepoel method, we construct the envelopes through a spline algorithm reading off the extremes from the transmittance spectrum in the photon energy representation. In this way we reduce the separation between the extremes, thereby improving the envelope construction. Our method uses the same envelopes as in the case of Swanepoel, however only to obtain the T_α curve (step 3). The starting values for the fitting procedures can be estimated using the Swanepoel's method.

The Levenberg-Marquardt fit with fitting parameters A_0, A_2, A_4 and d is performed with a maximum of 500 iterations. The PUMA method runs in three stages consisting of 3000, 5000 and 50000 iterations, respectively. The thickness step search is of 20.0, 5.0 and 0.5 nm, respectively in the present application. No starting values but searching regions are

Tesis publicada con autorización del autor
No olvide citar esta tesis

ET LUX IN TENEBRIS LUCET MCMXVII PUCP

used in the PUMA procedure, which in this case were chosen containing the simulated values.

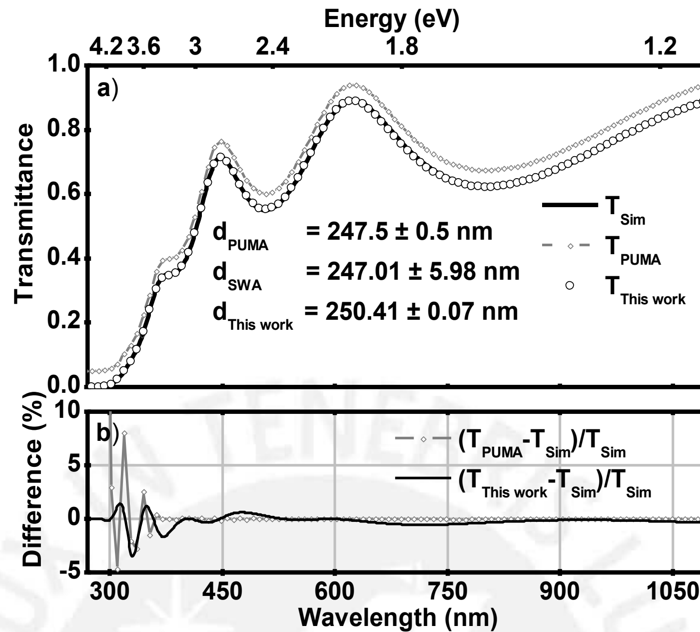

Figure A.1.3. Transmittance fits using the PUMA method and the method proposed here, with the respective calculated thicknesses, the fit of PUMA is shifted 0.05 units upwards for viewing reasons (a). Relative difference between the fits and the simulated curve (b).

The resultant transmittance curves are shown in figure A.1.3. There is an excellent agreement between the fitted transmittance spectra of our proposal and the PUMA method. Also the Swanepoel method fits equally well. The latter has not been included in the figure for clarity reasons only. The thickness agrees with the simulated value of 250 nm within error bars for all three methods, but the Swanepoel method shows the largest uncertainty. This can be traced back to its critical dependence on the number of fringes in the transmittance spectra [Poe03]. Since the PUMA method and the present one are largely independent of this feature, the thickness determination produces more reliable values with lower uncertainty. In the low wavelength region both methods depart the most from the simulated spectrum. Nevertheless, our method shows less deviation, which hints at a more reliable thickness determination and a lower overall error, as compared to the PUMA method.

Tesis publicada con autorización del autor
No olvide citar esta tesis
PUCP

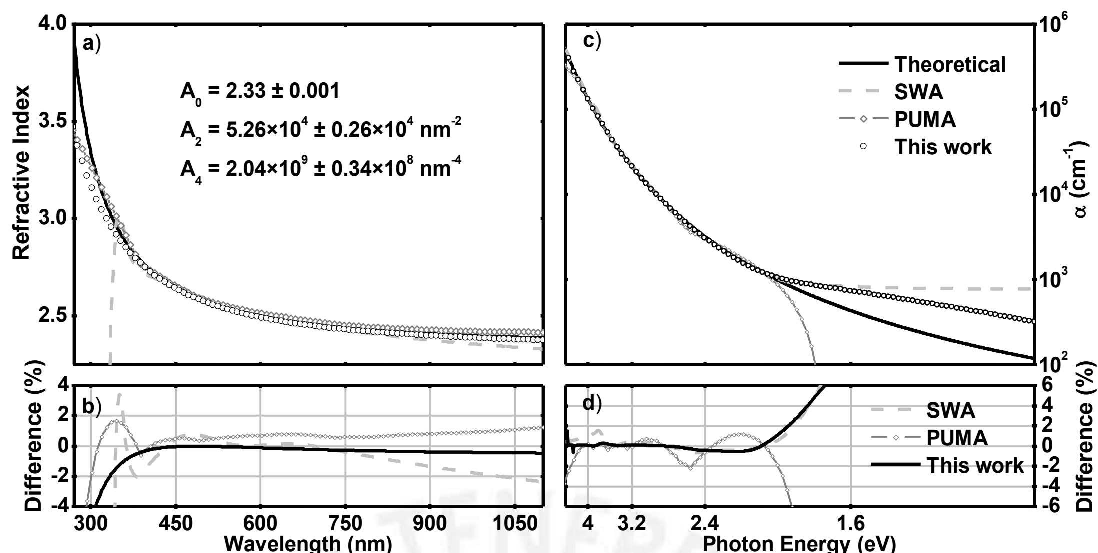

Figure A.1.4. Calculated refractive index using the three methods (a) and their relative difference with the simulation (b). Corresponding calculated absorption coefficients using the three methods (c) and their relative difference between the logarithm of the obtained α and the logarithm of the simulated α (d).

In figure A.1.4, upper panels (a) and (c), we show the refractive index and the absorption coefficient, respectively. These optical constants were calculated with the three methods and are plotted along with the theoretical ones. The lower panels (b) and (d) show the deviations of each method from the simulation. Note that the absorption coefficient is plotted in logarithmic scale, revealing a strong deviation of all three methods in the long wavelength region which cannot be seen in the respective transmittance curves (figure A.1.3). This is due to the fact that the absorption coefficient is calculated from equation A.1.3, thereby a small error in the vicinity of x near $x \rightarrow 0$ or $x \rightarrow 1$ tends to become a large error in $\log(\alpha)$ following $\Delta \log(\alpha) = \Delta x\, d/(x \log(x))$. This systematic error is clearly considerable in the short wavelength and long wavelength regions. However, the T_α curve is exactly the measured transmittance for the regime $x \rightarrow 0$ and therefore the error in the short wavelength region is attributed to the error of the measurement plus the difference between the transmittance equation and the experiment model and the error incurred by using a simplified refractive index model. On the other hand, in the long wavelength region ($x \rightarrow 1$) the T_α curve also contains the error carried along through the estimation of the envelopes. Nevertheless ours and Swanepoel's method come significantly closer to the simulated curve in comparison to the PUMA method. We

Tesis publicada con autorización del autor
No olvide citar esta tesis
PUCP

attribute this to the fact that only the PUMA method models the absorption coefficient which is obviously not optimized for very low absorption coefficients. We overcome here also the Swanepoel method, since it fails when the number of fringes is low, as already stressed.

Although we see a deviation in the retrieving of the absorption coefficient, even more remarkable is the deviation in the refractive index. Here we see why it is preferable to model the refractive index rather than the absorption coefficient and the related advantages of our method. In the case of the Swanepoel method this is to be expected since the strong absorption suppresses the interference fringes completely so that this method (depending essentially on the fringes) exhibits a break down at short wavelengths, as it is seen in the figure A.1.4.

Confidence analysis

For testing the reliability of the above mentioned methods, we added Gaussian white noise with a standard deviation of $\sigma_T = 0.01$ to the simulated transmittance spectrum (not shown). In this way, our simulation mimics more closely a real measurement. We simulated 48 transmittance spectra with same film parameters. The three methods were applied to these simulations. Fits on the resulting refractive index and absorption coefficient were performed, from which the Cauchy expansion parameters were obtained. In the case of the absorption coefficient we recovered the parameters of the Cauchy-Urbach model. Since it is not possible to determine α_0 and E_0 independently [Gue11] we rewrite equation A.1.5 in the logarithm scale as

$$\psi = \psi_0 + \beta E + \ln(E),$$

where

$$\psi = \ln(\alpha) \text{ and } \psi_0 = \ln(\alpha_0) - \beta E_0.$$

Tesis publicada con autorización del autor
No olvide citar esta tesis
PUCP

The intercept of this curve ψ_0 and the Urbach slope β are calculated through a fit. The fitted parameters obtained from the calculated curves are used to compare precision and accuracy of the methods.

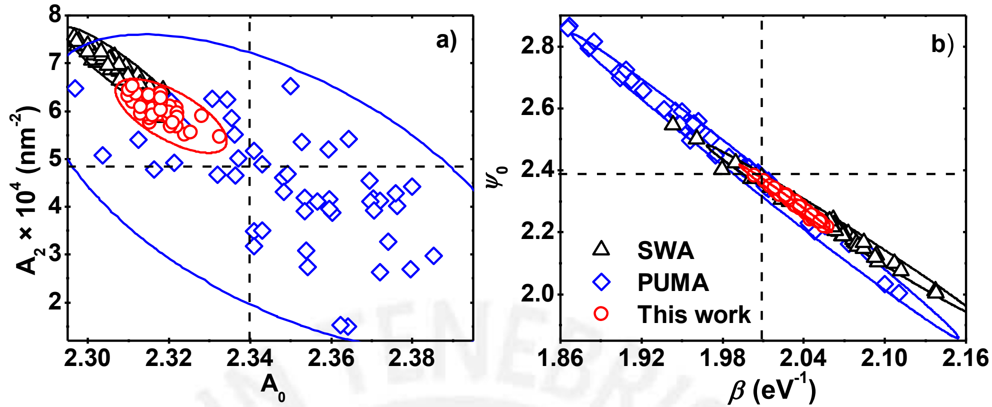

Figure A.1.5. Refractive index (a) and the absorption coefficient (b) parameters for each method, along with the confidence regions at 95%. The high dispersion presented by PUMA is most likely due to the number of data points used in the optimization process. While in our method the number of data points used were 851, i.e. from 250 to 1100 nm with a step of 1 nm, PUMA uses a maximum of 200 points equaled spaced only. The theoretical values are denoted by the intersecting dashed lines.

At this point it is important to remark that the maximum number of data points used in the optimization process in the PUMA method is limited to 200. The authors recommend the use of 100 points. In the case of the Swanepoel method the number of data points used in the calculations is limited only by the number of points generated through the interpolation of the envelopes. In the case of our method, the number of used data points in the fitting procedure is limited only by the measurement itself. These features have an impact when comparing the methods. For instance, the confidence regions become broader if there are fewer points to fit.

Tesis publicada con autorización del autor
No olvide citar esta tesis
PUCP

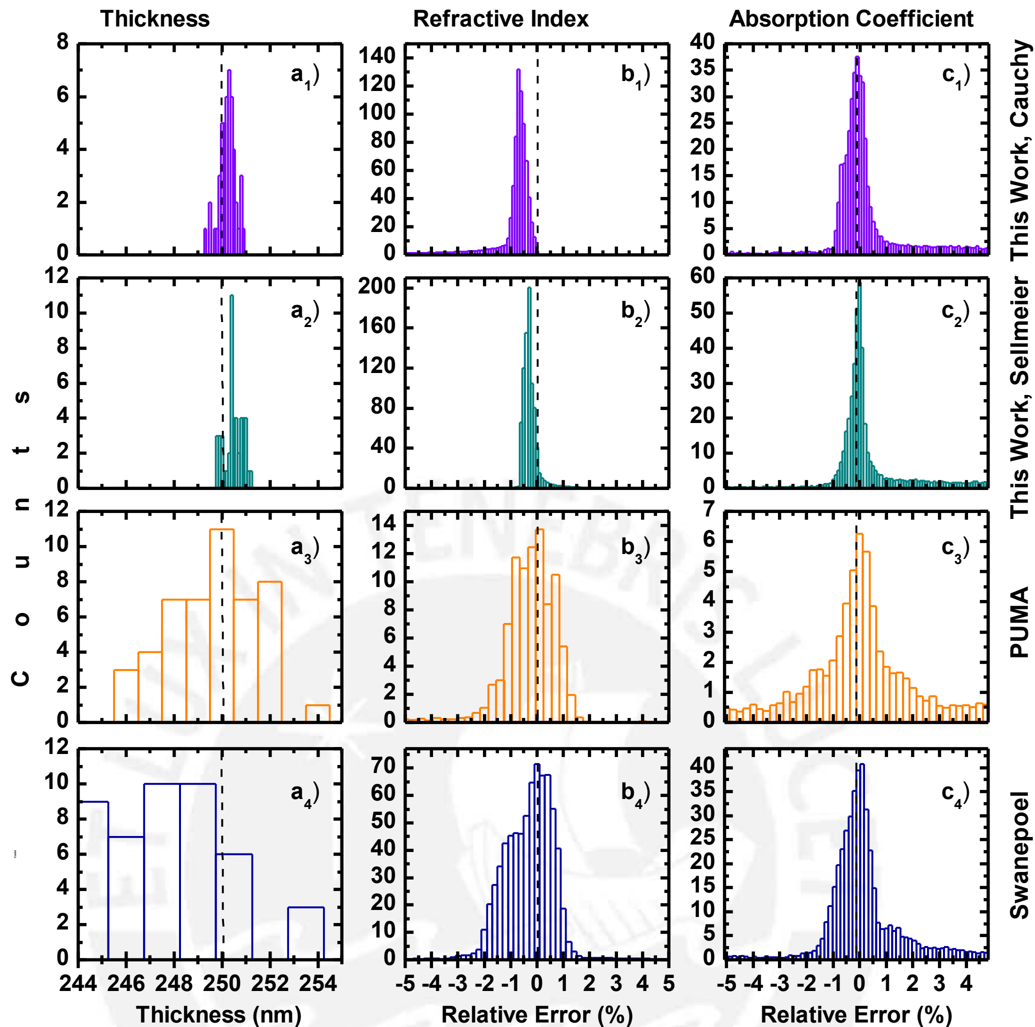

Figure A.1.6. Calculated thickness distribution for the 48 simulations (a). Cumulative relative error histograms of the refractive index (b) and absorption coefficient (c). The histograms are generated after applying the three methods to the 48 simulations. Additionally, for comparison reasons we apply the here proposed method using the Sellmeier equation to recover the refractive index. Notice that even when using the Sellmeier model, both the thickness and refractive index exhibit an off shift to the ideal value of 0.5 nm and 0.25%, respectively.

The parameters corresponding to the Cauchy model fit and the Cauchy-Urbach model fit with confidence regions of 95% are plotted in figure A.1.5. The dashed lines indicate the expected parameters. The recovered values should be as close as possible to them. The ellipses (closed lines) show the confidence regions at 95% confidence for each method. The confidence in a method can be characterized by two indicators: First, the smaller the area of the confidence ellipses, the more reliable is the method. Second, the confidence

Tesis publicada con autorización del autor
No olvide citar esta tesis
PUCP

ellipses should be centered at the true value. It is evident that our method overcomes the other ones, since it has the smallest confidence ellipses in all cases, especially for the parameters of the absorption coefficient. Note that although our method is off-centered for the model of the refractive index, it is still closer to the simulated value than in the case of the Swanepoel method. It should be mentioned that the PUMA method can be enhanced by augmenting the number of iteration loops. Nevertheless, the related increase of calculation time makes this approach impractical. The iterations in the present work corresponding to 48 fits where performed in a cluster of 48 cores (one fitting procedure per core). It took 33 hours and 20 min. A lower number of iteration loops (e.g. 500, 2500 and 5000 for the respective stage) shortened the calculation time to 20 min approximately, thereby reducing the accuracy of the calculation. The fitting procedure here proposed takes no more than one minute. The main time-consuming part of the proposed method is the estimation of the envelopes.

The results concerning the thickness calculation are depicted in figure A.1.6. Additionally in order to go through the behavior of the displayed optical constants recovery shown lines above, we construct histograms of the overall relative difference between the calculated curves of the refractive index and absorption coefficient with their theoretical counterparts (see figure A.1.6). The simulated thickness is 250 nm. Our and the PUMA method are well centered at this value. Notice the achieved low dispersion of our method in contrast to PUMA and Swanepoel's. The latter even demonstrates clearly its unreliability in the determination of the thickness, mainly due to the low number of interference fringes to be used in the thickness calculation procedure. Furthermore, the systematical bias of the method proposed here that was noted in figure A.1.5 is also recovered in these histograms.

Final remarks

Finally it is important to remark the reliability of the three methods that have been compared above, concerning their capability to measure the Urbach and Tauc regions of the absorption coefficient. In order to do so we simulate the absorption coefficient using

Tesis publicada con autorización del autor
No olvide citar esta tesis
ET LUX IN TENEBRIS LUCET MCMXVII PUCP

the equation 3.1.23 proposed in section 3.1 so as to distinguish the Urbach and Tauc regions (see figure A.1.7).

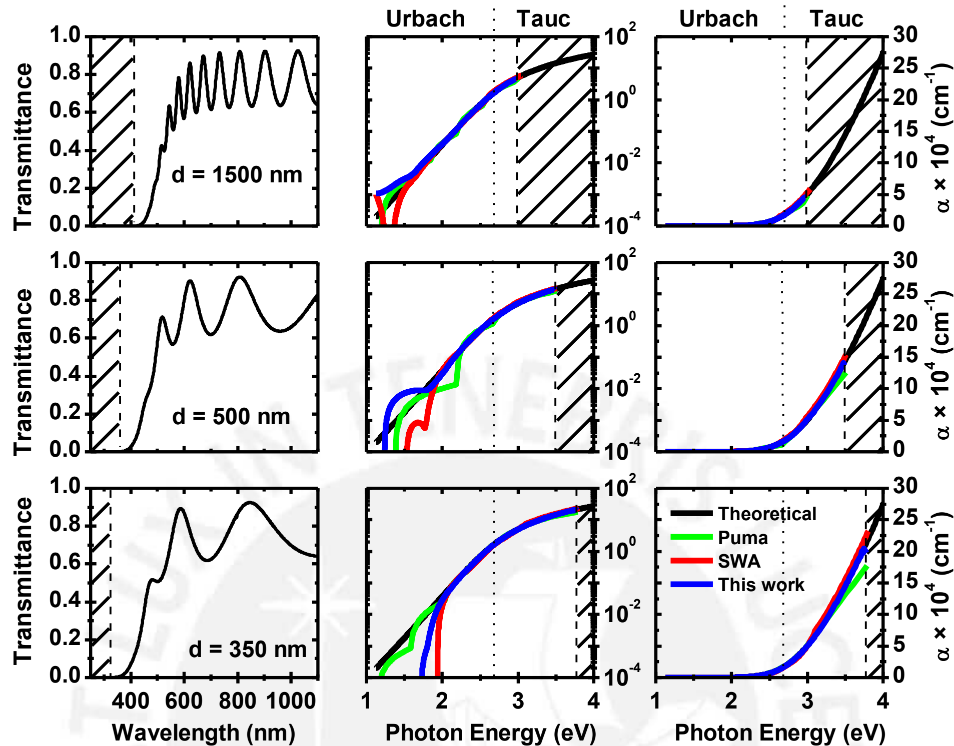

Figure A.1.7. Simulated transmittance in which the absorption coefficient was modeled with equation 3.1.23 ($\alpha_0 = 12 \times 10^5$ cm^{-1} eV, $1/\beta = 150$ meV and $E_0 = 2.5$ eV) for three different thicknesses (a). Recovered absorption coefficient shown in two scales in order to observe the compromise between the thickness and the reliability of the methods to extract the absorption coefficient in the Urbach and Tauc regions (b) and (c). The shadowed region denotes a fixed sensitivity limit ($T \geq 10^{-3}$).

Notice that for thicker samples the three methods are able to obtain the absorption coefficient with a good reliability, however the sensitivity limit limits the spectral extent of the measured absorption coefficient and therefore the fundamental absorption region is screened by the absorbance of the film as it is shown by the shadowed region in figure A.1.7. This behavior establishes a compromise between the thickness and capability to measure the fundamental absorption of thin films. Thenceforth, if we reduce the thickness of the film, the number of interference fringes is also reduced and therefore the capability of the methods that take advantage of the fringes to calculate the thickness drops dramatically (e.g. SWA). Moreover, the fitting methods, PUMA and the here proposed,

Tesis publicada con autorización del autor
No olvide citar esta tesis
PUCP

can still calculate the absorption coefficient. However while PUMA calculates the Urbach region robustly it fails in the fundamental absorption region contrary to the obtained absorption coefficient by the SWA and the here proposed methods. In this sense and based on what is exposed in this appendix we select the method proposed here to measure the thickness and fundamental absorption region of the thin films under study.

A.2 Multiphonon transitions

The static interaction between 4f electrons and the surrounding ions give rise to crystal field splitting. Additionally the dynamic crystal field with 4f-electrons produces phenomena that should be considered. This interaction is partly responsible for the occurrence of the 4f-4f transitions, and is the origin of most of the line widths observed in optical spectra. An excited RE can decay via the emission of phonons instead of a photon. Such transitions are called multiphonon transitions and are the result of the modulations of the crystal field due to vibrations of the ligands. This electron-phonon interaction was named H_L in equation 3.2.1 and corresponds to the dynamic component of the crystal field. While the static component was developed in section 3.2 and was named H_{CF} in the Hamiltonian, here is renamed $H_{CF-static}$ and we will focus on the dynamic component $H_{CF-dynamic} = H_L$, see equations A.2.1 and A.2.2.

$$H_{CF} = H_{CF-static} + H_{CF-dynamic} \qquad \text{(A.2.1)}$$

$$H_{CF-dynamic} = \sum_i \frac{\partial V}{\partial Q_i} + higher\ order\ terms \qquad \text{(A.2.2)}$$

In equation A.2.2 V is the potential experimented by the electrons and Q_i are the normal vibrational modes. The first and higher order terms describe the modulations of the crystal field due to the vibration of the ligands. This couples the motion of the electron to the motion of the lattice allowing phonon transitions between electronic states see figure A.2.1.

Tesis publicada con autorización del autor
No olvide citar esta tesis
ET LUX IN TENEBRIS LUCET MCMXVII PUCP

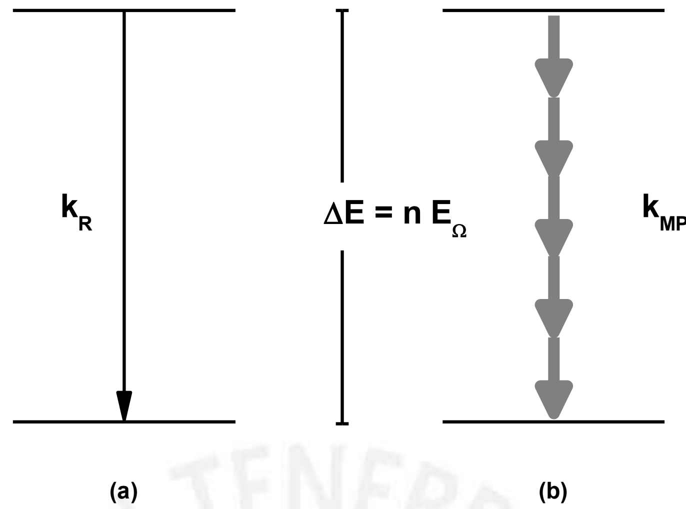

Figure A.2.1. Two level system showing the radiative electronic transition (a) and multiphonon electronic transition (b). The phonon emission is denoted by a thick gray arrow. The energy difference ΔE between states matches with the number n of emitted phonons. k_R and k_{MP} stand for the radiative and multiphonon electronic transition rates, respectively.

In order to develop an expression for the multiphonon decay rate k_{MP} one may take the first order to the nth term of the perturbation in equation A.2.2 or viceversa. In any case, the result takes the form shown in equation A.2.3 where ξ is a constant much less than unity. Equation A.2.3 leads to the energy gap law (see equation A.2.4).

$$k_{MP}(n) = k_{MP}(n-1)\xi \qquad \text{(A.2.3)}$$

$$k_{MP}(n) = k_0 \exp(-\,\varepsilon\,\Delta E) \qquad \text{(A.2.4)}$$

In equation A.2.4, k_0 is a constant, ΔE is the energy difference to the next lowest state and ε is a constant that describes the ion-lattice coupling strength and is determined empirically. The energy gap law has been found to be valid in RE ions [Vij06, Web73]. Additionally, an alternative procedure for developing the description of the multiphonon decay rate is to express a non-adiabatic interaction Hamiltonian in the adiabatic approximation, leading to a similar energy gap law for the case of RE ions. The

Tesis publicada con autorización del autor
No olvide citar esta tesis
ET LUX IN TENEBRIS LUCET MCMXVII PUCP

temperature dependence of this process is obviously related to the number of available phonons in the host, in particular the high energy phonons. The high energy phonons play the dominant role since fewer phonons are required, thus lowering the order of the process. The average occupation number of phonons in the ith mode is $N(\nu_i) = (\exp(h\nu_i/k_B T) - 1)^{-1}$, and the emission of a phonon is proportional to $(N(\nu_i) + 1)$. The nth order multiphonon decay rate goes as $(N(\nu_i) + 1)^n$. This temperature dependence has been verified [Vij06, Moo70].

Finally, observations have led to the following thumb rule for RE ions: if the energy difference ΔE to the next lowest level requires seven phonons or more, the dominant decay mechanism is radiative. Otherwise is more likely that the electronic transition occurs non-radiatively.

A.3 Up-conversion

Up-conversion concerns to the processes whereby a system lets say excited with $\hbar\omega_1$ photons emits photons with an energy $\hbar\omega_2 \gg \hbar\omega_1$. Figure A.3.1 depicts the possible up-conversion paths. These are summarized as follows:

i) The excited state absorption process (ESA) which involves a single ion. In this process two photons are absorbed sequentially, the intermediate state should remain sufficiently enough till the second photon is absorbed. Er^{3+} is an example of this process when excited with a high power density [Ken02].

ii) Two-photon absorption (TPA). A single ion is also involved, and in this case, two photons are absorbed simultaneously and the intermediate state is actually a virtual one.

iii) Up-conversion by energy transfer (ETU). In this case the activator is initially in an excited state and reach a higher energy state after the energy transfer from the sensitizer (see figure A.3.1). Additionally there is the possibility of cooperative energy transfer upconversion involving more ions, such process has been observed but in general is very weak [Auz04].

Tesis publicada con autorización del autor
No olvide citar esta tesis
PUCP

Upconversion processes are nonlinear due to the fact that they require the absorption of at least two photons. ESA and ETU are the most common. Experimentally these two mechanisms can be distinguished by examining the system's response to pulsed laser excitation. For instance, in the case of ESA-type upconversion, the rise time is within the lifetime of the pump laser pulse. Whilst for the ETU-type the luminescence peak appears after the laser pulse is over [Vij06].

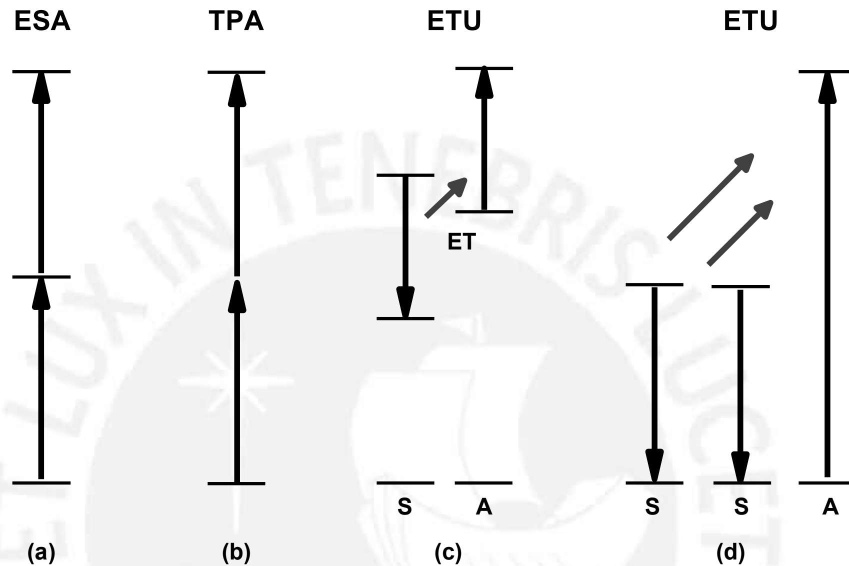

Figure A.3.1. Possible upconversion processes: excited state photon absorption (a), two photon absorption (b), two ions upconversion by energy transfer (c), and three ions cooperative energy transfer upconversion (d).

A.4 On the conversion of atomic concentration of RE into average ion interdistance

An increase in the RE concentration in the host matrix can be translated into a decrease of the mean RE ion interdistance. In order to calculate this average distance it is first necessary to convert the atomic concentration in number density. Thenceforth, using the number density and assuming a random distribution of REs in the solid the mean REs interdistance is calculated.

On the conversion of the atomic concentration of REs into number density

The aim is to convert the RE concentration given in atomic % of a host solid with a known stoichiometry into number density, that is the number of RE atoms per unit cubic

Tesis publicada con autorización del autor
No olvide citar esta tesis
PUCP

cm. Let us take for example the SiC:Tb material and assume that the ratio of Si and C atoms is 1:1 independently of the doping. ρ is the mass density of the doped film, m the total mass within a finite volume V of the film. Within this finite volume we have a total number of N atoms which is the sum of the different particles, silicon, carbon and terbium:

$$N = N_{\mathrm{Si}} + N_{\mathrm{C}} + N_{\mathrm{Tb}} \tag{A.4.1}$$

Dividing by N we obtain the atomic concentration of the individual species:

$$\frac{N_{\mathrm{Si}}}{N} + \frac{N_{\mathrm{C}}}{N} + \frac{N_{\mathrm{Tb}}}{N} = n_{\mathrm{Si}} + n_{\mathrm{C}} + n_{\mathrm{Tb}} = 1 \tag{A.4.2}$$

Additionally, the total mass can be expressed as a sum of the individual atomic masses:

$$m = N_{\mathrm{Si}} m_{\mathrm{Si}} + N_{\mathrm{C}} m_{\mathrm{C}} + N_{\mathrm{Tb}} m_{\mathrm{Tb}} \tag{A.4.3}$$

Now, from equations A.3.2 and A.3.3 we can write

$$\begin{aligned} \rho = \frac{m}{V} = \frac{N_{\mathrm{Si}} m_{\mathrm{Si}} + N_{\mathrm{C}} m_{\mathrm{C}} + N_{\mathrm{Tb}} m_{\mathrm{Tb}}}{V} \\ = \frac{N_{\mathrm{Si}} m_{\mathrm{Si}} + N_{\mathrm{C}} m_{\mathrm{C}} + N_{\mathrm{Tb}} m_{\mathrm{Tb}}}{N} \frac{N}{V} \\ \Rightarrow \rho = (n_{\mathrm{Si}} m_{\mathrm{Si}} + n_{\mathrm{C}} m_{\mathrm{C}} + n_{\mathrm{Tb}} m_{\mathrm{Tb}}) \frac{N}{V} \end{aligned} \tag{A.4.4}$$

and thus the total number density

$$\tilde{n} = \frac{N}{V} = \frac{\rho}{n_{\mathrm{Si}} m_{\mathrm{Si}} + n_{\mathrm{C}} m_{\mathrm{C}} + n_{\mathrm{Tb}} m_{\mathrm{Tb}}} \tag{A.4.5}$$

The terbium number density $\tilde{n}_{Tb} = \tilde{n} \times n_{Tb}$. Finally by taking the stoichiometry information, in this case the assumption of equal number of Si and C atoms we know that $n_{Si/C} = N_{Si/C}/N = 1/2(1 - n_{Tb})$ and we obtain the final form for the total and terbium number densities shown in equation A.4.6.

Tesis publicada con autorización del autor
No olvide citar esta tesis
PUCP

$$\tilde{n} = \frac{\rho}{1/2(1-n_{\mathrm{Tb}})m_{\mathrm{Si}} + 1/2(1-n_{\mathrm{Tb}})m_{\mathrm{C}} + n_{\mathrm{Tb}}m_{\mathrm{Tb}}}$$
$$\tilde{n}_{\mathrm{Tb}} = \frac{\rho}{1/2(1-n_{\mathrm{Tb}})m_{\mathrm{Si}} + 1/2(1-n_{\mathrm{Tb}})m_{\mathrm{C}} + n_{\mathrm{Tb}}m_{\mathrm{Tb}}} n_{\mathrm{Tb}} \quad \text{(A.4.6)}$$

Distribution of the nearest neighbor in a random distribution of particles

The following section concerns with the distribution of the nearest neighbor in a random distribution of particles in a defined volume [Cha43]. Per definition if we draw a circle with center in the particle P and radius the distance between the particles P and Q (see figure A.4.1), Q is the nearest neighbor of P always and only that there is no other particle within the circle. Make this geometric analysis for many particles and write down the number of particles within a distance r and $r+dr$. Relate this number to the unit line and this is the distribution density $\rho(r)dr$ of the nearest neighbor of a particle distribution. Notice that $\rho(r)$ is a line density and not a volume density, this makes sense for isotropic distributions, e.g. random distributed particles, since the volume distribution can be written as $w(r) = 4\pi\rho(r)$.

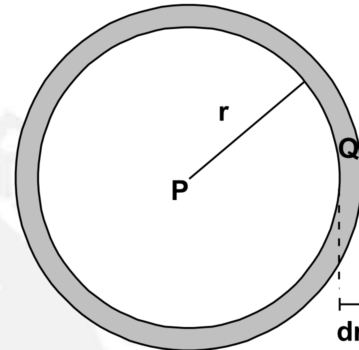

Figure A.4.1. Schematic representation of the nearest neighbor Q of a particle P.

The probability of finding at least one nearest neighbor particle within the ring with radius r and thickness dr is given by $\rho(r)dr$. Whilst the probability of finding any particle within the sphere of radius r is given by $\int_0^r dr'\rho(r')$ and the probability of finding no particle within the same radius is $1 - \int_0^r dr'\rho(r')$. Additionally, from the random distribution of particles follows that equal part of volumes are filled with equal parts of number of particles, thus any volume ratio is equal to the number of particle ratios:

Tesis publicada con autorización del autor
No olvide citar esta tesis
PUCP

$$\frac{V_{shell}}{V_{sphere}} = \frac{N_{shell}}{N_{sphere}} \tag{A.4.7}$$

Therefore we can write the probability of finding at least one nearest neighbor particle within the ring with radius *r* and thickness *dr* as shown in equation A.4.8, where $\tilde{n}_p$ is the particle density (or number denstity of particles) defines as $\tilde{n}_p = N_{sphere}/V_{sphere}$.

$$\begin{aligned} \rho(r)dr &= \left(1 - \int_{r_0}^{r} dr'\rho(r')\right) N_{\text{shell}} \\ &= \left(1 - \int_{r_0}^{r} dr'\rho(r')\right) \frac{V_{\text{shell}}}{V_{\text{sphere}}} N_{\text{sphere}} \\ &= \left(1 - \int_{r_0}^{r} dr'\rho(r')\right) 4\pi(r^2 - r_0^2)dr\, \tilde{n}_p \end{aligned} \tag{A.4.8}$$

Canceling the term *dr* in equation A.4.8 we obtain the integral equation for $\rho(r)$ as shown in equation A.4.9. Notice that in the limiting case for the particle radius r_0 then $\rho(r \to r_0) = 4\pi(r^2 - r_0^2)\tilde{n}_p$.

$$\begin{aligned} \rho(r) &= \left(1 - \int_{r_0}^{r} dr'\rho(r')\right) 4\pi r^2 \tilde{n}_p \\ &\Rightarrow \frac{\rho(r)}{4\pi(r^2 - r_0^2)\tilde{n}_p} = 1 - \int_{r_0}^{r} dr'\rho(r') \end{aligned} \tag{A.4.9}$$

In order to solve the integral equation shown previously, it is convenient to convert it into a differential equation (by applying the operator d/dr on both sides) and perform the following substitution:

Tesis publicada con autorización del autor
No olvide citar esta tesis
PUCP

$$\frac{\boldsymbol{d}}{\boldsymbol{dr}}\left(\frac{\rho(r)}{4\pi(r^2-r_0^2)\tilde{n}_p}\right)=\frac{\boldsymbol{d}}{\boldsymbol{dr}}\left(1-\int_{r_0}^{r}dr'\rho(r')\right)=-\rho(r)$$

$$\boldsymbol{f(r)}:=\frac{\boldsymbol{\rho(r)}}{\boldsymbol{4\pi(r^2-r_0^2)\tilde{n}_p}} \tag{A.4.10}$$

$$\Longrightarrow \frac{d}{dr}f=-4\pi(r^2-r_0^2)\tilde{n}_p f$$

$$\Longrightarrow f'+4\pi(r^2-r_0^2)\tilde{n}_p f=0$$

The standard differential equation can be solved by the procedures of separation of variables. It follows as shown in the equation A.4.11, where the limit case $f(r\to r_0)=1$ has been used.

$$\frac{df}{f}=-4\pi(r^2-r_0^2)\tilde{n}_p \quad \Rightarrow \int_{f(r_0)}^{f(r)}\frac{df}{f}=-4\pi\tilde{n}_p\int_{r_0}^{r}dr\,r^2$$

$$\Rightarrow \ln\frac{f(r)}{f(r_0)}=-\frac{4}{3}\pi\tilde{n}_p(r^3-r_0^3) \tag{A.4.11}$$

$$\Rightarrow f(r)=f(r_0)\exp\left(-\frac{4}{3}\pi\tilde{n}_p(r^3-r_0^3)\right)$$

$$f(r)=\exp\left(-\frac{4}{3}\pi\tilde{n}_p(r^3-r_0^3)\right)$$

Finally we obtain the unknown distribution as depicted in equation A.4.12. Notice that this distribution is asymmetric, therefore the mean distance of the nearest neighbor does not coincide with the most probable distance.

$$\rho(r)=4\pi(r^2-r_0^2)\,\tilde{n}_p\exp\left(-\frac{4}{3}\pi\tilde{n}_p(r^3-r_0^3)\right) \tag{A.4.12}$$

The mean distance is calculated as:

$$\bar{r}=\int_0^\infty dr\,r\,\rho(r)=\int_0^\infty dr\,4\pi r^3 n\,e^{-\frac{4}{3}\pi n r^3}=\frac{\Gamma\left(\frac{4}{3}\right)}{\left(\frac{4\pi}{3}\right)^{1/3}}n^{-1/3} \tag{A.4.13}$$

$$\approx 0.55396\ldots n^{-1/3}$$

Tesis publicada con autorización del autor
No olvide citar esta tesis
ET LUX IN TENEBRIS LUCET MCMXVII PUCP

While the most probable distance is calculated as the maximum value of the distribution $\rho(r)$:

$$\frac{d}{dr}\rho(r) = 0 \Rightarrow \ r_{max} = \frac{1}{(2\pi)^{1/3}} n^{-1/3} \approx 0.541926 \ldots n^{-1/3} \tag{A.4.14}$$

Tesis publicada con autorización del autor
No olvide citar esta tesis
PUCP

References

[Aba99] B. Abay, H. S. Güder, H. Efeoglu, and Y. K. Yogurtçu, J. Phys. D: Appl. Phys. **32** (1999) 2941.

[Abe11] S. Abedrabbo, B. Lahlouh, A.T. Fiory J. of Phys. D: Appl. Phys. **44** (2011) 315401.

[Ada04] Binary Rare Earth Oxides, edited by G. Adachi, N. Imanaka, Z.C. Kang, Kluwer Academic Publishers, 2004.

[Ada07] D. Adachi, R. Kitike, J. Ota, T. Toyama and H. Okamoto, J. Mater. Sci.: Mater. Electron. **18** (2007) S71.

[All81] P.B. Allen, and M. Cardona, Phys. Rev. B **23** (1981) 1495.

[And58] P. W. Anderson Phys. Rev. **109** (1958) 1492-505.

[Auz04] F. Auzel, Chem. Rev. **104** (2004) 139.

[Bar10] A. Barybin and V. Shapovalov, *International Journal of Optics*, **2010** (2010) 137572 1-18

[Bas09] B. Bastek, F. Bertram, J. Christen, T. Hempel, A. Dadgar, and A. Krost, Applied Physics Letters **95** (2009) 032106.

[Bec07] J. Becquerel Le Radium **4** (1907) 328

[Ben12] F. Benz and H. Strunk, AIP Advances **2** (2012) 042115

[Ben13] F. Benz, J. A. Guerra, Y. Weng, A. R. Zanatta, R. Weingärtner, H. P. Strunk, J. Lumi. **137** (2013) 73.

[Ben13p] F. Benz, J. A. Guerra, Y. Weng, R. Weingärtner, H. P. Strunk, Phys. Stat. Sol. **10** (2013) 109.

[Bic10] M. Bickermann, B. Epelbaum, O. Filip, P. Heimann, S. Nagata, and A. Winnacker, Phys. Stat. Sol. **24** (2010) 21.

[Bra10] A. Braud, Topics in Applied Physics, Chap. 9, **124** (2010) 269-307.

[Bul87] J. Bullot, Phys. Stat. Sol. (b) **143** (1987) 345.

[Cha43] S. Chandrasekhar, Rev. Mod. Phys. **15** (1943) 86.

[Cha97] I. Chambouleyron et al, *Appl. Opt.* **36** (1997) 8238-4.

[Cha98] I. Chambouleyron, J. M. Martinez, A. C. Moretti and M. Mulato, *Thin Solid Films* **317** (1998) 133-6.

[Che10] S. Chen, B. Dierre, W. Lee, T. Sekiguhi, S. Tomita, H. Kudo and K. Akimoto, Appl. Phys. Lett. **96** (2010) 181901.

[Cod81] G.D. Cody, T. Tiedje, B. Abeles, B Brooks and Y. Goldstein, Phys. Rev. Lett. **47** (1981) 1480-3.

[Cod05] G. D. Cody, Mater. Res. Soc. Symp. Proc. **862** (2005) A1.3.1.

[Cui01] J. Cui, Rusli, S.F. Yoon, M.B. Y, K. Chew, J. Ahn, Q. Zhang, E.J. Teo, T. Osipwicz, and F. Watt, J. Appl.

[Dex53] D.L. Dexter J. Chem. Phys. **21** (1953) 836

[Die68] G. H. Dieke *Spectra and Energy Levels of Rare Earth Ions in Crystals,* Crosswhite, H. M. Crosswhite and H. Crosswhite, (NY: Interscience, 1968).

[Dor03] P. Dorenbos, J. Phys. Cond. Mat. **15** (2003) 455.

[Dor08] P. Dorenbos and A.J.J. Bos Rad. Meas. **43** (2008) 139.

Tesis publicada con autorización del autor
No olvide citar esta tesis
ET LUX IN TENEBRIS LUCET MCMXVII PUCP

[Dor13] P. Dorenbos ECS Journal of Solid State Science and Technology 2, 2013.

[Dow71] J.D. Dow and D. Redfield, Phys. Rev. Lett. **26** (1971) 762

[Dun83] D. J. Dunstan, J. Phys. C: Solid State Phys. **16** (1983), L567-L571.

[Dun85] D. J. Dunstan, J. Phys. C: Solid State Phys. **18** (1985), 5429.

[Ena08] M. Enachi, V. Trofim, V. Coseac, I.M. Tiginyanu, V.V. Ursaki, Moldavian Journal of the Physical Sciences, **8** (2009) 207.

[För46] T. Förster, Naturwiss. **33** (1946) 166.

[För59] T. Förster, Discuss. Faraday Soc. **27** (1959), 7-17.

[För60] T. Förster, Z. Elektrochem. **64** (1960) 157.

[Fre62] A. J. Freeman and R. E. Watson, *Phys. Rev.* **127** (1962) 2058.

[Fuh97] W. Fuhs, I. Ulber, G. Weiser, M. Bresler, O. Gusev, A. Kuzentsov, V. Kudoyarova, E. Terukov and I. Yassievich, Phys. Rev. B. **56** (1997) 9545.

[Gal68] J. B. Gallivan, J. S. Brinen and J. G. Koren J. Mol. Spectros. **26** (1968) 24-35.

[God94] M. Godlewski, K. Swiatek, and B. Monemar, J. Luminescence **58** (1994) 303.

[Gon02] J. Gonzáles-Leal, R. Prieto-Alcón, J. Angel, D. A. Minkov and E. Márquez, *Appl. Opt.* **41** (2002) 7300-8.

[Gör98] C. Görller-Walrand and K. Binnemans, Handbook on the Physics and Chemistry of Rare Earths, edited by K.A. Gscheidner Jr. and L. Eyring, volume 25, pp. 101–264, Elsevier Science B.V., 1998.

[Gru01] J. Gruber et al, J. Appl. Phys. **89** (2001) 7973

[Gru02] J. Gruber et al, J. Appl. Phys. **91** (2002) 2029

[Gru02a] J. Gruber et al, J. Appl. Phys. **92** (2002) 5127

[Gue10t] J. A. Guerra, *Determination of the optical bandgap of amorphous $(SiC)_{1-x}(AlN)_x$ films produced by radio frequency dual magnetron sputtering* (Master Thesis PUCP, Lima-Peru, 2010).

[Gue11] J. A. Guerra, L .Montañez, O. Erlenbach, G. Galvez, F. De Zela, A. Winnacker, and R. Weingärtner, J. Phys. Conf. Ser. **274** (2011) 012113.

[Gue13] J.A. Guerra, F. Benz, A. Zanatta, H. P. Strunk, A. Winnacker and R. Weingärtner, Phys. Stat. Sol. **10** (2013) 68.

[Gue13m] J.A. Guerra, L. Montañez, F. De Zela, A. Winnacker and R. Weingärtner, MRS Proc. **1536** (2013) 753.

[Gue13q] J.A. Guerra, F.Benz, L. Montañez, R. Grieseler, P. Schaaf, F. De Zela, A. Winnacker, H. P. Strunk and R. Weingärtner, MRS Proc. **1571** (2013) 768.

[Gue15] J.A. Guerra, L. Montañez, A. Winnacker, F. De Zela and R. Weingärtner, Phys. Stat. Sol. **12** (2015) 1183.

[Gue16] J.A. Guerra, et al, J. Phys. D: Appl. Phys. **49** (2016) 195102.

[Hua10] C. Huang *Rare Earth Coordination Chemistry: Fundamentals and Applications*, John Wiley & Sons (Asia) 2010.

[Hub79] D.L. Huber, Phys. Rev. B. **20** (1979) 2307

[Hüf78] S. Hüfner *Optical Spectra of Transparent Rare Earth Compounds*, Academic Press, New York-San Francisco-London 1978.

[Jam11] B.C. Jamalaiah, M.V. Vijaya Kumar, K. Rama Gopal, Physica B **406** (2011) 2871.

Tesis publicada con autorización del autor
No olvide citar esta tesis
ET LUX IN TENEBRIS LUCET MCMXVII PUCP

[Jan03] A. Janotta, M. Schmidt, R. Janssen, Stutzmann, and Ch. Buchal, Phys. Rev. B **68** (2003) 165207.

[Jud62] B. R. Judd Phys. Rev. **127** (1962) 750.

[Jud66] B. R. Judd, Phys. Rev. **141** (1966) 4.

[Jud97] B. R. Judd *Operator thecniques in atomic spectra* Princeton University Press 1997.

[Kal94] J.A. Kalomiros, A. Papadopoulos, S. Logothetidis, L. Magafas, N. Georgoulas, and A. Thanailakis, Phys. Rev. B **49** (1994) 8191.

[Kan05] T. Kaneko, D. Nemoto, A. Horiguchi and N. Miyakawa, J. Cryst. Grow. **275** (2005) 1097.

[Ken02] A. J. Kenyon, Progress in Quantum Electronics **26** (2002) 225-84.

[Kiel65] T. Kiel, Phys. Rev. 140 A601, 1965.

[Kim02] K. Yong-Tak, C. Sung-Min, H. Byoungyou, S. Su-Jeong, J. Gun-Eik and Y. Dae-Ho, Mater. Trans. **43** (2002) 2058.

[Kir06] A. V. Kir'yanov, Y. O. Barmenkov, and I. L. Martinez, Opt. Exp. **14** (2006) 3981.

[Kit00] I.V. Kityk, A. Kassiba, K. Plucinski, J. Berdowski, Phys. Lett. A **265** (2000) 403.

[Kiy04] Kiyotaka Wasa, Makoto Kitabatake, and Hideaki Adachi, *Thin Fim Materials Technology - Sputtering of Compound Materials* (Springer, Heidelberg, 2004).

[Kuz09] H. Kuzmany, *Solid State Spectroscopy: An Introduction,* 2nd edition, Springer 2009.

[Lan82] J. S. Lannin Semicond. Semimetals B, **21** (1982) 162.

[Lan84] J. S. Lannin, L. J. Pilione, S. T. Kshirsagar, R. Messier and R. C. Ross, Phys. Rev. B **26** (1982) 1071.

[Lee00] M. Lee and S. F. Bent, J. Appl. Phys. **87** (2000) 4600.

[Lee03] D.S. Lee, and A.J. Steckl, Appl. Phys. **83** (2003) 2094.

[Let10] M. Letz, A. Gottwald, M. Richter, V. Liberman, and L. Parthier, Phys. Rev. B **81** (2010) 155109.

[Lia13] H. Lian, Z. Hou, M. Shang, D. Geng, Y. Zhang, J. Lin, Energy **57** (2013) 270.

[Loz93] H.J. Lozykowski, Phys. Rev. B **48** (1993) 17758

[Loz07] H.J. Lozykowski and W. M. Jadwisienczak Phys. Stat. Sol. **244** (2007) 2109.

[Lu02] F. Lu, R. Carius, A. Alam, M. Heuken and Ch. Buchal J. Appli. Phys. **92** (2002) 2457.

[Mac86] H. A. Macleod, *Thin-Film Optical Filters,* 2nd edition, Institute of Physics, Bristol, UK, 1986.

[Mag98] L. Magafas, J. Non-Cryst. Solids **238** (1998) 158.

[Man76] J. C. Manifacier, J. Gasiot and J. P. Fillard, J. Phys. E: Sci. Instrum. **9** (1976) 1002-4.

[Men06] H. Mendel, S.B. Aldabergenova, R. Weingärtner, G. Frank, H.P. Strunk, A.A. Andreev, Opt. Mat. **28** (2006) 794.

[Mir11] S.M.C. Miranda, M. Peres, T. Monteiro, E. Alves, H.D. Sun, T. Geruschke, R. Vianden, K. Lorenz **33** (2011) 1139.

[Moo70] H.W. Moos, J. Luminescence **1** (1970) 2.

[Mon13] L. Montañez, J.A. Guerra, K. Zegarra, S. Kreppel, F. De Zela, and A. Winnacker, R. Weingärtner, Proc. of SPIE **8785** (2013) 87859S.

[Mor99] K. Morigaki *Physics of Amorphous Semiconductors*, London: World Scientific Publishing Company, 1999.

Tesis publicada con autorización del autor
No olvide citar esta tesis

[Mor82] C. A. Morrison and R. P. Leavitt (1982) *Handbook on the Physics and Chemistry of Rare Earths*. K. A. Gschneidner and L. Eyring, Amsterdam: North-Holland.
[Mos78] L. L. Moseley, and T. Lukes, Am. J. Phys. **46** (1978) 676.
[Mot79] N.F. Mott and E.A. Davis *Electronic Processes in Non-Crystalline Materials* Oxford: Clarendon 1979.
[Mue07] R.E. Muenchausen, L.G. Jacobsohnm, B.L. Bennet, E.A. McKigney, J.F. Smith, J.A. Valdez, and D.W. Cooke, J. Lumin **126** (2007) 838.
[Mus97] Musumeci, P., Reitano, R., Calcagno, L., Roccaforte, F., Makhtaris, A., Grimaldi, M.G., Philosophical Magazine B **76** (1997) 323.
[New00] D. Newman and B. Ng, editors, *Crystal Field Handbook*, Cambridge University Press, 2000.
[Nie63] C. W. Nielson and George F. Koster "Spectroscopic coefficients of the p^n, d^n, and f^n configurations" The M.I.T Press, Cambridge, 1963.
[Nyk06] M. Nyk, R. Kudrawiec, W. Strek, J Misiewicz **28** (2006) 767.
[ODo10] O'Donnel and Volkmar Dierolf, Topics in Applied Physics: *Rare Earth Doped III-Nitrides for Optoelectronic and Spintronic Applications* Springer 2010.
[Ofe62] G. S. Ofelt J. Chem. Phys. **37** (1962) 511-520.
[OLe95a] S. K. O'Leary, S. Zukotynski and J. M. Perz, Phys. Rev. B **52** (1995) 7795-7.
[OLe95b] S. K. O'Leary, S. Zukotynski and J. M. Perz, Phys. Rev. B **51** (1995) 4143-9.
[OLe98] S. K. O'Leary APL **72** (1998) 1332-4.
[OLe02] S. K. O'Leary J. Appl. Phys **92** (2002) 4276.
[OLe04] S. K. O'Leary J. Appl. Phys **96** (2004) 3680.
[Ora04] F. Orapunt, and S.K. O'Leary, Appl. Phys. Lett. **84** (2004) 523.
[Poe03] D. Poelman and P. F. Smet, *J. Phys. D: Appl. Phys.* **36** (2003) 1850.
[Pur90] H. G. Purwins and A. Lesson *Adv. Phys.* **39** (1990) 309.
[Raj03] T. Rajagopalan, X. Wang, B. Lahlouh, and C. Ramkumar, Partha Dutta, S. Gangopadhyay, J. Appl. Phys. **94** (2003) 5252.
[Raj63] K. Rajnak and B. Wybourne, Phys. Rev. **132** (1963) 280.
[Ric02] H.H. Richardson, P.G. Van Patten, D.R Richardson, and M.E. Kordesch, Appl. Phys. Lett **80** (2002) 2207.
[Run56] W. A. Runciman *Stark-splitting in crystals* Phil. Mag. **1** (1956) 1075.
[Ryu95] C. K. Ryu, H. Choi, K. Kim, Appl. Phys. Lett. **66** (1995) 2496.
[Sad99] A. Sadao *Optical Properties of Crystalline and Amorphous Semiconductors*, Boston: Kluwer Academic Publishers, 1999.
[Saj86] J. Sajeev, C. M. Soukoulis, M. H. Cohen, and E. N. Economou, Phys. Rev Lett. **57** (1986) 1777.
[Sal03] G. M. Salley, R. Valiente, and H. U. Güdel, Phys. Rev. B **67** (2003) 134111.
[Sha07] A. Shalav, B.S. Richards, M.A. Green, Sol. Energy Mater. Sol. Cells **91** (2007) 829.
[Sin03] J. Singh and K. Shimakawa *Advances in Amorphous Semiconductors*, London: Taylor & Francis, 2003.
[Sob72] I. Sobel'man, Introduction to the Theory of Atomic Spectra, First ed. Pergamon Press Ltd, Oxford, 1972.
[Sou84] C. M. Soukoulis, M. H. Cohen, and E. N. Economou, Phys. Rev. Lett. **53** (1984) 616.

Tesis publicada con autorización del autor
No olvide citar esta tesis
PUCP

[Spa90] Spanget-Larsen, J., Waluk, J. & Thulstrup, E.W. J. Phys. Chem. **94** (1990) 1800.

[Spe75] A.R. Speed, G. F. J. Garlick, and W.E. Hagston, Phys. Stat. Sol. (a) **27** (1975) 477.

[Spo79a] A.R. Spowart, J. Phys. C: Sol. Stat Phys. **12** (1979) 3369.

[Spo79b] A.R. Spowart, J. Phys. C: Sol. Stat Phys. **12** (1979) 3375.

[Ste99] A. J. Steckl and J. M Zavada MRS Bull **24** (1999) 16.

[Str91] R. A. Street *Hydrogenated Amorphous Silicon*, Cambridge: Cambridge University Press, 1991.

[Stu89] M. Stutzmann, Philosophical Magazine B, **60** (1989) 531.

[Sum04] C. Summonte, R. Rizzoli, M. Bianconi, A. Desalvo, D. Iencinella and F. Giorgis, J. Appl. Phys. **96** (2004) 3987.

[Swa83] R. Swanepoel, *J. Phys. E: Sci. Instrum.* **16** (1983) 1214-22.

[Tau68] J. Tauc, MRS Bull. **3** (1968), 37.

[Tes95] L. Tessler and I. Solomon, Phys. Rev. B. **52** (1995) 10962.

[Toy71] H. Sumi, and Y. Toyazawa, J. Phys. Soc. Jpn. **31** (1971) 342.

[Toy81] S. Abe and Y. Toyazawa, J. Phys. Soc. Jpn. **50** (1981) 2185.

[Urb53] F. Urbach Phys. Rev **92** (1953) 1324.

[Vas11] A.V. Vasin, Sh. Muto, Y. Ishikawa, A.V. Rusavsky, T. Kimura, V.S. Lysenko, A.N. Nazarov, Thin Solid Films **519** (2011) 2218.

[Vij06] D.R. Vij, *Handbook of Applied Solid State Spectroscopy,* Springer 2006.

[Vle37] J. H. Van Vleck *The Puzzle of Rare-Earth Spectra in Solids*, J. Phys. Chem **41** (1937) 67.

[Wak08] A. Wakahara, K. Takemoto, F. Oikawa, H. Okada, T. Ohshima, and H. Itoh, Phys. Stat. Sol. (a) **205** (2008) 56.

[Wan09] F. Wang, Z.G. Liu, Chem. Sic. Rev. **38** (2009) 976.

[Wan10] L. Wang, L. Shi, H. Jia, P. Du, Z. Xi, and D. Jin, Mater. Chem. Phys. **119** (2010) 490.

[Wan11] H.Q. Wang, M. Batentshuck, A. Osvet, L. Pinna, and C. J. Brabec. Adv. Maer. **24** (2011) 2675.

[Wan14] X. Wang, C. Liu, T. Yu and X. Yan Phys. Chem. Chem. Phys. **16** (2014) 13440.

[Web73] M.J. Weber, Phys. Rev. B **8** (1973) 54.

[Wei01] R. Weingärtner, M. Bickermann, S. Bushevoy, D. Hofmann, M. Rasp, T. L. Straubinger, P. J. Wellmann, and A. Winnacker, Materials Science and Engineering: B **80** (2001) 357.

[Wei02] R. Weingärtner, P. J. Wellmann, M. Bickermann, D. Hofmann, T. L. Straubinger, and A. Winnacker, Applied Physics Letters **80** (2002) 70.

[Wei06] R. Weingärtner, O. Erlenbach, A. Winnacker, A. Welte, I. Brauer, H. Mendel, H.P. Strunk, C.T.M. Ribeiro, A.R. Zanatta Optical Materials **28** (2006) 790.

[Wei10] R. Weingärtner, J.A. Guerra, O. Erlenbach, G. Gálvez, F. De Zela, A. Winnacker, Mater. Sci. Eng. B **174** (2010) 114.

[Wyb65] B. G. Wybourne, "*Spectroscopic Properties of Rare Earths*" Wiley, New York, 1965.

[Yen07] Phosphor Handbook 2nd Edition, edited by William M. Yen, Shigeo Shionoya, Hajime Yamamoto, CRC Press, 2007.

Tesis publicada con autorización del autor
No olvide citar esta tesis
PUCP

[YuC04] Y. Cardona *Fundamentals of Semiconductors* Springer 3rd Edition, 2004.

[Zan03] A. R. Zanatta Applied Physics Letters **82** (2003) 1395-7.

[Zan07] A.R. Zanatta, A. Khan, M.E. Kordesch, J. Phys.: Cond. Matt. **19** (2007) 436230.

[Zan09] A.R. Zanatta J. Phys. D: Appl. Phys. **42** (2009) 025109.

[Zan12] A. R. Zanatta J. Appl. Phys. **111** (2012) 123105.

[Zav03] J. Zavada, S. Jin, N. Nepa, J.Y. Lin, H.X. Jiang, P. Chow, B. Hertog, Appl. Phys. Lett. **84** (2004) 1061.

[Zha92] F. Zhang, H. Xue, Z. Song, Y. Guo, and G. Chen, Phys. Rev. B **46** (1992) 4590.

[Zim61] H. Zimmerman and N. Joop, Z. Electrochem. **65** (1961) 66.

Tesis publicada con autorización del autor
No olvide citar esta tesis
PUCP